Faculty of Engineering

The Effect of Specific Surface Area of Silicomanganese Slag as Cement Replacement on Properties of Concrete

Li Feng

Doctor of Philosophy
2026

The Effect of Specific Surface Area of Silicomanganese Slag as Cement Replacement on Properties of Concrete

Li Feng

A thesis submitted

In fulfillment of the requirements for the degree of Doctor of Philosophy

(Civil Engineering)

Faculty of Engineering
UNIVERSITI MALAYSIA SARAWAK
2026

DECLARATION

I declare that the work in this thesis was carried out in accordance with the regulations of Universiti Malaysia Sarawak. Except where due acknowledgements have been made, the work is that of the author alone. The thesis has not been accepted for any degree and is not concurrently submitted in candidature of any other degree.

Signature

Name: Li Feng

Matric No.: 19010147

Faculty of Engineering

Universiti Malaysia Sarawak

Date: 7 January 2026

ACKNOWLEDGEMENT

I am sincerely grateful to my supervisor, Professor Dr. Ng Chee Khoon, for his professional, continuous guidance and selfless help throughout my doctoral research. His academic insights have not only enhanced my capabilities in doctoral research but have also significantly contributed to my teaching and engineering management endeavours. I extend my heartfelt gratitude once again. I am also grateful to my co-supervisors, Dr. Idawati binti Ismail and Dr Leonard Lim Lik Pueh, who gave professional advice on my thesis. I am profoundly grateful to my family. Leaving my home in China, I embarked on a nearly two-year doctoral study in Malaysia. My wife, Mrs. Shi, has been my rock, offering unwavering support and understanding. She has always been shouldering the responsibilities of our family, which made it possible for me to focus on my studies. I am also deeply thankful to my classmates, especially Ms. Zhao and Mr. Imtiyaz, for their timely altruistic support and assistance. Furthermore, I am immensely grateful to my parents for their unconditional support and encouragement throughout my academic pursuits. I would like to extend my gratitude to the leaders and lecturers of the Faculty of Engineering. The professional courses and guidance they provided have been instrumental in my doctoral studies, greatly enriching my academic experience. Furthermore, I am thankful to the UNIMAS CGS and its dedicated staff for their friendly and helpful assistance to graduate students. The Spring Festival Gala and other events organized by them have made us feel the warmth of home, away from our homeland. Lastly, I would like to express my heartfelt thanks to the management of the Universiti Malaysia Sarawak for providing me with the opportunity to complete my studies in this esteemed institution. Thank you all for your support and contributions.

ABSTRACT

Silicomanganese slag (SiMnS), an electrolytic manganese byproduct, poses environmental risks through unsustainable storage/landfilling, leaching pollutants (e.g., heavy metals) into ecosystems, but pretreatment (drying/grinding) unlocks its pozzolanic potential for cement substitution in concrete, offering dual waste valorization and resource conservation. At present, most of the research on SiMnS concrete at home and abroad is limited to the influence of SiMnS content on concrete performance, and there is very little research on the effect of SiMnS specific surface area (SSA) on workability, mechanical properties, and durability of concrete. This study investigated the effects of the SSA of SiMnS on concrete properties. Employing a controlled variable approach, the experimental design sets SSA levels of 60 m^2/kg, 120 m^2/kg, 235 m^2/kg, and 400 m^2/kg with cement replacement ratios from 0% to 40%wt. Concrete specimens are prepared under standard curing conditions. Performance tests include slump measurement, compressive/flexural strength evaluation, freeze-thaw resistance, chloride ion penetration resistance, and sulfate attack resistance. Data analysis integrates the AHP-entropy method with statistical techniques to assess indicator weights. Results indicate that SiMnS with an SSA of 235 m^2/kg, when used to replace 10%wt of the cement, provides optimal performance in concrete. Concrete with this combination demonstrated enhanced compressive strength, improved resistance to freeze-thaw cycles, and higher sulphate and chloride ion penetration resistance compared to other configurations. The experimental data were statistically evaluated using a combination of the analytic hierarchy process (AHP) and the entropy weight method, referred to as the AHP-entropy method. Based on the comprehensive ranking of SiMnS SSA schemes, the optimal scheme (SSA = 235 m^2/kg, dosage = 10%wt) was identified, which aligns with the experimental conclusions, thereby validating the experimental results. When the SiMnS content exceeded

10%wt, or SSA surpassed 400 m²/kg, the compressive strength and durability decreased, indicating that excessive fineness or slag content could undermine the comprehensive properties of concrete. The findings show that the larger SSA of SiMnS enhances pozzolanic reactivity while appropriate SiMnS content balances strength and durability. However, excessive SiMnS content or a smaller SSA leads to reduced performance due to lower hydration efficiency and structural instability. This study demonstrates that SiMnS with a SSA of 235 m²/kg and 10% cement replacement optimally balances workability, mechanical strength (1.79% and 2.87% improvements in compressive and flexural strength, respectively), and durability (25% higher chloride resistance, 10.1% improved sulfate resistance). While higher SSA enhances pozzolanic reactivity, excessive replacement (>10%) or SSA (>400 m²/kg) reduces performance due to hydration inefficiency and microstructural instability. The AHP-entropy method validates this synergy, providing a data-driven framework to industrialize SiMnS utilization—reducing CO_2 emissions and landfill waste while advancing circular economy goals in construction. Future work should optimize SSA via grinding or admixtures and assess long-term environmental impacts, particularly the leaching effects of heavy metals.

Keywords: Silicomanganese slag, specific surface area, concrete, workability, mechanical property, durability, AHP-entropy method

Kesan luas permukaan khusus sanga silicomangan sebagai pengganti simen pada sifat konkrit

ABSTRAK

Slag silikomangan (SiMnS), sejenis hasil sampingan mangan elektrolitik, menimbulkan risiko alam sekitar melalui penyimpanan/pembuangan yang tidak lestari dan peleraian pencemar (contohnya logam berat) ke dalam ekosistem, tetapi rawatan awal (pengeringan/penggilingan) membuka potensi pozzolaniknya untuk penggantian simen dalam konkrit, menawarkan pemulihan sisa dua hala dan pemuliharaan sumber. Pada masa ini, terdapat sangat sedikit penyelidikan mengenai kesan luas permukaan spesifik (SSA) SiMnS terhadap kebolehkerjaan, sifat mekanikal, dan ketahanlasakan konkrit. Kajian ini menyiasat kesan SSA SiMnS terhadap sifat konkrit. Menggunakan pendekatan pembolehubah terkawal, reka bentuk eksperimen menetapkan tahap SSA sebanyak 60, 120, 235, dan 400 m²/kg dengan nisbah penggantian simen dari 0% hingga 40% berat. Spesimen konkrit disediakan di bawah keadaan penyembuhan piawai. Ujian prestasi merangkumi pengukuran slump, penilaian kekuatan mampatan/lekukan, ketahanan beku-cair, ketahanan penembusan ion klorida, dan ketahanan serangan sulfat. Analisis data menggabungkan kaedah AHP-entropi dengan teknik statistik untuk menilai berat penunjuk. Keputusan menunjukkan bahawa SiMnS dengan SSA 235 m²/kg, apabila digunakan untuk menggantikan 10% berat simen, memberikan prestasi optimum dalam konkrit. Konkrit dengan gabungan ini menunjukkan kekuatan mampatan yang dipertingkatkan, ketahanan yang lebih baik terhadap kitar beku-cair, dan ketahanan penembusan ion sulfat dan klorida yang lebih tinggi berbanding konfigurasi lain. Data eksperimen dinilai secara statistik menggunakan gabungan proses hierarki analitik (AHP) dan kaedah berat entropi, yang dirujuk sebagai kaedah AHP-entropi. Berdasarkan penarafan menyeluruh skema SSA

SiMnS, skema optimum (SSA = 235 m²/kg, dos = 10%wt) telah dikenal pasti, yang selari dengan kesimpulan eksperimen, sekaligus mengesahkan keputusan eksperimen tersebut. Apabila kandungan SiMnS melebihi 10% berat, atau SSA melebihi 400 m²/kg, kekuatan mampatan dan ketahanan berkurangan, menunjukkan bahawa keteluran yang berlebihan atau kandungan slag boleh menjejaskan sifat menyeluruh konkrit. Penemuan menunjukkan bahawa SSA yang lebih besar bagi SiMnS meningkatkan reaktiviti pozzolan manakala kandungan SiMnS yang sesuai mengimbangkan kekuatan dan ketahanan. Walau bagaimanapun, kandungan SiMnS yang berlebihan atau SSA yang lebih kecil menyebabkan prestasi menurun disebabkan kecekapan hidrasi yang lebih rendah dan ketidakstabilan struktur. Kajian ini menunjukkan bahawa SiMnS dengan SSA sebanyak 235 m²/kg dan penggantian simen 10% mengimbangi dengan optimum kebolehkerjaan, kekuatan mekanikal (peningkatan 1.79% dan 2.87% dalam kekuatan mampatan dan lenturan, masing-masing), dan ketahanan (ketahanan klorida 25% lebih tinggi, ketahanan sulfat dipertingkatkan sebanyak 10.1%). Walaupun SSA yang lebih tinggi meningkatkan reaktiviti pozzolan, penggantian berlebihan (>10%) atau SSA (>400 m²/kg) mengurangkan prestasi disebabkan kecekapan penghidratan yang rendah dan ketidakstabilan mikrostruktur. Kaedah entropi AHP mengesahkan sinergi ini, menyediakan kerangka berasaskan data untuk memindustrialkan penggunaan SiMnS—mengurangkan pelepasan CO_2 dan sisa tapak pelupusan sambil memajukan matlamat ekonomi kitaran dalam pembinaan. Kerja akan datang perlu mengoptimumkan SSA melalui pengilangan atau bahan tambahan dan menilai impak alam sekitar jangka panjang, terutamanya kesan larutan logam berat.

Kata kunci: *Slag silikomangan, luas permukaan khusus, konkrit, kebolehkerjaan, sifat mekanikal, ketahanan, kaedah AHP-entropi*

TABLE OF CONTENTS

		Page
DECLARATION		i
ACKNOWLEDGEMENT		ii
ABSTRACT		iii
ABSTRAK		v
TABLE OF CONTENTS		vii
LIST OF FIGURES		iv
LIST OF ABBREVIATIONS		vii
CHAPTER 1 INTRODUCTION		1
1.1	Research Background	1
1.2	Problem Statement	6
1.3	Research Gaps	8
1.4	Objectives	9
1.5	Scope	10
1.6	Research Significance	11
1.7	Thesis Outline	13
CHAPTER 2 LITERATURE REVIEW		15
2.1	Overview	15

2.2 Effect of the Specific Surface Area of Metal Slag on its Reactivity 15

2.3 An Overview of Manganese Slag 18

2.3.1 Material Properties of Manganese Slag 18

2.3.2 Behavioral Characteristics of Manganese Slag 22

2.4 Basis and Advantages of Partial Cement Replacement with Manganese Slag 29

2.5 Environmental Challenges and the Imperative for Cement substitution 37

2.6 Design of Manganese Slag Concrete 39

2.7 Effect of Manganese Slag on the Performance of Cement Mortar 41

2.8 Effect of Manganese Slag on the Workability of Concrete 45

2.9 Effect of Manganese Slag on the Mechanical Properties of Concrete 50

2.10 Effect of Manganese Slag on the Durability of Concrete 61

2.10.1 Effect of Manganese Slag on the Frost Resistance of Concrete 63

2.10.2 Effect of Manganese Slag on the Resistance of Concrete to Chloride Ion Penetration 68

2.10.3 Effect of Manganese Slag on the Resistance of Concrete to Sulphate Corrosion 72

2.11 Microstructure of Manganese Slag 77

2.12 Statistical Methods for Multi-Criteria Decision-Making: AHP and Entropy Method 80

2.12.1 Analytic Hierarchy Process (AHP) 81

2.12.2 Entropy Method 81

2.12.3 Comparative Analysis of MCDM Methods and Rationale for Hybrid Approach 81

2.12.4 Applications in Concrete and Construction Materials 84

2.12.5 Justification and Suitability for the Present Study 87

2.13 Knowledge Gap and Research Content of the Research 90

2.14 Summary of Literature Review 91

CHAPTER 3 METHODOLOGY 93

3.1 Introduction 93

3.2 Material Preparation 94

3.2.1 Silicomanganese Slag 94

3.2.2 Water and Admixtures 99

3.2.3 Cement and Aggregate 99

3.3 Preparation and Testing of Cement Mortar 101

3.3.1 Mix Ratio 101

3.3.2 Test Specimen Preparation and Fluidity Test of Cement Mortar 101

3.3.3 Compressive Strength Test of Cement Mortar 102

3.4 Preparation and Testing for Workability and Mechanical Properties of Concrete 103

3.4.1 Mix Ratio 103

3.4.2 Test Specimen Preparation 104

3.4.3 Workability Test of Concrete 106

3.4.4 Compressive Strength Test of Concrete 106

3.4.5 Flexural Strength Test of Concrete 107

3.5 Durability Properties Test of Concrete 108

3.5.1 Chloride Ion Penetration Resistance Test 108

3.5.2 Sulphate Corrosion Resistance Test 112

3.5.3 Concrete Freeze-Thaw Resistance Test 114

3.6 Microscopic Analysis 116

3.7 The AHP-entropy Method 117

3.7.1 Analytic Hierarchy Process 118

3.7.2 Entropy Method 126

3.7.3 Calculation of Combined Weight 129

3.7.4 Calculation of the Comprehensive Score for SSA SiMnS Concrete Schemes 130

CHAPTER 4 RESULTS AND DISCUSSION 131

4.1 Overview 131

4.2 Effect of SiMnS SSA on Cement Mortar Properties 131

4.2.1 Effect of SiMnS SSA on Cement Mortar Fluidity 131

4.2.2 Effect of SiMnS SSA on the Compressive Strength of Cement Mortar 137

4.3 Effect of the SSA of SiMnS on the Workability of Concrete 144

4.4 Effect of SSA of SiMnS on Mechanical Properties of Concrete 151

4.4.1 Effect of SSA of SiMnS on Compressive Strength of Concrete 151

4.4.2 Effect of SSA of SiMnS on the Flexural Strength of Concrete 157

4.4.3 Mechanism Analysis: How SSA Influences the Mechanical Properties of SiMnS Concrete 162

4.5 Effect of SiMnS SSA on Concrete Durability 165

4.5.1 Effect of SiMnS SSA on Freeze-Thaw Resistance of Concrete 165

4.5.2 Effect of SiMnS SSA on Concrete Resistance to Chloride Ion Penetration 171

4.5.3 Effect of SiMnS SSA on Concrete Resistance to Sulphate Attack 175

4.5.4 Mechanism Analysis of SSA Affecting Durability Performance 184

4.6 Microscopic Analysis of SiMnS Concrete 186

4.7 Evaluation of SSA Impact on Concrete Performance Using the AHP-entropy Method 190

4.7.1 Subjective Weight Calculation Using the AHP Method 191

4.7.2 Objective Weight Calculation Using the Entropy Method 200

4.7.3 Calculation of Combined Weight 201

4.7.4 Comprehensive Analysis of the Effect of SiMnS SSA on the Performance of Concrete Based on the AHP-entropy Method 204

4.8 Chapter Summary 206

4.8.1 Influence of SiMnS SSA on Workability 207

4.8.2 Influence of SiMnS SSA on Mechanical Properties 207

4.8.3 Influence of SiMnS SSA on Durability 208

4.8.4 Microstructural Insights from SEM Analysis 209

4.8.5 Analysis via the AHP-Entropy Method 209

4.8.6 Optimal SSA Selection and Practical Implications 210

CHAPTER 5 CONCLUSION 211

5.1 Review of Work Done 211

5.2 Conclusion of Study 211

5.3 Recommendation for Future Work 214

REFERENCES 216

APPENDICES 244

LIST OF TABLES

		Page
Table 2.1	World Mine Production and Reserves of Manganese Ore	19
Table 2.2	Reserves of Manganese Ore in China	20
Table 2.3	Analysis of the Oxide Concentration of Ferromanganese Slag, Silicomanganese Slag, and Regular Portland Cement	31
Table 2.4	Main Chemical Composition of SiMnS	33
Table 2.5	Overview of Manganese Slag Concrete Design	39
Table 2.6	Slump Comparison of Three Concrete Sample	48
Table 2.7	Literature Summary on the Effect of MnS Content on Concrete Workability	49
Table 2.8	Literature Summary on the Effect of Manganese Slag Content on Mechanical Properties of Concrete	39
Table 2.9	Literature Summary on the Effect of Manganese Slag Content on Frost Resistance of Concrete	68
Table 2.10	SLiterature Summary on the Effect of Manganese Slag Content on Chloride Resistance of Concrete	72
Table 2.11	Literature Summary on the Effect of Manganese Slag Content on Sulfate Resistance of Concrete	76
Table 2.12	Comparison of Multi-Criteria Decision-Making Methods for Engineering Materials	82
Table 2.13	Application Cases of Multi-Criteria Decision-Making Methods in Engineering Materials Research	85
Table 2.14	Justification for Selecting the AHP Entropy Method	87
Table 2.15	Suitability of AHP Entropy Method for Concrete Performance Evaluation	89
Table 3.1	Test Results of Natural Moisture Content of SiMnS	96
Table 3.2	Main Chemical Composition of SiMnS	99
Table 3.3	Performance Indexes of Water-reducing Agent	99
Table 3.4	Main Chemical Composition of Cement	99

Table 3.5	Properties of Cement	100
Table 3.6	Performance Indexes of Sand	100
Table 3.7	Experimental Design Matrix for Concrete Strength Test Specimens	124
Table 3.8	Saaty Scale Method	124
Table 3.9	Values of Average Random Consistency Index RI	126
Table 3.10	The Attributes of Each Secondary Indicator	128
Table 4.1	Variation of Cement Mortar Fluidity with SSA of SiMnS	135
Table 4.2	Variation of the Slump of Concrete with SSA of SiMnS	145
Table 4.3	Electric Flux of SiMnS Concrete under Chloride Ion Penetration	172
Table 4.4	Sulphate Corrosion Mass Loss Rate of SiMnS Concrete	178
Table 4.5	Sulfate Resistance Coefficient of SiMnS Concrete	181
Table 4.6	First-level Judgment Matrix (Experts 1-6)	192
Table 4.7	First-level Judgment Matrix (Experts 7-12)	192
Table 4.8	First-level (layer A) Group Decision-making Judgment Matrix	192
Table 4.9	Second-level B1 Judgment Matrix (Experts 1–4)	193
Table 4.10	Second-level B1 Judgment Matrix (Experts 5–8)	193
Table 4.11	Second-level B1 Judgment Matrix (Experts 9–12)	194
Table 4.12	Second-level B2 Judgment Matrix (Experts 1–2)	194
Table 4.13	Second-level B2 Judgment Matrix (Experts 2–4)	194
Table 4.14	Second-level B2 Judgment Matrix (Experts 5–6)	195
Table 4.15	Second-level B2 Judgment Matrix (Experts 7–8)	195
Table 4.16	Second-level B2 Judgment Matrix (Experts 9–10)	196
Table 4.17	Second-level B2 Judgment Matrix (Experts 11–12)	196
Table 4.18	Second-level (layer B1) Group Decision-making Judgment Matrix	197
Table 4.19	Second-level (layer B2) Group Decision-making Judgment Matrix	198
Table 4.20	Results of Consistency Check (B1)	198

Table 4.21 Results of Consistency Check (B2) 199

Table 4.22 Comprehensive Weights of Influencing Factors under the AHP 199

Table 4.23 The Evaluation Indicators System 201

Table 4.24 The Entropy Value and Weight of the Eight Evaluation Indicators 202

Table 4.25 The Combined Weight of the Eight Evaluation Indicators 202

Table 4.26 Combined Weight Ranking of the Eight Evaluation Indicators 203

LIST OF FIGURES

		Page
Figure 1.1	Schematic Diagram of the Production Process of Electrolytic Manganese	2
Figure 1.2	Open-air Storage of Manganese Slag.	3
Figure 1.3	Landfill Treatment of Manganese Slag.	4
Figure 1.4	China's Monthly Cement Production and Growth Rate since 2018	5
Figure 2.1	The Correlation between Specific Surface Area (SSA) and the Hydration Activity Index of GGBFS	17
Figure 2.2	Production Process Flow for Electrolytic Manganese	18
Figure 2.3	Pattern of EMR Diffraction in X-rays	23
Figure 2.4	SEM Pictures of the Microstructures of Pastes, including Regular Cement (left) and Slag (right), after 7 Days of Curing at 10,000× Magnification	24
Figure 2.5	SEM Pictures of the Microstructures of Pastes, including Regular Cement (left) and Slag (right), after 120 Days of Curing at 2500× Magnification	24
Figure 2.6	The Mineralogical Composition of MnS	26
Figure 2.7	Particle Size Distribution of MnS Derived from BET Analysis	26
Figure 2.8	Mineralogical Composition of SiMnS	27
Figure 2.9	Pozzolanic Action of SiMnS	28
Figure 2.10	Relationship between Grinding Time and SSA	29
Figure 2.11	Typical Manganese Slag Production in a Closed Furnace	30
Figure 2.12	The Top Ten Global Producers of SiMnS in 2020 based on the International Manganese Institute (2020)	31
Figure 2.13	X-ray Diffractogram of Mixed Cement Pastes after 28 Curing Days	35
Figure 2.14	Relationship between Cement Strength and MnS Mixture Content	42
Figure 2.15	Flexural Strength (left) and Compressive Strength (right) of Cement Mortars with Different EMR Contents at Different Hydration Ages	43

Figure 2.16 Development of Cement Mortar Flexural and Compressive Strengths 44

Figure 2.17 Influence of Manganese Slag Content on the Slump of Fresh Concrete 46

Figure 2.18 Workability of Concrete Measured with Slump Test 47

Figure 2.19 Electrolytic Manganese Residue-activated Cementitious Fixaion Mn^{2+} and NH4 52

Figure 2.20 Relationship between MnS Dosage and Compressive and Flexural Strength of MnS Concrete 53

Figure 2.21 Compressive Strength and Construction Performance of Early High-strength Shotcrete with Different Mineral Fillings 57

Figure 2.22 Scanning Electron Microscopy Image of MnS after Calcination at 1100 Degrees Celsius 58

Figure 2.23 The Distribution of Frozen Soil in China in the Mid-to-late 20th Century 64

Figure 2.24 Strength Loss of Concrete after Freeze-thaw Cycles 67

Figure 2.25 Morphology of Concrete Subjected to Long-term Chloride and Sulphate Attack 69

Figure 2.26 SEM Images of the Original MnS: (a) Overall Visual Representation, (b) Magnified at ×1500, (c) Magnified at ×3000 77

Figure 3.1 Flowchart of Research Process 94

Figure 3.2 The SiMnS Pilling Outdoor 95

Figure 3.3 The Specific Surface Area and Porosity Analyzer (ASIQM0010-4) 98

Figure 3.4 Silicomanganese Slag after Grinding 98

Figure 3.5 Concrete Curing in the Curing Room 105

Figure 3.6 Slump Test Diagram 106

Figure 3.7 Immersion of Concrete Test Blocks 113

Figure 3.8 Flowchart of the integrated AHP-entropy weight method applied for the mix proportion selection of SiMnS concrete 113

Figure 3.9 A Hierarchical Analysis Structure Model for Comprehensive Performance Analysis of SiMnS Concrete 120

Figure 3.10 Matrix Relationship Diagram 121

Figure 4.1 Effect of SSA of SiMnS on the Fluidity of Cement Mortar 132

Figure 4.2 Effect of SSA of SiMnS on Compressive Strength of Cement Mortar 139

Figure 4.3 Effect of SSA of SiMnS on the Slump of Concrete 1466

Figure 4.4 Compressive Strength of SiMnS Concrete with SSA of 60 m^2/kg 152

Figure 4.5 Compressive Strength of SiMnS Concrete with SSA of 120 m^2/kg 152

Figure 4.6 Compressive Strength of SiMnS Concrete with SSA of 235 m^2/kg 153

Figure 4.7 Compressive Strength of SiMnS Concrete with SSA of 400 m^2/kg 153

Figure 4.8 Flextural Strength of SiMnS Concrete with SSA of 60 m^2/kg 157

Figure 4.9 Flextural Strength of SiMnS Concrete with SSA of 120 m^2/kg 158

Figure 4.10 Flextural Strength of SiMnS Concrete with SSA of 235 m^2/kg 158

Figure 4.11 Flexural Strength of SiMnS Concrete with SSA of 400 m^2/kg 159

Figure 4.12 Effect of SSA of SiMnS on the Mass Loss Rate of Concrete under Freeze-thaw Cycles 166

Figure 4.13 Effect of SSA of SiMnS on the Compressive Strength Loss Rate of Concrete under Freeze-thaw Cycles 168

Figure 4.14 Electric Flux at 28-day and 56-day Curing Ages of SiMnS Concrete 172

Figure 4.15 Effect of SiMnS SSA on Concrete Sulphate Corrosion Mass Loss Rate 179

Figure 4.16 Effect of SiMnSg SSA on Concrete Sulfate Resistance Coefficient 182

Figure 4.17 Scanning Electron Microscopy of SiMnS Concrete 188

Figure 4.18 Comprehensive evaluation scores of 30 schemes 205

LIST OF ABBREVIATIONS

AAMs	Alkaline Activated Materials
AC	Alternating Current
ACMT	Accelerated Chloride Migration Test
AFT	Aluminium Ferric Trisulphate
AHP	Analytic Hierarchy Process
ASC	Alkali-activated Slag Concrete
BET	Brunauer–Emmett–Teller
CASH	Calcium aluminate silicate hydrate
CCG	Center for China and Globalization
CI	Consistency Index
CR	Consistency Ratio
CSH	Calcium Silicate Hydrate
DC	Direct-Current
DTA	Differential Thermal Analysis
DEA	Data Envelopment Analysis
EDS	Energy-Dispersive Spectrometry
EMM	Electrolytic Manganese Metal
EMR	Electrolytic Manganese Residue
EMS	Electrolytic Manganese Slag
FA	Fly Ash
FeMnS	Ferromanganese slag
F-T	Freeze-Thaw
FTIR	Fourier-Transform Infrared spectroscopy

GGBFS	Ground Granulated Blast-Furnace Slag
ITZ	Interfacial Transition Zone
LCA	Life-Cycle Assessments
MnS	Manganese Slag
OPC	Ordinary Portland Cement
PCA	Principal Component Analysis
PCC	Portland Cement Concrete
RCM	Rapid Chloride Migration
RI	Random Consistency Index
SC	Sulphur Concrete
SCM	Supplementary Cementing Material
SEM	Scanning Electron Microscopy
SF	Silica Fume
SiMn	Silicomanganese
SiMnS	Silicomanganese slag
SSA	Specific Surface Area
TEM	Transmission Electron Microscopy
TOPSIS	Technique for Order Preference by Similarity to the Ideal Solution
UEA	United Expansive Agent
XCT	X-ray Computed Tomography
XRD	X-ray diffraction
XRF	X-ray fluorescence

CHAPTER 1

INTRODUCTION

1.1 Research Background

Manganese slag is one type of granulated blast furnace slag. Currently, a variety of artificial and natural supplementary cementitious materials, including fly ash, different types of slag, silica fume, and natural pozzolanic substances, are widely used as additives in the production of cement (Papadakis et al., 2002; Papadakis & Tsimas, 2002; Ramachandran et al., 2002). It is a global approach to sustainable development that conserves non-renewable raw materials and fuels. However, there are further advantages to using worthless industrial wastes as cement replacements, such as a notable rise in cement production and a notable decrease in greenhouse gas emissions. Fly ash and slags are two examples of industrial byproducts that are produced in enormous amounts all over the world.

Today, with the continuous development of science and technology, manganese metal has been used in many aspects: in aerospace, magnesium manganese alloy made of manganese metal, which has excellent characteristics of high-temperature resistance and corrosion resistance; in agricultural production, manganese metal as fertilizer or other special additives; in the aspect of electronic manufacturing, manganese-zinc ferrite is used as the basic material of electronic components or products. In steel products, manganese powder desulfurization is added to the steelmaking process to prepare high-strength steel. Since the emergence of electrolytic manganese companies in China, through people's challenging exploration, the production and consumption of electrolytic manganese slag in China can reach the highest globally (Wang et al., 2019; Zhou et al., 2013). According to statistics released by the Ministry of Land and Resources of China, China's manganese ore resource

reserves are approximately 711 million tons, accounting for approximately 5% of the world's total. China has over 1,570 ferromanganese alloy smelting companies (Sun et al., 2021). In 2020, about 1.50 million tons of electrolytic metal manganese (EMM) were produced in China, accounting for 96.5% of the total EMM production in the world (Lan et al., 2021; Wang et al., 2020). It can be concluded that the manganese metal industry has successfully promoted the development of China. However, the rapid development of manganese metal enterprises in China is matched by the problems of large enterprises concerning the environment, production safety, and resource exploitation. EMM production is a manufacturing process characterized by significant resource and energy demands, substantial pollution output, high operational costs, and minimal profitability (He et al., 2021). The production process of EMM is shown in Figure 1.1. The rapid increase in manganese production has brought about a tremendous amount of manganese slag waste, usually treated by open-air storage and landfills.

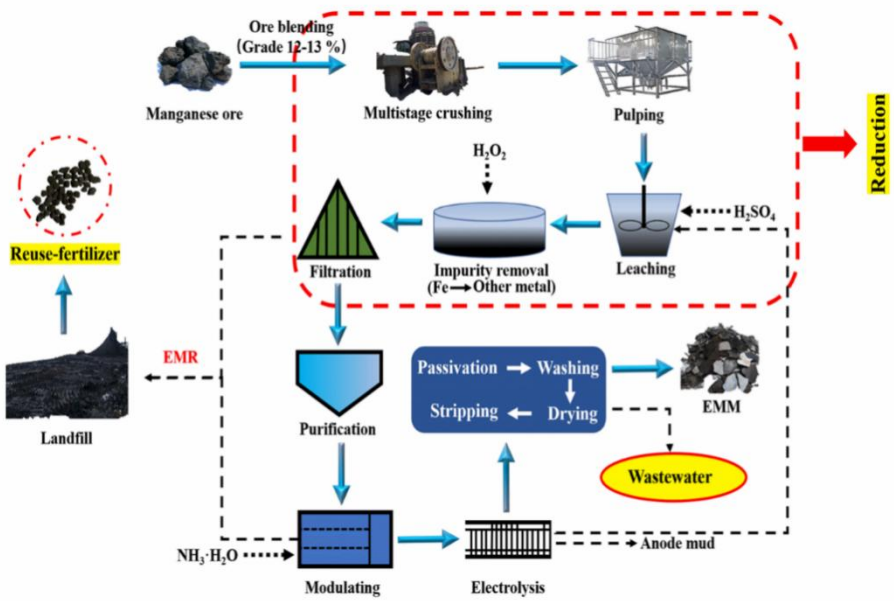

Figure 1.1: Schematic Diagram of the Production Process of Electrolytic Manganese

The open-air storage of manganese slag not only occupies a large amount of land (see Figure 1.2), increasing the cost of the enterprise, but also the pollutants such as ammonia nitrogen, manganese, sulphate, and heavy metals in the manganese slag can easily penetrate the soil and groundwater, seriously polluting the environment. For the landfill treatment of manganese slag, areas far away from densely populated areas and drinking water sources are usually selected as landfill sites (see Figure 1.3). Electrolytic manganese slag landfills pose significant environmental and health risks, including soil and groundwater contamination from heavy metals (e.g., Mn, Pb, As) exceeding regulatory limits by 10-50 times in soil and 3-20 times in groundwater (Geng et al., 2024), atmospheric pollution via particulate matter (PM_{10}/$PM_{2.5}$) and Cr(VI) exposure linked to respiratory inflammation and carcinogenic risks (Mitchell et al., 2019), and neurotoxic effects such as Parkinsonian symptoms from chronic manganese exposure (Peres et al., 2016). Therefore, the effective utilization of manganese slag has high ecological, social and economic benefits. China's strict safety inspection found that some enterprises have severe pollution phenomena and hidden safety dangers. These enterprises will be closed to realize the healthy development of the industry. This not only reflects the determination of the state to protect the environment but also makes the development of the manganese metal industry urgently needed to be solved.

Figure 1.2: Open-air Storage of Manganese Slag

Figure 1.3: Landfill Treatment of Manganese Slag

Judging from the present development situation, industrial by-products have been widely used (Saha et al., 2018). Although the waste manganese slag has been used in building materials, the factory cannot carry out mass production because there is no straightforward activation method for manganese slag. The production process of traditional Portland cement has been improved lately, and it has many advantages, such as excellent performance and low cost. However, cement production needs to consume a lot of precious resources. Furthermore, cement production releases many harmful substances and pollutes the environment. According to the National Bureau of Statistics' data since 2018 (Figure 1.4), China's cumulative cement production is projected to reach 850 million tons in the first half of 2024, with the peak of 2.3 billion tons occurring in 2020 (Chen, 2024).

The global scale of industrial solid waste generation and its associated environmental burden is substantial, as exemplified by the manganese processing and cement industries. In Europe alone, the annual production of electrolytic manganese dioxide generates approximately 55,000 tons of manganese-iron solid waste (Sikalidis et al., 2007), while worldwide silico-manganese alloy production in 2020, yielding about 16 million tons of

alloy, resulted in an estimated 1.2 to 1.4 tons of slag per ton of alloy produced (Nath et al., 2022). Concurrently, the cement industry, a pivotal yet major contributor to climate change, is responsible for 5–7% of global anthropogenic CO_2 emissions (Singh & Middendorf, 2020). This environmental challenge is poised to intensify, with Portland cement consumption projected to reach 6 billion tons annually by 2060 due to rising global demand for concrete (Raveendran & Vasugi, 2024), which would significantly increase the emission of CO_2, a primary greenhouse gas. To solve this problem, we can discuss whether part of the cement can be replaced by manganese slag in concrete to increase the content of manganese slag in concrete and reduce the use of cement to control the degree of environmental pollution. The most important thing is that it not only meets the needs of sustainable development but also can make manganese slag have a new value.

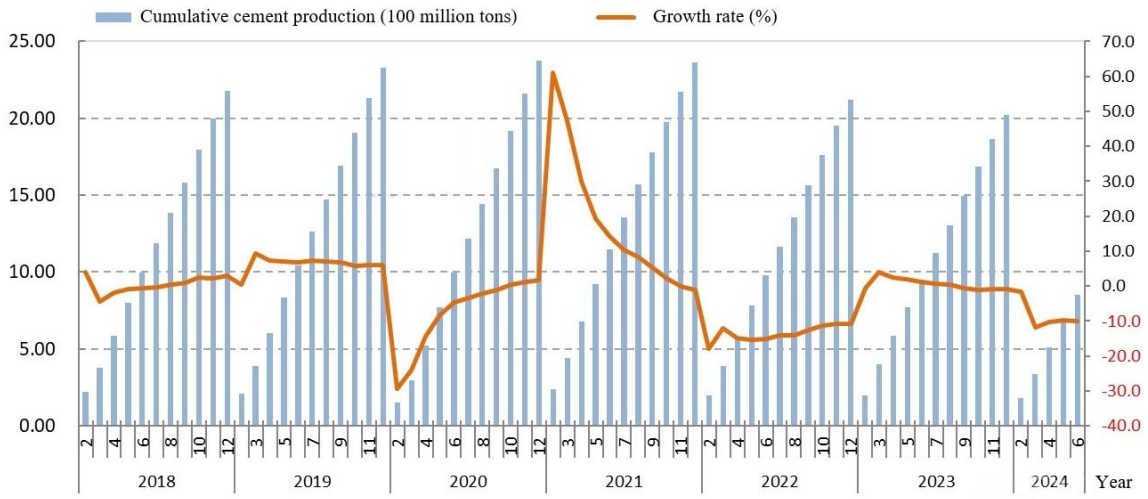

Figure 1.4: China's Monthly Cement Production and Growth Rate since 2018 (Chen, 2024)

Manganese slag has potential hydraulic and pozzolanic activity, which is lower than slag but higher than fly ash. Electrolytic manganese residue (EMR) has the properties of both gypsum and hydraulic industrial solid wastes due to its main chemical components,

$CaSO_4 \cdot 2H_2O$, SiO_2, and small amounts of Al_2O_3, Fe_2O_3, MnO_2, etc. (Frias et al., 2006). Therefore, manganese slag can be used to prepare cementitious materials widely used in cement and concrete and is no longer limited to lower-value applications such as filling roads or replacing aggregates to produce bricks and blocks (Li et al., 2020). It can even change the performance of concrete and finally realize the application of manganese slag in building materials (Yang et al.,2014).

One way to excite manganese slag reactivity is mechanical activation. Mechanical activation means grinding the manganese slag into fine powder through mechanical grinding. The original Mn slag particles have adverse effects to some extent on the volume stability of concrete because of the alveolate pore structure (Liu, 2012).

1.2 Problem Statement

The global metallurgical industry generates a substantial volume of manganese slag as a by-product, presenting considerable environmental challenges due to current disposal practices such as open-air storage and landfilling. These methods risk leaching harmful heavy metals and sulphates into soil and groundwater, necessitating effective utilization strategies for this industrial waste. Concurrently, the cement production sector remains a major contributor to global carbon dioxide emissions, accounting for a significant proportion of anthropogenic greenhouse gases. This high carbon footprint underscores the urgent need for sustainable alternatives within the construction industry.

Manganese slag, with its inherent pozzolanic and hydraulic properties, offers a promising solution to these dual environmental challenges by potentially serving as a partial replacement for cement in concrete formulations. Such application could simultaneously reduce cement consumption and provide a sustainable waste management pathway.

However, effectively leveraging the properties of manganese slag in concrete requires deeper understanding of its fundamental characteristics.

A critical factor influencing the slag's performance is its specific surface area (SSA), which directly determines particle fineness and consequently affects reactivity, hydration behavior, and overall contribution to the concrete matrix. While existing research has acknowledged the potential of manganese slag in concrete applications, systematic investigations into how varying SSA levels impact key performance metrics—including mechanical strength, workability, and durability—remain notably insufficient.

This research gap is particularly evident in the lack of optimization guidelines for achieving ideal SSA values that maximize compressive/flexural strength, ensure satisfactory workability, and enhance resistance to environmental stressors such as freeze-thaw cycles, chloride penetration, and sulphate attack. Addressing these questions is essential for advancing the effective utilization of manganese slag in sustainable construction practices.

The novelty of this study lies in its dual-focused approach. First, it shifts the research emphasis from merely examining slag content to investigating the fundamental role of SSA as a key influencing factor. Second, it introduces an innovative methodological framework by integrating the Analytic Hierarchy Process (AHP) with the Entropy Method to evaluate experimental data. This combined approach enables a comprehensive optimization analysis that balances subjective expert judgment with objective data-driven weighting, thereby identifying optimal solutions that bridge a critical gap in current research.

1.3 Research Gaps

Despite the growing interest in utilizing manganese slag as a sustainable supplementary cementitious material, significant knowledge gaps remain regarding its performance in cement and concrete applications. Most current research focuses on the effect of manganese slag dosage on concrete performance, with minimal attention given to the role of its SSA. A critical factor influencing the effectiveness of manganese slag is its SSA, which governs its reactivity and interaction within the concrete matrix. However, the detailed impacts of SSA on various performance aspects of cement mortar and concrete have not been comprehensively investigated.

Firstly, while studies have explored the general properties of manganese slag, limited attention has been given to the influence of its SSA on the workability of cement mortar. The specific surface area or the particle size of manganese slag can affect the hydration process and fluidity of the mortar, potentially altering its workability and ease of application. Understanding this relationship is essential for optimizing cement mortar formulations.

Secondly, the influence of SSA on concrete's workability remains insufficiently explored. Variations in SSA can significantly impact concrete's slump and flow characteristics, influencing its performance in practical construction scenarios. A clear understanding of how manganese slag’s SSA affects concrete’s fresh-state properties is necessary to ensure its suitability for diverse construction needs.

Thirdly, the mechanical properties of concrete, such as compressive and flexural strength, are directly affected by manganese slag's reactivity and filling ability, which depend on its SSA. While it is understood that finer particles or larger SSA enhances these properties,

the optimal SSA for achieving balanced strength and durability remains unclear. This limits the practical application of manganese slag as a reliable cement replacement.

Finally, the durability of manganese slag concrete in aggressive environments, particularly its resistance to chloride ion erosion, frost damage, and sulphate corrosion, is not well-documented in the context of SSA variations. These properties are critical for ensuring the long-term performance and sustainability of concrete structures. Investigating how different SSA levels influence these durability factors will provide valuable insights for improving the resilience of manganese slag concrete.

Addressing these research gaps is essential for fully utilizing manganese slag as a partial cement replacement. By systematically examining the effects of SSA on the workability, mechanical strength, and durability of cement mortar and concrete, this study seeks to bridge the existing knowledge gap and contribute to developing sustainable and high-performance construction materials.

1.4 Objectives

This thesis aims at using manganese slag as a cement replacement material to produce manganese slag cement mortar and manganese slag concrete. The mechanical properties, workability, frost resistance, chloride ion corrosion resistance, sulphate corrosion resistance and microstructure of manganese slag cement mortar and manganese slag concrete are studied. This study involved a series of experiments on manganese slag concrete, with a primary focus on evaluating the influences of the specific surface area and content of the manganese slag.

The aim can be achieved through the following set of objectives:

i. To investigate the effect of silicomanganese slag's SSA on concrete workability (slump) and the mechanical properties of mortar and concrete (compressive and flexural strengths).

ii. To assess the effect of SSA of silicomanganese slag on the durability of concrete (freeze-thaw resistance of concrete, chloride ion penetration, and resistance to sulphate attack).

iii. To evaluate the SSA and the percentage of silicomanganese slag in cement replacement based on statistical analysis, the AHP-entropy method, which uses a combination of the analytic hierarchy process (AHP) and the entropy weight method, is employed.

1.5 Scope

The overall scope of this research focuses on evaluating the effect of SiMnS SSA on the comprehensive performance of concrete. The work is structured as follows. First, it describes the preparation methods and fundamental characteristics of SiMnS concrete. It then details the designed methodology for obtaining SiMnS with controlled SSA, using source materials from Xingyang City, Henan Province. The research encompasses experimental investigations to assess the influence of SSA on key concrete properties: this includes standardized tests for workability, mechanical properties, and durability (specifically resistance to chloride ion penetration, freeze-thaw cycles, and sulfate attack). Furthermore, the study incorporates microstructural analysis using Scanning Electron Microscopy (SEM) to examine the material's internal morphology. Finally, the research integrates the experimental findings through a comprehensive statistical analysis, employing

the combined AHP-Entropy method for multi-criteria decision analysis, with the aim of providing a holistic understanding of SSA's effect on performance.

1.6 Research Significance

With the rapid development of China's economy and society, many manganese ore resources can be found, which have been rationally exploited and used. For example, mining manganese ore and manganese products has reached the leading level in China (Hong, 2011a). However, mining these products also produces a large amount of manganese slag, a very high content of manganese industrial waste (Yan, 2008). It consists mainly of calcium oxide and silicon dioxide, with the combined concentration of these two oxides exceeding 55%; it also contains aluminum oxide, manganese oxide, and other substances (Chen et al., 2010). According to research, a ton of manganese will produce about 3.5 tons of manganese slag (Zhou et al., 2012), which is 3.5 times the production rate. As a result, a large amount of manganese slag is discarded in farmland or other places, causing great harm to the natural environment. Similar circumstances are observed in Sarawak, Malaysia, where approximately 400,000 tons of industrial waste, of which an estimated 264,000 tons is silicomanganese slag (SiMnS) from the region's major producer, are landfilled annually at the Bintulu smelter (Ting et al., 2023). The current disposal approach not only incurs additional costs and land usage but also imposes environmental burdens. Therefore, we should do everything possible to realize the reuse of manganese slag and protect the environment.

Concrete is the most famous building material in infrastructure construction worldwide and one of the most used materials in various engineering constructions. The amount of concrete used is twice that of other construction materials, such as steel bars

combined (Gagg, 2014). The primary constituent materials of concrete are cement, sand, and crushed stone aggregates. As the primary material for making concrete, cement is the main substance that affects concrete's strength, durability, fluidity, and cohesiveness. Due to the easy acquisition of manufacturing materials and the rapid development of the global industrialization process, cement output has increased rapidly worldwide in the past 30 years. At this stage, global cement production is about 4.1 billion tons per year (Durastanti & Moretti, 2020). From 2006 to 2021, China, India, Europe, and the United States were the largest emitters of carbon dioxide (Hanifa et al., 2023). Cement production is growing at 2.5% per year and is expected to continue increasing to 5.8 billion tons by 2050 (Miller et al., 2018). Research on international and local levels shows that processed manganese slag can replace cement when making concrete (Nath et al., 2022; Navarro et al., 2017; Ng et al., 2024). This is beneficial for reducing carbon dioxide gas emissions and lowering global cement consumption.

Grinding manganese slag with excellent pozzolanic activity and then adding it to concrete can not only play a good micro-aggregate effect and improve the internal structure of concrete but also participate in the internal reaction of concrete and promote the internal hydration reaction. So, letting manganese slag as cementitious material replace part of cement in concrete will become the best way to turn manganese slag waste into fortune. On the other hand, using manganese slag in concrete reduces the amount of cement used, which helps reduce carbon dioxide emissions. Using manganese slag as an admixture auxiliary cementation material to make concrete can not only alleviate the problem of full utilization of abandoned manganese slag but also promote the green and healthy development of the manganese metal industry.

Current research focuses more on the effect of manganese slag dosage on the performance of concrete. For example, Wang et al. (2013) investigated how the amount of manganese slag affected the cement's setting time and mechanical strength. The ideal manganese slag range of proportions is determined to be a mixture of 20～40% (Wang et al., 2013). The tests of Rai et al. (2002), conclusively demonstrate that the compressive strength declines with increasing slag percentage; however, the 50:50 combination demonstrated 22 MPa and 33 MPa at 7 and 28 days of wet curing, respectively, meeting IS 455:1989 standards (Rai et al., 2002).

However, the specific surface area of manganese slag determines the particle size of manganese slag. It is also very important to know what effect the specific surface area of manganese slag has on the mechanical properties, workability, and durability of manganese slag concrete. A higher SSA typically leads to increased pozzolanic reactivity. It enhances the reaction surface area between SiMnS particles and water, accelerating the pozzolanic reaction and improving the early strength development of concrete. However, excessive SSA can raise the processing costs of SiMnS, particularly in terms of energy consumption and labor, which goes against the principles of green construction aimed at reducing carbon dioxide emissions. Therefore, it is important to study the SSA that provides the most balanced performance for concrete. Unlike other studies, which focus more on how SSA affects volcanic ash reactivity and the substitution ratio of SiMnS, this paper distinguishes itself by examining the specific impact of SSA on concrete performance.

1.7 Thesis Outline

Chapter 1 summarizes manganese slag production and its advantages in making concrete. It explains the research problem, research gap, and significance of studying the

specific surface area of manganese slag in manganese slag concrete and expresses four research objectives.

Chapter 2 presents a comprehensive review of existing research on manganese slag, manganese slag concrete, and statistical research methods. It critically examines the current state of knowledge in these areas and identifies key research gaps, which are subsequently addressed in this study.

Chapter 3 describes the preparation process of silicomanganese slag and silicomanganese slag concrete with different specific surface areas. At the same time, the mechanical testing, durability testing, and microscopic analysis test methods of silicomanganese slag concrete are described in detail. The AHP-entropy method is described for optimizing SSA and the percentage of silicomanganese slag in cement replacement of concrete.

Chapter 4 analyses and discusses the test results, which mainly include five parts. The first part focuses on the effect of silicomanganese slag specific surface area on the performance of cement mortar. The second part studies the effect of silicomanganese slag specific surface area on the slump of concrete. The third part analyses the influence of silicomanganese slag specific surface area on the mechanical properties of concrete. The fourth part focuses on the effect of silicomanganese slag specific surface area on the durability of concrete. The fifth part presents the microscopic analysis of silicomanganese slag concrete. Finally, the last part evaluates the SSA impact on concrete performance using a statistical analysis method—the AHP-entropy method.

Chapter 5 systematically presents the conclusions of the four research objectives by synthesizing the experimental results and statistical analyses.

CHAPTER 2

LITERATURE REVIEW

2.1 Overview

This chapter provides a comprehensive literature review on manganese slag utilization in concrete, addressing environmental significance, material properties, and performance impacts. It establishes research context through industrial waste management and sustainable construction challenges. The chapter systematically examines slag reactivity, material classification, cement substitution theory, performance benefits, concrete design procedures, mechanical/durability properties, microstructural characteristics, and statistical evaluation methods. Through progressive analysis of theoretical foundations, practical guidelines, quantitative evaluation, and microstructural mechanisms, it identifies critical research gaps in SSA effects on concrete performance, culminating in research objectives aligned with sustainable development goals and technical problem-solving in slag utilization.

2.2 Effect of the Specific Surface Area of Metal Slag on its Reactivity

The activation performance of slag powder can be modified by adjusting its fineness (Khan & Amin, 2017; Liu & Li, 2014). The specific surface area is an important indicator for describing the fineness of manganese slag. The length, width, and thickness can be determined by determining particle shape. Specific surface area (SSA) indicates particle size, shape, and surface texture. The SSA of aggregates, fillers, and binders plays a significant role in influencing both the fresh and hardened properties of concrete (Ghasemi et al., 2018). The SSA of the SiMnS is usually determined by the Brunauer–Emmett–Teller (BET) method (Jayakantha et al., 2021). Tests indicate that increasing the fineness of supplementary

cementitious materials enhances their filling ability, hydration reactivity, and pozzolanic characteristics (Khan & Amin, 2017).

The hydration activity and compressive strength of ground granulated blast-furnace slag (GGBFS) based concrete generally improve with an increase in the specific surface area of the ground slag, although this effect plateaus when the surface area exceeds 350 m^2/kg, as demonstrated by a grey correlation analysis (Shi et al., 2015). While finer particles typically enhance the fluidity of concrete, a combination of coarse and fine particles has been shown to improve strength further (Her & Lim, 2010; Sharmila & Dhinakaran, 2016). Moreover, studies on nano-slag effects in high-strength concrete have evaluated key parameters such as absorption properties, porosity, compressive strength, and resistance to chloride-ion penetration (Sharmila & Dhinakaran, 2015).

As illustrated in Figure 2.1, the hydration activity index of GGBS exhibits a nearly linear relationship with its specific surface area across all tested ages, in addition to showing a general increasing trend over time (Dai et al., 2019). As the proportion of fine particles in slags increases, the specific surface area rises, leading to improved coherence and more efficient filling of voids between cement particles.

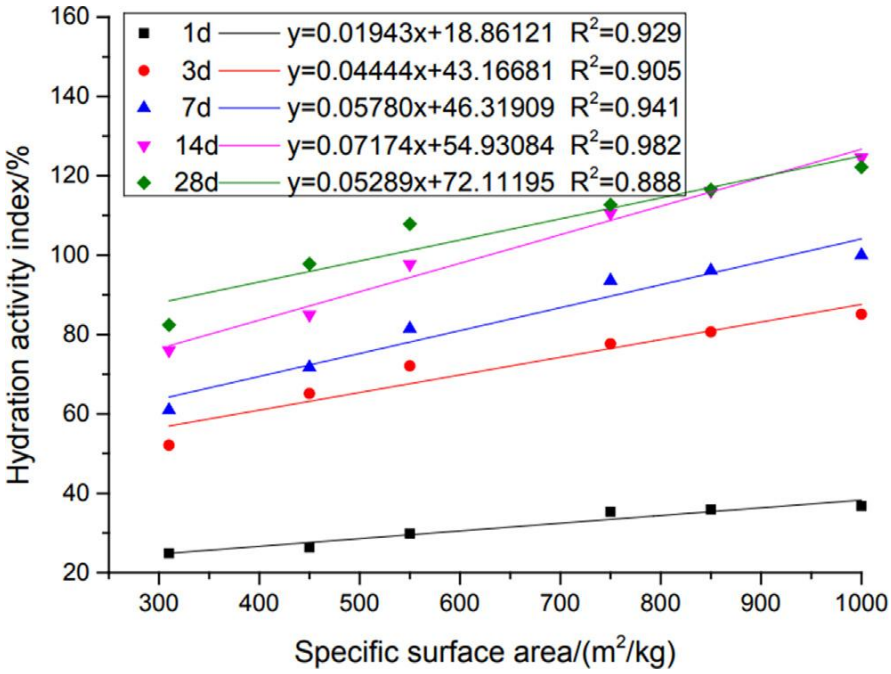

Figure 2.1: The Correlation between Specific Surface Area (SSA) and the Hydration Activity Index of GGBFS (Dai et al., 2019)

High SSA reduces pore size distribution, creating a denser and more compact matrix. SSA plays a critical role in determining the pozzolanic activity index of manganese slag. Increased SSA enhances the slag's ability to react with $Ca(OH)_2$, forming more secondary hydration products. Finer grinding exposes more amorphous silica and alumina, which are crucial for pozzolanic reactions (Snellings et al., 2023). Increasing SSA exposes more reactive sites on the particle surface, facilitating interactions with water and calcium hydroxide to produce cementitious compounds such as calcium silicate hydrate (CSH) and calcium aluminates. High SSA dissolves more rapidly in an alkaline environment, allowing quicker release of reactive ions (e.g., Si^{4+}, Mn^{2+}, and Al^{3+}). This accelerates hydration and pozzolanic reactions (Wang et al., 2024).

2.3 An Overview of Manganese Slag

The characteristics of manganese slag are systematically summarized in this section with respect to two key aspects: material properties and behavioral characteristics.

Material Properties of Manganese Slag

Manganese slag (MnS) is a filter residue produced by electrolytic production of manganese dioxide by adding sulfuric acid solution to manganese carbonate ore powder (Hagelstein, 2009). The electrolysis of manganese metal is illustrated in Figure 2.2 (Han & Wu, 2019). The crushing and grinding of ore, sulfuric acid leaching, filter pressing, electrolytic passivation, and drying stripping are all steps in the manganese electrolysis process flow. The manganese reserves of the primary nations with abundant manganese ore resources are listed in Table 2.1 (USGS, 2024). The data are given in gross weight in thousand metric tons (1 kmt). Manganese ore deposits are abundant in China, although they are distributed unevenly among the nation's 23 provinces, municipalities, and autonomous areas listed in Table 2.2 (Hong, 2011).

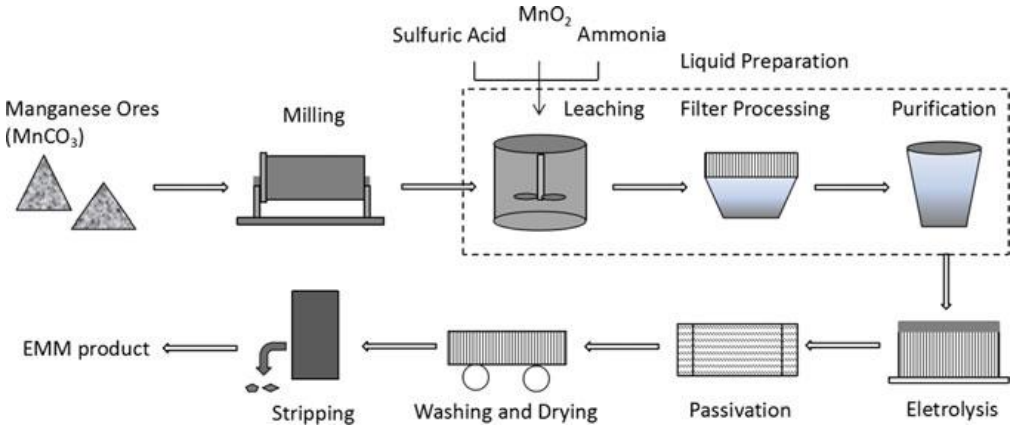

Figure 2.2: Production Process Flow for Electrolytic Manganese (Han & Wu, 2019)

Table 2.1: World Mine Production and Reserves of Manganese Ore (USGS, 2024)

Country	Production in 2022 (1 kmt gross weight)	Production in 2023 (1 kmt gross weight)	Reserves (1 kmt gross weight)
Australia	3040	3000	500000
Brazil	624	620	270000
Burma	207	210	NA
China	743	740	280000
Gabon	4670	4600	61000
Georgia	166	160	NA
Ghana	844	840	13000
India	721	720	34000
Kazakhstan	129	130	5000
Malaysia	247	250	NA
Mexico	221	220	5000
South Africa	7300	7200	600000
Ukraine	323	320	140000
Vietnam	155	160	NA
Other countries	325	330	Small
World total (rounded)	19200	20000	1900000

The worldwide serving industries that account for most of the manganese demand are transportation (11%), machinery (14%), and construction (23%). Recycled manganese is found in iron and steel scraps; a tiny quantity is found in used aluminium beverage cans.

The recycling rate of manganese is approximately 37%, with a corresponding recycling efficiency—representing the proportion of available scrap that is successfully recycled—estimated at 53% (Hagelstein, 2009). The manufactured slag is used only for landfilling; it has no other value-added uses. As a result, a massive stock of slag has been created. Quantifying the overall amount of slag dumped worldwide is impossible because there is no way to determine the accumulation quantity using regular consumption data from each producing plant.

Table 2.2: Reserves of Manganese Ore in China (Hong, 2011)

Region	Basic reserves (10,000 t)	Resource (10,000 t)	Identified reserves (10,000 t)
Whole country	22443.72	56849.74	79293.46
Guangxi	7954.63	20171.25	28125.88
Hunan	5907.79	9937.24	15845.03
Yunnan	897.74	8317.97	9215.71
Guizhou	2502.72	5478.77	7981.49
Liaoning	1216.04	2974.10	4190.14
Chongqing	1876.14	2251.42	4127.56
Sichuan	29.55	2858.43	2887.98
Hubei	874.7	610.10	1484.80
Shanxi	313.42	904.94	1218.36
Gunagdong	214.48	780.93	995.41
Xinjiang	467.8	554.06	1021.86
Fujian	84.28	366.69	450.97
Other provinces	104.43	1643.84	1748.27

The demand for industrial manganese in China is significant. In the past three years, with the rapid growth of the output of steel, electronic batteries, and new energy vehicles, China's demand for industrial manganese has become more outstanding. Since the domestic manganese ore is mainly lean ore, 8–12 tons of electrolytic manganese slag is produced for 1 ton of manganese metal production, and the existing electrolytic manganese slag stock is about 160 million tons (Dong et al., 2024; Han & Wu, 2019). Since the emergence of electrolytic manganese companies in China, through people's challenging exploration, the production and consumption of electrolytic manganese in China can reach the world's leading level (Wang et al., 2019).

According to statistics released by the Ministry of Land and Resources of China, China's manganese ore resource reserves are approximately 711 million tons, accounting for approximately 5% of the world's total. China has over 1,570 ferromanganese alloy smelting companies (Sun et al., 2021). In 2020, about 1.50 million tons of electrolytic manganese metal (EMM) were produced in China, accounting for 96.5% of the total EMM production in the world (Lan et al., 2021; Wang et al., 2020).

Over 160 million tons of EMR have been generated in China in the past decades, which is still increasing to 10 million tons annually (Duan et al., 2011). With the existing electrolytic manganese metals production technology, every ton of produced manganese metal generates 8–12 tons of EMS (Lan et al., 2021). After decades of development, China alone has an inventory of over 100 million tons of EMS. This inventory has not been adequately taken care of in 2020. Moreover, with the continuous reduction of manganese

ore resources in nature, the rate of new EMS production is expected to exceed 10 million tons per year (He et al., 2021).

One type of ferroalloy that gives steel better mechanical qualities is silicomanganese (SiMn). Silicomanganese slag (SiMnS) results from the carbothermic reduction of source materials in a submerged arc furnace used to create SiMnS alloy. The ninety per cent increase in raw steel production and the modernization of ferroalloys, including ten US facilities, are linked to the usage of manganese. Manganese is used in nonferrous applications such as manufacturing dry cell batteries, parts for plant fertilizer, animal feed, and brick colouring. Global production of manganese ore (high grade, 35 per cent Mn) is approximately 6 million tons yearly, while production of manganese alloys is approximately 8 million tons yearly (Roskill Metals and Minerals Reports, 2005). Ferromanganese (FeMn) and silicomanganese (SiMn) are types of manganese alloys that are created by reducing manganese oxides and quartz with carbon in a submerged-arc furnace (Sparta & Risinggård, 2021). The density of cement is determined through the test method for determining cement density (BS EN 12350-6:2019), and the SSA of cement is determined by the Brunauer–Emmett–Teller (BET) method (Jayakantha et al., 2021). When MnS replaces a portion of cement, these indicators can still be obtained in the same ways.

2.3.2 Behavioral Characteristics of Manganese Slag

The X-ray diffraction pattern (XRD) of MnS is depicted in Figure 2.3 (Yang et al., 2014). The primary minerals of MnS include muscovite ($Fe_2O_3 \cdot H_2O$), gypsum ($CaSO_4 \cdot 2H_2O$), kaolinite ($Al_2Si_2O_5(OH)_4$), fine-crystalline quartz (SiO_2), and muscovite ($KAl_2AlSi_3O_{10}(OH)_2$). With X-ray fluorescence for chemical analysis, the slag's primary constituents were SiO_2, Al_2O_3, SO_3, and Fe_2O_3, making up 83% of the total composition.

The slag has a significant concentration of CaO, MnO, and MgO in addition to a small quantity of trace metals like Cd, Cu, Ni, Zn, Cr, Pb, and Se. Rain causes the soluble sulfates in MnS to dissolve, and as time passes in the pond, the number of soluble sulfates will decrease (Qiao et al., 2010). It is highly possible that more of these sulfates may dissolve and create pollution if incorrectly disposed of, despite the well-known risk of these sulfates polluting rivers and soil.

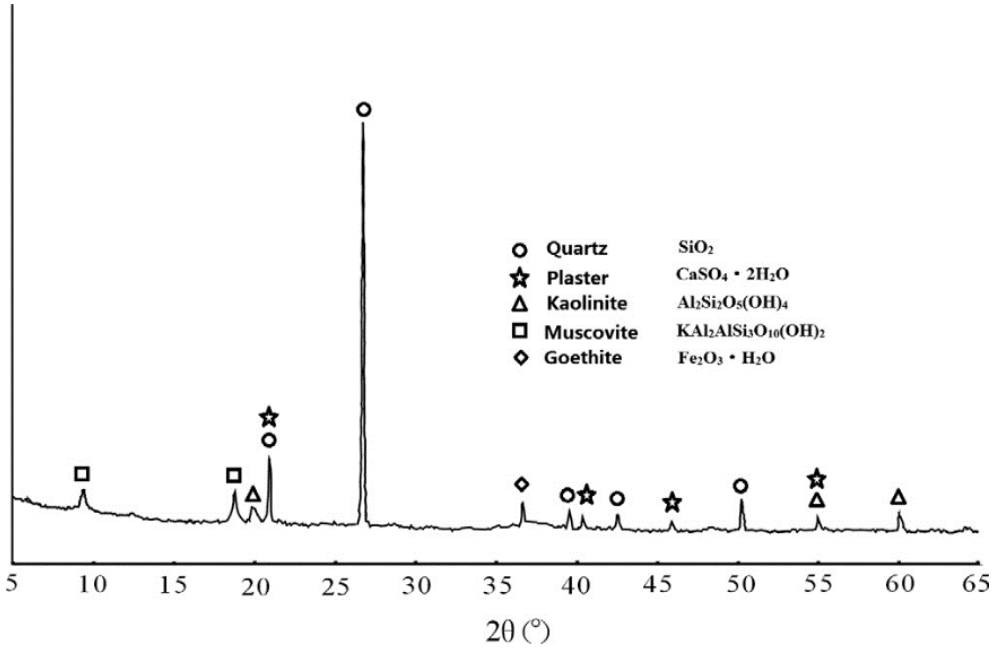

Figure 2.3: Pattern of EMR Diffraction in X-rays (Yang et al., 2014)

Allahverdi and Ahmadnezhad (2014) showed that in contrast to control pastes, SiMnS containing pastes that were cured for 7 and 120 days displayed microstructural morphologies that were identical, disregarding the non-reacted silicomanganese slag particles. After 7 and 120 days of curing, respectively, scanning electron microscopy (SEM) images from the microstructures of the cement pastes containing silicomanganese slag and plain cement paste are shown in Figure 2.4 and Figure 2.5. As observed, after seven days of curing, the microstructures are made up of tiny, finely distributed ettringite crystals that

resemble tiny needles and early-age hydration products surrounding cement and slag particles. The Portlandite crystals are hexagon-shaped. Ettringite crystals vanished, and more compact microstructures emerged after 120 days of cure.

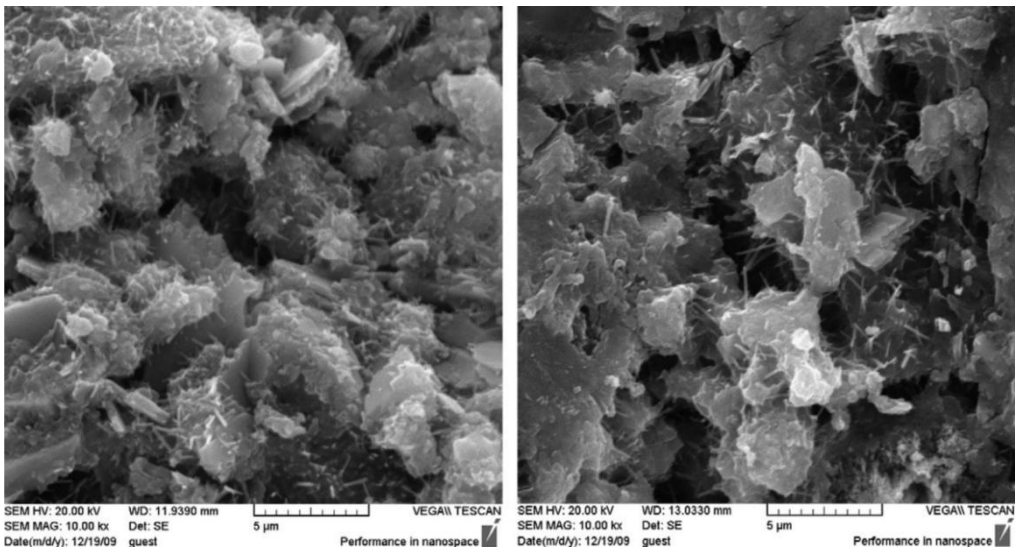

Figure 2.4: SEM Pictures of the Microstructures of Pastes, including Regular Cement (left) and Slag (right), after 7 Days of Curing at 10,000× Magnification (Allahverdi & Ahmadnezhad, 2014)

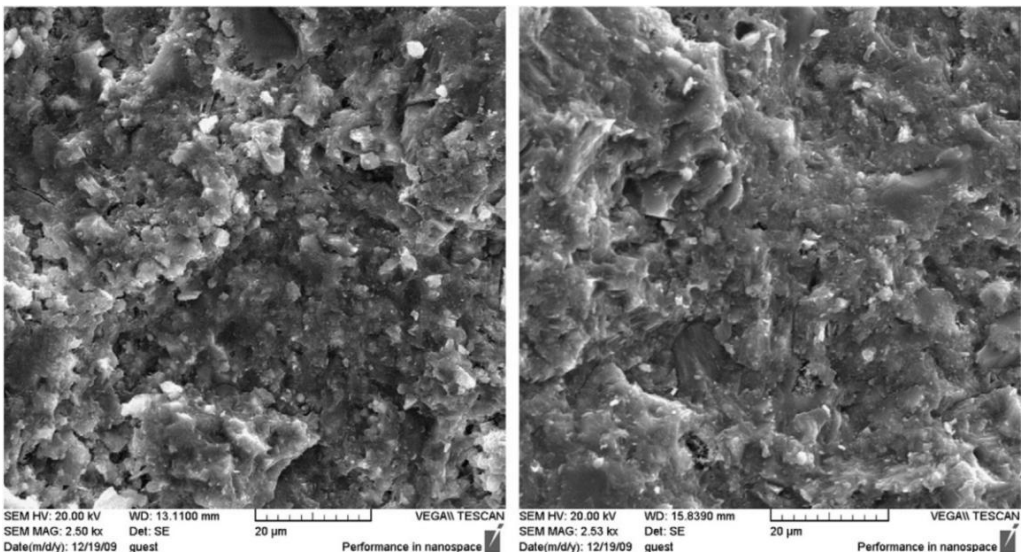

Figure 2.5: SEM Pictures of the Microstructures of Pastes, including Regular Cement (left) and Slag (right), after 120 Days of Curing at 2500× Magnification (Allahverdi & Ahmadnezhad, 2014)

He et al. (2021) analyzed the XRD pattern of dried MnS obtained from the experiment (Figure 2.6). Dried MnS primarily comprises sulphate-soluble minerals such as jarosite, quartz, hematite, limonite, muscovite, and dihydrate gypsum. On the one hand, these mineral phases are produced from low-grade manganese ore's extra mineral phases. Conversely, a significant amount of soluble sulphate was accumulated during the hydrometallurgical process of sulfuric acid leaching in conjunction with the two-step ore (pyrite) method. The addition of sulfuric iron ore resulted in a significant rise in the iron phase concentration compared to the previous MnS. Under the intense chemical reaction and sulfuric acid leaching, the manganese ore generated fine particles and reconfigured into a porous particle shape. The quartz and gypsum phase crystals have the most intact and sharp diffraction peaks at 26.6◦ and 11.6◦ (2θ), respectively, as shown in Figure 2.6. The microstructure of MnS was analyzed using SEM (Figure 2.7a). The observations revealed ground MnS particles exhibiting varying sizes and morphologies, with smaller particles tending to aggregate around larger ones. The particle size distribution of MnS was measured using a particle size analyzer, as presented in Figure 2.7b. Other mineral phases feature dispersed peak morphologies, lesser intensity peaks, and reduced crystallinity. Goethite and dihydrate gypsum are the byproducts of neutralization and precipitation of the leaching substrate. In contrast, jarosite and sulphates are the products of acid leaching, according to the production of EMR. However, gypsum, iron phase, and minerals resembling clay all play a part in the high-water absorption of EMR. Additionally, it has been shown that some water remains in the delicate capillary dissolving pores of EMR, and the conventional drying temperature did not wholly evaporate this portion of the moisture. This could also play a crucial role in explaining EMR's high viscosity and strong water absorption (Wang et al., 2022).

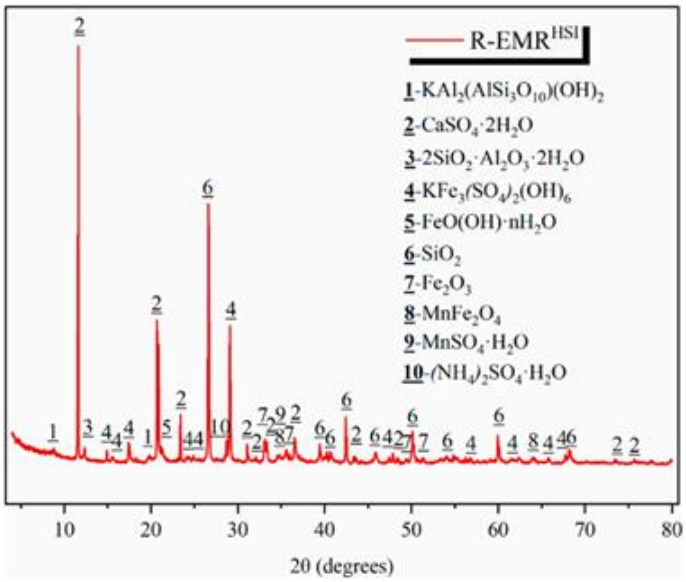

Figure 2.6: The Mineralogical Composition of MnS (He et al., 2021)

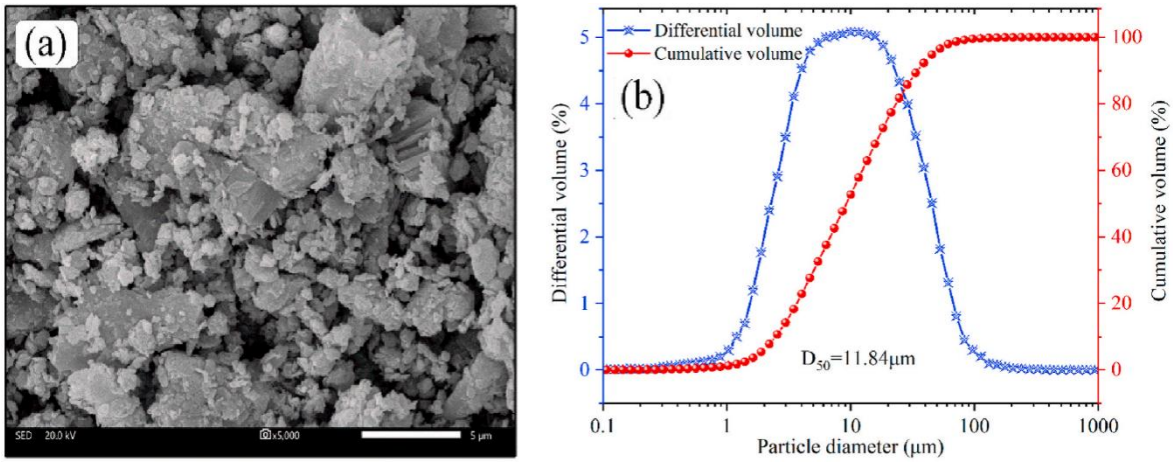

Figure 2.7: Particle Size Distribution of MnS Derived from BET Analysis (Wang et al., 2022)

Frias et al. (2006) have investigated the mineralogical composition and pozzolanic activity of SiMnS. Following an XRD examination of SiMnS, the following crystalline components were found: The primary compounds found in the slag are akermanite (calcium magnesium silicate) (1), calcium aluminium silicide (2), potassium magnesium silicate (3), manganese oxides (4), larnite (5), quartz (6), and sulphides (mostly manganese sulphides) (7) (Figure 2.8). This type of slag may contain additional compounds, including iron and

titanium oxides. However, it is unlikely that XRD can identify these because their distinctive peaks overlap with those of the manganese oxides. The XRD pattern of the slag sample revealed a diffuse wide band from a glassy phase that spanned from roughly 20 to 40 and localized at 30 (2-theta). The fixed lime content fluctuation as a function of SiMn slag reaction time is plotted in Figure 2.9. The results for fly ash (FA) and silica fume (SF), two pozzolanic ingredients often utilized in commercial cement blocks, are also displayed in the figure. SiMn slag exhibits an intermediate pozzolanic activity during the first 28 days of curing, falling between FA and SF. The lime consumption for SiMnS is essentially negligible after 28 days, and by the conclusion of the test (90 days of curing), it accounted for just 55% of the total lime supply. These findings suggest that SiMnS has pozzolanic activity, primarily at younger ages (less than 28 days) (Frias et al., 2006).

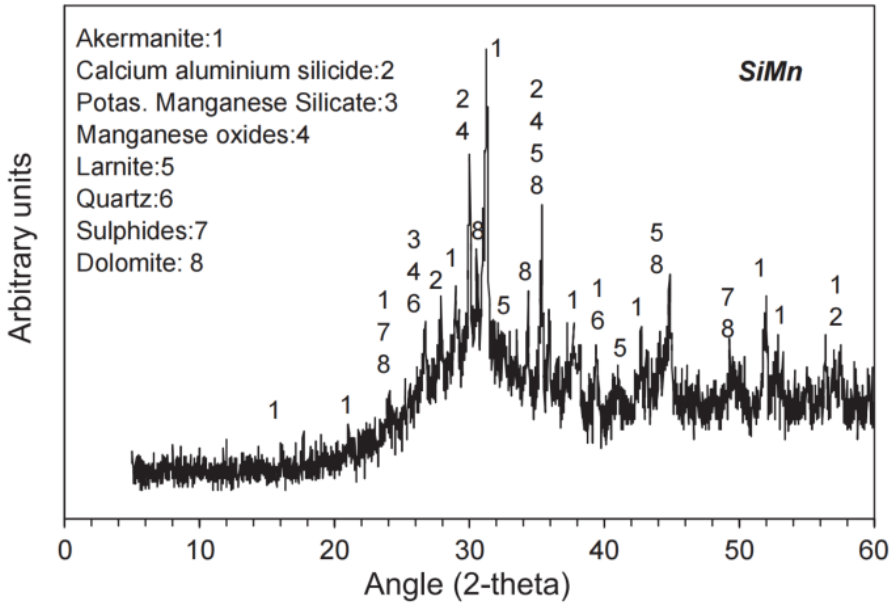

Figure 2.8: Mineralogical Composition of SiMnS (Frias et al., 2006)

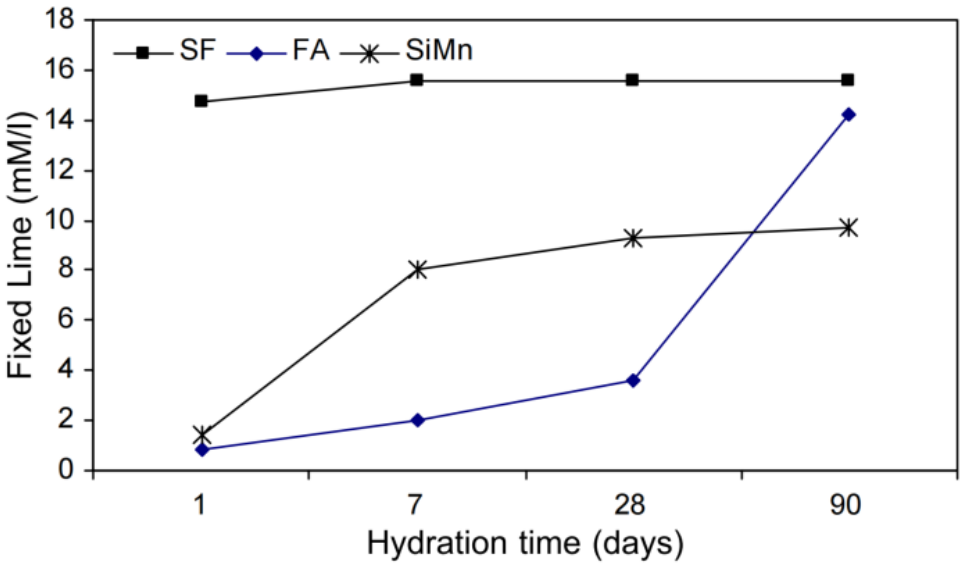

Figure 2.9: Pozzolanic Action of SiMnS (Frias et al., 2006)

Research on the use and disposal of EMRs has been conducted. Manganese slag was employed as a cement setting retarder (Feng & Xu, 2006). Fly ash and burnt MnS were utilized as a complicated cement ingredient (Li et al., 2007). The extra MnS was applied in small amounts (less than 15%) and not on a big scale. Investigations were conducted on the application of MnS to roadbed backfill and the use of MnS for crops (Lan, 2006; Lan & Wang, 2006; Lan & Unhelkar, 2005).

Xing et al. (2024) used a fully automatic specific surface area analyzer to determine the effect of different grinding times on the specific surface area of silicon manganese slag. The results are shown in Figure 2.10. When the grinding time increased from 5 min to 15 min, the specific surface area growth rate was 23%, while when the grinding time increased from 15 min to 25 min, the specific surface area growth rate was 29.4%. With the increase in grinding time, the specific surface area of SiMnS powder showed an upward trend. In the early grinding stage, the SSA of SiMnS powder increased slowly. As the subsequent grinding time increased, the specific surface area of silicon manganese slag powder gradually increased faster. This is because, in the early powder stage, the particle size of

silicon manganese slag is large, and the structure is compact. The energy consumption during the grinding process is large, and the degree of damage to the particles is small. As the grinding time increases, the silicon manganese slag particles gradually become finer, and defects in the internal structure occur, resulting in less energy consumption during the grinding process and more significant damage to the particles (Xing et al., 2024).

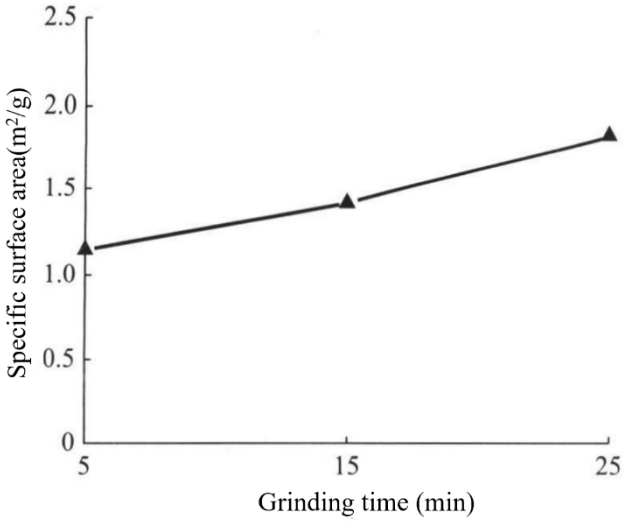

Figure 2.10: Relationship between Grinding Time and SSA (Xing et al., 2024)

2.4 Basis and Advantages of Partial Cement Replacement with Manganese Slag

According to previous research, the composition of ferromanganese and silicomanganese slags is comparable to that of traditional Portland cement. Manganese slag has pozzolanic qualities, which enable it to be used in substitutes for cement (Ng et al., 2024). Figure 2.11 illustrates the two forms of manganese slag that are typically produced from the metal smelting process (Tangstad et al., 2021): ferromanganese slag and silicomanganese slag. The amount of silica (SiO_2) and manganese oxide (MnO) distinguishes these two varieties of manganese slag (Lee & Kolbeinsen, 2021).

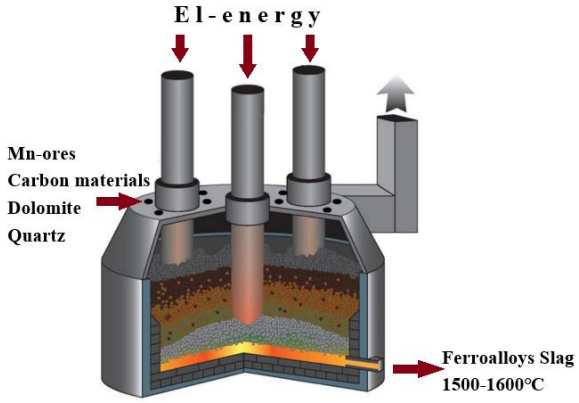

Figure 2.11: Typical Manganese Slag Production in a Closed Furnace (Tangstad et al., 2021)

Table 2.3 presents a comparison of the contents of MnO, SiO_2, calcium oxide (CaO), magnesium oxide (MgO), aluminium oxide (Al_2O_3), also known as alumina, and iron (III) oxide (Fe_2O_3) in regular Portland cement, ferromanganese slag (FeMnS), and SiMnS (Frias et al., 2006; Groot et al., 2013; Shahidan et al., 2017) .

Silicomanganese slag (SiMnS) is a byproduct from the manufacturing of silico-manganese alloy, a crucial component in steel production. Traditionally, this alloy is produced through carbothermic reduction of manganese ore in electric furnaces. Slag mainly contains oxides such as MnO, SiO_2, Al_2O_3, CaO, and MgO derived from ore, reducers, and fluxes (Tangstad, 2013; Tranell, 2006). The mineralogical composition of SiMnS varies based on the production process and raw material content. It typically contains crystalline and glassy phases (Nath et al., 2022; Tangstad, 2013). China leads the world in non-ferrous metal production, producing 73% of the silico-manganese produced worldwide. It is also the leader in research output about the application of SiMnS in alkali-activated material. India accounts for 9% of global manufacturing, followed by Ukraine at 4%, Malaysia and Russia totally at 2% (Figure 2.12).

Table 2.3: Analysis of the Oxide Concentration of Ferromanganese Slag, Silicomanganese Slag, and Regular Portland Cement

Compound (%)	SiO_2	Al_2O_3	CaO	Fe_2O_3	MgO	MnO
Ferromanganese slag (Groot et al., 2013)	28~30	5~5.5	28~30	1~1.3	6~6.5	28~30
Silicomanganese slag (Frias et al., 2006)	42.60	12.20	25.20	1.0	4.20	4.20
Normal Portland cement (Shahidan et al., 2017)	21.06	6.10	57.98	3.08	2.74	/

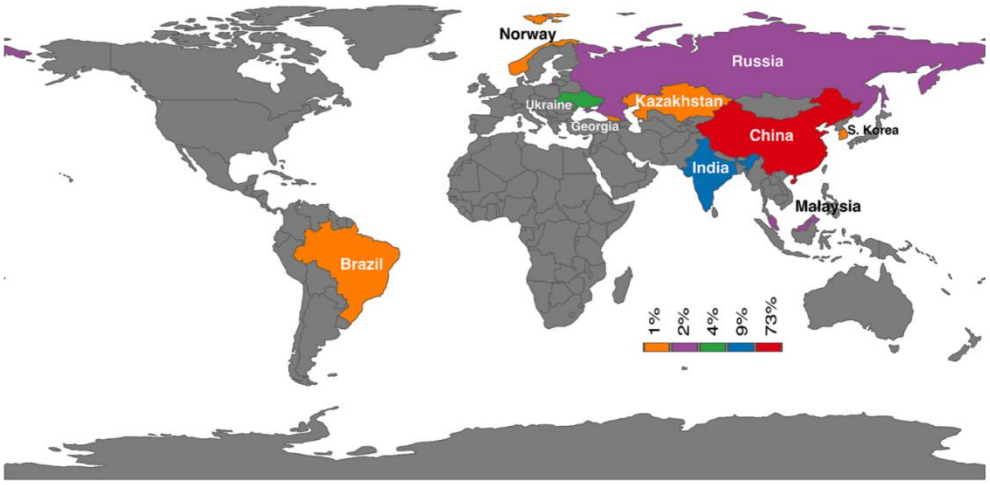

Figure 2.12: The Top Ten Global Producers of SiMnS in 2020 based on the International Manganese Institute (2020) (Cota et al., 2023)

Silicon manganese slag is produced by charging various raw materials within a furnace along with manganese ores, quartz (or quartzite), coke, and high-carbon FeMnS. Silicomanganese (SiMn) is a unique type of ferroalloy that enhances the mechanical properties of steel. It is produced through the carbothermic reduction of raw materials in a submerged arc furnace, generating SiMnS as a byproduct (Nath et al., 2022). A process with

a temperature range of 1600 to 1650℃ must produce metal with sufficiently high Si content and discard slag with low MnO content (Olsen et al., 2007). Equation 2.1 and Equation 2.2 are the primary element reduction reactions in the SiMn production process (Ma et al., 2018):

$$MnO + C \rightarrow Mn + CO \qquad \text{Equation 2.1}$$

$$SiO_2 + 2C \rightarrow Si + 2CO \qquad \text{Equation 2.2}$$

Table 2.4 displays the chemical composition of a portion of SiMnS. These data were gathered from published publications that originated from various plants in various parts of the world(Allahverdi & Ahmadnezhad, 2014; Frias et al., 2006; He et al., 2019; Kumar et al., 2013; Navarro et al., 2017). SiMnS is usually silico-calcic. It is comparable to blast furnace slag but differs somewhat in composition from it in that it contains slightly more MnO and less CaO (Navarro et al., 2018).

Table 2.4: Main Chemical Composition of SiMnS

Source	MnO	SiO_2	Al_2O_3	CaO	Fe_2O_3	MgO	Na_2O	K_2O	SO_3
He et al. (2019)	11.58	28.34	18.45	21.86	ND	4.72	0.41	1.04	2.23
Nath & Kumar (2017)	11.23	36.4	25.94	17.74	1.2	4.27	0.21	0.37	0.84
Navarro et al. (2017)	12.23	36.53	9.86	29.1	0.92	4.69	0.34	1.08	2.77
Nath & Kumar (2016)	10.06	40.33	14.55	26.17	0.75	5.74	0.21	0.92	1.57
Allahverdi & Ahmadnezhad (2014)	10.29	38.17	14.78	29.3	1.79	2.77	0.42	0.76	0.12
Frías et al. (2009); Frias et al. (2006)	9.9	42.6	12.2	25.2	1.0	4.2	0.36	2.2	0.12

Silicomanganese slag has potential hydraulic and pozzolanic activity, which is lower than silica fume but higher than fly ash. Manganese slag has the properties of gypsum and hydraulic industrial solid wastes due to its main chemical components, $CaSO_4 \cdot 2H_2O$, SiO_2, and small amounts of Al_2O_3, Fe_2O_3, MnO_2, etc. (Frias et al., 2006). Therefore, manganese slag can be used to prepare cementitious materials widely used in cement and concrete and is no longer limited to lower-value applications such as filling roads or replacing aggregates to produce bricks and blocks (Li et al., 2020). It can even change the performance of concrete and finally realize the application of manganese slag in building materials (Yang et al.,2014). The original Mn slag particles have adverse effects to some extent on the volume stability of concrete because of the alveolate pore structure (Liu, 2012). One way to excite manganese slag activity is mechanical activation. Mechanical activation means grinding the manganese slag into fine powder through mechanical grinding.

On the one hand, it increases the specific surface area of the MnS; that is, it increases the contact area between the MnS and water, accelerating the hydration reaction; on the other hand, it increases the hydration reaction in the MnS. The crystal structure is destroyed, and more defects are generated on the particle surface to increase the activity of MnS (Xu et al., 2019). Mechanical activation has a noticeable effect on the activation of manganese slag. The finer the manganese slag, the higher its activity (Wang et al., 2022). After mechanical activation, SiMnS cement paste achieved high strength, 101 MPa, after 28 days of curing, which is three times better than the strength in the case of ball milling of the same slag. This result can be explained by the different particle size distributions and reactivity of powder samples due to physicochemical changes in the surface and bulk of the particles (Nath et al., 2022). Observing the XRD pattern shown in Figure 2.13, it is found that calcium aluminate silicate hydrate (CASH) gel is also the hydration product of manganese slag cement slurry

except for calcium hydrate crystal and CSH gel. (Nath & Kumar, 2016). The sulphate in the electrolytic manganese slag can react with the aluminum minerals in the concrete, effectively improving the volume stability. The dense concrete structure can effectively solidify the heavy metal ions in the electrolytic manganese slag (Chousidis et al., 2015).

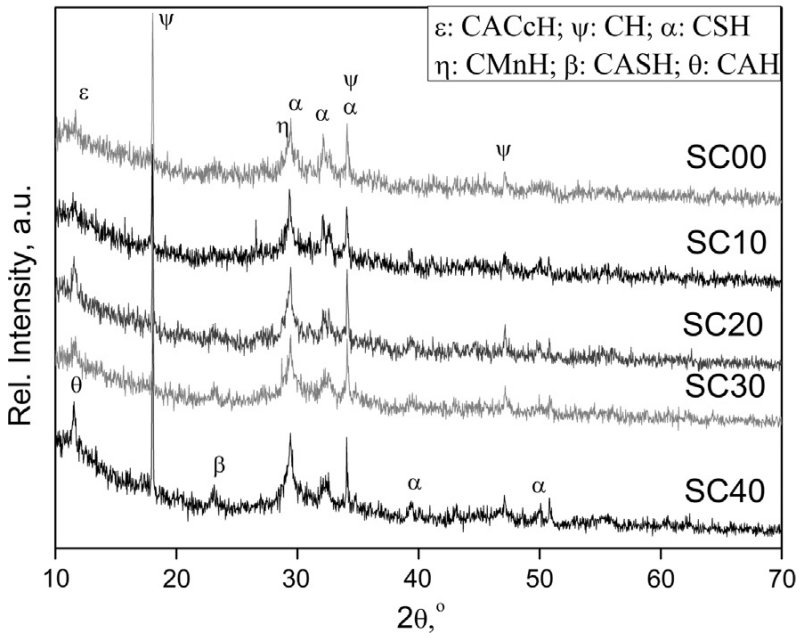

Figure 2.13: X-ray Diffractogram of Mixed Cement Pastes after 28 Curing Days

So far, the two primary types of cement made with electrolytic manganese residue (EMR) are sulpho-aluminate and Portland fly ash cement. To create blended hydraulic cement, Li et al. mixed 25% admixture—by combining 15% EMR treated at 300–850 °C with 85% fly ash—with 75% 42.5 ordinary Portland cement (OPC) (Li et al., 2007). Hou et al. calcined massive amounts of EMR with limestone and kaolin at about 1200°C to create quasi-sulphoaluminate cementitious material (Hou et al., 2012). Few studies have been published on using EMR as an activator in the production of GGBFS cement, which is granulated blast furnace slag with minimal or no clinker crushed. Glassy-state minerals in a three-dimensional structure created by active CaO, SiO_2, and Al_2O_3 make up GGBFS. Scanning electron microscopy (SEM) analysis revealed that the primary constituents of the

hardened GGBFS cement paste were ettringite (AFt) and fibrous calcium silicate hydrates (CSH) (Kumar et al., 2008). The active Al_2O_3 component in GGBFS reacts with a sulphate activator to create Aft (Pourchez et al., 2009). Since EMR contains more than 40% $CaSO_4$, mixing it with GGBFS should produce a cement that works well.

According to a study by Frias et al. (2006), SiMnS blended cement exhibits several advantageous qualities, including equivalent strength values to control mortar, volume stability, and a denser matrix. Because of these pozzolanic features, the cement can be blended with it. Additionally, Allahverdi and Ahmadnezhad (2014) demonstrate that blended cement, including SiMnS, does not show any volume instability and meets the chemical criteria of standard specifications. Significant strength development happens at a later age in cement, even though its beginning strength might not be sufficient (Frias et al., 2006; Nath et al., 2022). When used as an SCM, it participates in secondary hydration reactions. The hydration products of cementitious systems incorporating SiMn slag typically include portlandite and CSH phases, with the potential formation of manganese-rich hydrated phases contributing to the system's stability (Nath & Kumar, 2016). The primary environmental benefit of using SiMn slag lies in the valorization of a significant industrial waste. The ferroalloy industry generates substantial amounts of this slag, which traditionally consumes landfill space and poses long-term environmental risks due to the potential leaching of metallic elements into the soil and groundwater (Ting et al., 2020; Delgado-Plana et al., 2023). By diverting this slag for use in cement and concrete, the construction industry can contribute to a circular economy, reducing solid waste and its associated environmental hazards.

2.5 Environmental Challenges and the Imperative for Cement substitution

With the development of the globalized industrial economy, various countries are vigorously developing infrastructure construction, such as construction projects and road and bridge projects. Concrete is the most widely used building material in infrastructure construction worldwide and is one of the most used materials in various engineering constructions. The amount of concrete used is twice that of other construction materials, such as steel bars combined (Gagg, 2014). The reinforced concrete frame structure is one of the world's most used building structures. In this structure, the cost of concrete accounts for about half of the total cost of building structure materials. The primary constituent materials of concrete are cement, sand, and crushed stone aggregates. Because these materials are easy to obtain, highly economical, and have stable performance, concrete is widely used in industrial and civil buildings, bridges, and roads.

As the primary material for making concrete, cement is the main substance that affects concrete's strength, durability, fluidity, and cohesiveness. The main components of standard Portland cement are CaO (62.4%), SiO_2 (20.6%), Al_2O_3 (4.2%), MgO (3.4%), SO_3 (3.2%), Fe_2O_3 (2.1%), K_2O (1.1%) and Na_2O (0.2%) (Andersson, 1989). The primary raw materials for making cement are limestone and clay in nature. Due to the easy acquisition of manufacturing materials and the rapid development of the world's industrialization process, cement output has increased rapidly worldwide in the past 30 years. At this stage, global cement production is about 4.1 billion tons per year (Durastanti & Moretti, 2020). Cement production is growing at 2.5% per year and is expected to continue increasing to 5.8 billion tons by 2050 (Miller et al., 2018).

Large amounts of carbon dioxide are produced during the cement production process. For each ton of cement produced in 2020, approximately 0.59 tons of CO_2 were typically emitted (IEA, 2021). According to global carbon dioxide emission data, global cement plants emitted 2.9 billion tons of carbon dioxide in 2021, an increase of nearly five times from 570 million tons in 1990 (Benhelal et al., 2013). From 2006 to 2021, China, India, Europe, and the United States were the largest emitters of carbon dioxide (Hanifa et al., 2023).

Between 4 and 6% of the world's CO_2 emissions from the building sector come from the manufacturing of cement (Amran et al., 2020; Benhelal et al., 2013; Onn et al., 2019; Zareei et al., 2019). The direct emissions from the calcium carbonate's calcination and the indirect emissions from burning fossil fuels, processing minerals, and transportation contribute to the cement industry's carbon footprint (Crossin, 2015; Teh et al., 2017). Tremendous efforts have been made to lower the carbon footprint connected to cement production to minimize environmental effects (Paris et al., 2016; S. A. Zareei et al., 2019). Cement production has also become the third largest source of anthropogenic carbon dioxide emissions. Therefore, it is necessary to find suitable cementitious materials to replace cement (Kwan & Chen, 2013; Lomboy et al., 2012). One of these is cement replacement, in which ground granulated blast-furnace slag (GGBFS), for example, is used to replace cement partially (Ameri et al., 2020; Ameri et al., 2019; Awoyera & Adesina, 2019; Zamanabadi et al., 2019; Shoaei et al., 2020; Shoaei et al., 2019) in order to create blended cement (Miller et al., 2015).

Owing to its chemical resemblance to blast furnace slag, silicomanganese slag has been studied as a potential clinker substitute in slag cement formulations (Nath et al., 2022).

The utilization of processed slag in concrete consequently reduces the carbon footprint associated with cement production (Allahverdi & Ahmadnezhad, 2014). This reduces carbon dioxide gas emissions and lowers global cement consumption.

2.6 Design of Manganese Slag Concrete

The design of concrete mixtures incorporating manganese slag as a supplementary cementitious material or aggregate has been extensively studied to enhance sustainability and utilize industrial waste effectively (Tamayo et al., 2023). Researchers have extensively studied the design of manganese slag concrete, focusing on incorporating manganese slag as a sustainable supplementary cementitious material. This process aims to enhance concrete performance, reduce environmental impact, and utilize industrial waste effectively. This process involves critical steps such as the granulation and grinding of slag to achieve a reactive particle size, followed by a tailored mix design to optimize performance. Table 2.5 provides a synthesized overview of prior studies, comparing their mix design parameters, performance observations, and key innovations or limitations.

Table 2.5: Overview of Manganese Slag Concrete Design

References / Slag Type	Mix Design Parameters	Performance Observations	Innovations or Limitations
Nath et al. (2022) (SiMnS)	Role: Cementitious material. Process: Granulation (water quenching) & grinding	Granulated slag requires fine grinding to be suitable as a precursor material. The optimal fineness is critical for enhancing reactivity.	Fine grinding is a prerequisite for activating the slag's hydraulic and pozzolanic properties for use in concrete.

Table 2.5 continued

Allahverdi et al. (2015) (Water-quenched MnS)	Replacement: 35% of cement by weight. Test Age: 28 days.	Strength: 28-day compressive strength > 35 MPa. Durability: Exhibited satisfactory volume stability.	Demonstrates the feasibility of significant cement replacement without compromising strength and stability, suitable for structural applications.
Kumar et al. (2013; 2016) (Ball-milled SiMnS)	Role: Cementitious Material. Process: Ball milling to improve activity and fineness.	Microstructure: Hydration products were CSH gel and tobermorite, similar to cement.	Mechanical activation (ball milling) successfully enhances the slag's reactivity, producing an effective cementitious material.
Frias et al. (2006) (SiMnS)	Replacement: 15% of cement. Curing: 45 days in different aggressive solutions.	Durability: Significantly improved resistance to seawater erosion compared to ordinary concrete.	Highlights the contribution of SiMnS to enhancing concrete durability in aggressive environments, such as marine structures.
Ng et al. (2024) (Grinding MnS)	Role: Cementitious Material Substitute. Replacement Rate: 10% (by weight)	Workability: Increases slump of fresh concrete. Strength: Slight reduction at 10% substitution.	At a low substitution rate of 10%, the impact on engineering performance is acceptable. Long-term durability and environmental effects need attention.

2.7 Effect of Manganese Slag on the Performance of Cement Mortar

In China, the fluidity of cement mortar is determined using the test method for the fluidity of cement mortar (GB/T2419-2005, 2005), and the compressive strength of cement mortar is evaluated in accordance with the methods for testing the strength of cement mortar (ISO method) (GB/T17671-2021, 2021). When MnS substitutes for a portion of cement, these indicators can also be obtained by utilizing the same tests. Wang et al. (2013) investigated how the amount of MnS affected the cement's setting time and mechanical strength. Experiments indicate that when the MnS combination content increases, the setting time gets longer and subsequently shorter. Manganese slag is the main ingredient in the combination and is primarily made of gypsum. When the mixture content is less than 20–25% at the start of hydration, the gypsum and active Al_2O_3 in GGBS react swiftly to generate ettringite (AFt). As a result, a thin layer of AFt surrounds the cement particles, delaying the first and final setting times from 75 to 200 minutes and from 105 to 355 minutes, respectively, and stopping the hydration of active silicate. More AFt is produced and develops as acicular crystals that overlap amid the cement particles to form a reticular structure when the mixture percentage is over 20–25%. This results in a typical slurry setting, cutting the initial and final setting times to 175 minutes and 315 minutes, respectively. For MnS-GGBS cement applications, initial setting periods of about 3 hours and ultimate setting times of about 5–6 hours are ideal, even though all samples completely comply with international requirements for setting times. Thus, the ideal range of proportions is determined to be a mixture of 20–40%. Figure 2.14 displays the strengths of cement that contain different amounts of MnS mixture (Wang et al., 2013). With increased MnS mixture content, the compressive and flexural strengths first rise and subsequently fall. When enough of the mixture is added to GGBS and clinker, the SiO_2 and Al_2O_3 are fully activated. This increases the degree of

hydration, strengthening the cement paste once it has hardened. However, when the combination quantity increases, the total amount of GGBS and clinker present reduces adversely, decreasing silicate and aluminate levels and strength.

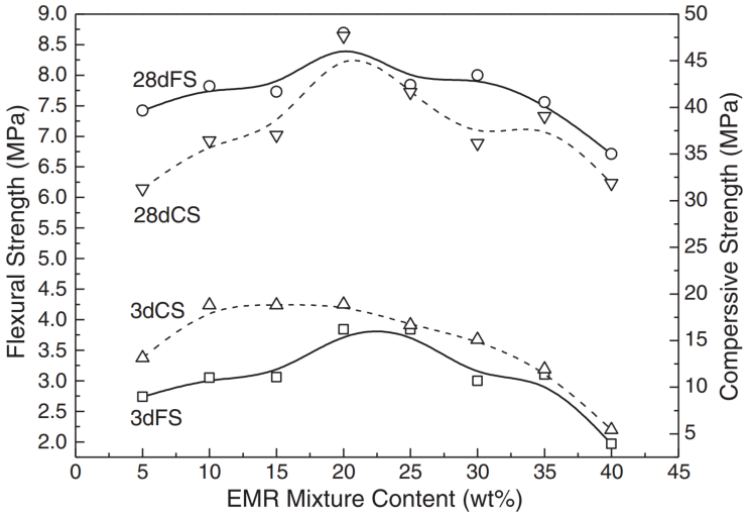

Figure 2.14: Relationship between Cement Strength and MnS Mixture Content (Wang et al., 2013)

In the Xu et al. (2019) test, the flexural strength and compressive strength of cement mortar with different hydration ages containing EMR are shown in Figure 2.15. It can be seen from the figure that with the change in v dosage, both the early strength and the late strength have a peak value, and the difference in early strength is more prominent. Electrolytic manganese residue 15% (EMR 15%) has the best 3 days strength, and its 3 days flexural strength and compressive strength can reach 6.8 MPa and 32.9 MPa, respectively. Compared with EMR 10%, its 3 days strength is increased by 41.7% and 60.5%, respectively, and compared with EMR 20%, its 3 days strength is increased by 70% and 72.8%, respectively. The reason the strength of EMR 15% is much higher than that of EMR 10% may be that sulphate accelerates the secondary hydration reaction of blast furnace slag (BFS). The mechanical properties of EMR 20% and EMR 25% are lower than those of the other

three samples. The results show that an appropriate amount of EMR can effectively promote the development of early strength (Xu et al., 2019).

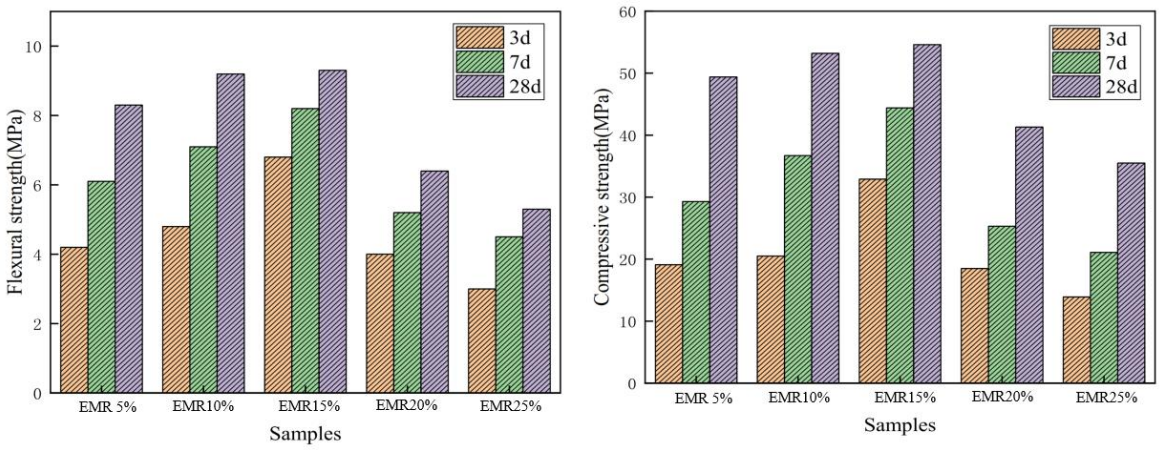

Figure 2.15: Flexural Strength (left) and Compressive Strength (right) of Cement Mortars with Different EMR Contents at Different Hydration Ages (Xu et al., 2019)

In the tests of Rai et al. (2002), various compositions of regular Portland cement and 20–60% low MnO granulated manganese slag were ground in a ball mill to a fineness of 3000 cm^2/g (Blaine permeability test IS 5516:1969). The physical characteristics of the compositions were compared to those listed in IS 455:1989 for Portland slag cement. According to IS 4031:1988 (Sections 4, 5, 3, and 6, respectively), standard consistency, setting time (Vicat), solidity, and compressive strength tests were carried out on hydraulic cement. Except for the 50:50 composition (SI Nos. 1–5), every result complied with IS 455:1989 for Portland slag cement. The results conclusively demonstrate that the compressive strength declines with increasing slag percentage; however, the 50:50 combination demonstrated 22 MPa and 33 MPa at 7 and 28 days of wet curing, respectively, meeting IS 455:1989 standards (Rai et al., 2002).

Frias et al. (2006) studied the effect of SiMnS on the mechanical properties of cement mortar. The fluctuation of flexural strength versus hydration time is depicted in

Figure 2.16 (left). Mortars containing SiMnS show less flexural strength than the control mortar during the initial curing days. The strength decreases with increasing SiMn concentration. The flexural strength values for blended mortars rise significantly after 7 days and resemble the control after 28 days of curing. Ninety days later, the flexural strength of the control mortar was not different from that of the mortar containing 5% SiMnS, while the mortar containing 15% slag was only 5% stronger than the control. Figure 2.16 (right) illustrates the compressive strength development over time. Up to 28 days, increasing SiMnS content slightly reduces strength, but by 90 days, values are comparable to the control. Strength loss after 7 days correlates with the slag replacement level. The reduction of the compressive strength loss decreases from 7.8% and 13.4% for 5% and 15% mortars, respectively, to 0% and 3.2% for extended curing times (7–90 days). The blended cement mortars' compressive strength values at 90 days are comparable to the control mortar's strength values (Frias et al., 2006).

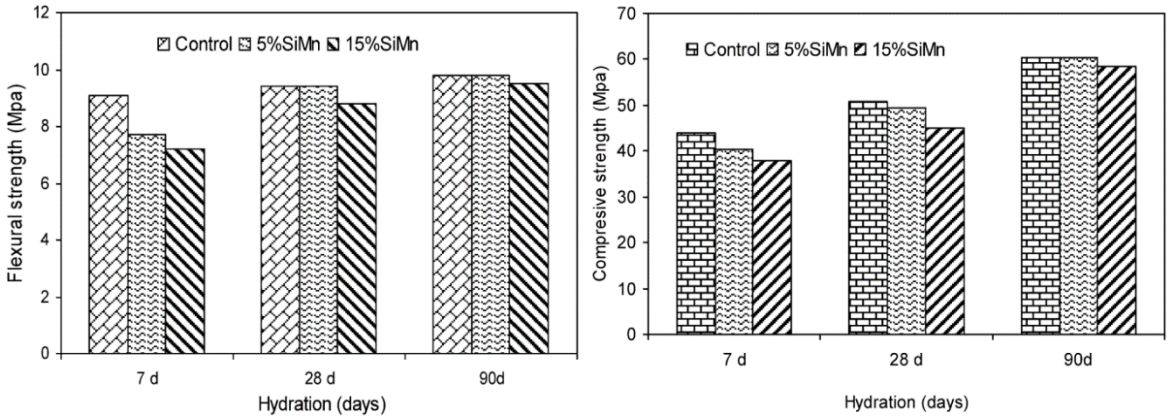

Figure 2.16: Development of Cement Mortar Flexural and Compressive Strengths (Frias et al., 2006)

Navarro et al. (2018) investigated the mechanical performance and dimensional stability of mortars made with alkali-activated of ground granulated SiMnS. They added various aggregates, including silica sand, limestone sand, and recycled sand made from

recycled concrete, and utilized sodium hydroxide and water glass solutions as activators. Their findings show that the optimum flexural and compressive strength results were obtained using an aggregate-to-slag ratio of 2:1, with silica sand as the aggregate and water glass as the activator. On the other hand, compared to aggregates made of silica and limestone, recycled concrete aggregate produced far less mechanical strength. Higher shrinkage was seen in mortars activated with water glass, but autogenous shrinkage was generally minimal for all types of activators and aggregates except for those with recycled concrete. Silica sand is the most effective aggregate for mortar preparation, but limestone sand also works well. These findings help explain how different aggregates and activators affect mortars' mechanical characteristics and dimensional stability with alkali-activated ground granulated SiMnS (Navarro et al., 2018).

2.8 Effect of Manganese Slag on the Workability of Concrete

Liang et al. (2011) studied the workability of concrete made with different amounts of manganese slag in accordance with the standard for testing the performance of ordinary fresh concrete (BS EN 12350-2:2019). In the test, the cement's specified strength is C35, and it was modified by replacing 0%, 15%, 30%, and 45% of the manganese slag with cement; 0% served as the reference group. As illustrated in Figure 2.17, when replacement exceeded 35%, there was a noticeable rise in the slump of freshly laid concrete. The cement constant was dropping along with the replacements, which caused the glue to hydrate slowly and function poorly (Liang et al., 2011).

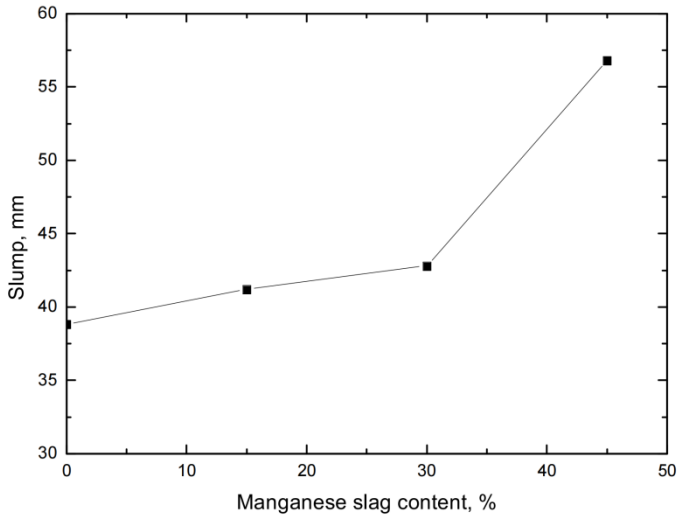

Figure 2.17: Influence of Manganese Slag Content on the Slump of Fresh Concrete (Liang et al., 2011)

Liu et al. (2012) studied the workability of concrete made with different amounts of ferromanganese slag (FeMnS). The fresh concrete mixture is well-workable and has no bleeding or segregation issues. The slump loss for concrete without FeMnS is 52.7% from 0 to 45 minutes. Slump loss for concrete with 20% FeMnS is 27%, clearly less than that of concrete without FeMnS. The tight-aligned alveolate pore structure is directly related to the early slump of FeMnS concrete. As the FeMnS content increases, more water is absorbed by its pore structure. With a fixed total water amount, less water is available to lubricate and coat the cement particles, leading to a noticeably lower initial slump. However, the glassy nature of FeMnS and its resulting ball-bearing effect make the cementitious particles flow more easily (Liu et al., 2012). Ng et al. (2024) have investigated the effect of MnS content on concrete slumps. At 20% MnS content, the maximum improvement in the slump of MnS concrete was 157% compared to the concrete batch with 0 MnS content (Figure 2.18). However, a higher water requirement and an increase in the pozzolan's surface area will result from the concrete mix's increased MnS concentration. There will not be enough water to function as a lubricant between particles if the MnS replacement surpasses 20% because

the water content is the same for all designed mixes. The workability drops when the replacement percentage of MnS is raised to 30%. In general, fresh concrete will be easier to work with when ground MnS is used in place of cement (Ng et al., 2024). However, they noted that when MnS replacement exceeded 20%, the water requirement increased due to the higher pozzolan's surface area, leading to reduced workability. Both studies indicate that while moderate amounts of MnS (up to 20%) can improve concrete workability, excessive amounts (beyond 20-30%) can reduce workability due to increased water demand and altered particle packing. This suggests an optimal range for MnS replacement exists, likely between 15-20%, where workability is maximized without compromising other properties.

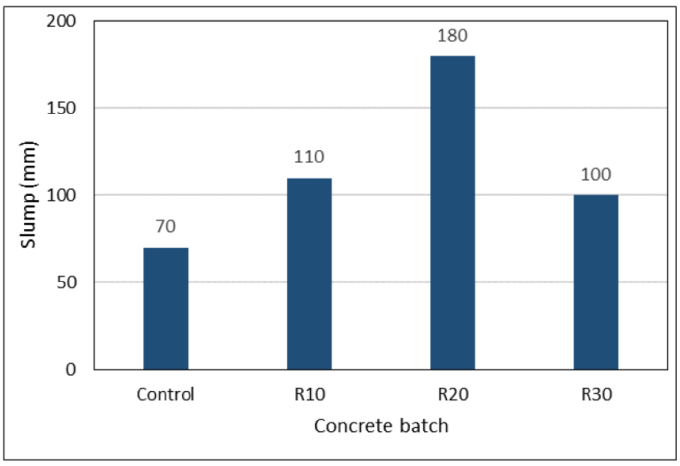

Figure 2.18: Workability of Concrete Measured with Slump Test (Ng et al., 2024)

Cota et al. (2023) attributed the improvement in compressive strength of alkali-activated samples of silicon-manganese slag to the improvement in microstructural density, gel formation and reaction products (Cota et al., 2023; Criado et al., 2018; Kumar et al., 2013; Nath & Kumar, 2017; Su et al., 2022). Su et al. (2022) found that the material's dissolving and initial reaction periods did not yield enough gel product to achieve equivalent strength until 3 hours. Additionally, Navarro et al. (2017) reported that manganese appeared to harm the reactivity and strength of SiMnS in the early phases but did not interfere with

long-term activation. These findings highlight the significance of giving enough time for structural and chemical alterations, which can result in improved mechanical characteristics.

Table 2.6: Slump Comparison of Three Concrete Samples

Sample	Slump (mm)	Slump after 1h (mm)	1h slump loss rate (%)
BC	145	100	31.0
MC	185	145	21.6
SC	195	110	43.6

A baseline C30 concrete without any admixture (sample name: BC) is taken as the base, and its slump design value is 120 - 140 mm. Based on this ratio, manganese slag is used to replace 30% of the cement to produce manganese slag concrete (sample name: MC), and 30% slag micronized concrete (sample name: SC) is set up for comparison. As shown in Table 2.6, manganese slag and slag micronized powder can improve the fluidity of fresh concrete, with manganese slag being slightly inferior to slag micronized powder. The 1h slump loss rate of the benchmark concrete is 31.0%, which is lower after adding manganese slag, and the slump retention performance is improved by nearly 10%. Meanwhile, the loss rate of ordinary slag micronized concrete is the largest, indicating that the manganese slag admixture can improve the workability of concrete (Gao et al., 2009).

The influence of MnS content on concrete workability, as synthesized from the literature in Table 2.7, reveals a non-linear relationship. At low to moderate replacement levels (typically below 20-30%), the spherical particle shape and micro-filler effect of MnS can improve particle packing and lubrication, potentially maintaining or even slightly enhancing slump. However, a consensus emerges from the literature that when the MnS

content exceeds approximately 20-30%, the workability of concrete begins to decline significantly. This decline is attributed to the increased water demand of fine MnS particles and the reduced content of cementitious materials, which adversely affect mix cohesion and flowability.

Table 2.7: Literature Summary on the Effect of MnS Content on Concrete Workability

References	Content	Critical Factors	Main Findings
Liang et al. (2011)	0%, 15%, 30%, 45%	Substitution ratio, total cementitious materials	Slump increases significantly when content exceeds 35%; reduction in cementitious materials leads to slower hydration and decreased workability.
Liu et al. (2012)	20% (FeMnS)	Pore structure and particle morphology	Slump loss of concrete with 20% FeMnS (27%) is lower than ordinary concrete (52.7%); porous structures absorb water reducing initial slump, but glassy particles improve flowability.
Ng et al. (2024)	0% - 30%	Relationship between substitution ratio, SSA and water demand	At 20% substitution, slump increases by 157%; beyond 20%, increased water demand leads to decreased work efficiency.
Gao et al. (2009)	30% (comparison with slag powder)	Particle fineness and water retention	Slump of MnS concrete is slightly lower than slag powder concrete, but 1-hour slump loss rate is lower (improved by ~10%).

Therefore, to ensure the concrete in this study possesses reliable and consistent fresh properties—a prerequisite for any meaningful investigation into hardened properties—the

upper limit for MnS replacement is set at 20%. This conservative dosage not only aligns with the reported threshold before significant workability loss but also provides a stable and workable baseline mixture. This allows the subsequent experimental program to focus unequivocally on investigating the influence of the key variable: Specific Surface Area.

2.9 Effect of Manganese Slag on the Mechanical Properties of Concrete

The primary chemical components of EMR are SiO_2, Al_2O_3, and Fe_2O_3, together with trace quantities of sulphate, MnO_2, and CaO. Electrolytic manganese residue is a source of building materials, such as brick, ceramic, and concrete, just like gypsum and hydraulic industrial solid wastes (Du et al., 2014; Hou et al., 2012; Qian et al., 2012). 5–10% electrolytic manganese residue might generate C25/C30 concrete with good compressive strength, Young's modulus, and resistance to chloride ion attack (Chousidis et al., 2018). When 30% EMR is added as a filler, the sulfur concrete's compressive and flexural strengths reach 63.17 MPa and 9.47 MPa, respectively, and its leaching toxicity meets GB 8978-1996 (Yang et al., 2014). Unfortunately, this process is challenging to apply on a wide scale because of the high cost of sulfur, the difficulties in obtaining polysulfide rubber, and the high production costs. Furthermore, 45% EMR may be used to create electrolytic manganese residue-activated cementitious material, which can fix Mn^{2+} and NH_4^+ (Figure 2.19) (Zhang et al., 2017) and have a compressive strength of 30 MPa at 28 days (Wang et al., 2020). Concrete's low activity, expense, and dearth of effective activation technologies are the reasons behind the restriction on EMR reuse.

Escalante-Garcia et al. (2009) examined the effect of industrial by-products, including manganese slag, on concrete compressive strength. The study highlighted those concrete mixes with 30% MnS replacement exhibited a 15% increase in compressive

strength at 56 days compared to ordinary Portland cement (OPC) concrete. This was due to the slag's latent hydraulic properties, which contributed to long-term strength development. However, excessive slag content reduced the strength gain rate, as the pozzolanic reaction slowed over time (Escalante-Garcia et al., 2009). Kumar et al. (2008) investigated the compressive strength of concrete containing MnS in high proportions. Results showed that incorporating up to 25% MnS led to a 12% improvement in 28 days of compressive strength. Beyond this level, strength gains diminished as substituting clinker-rich cement with MnS reduced the availability of active hydration sites. Kumar concluded that MnS is a viable supplementary cementitious material used within optimal replacement percentages. They analysed the flexural properties of MnS-based concrete and observed a 10% improvement at 15% replacement. The enhancement was linked to the micro-filler effect of MnS particles, which contributed to the densification of the concrete matrix. However, at 30% replacement, the flexural strength gains diminished, with only a 5% increase compared to the control. Kumar emphasized that MnS content should be optimized to balance flexural performance, workability, and hydration rates (Kumar et al., 2008). The two studies agree that MnS can enhance concrete strength within an optimal replacement range (15-30%). Beyond this range, the strength improvements diminish due to the dilution of clinker and reduced binder efficiency.

Escalante-Garcia et al. (2009) also studied flexural strength and found a 15% improvement at 30% MnS replacement. The findings suggested improved tensile performance from enhanced matrix integrity and stress distribution within the mix. However, further increases in MnS content led to minor reductions in strength due to an over-reliance on the pozzolanic reaction, which could not fully compensate for the lack of primary hydration products (Escalante-Garcia et al., 2009).

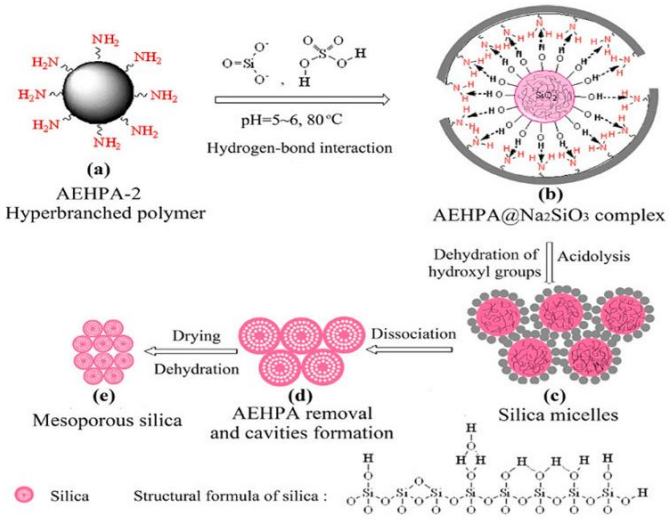

Figure 2.19: Electrolytic Manganese Residue-activated Cementitious Fixaion Mn^{2+} and NH_4^+ (Zhang et al., 2017)

The compressive and flexural strength of MnS concrete, tested per BS EN 12390-3:2019 and BS EN 12390-5:2019, generally exhibited a declining trend with increasing MnS substitution (0-30%) in the study by Qin and Zhou (2009). For instance, at 20% substitution, the 28-day compressive strength was 19% lower than the reference group, falling below the C35 grade requirement. This decline contrasts with findings from Gómez-Casero et al. (2023), who reported that alkali-activated SiMnS could achieve compressive strengths up to 11.6 MPa under specific activator conditions. The discrepancy may stem from key differences in binder systems (ordinary Portland cement vs. alkali-activated cement) and activation methods. In Qin and Zhou's study, the primary reason for the strength reduction could be the dilution effect of cement and potential changes in the microstructure. However, it is noteworthy that even in their results, the loss in flexural strength (6% at 20% substitution) was significantly less pronounced than the loss in compressive strength. This suggests that MnS might contribute differently to the tensile properties of the concrete matrix, a phenomenon observed in other industrial by-product studies (e.g., Wang et al., 2025, who noted improved early strength in microwave-cured alkali-extracted lithium slag systems).

Therefore, the observed "deterioration" is not absolute but highly dependent on the mix design and curing regime. A critical synthesis indicates that while simple partial cement replacement with MnS in ordinary Portland cement systems often leads to strength reduction, employing activation strategies (alkali or thermal) or utilizing MnS in alternative binder systems can unlock its latent hydraulic/pozzolanic potential, potentially leading to performance improvements.

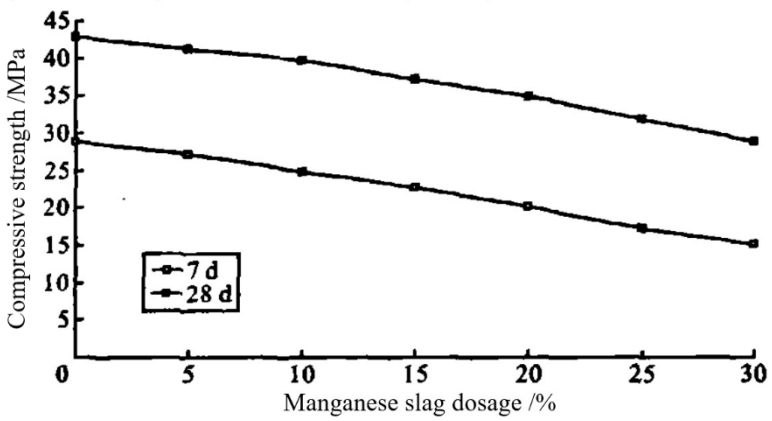

(a) Compressive strength of manganese slag concrete

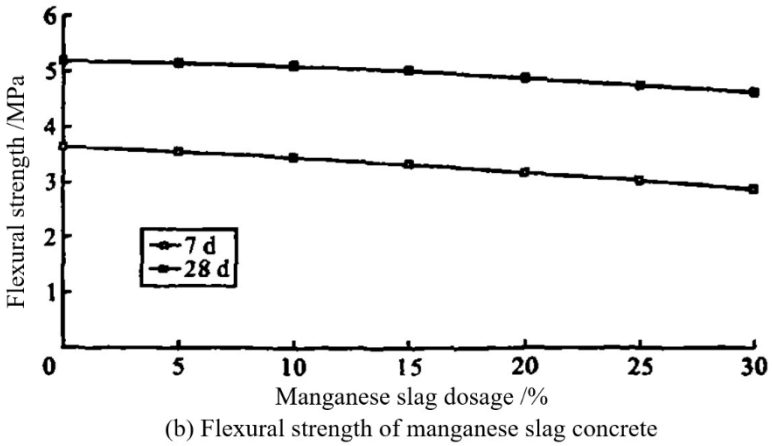

(b) Flexural strength of manganese slag concrete

Figure 2.20: Relationship between MnS Dosage and Compressive and Flexural Strength of MnS Concrete (Qin & Zhou, 2009)

Ismail et al. (2013) investigated the effects of various supplementary materials, including MnS, on the permeability and strength of concrete. Their research revealed that using 20% MnS not only increased compressive strength by 12% at 28 days but also reduced

water permeability by 30%. This reduction in permeability is crucial for enhancing the longevity of concrete structures, particularly in environments exposed to water and chloride ions. The authors highlight the importance of incorporating such materials to achieve both strength and durability in concrete (Ismail et al., 2013).

Rai et al. (2002) reported that including MnS in concrete mixtures can substantially improve mechanical properties. Their study found that a 25% replacement of cement with MnS resulted in a compressive strength of 45 MPa, which is a 20% increase compared to control samples. Furthermore, they observed an increase in flexural strength, achieving values of 8 MPa versus 6.5 MPa for the control mix. The authors suggest that the synergistic effects of MnS with other industrial by-products can further enhance concrete's performance (Rai et al., 2002). Parimi and Satyanarayana (2021) explored the stabilization of soils using MnS and its implications for concrete strength. Their findings indicated that adding 30% MnS led to an 18% increase in compressive strength, reaching 42 MPa at 28 days, while flexural strength improved by 22%, achieving 7 MPa. The authors emphasize the potential of MnSg not only as a concrete additive but also in improving the mechanical properties of other construction materials, thus contributing to sustainable building practices (Parimi & Satyanarayana, 2021).

Lavanya and VenkatRao (2023) analysed the flexural strength of concrete with MnS and supplementary materials like fly ash. The study found that replacing 25% of cement with MnS increased flexural strength by 20% at 28 days. The synergistic interaction between MnS and fly ash contributed to matrix densification and reduced microcracking. However, replacement levels beyond 30% showed only a 5% improvement due to insufficient binder content (Lavanya & VenkatRao, 2023). Yang et al. (2024) tested flexural strength using MnS

in high-performance concrete. The results showed a 14% improvement at 20% MnS replacement, attributed to improved bonding at the interfacial transition zone (ITZ) and reduced shrinkage cracking. Beyond 30%, flexural strength gains diminished, with only a 6% increase compared to the control, indicating that higher replacement levels weakened the tensile properties of the matrix (Yang et al., 2024).

Liang et al. (2011) explored the influence of MnS on compressive strength in blended cement systems. The study observed that concrete with 30% MnS exhibited a 10% improvement in compressive strength at 90 days, highlighting the material's long-term pozzolanic activity. However, the study warned that higher replacement levels (e.g., 40%) could lead to strength reductions due to the reduced availability of cementitious compounds for early hydration (Liang et al., 2011).

He et al. (2024) examined MnS replacement at 15%, 25%, and 40% in standard concrete. The study revealed a 12% compressive strength increase at 15% MnS replacement, attributed to improved particle packing density and pozzolanic activity. At 40%, compressive strength decreased by 10% compared to the control due to the excessive dilution of clinker and slower hydration rates (He et al., 2024).

Deng et al. (2024) studied the effects of different mineral filling components, such as silicon manganese slag powder, on the performance of early high-strength shotcrete. Figure 2.21 shows the effects of SiMnS powder, silica ash, fly ash, and sulphoaluminate cement on the compressive strength and construction performance of early high-strength shotcrete. Compared with other mineral filling materials, SiMnS powder has certain advantages in improving early strength and working performance. Among them, when SiMnS mineral filling is used, the 8 hours, 1 day, and 28 days compressive strength of

shotcrete will increase, the 2 hours slump will decrease by 10 mm, and the collapse time will increase. This is because SiMnS is rich in silicon dioxide and manganese ions. Under the stimulation of alkaline substances such as sodium nitrite, the content of active silicon dioxide and the hydraulic activity of ferrite are significantly increased, the retarding effect of gypsum on ferrite is alleviated, and the early strength of ferrite is improved. At the same time, the microstructure of SiMnS is not round, and there is a porous structure, which increases the viscosity of concrete. Generating multiple mineral components further compacts the cement hydration structure and improves the later strength of concrete (Deng et al., 2024).

Xu et al. (2024) focused on high-strength concrete with MnS as a partial cement replacement. The research demonstrated that replacing 25% of cement with MnS increased compressive strength by 18% at 56 days. The long-term strength gain was attributed to the slow pozzolanic activity of MnS, which contributed to the continuous formation of CSH. However, at replacement levels exceeding 35%, compressive strength began to decline due to insufficient primary hydration products (Xu et al., 2024).

Su et al. (2023) investigated the compressive strength of concrete incorporating MnS at 10%, 20%, and 30% replacement levels. The study found that a 20% replacement led to a 15% improvement in compressive strength at 28 days compared to the control. The improvement was attributed to the reactive silica and alumina content of MnS, which enhanced the hydration process. At 30% replacement, the strength increase was marginal (4%) due to reduced clinker content and dilution of the cement matrix (Su et al., 2023).

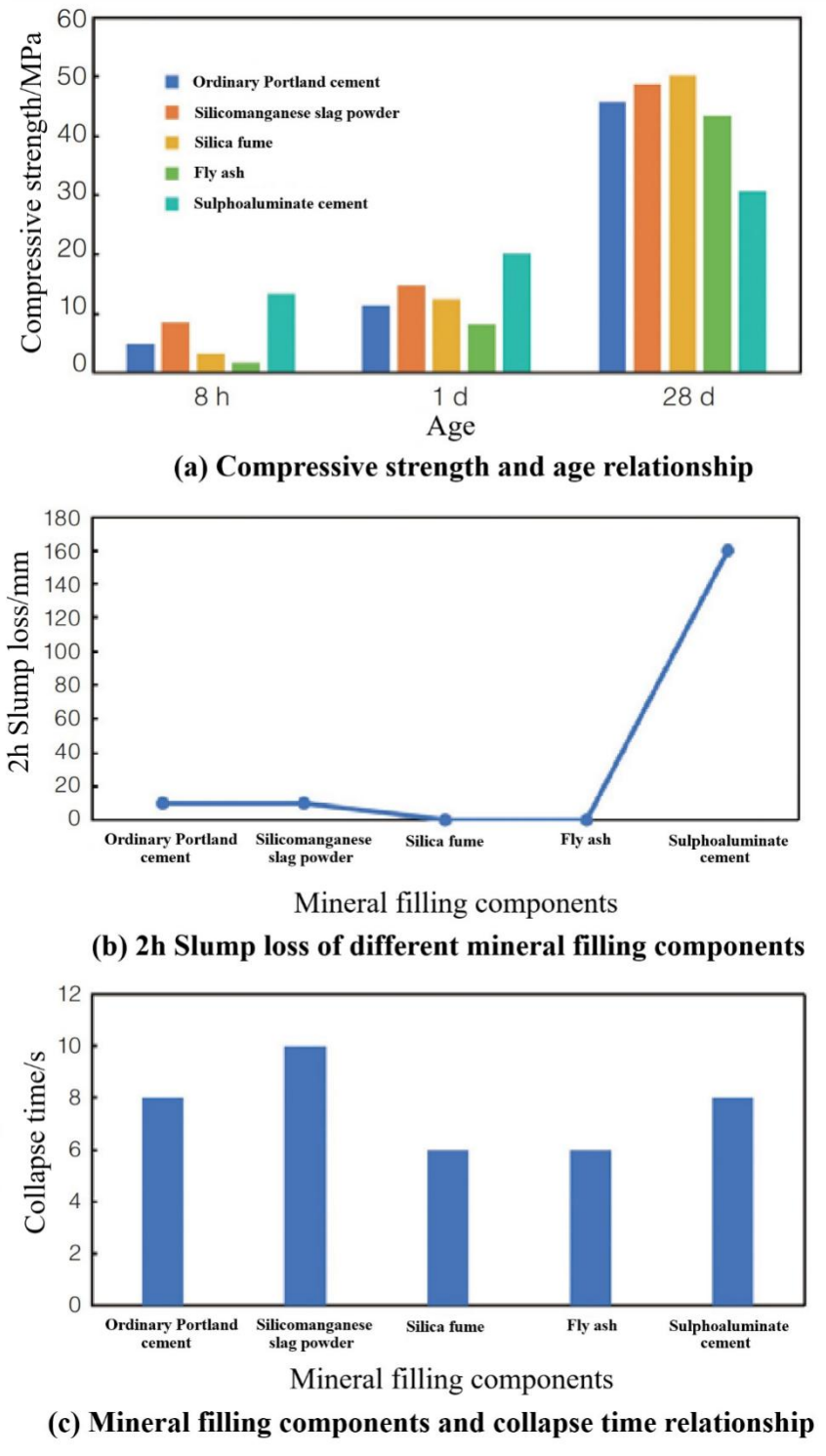

Figure 2.21: Compressive Strength and Construction Performance of Early High-strength Shotcrete with Different Mineral Fillings (Deng et al., 2024)

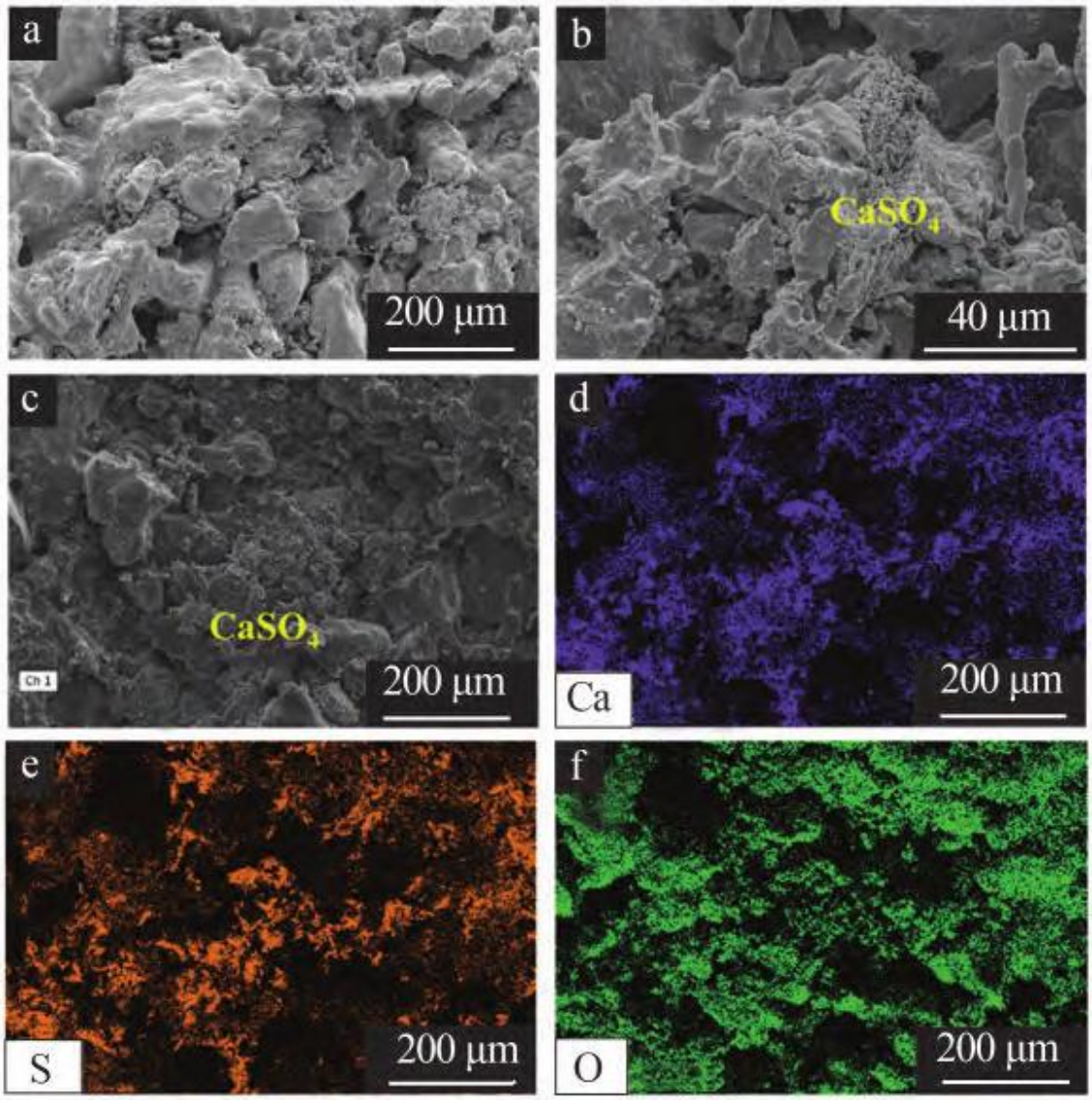

Figure 2.22: Scanning Electron Microscopy Image of MnS after Calcination at 1100 Degrees Celsius (Ye et al., 2024)

Ye et al. (2024) found through experiments that MnS, after high-temperature sintering, has been vitrified and has high compressive strength. After crushing and grading, it can replace aggregate in concrete. The surface morphology of MnS after calcination at 1100°C is shown in Figure 2.22. As shown in Figure 2.22a–c, there are many large grains and many holes on the surface of the calcined MnS. Some small grains are distributed around the large grains. Combined with the surface distribution diagram of Ca, S, and O elements (Figure 2.22d–f), these tiny particles are mainly $CaSO_4$. The presence of $CaSO_4$ can promote

the formation of calcium vanadium during cement hydration. $CaSO_4$ will hydrolyze SO_4^{2-} and react with alumina and silica in cement to form CSH gel, fill the pores of concrete, improve the interface between aggregate and cement, make the structure denser, and ultimately help improve the flexural strength (Ye et al., 2024).

Studies on MnS replacement (5–40%) show varied strength outcomes. Most research suggests an optimal range of 15–30% enhances compressive strength (e.g., +15% at 56 days with 30% MnS; Escalante-Garcia et al., 2009), while exceeding ~30–40% often reduces strength due to clinker dilution (He et al., 2024; Qin & Zhou, 2009). Flexural strength follows a similar trend, with gains of 10–15% within 15–30% replacement (Kumar et al., 2008; Escalante-Garcia et al., 2009) but diminishing returns beyond 30% (Lavanya & VenkatRao, 2023; Yang et al., 2024). The significant scatter in reported strength data (e.g., compressive: +10 to +20%; flexural: +14 to +22%, with some decreases) is attributed to two factors: differing replacement ratios and, more critically, variations in the SSA of MnS. SSA of the MnS is often overlooked but can significantly affect hydration kinetics and strength development. Consequently, SSA is poised to impact the workability and mechanical attributes of concrete. This assumption is articulated in Chapter 1 of the research gaps, as mentioned in this thesis. Further research is needed to clarify the role of SSA in optimizing MnS utilization in concrete and it is consistent with one of the research objectives of this thesis.

The effect of manganese slag content on the mechanical properties of concrete exhibits an optimal range. Table 2.8 summarizes key findings from the literature, indicating that compressive and flexural strengths are typically maximized or meet standard requirements when the replacement level is between 15% and 25%. Strength gains diminish

or decline beyond 25%-30% due to the dilution of effective cementitious components. This consensus provides a strong foundation for parameter selection. Aligned with the workability findings (Section 2.8), and to ensure a balance between fresh and hardened properties, a replacement level of 20% was selected as the fixed variable for the core concrete experiments in this study, enabling a focused investigation into the effect of SSA.

Table 2.8: Literature Summary on the Effect of Manganese Slag Content on Mechanical Properties of Concrete

References	Content	Key Findings	Mechanistic Insights
Wang et al. (2013)	≤20-25%	Compressive strength meets standards at ≤25% replacement.	MnS (>25%) reduces strength due to dilution of cementitious phases.
Xu et al. (2019)	10–25%	Peak strength at 15% MnS: 32.9 MPa (3-day compressive strength, +60.5% vs. 10% MnS). Higher replacements decrease strength.	Optimal content balances activation and clinker dilution.
Rai et al. (2002)	20–60%	50:50 cement-MnS mix achieves 22 MPa (7d) and 33 MPa (28d). Strength declines with higher MnS.	Fineness and pozzolanic activity contribute to strength. Excessive MnS reduces reactive components.
Nath & Kumar (2016)	5–15%	28-day compressive strength reaches 101 MPa with finely ground MnS.	Mechanical activation (high SSA) enhances reactivity
Frias et al. (2006)	5–15%	90-day compressive strength comparable to control (≤3.2% difference at 15% MnS).	Contributes to long-term strength via pozzolanic reactions.

Table 2.8 continued

Kumar et al. (2008)	≤25%	Compressive strength increased by 12% at 28 days.	>25% MnS reduces gains.
Escalante-Garcia et al. (2009)	30%	15% increase in compressive strength at 56 days.	Enhances long-term strength due to latent hydraulic properties.
Parimi & Satyanarayana (2021)	30%	18% increase in compressive strength (42 MPa).	MnS stabilizes soils and improves concrete strength.

2.10 Effect of Manganese Slag on the Durability of Concrete

The incorporation of manganese slag as a supplementary cementitious material influences concrete durability by modifying pore structure and reducing permeability. When water freezes and expands by roughly 9% within concrete pores, the finer particle size and enhanced reactivity of MnS can reduce pore connectivity, thereby mitigating internal pressure buildup during freeze-thaw cycles (He et al., 2024). Studies have shown that optimized MnS content (e.g., 10–20% cement replacement) improves resistance to chloride ion penetration and freeze-thaw damage (Liu et al., 2012； Otieno al., 2014), aligning with sustainability goals through effective industrial waste utilization.

Durability to freezing and thawing cycles is one of the factors affecting the durability of concrete structures in cold regions. Porousness is a natural characteristic of concrete. Its freezing and melting power depend mainly on the adhesive composition. For example, porosity, pore size, capillarity, distribution and pore type (open or closed) (Shahrajabian & Behfarnia, 2018). The testing methods for concrete durability generally correspond to those specified in the BS EN 12390 series (Parts 8, and 9). Fu et al. (2011)

studied the durability of alkali-activated slag concrete (ASC) against freeze and thaw cycles. Their results showed that the final reaction product in ASC is CSH gel with a low Ca/Si ratio. The adhesive strength prevents water penetration, freezing and soaking, thereby increasing the durability of concrete against freezing and thawing cycles (Fu et al., 2011).

Concrete's durability is significantly impacted by freeze-thaw damage and chloride corrosion, which have a major impact on structural performance and service life (Li et al., 2021). Cl^- keeps diffusing in concrete exposed to a chlorine salt environment. On the one hand, the hydration products in concrete react chemically with Cl^-, loosening the internal structure of the concrete material (Zhang et al., 2021). The alternating fluctuations in temperature, both positive and negative, impact the porosity and permeability of concrete, altering its mechanical qualities (Shen et al., 2020). Concrete damage occurs when salt corrosion and freeze-thaw cycles combine to create a more complicated damaging mechanism. Conventional research primarily focuses on the behavior of concrete deterioration under a single environmental component, although salt corrosion and freeze-thaw cycles frequently affect the environment on engineering sites. Concrete degradation may worsen due to a combination of variables that exacerbate the deterioration of concrete's durability (Heidari et al., 2017; Wang & Niu, 2016). During long-term use, microcracks in concrete significantly negatively impact its durability. The growth of microcracks in concrete can be attributed to various factors. The majority of these are chemical reactions, such as the alkali-silica reaction, sulphate attack, carbonation, and combustion, while others are physical processes, like ice-freezing and cargo damage. The generated particles impair the cement matrix's cohesiveness and the interfacial bonding forces between the aggregates and their respective cement matrices (Mehta, 2006). This section synthesizes key

mechanisms by which MnS enhances durability, drawing on empirical evidence from recent peer-reviewed studies.

2.10.1 Effect of Manganese Slag on the Frost Resistance of Concrete

Relevant statistics show that, worldwide, the area covered by the seasonal frost zone and the many years of frozen zone makes up close to 50% of the total geographical area; in China, this ratio exceeds 70% (Wei & Wang, 2012). The distribution of frozen soil in China in the mid-to-late 20th century is shown in Figure 2.23, where blue represents permafrost, yellow represents seasonal frozen soil, and orange represents temporary frozen soil (Wang et al., 2014). In the high latitude of northern China and the high altitude region of western China, the low-temperature span is long, the temperature difference between day and night is significant, the distribution range of permafrost is vast, and the repeated freezing and thawing action has become one of the main factors of the deterioration of the mechanical properties of the concrete structures in this region, the reduction of the load bearing capacity, and the damage of the failure (Li et al., 2022). As one of the main factors of concrete damage, since the 20th century, Chinese and foreign scholars have conducted a large number of studies on the damage mechanism, mechanical property deterioration and damage evolution, which provide important theoretical support and practical guidance for the prevention and control of concrete freeze-thaw disaster, to ensure the safe operation of significant engineering projects in cold regions, and to solve the problem of roadbed construction in high-altitude areas. The freeze-thaw damage of concrete comes from two aspects. One is that the volume of water in saturated concrete increases after freezing, thus generating expansion stress; the other is that the free water in the concrete migrates and redistributes in the voids, which circulates repeatedly and eventually causes freeze-thaw fatigue damage to the concrete (Mohamed et al., 2000).

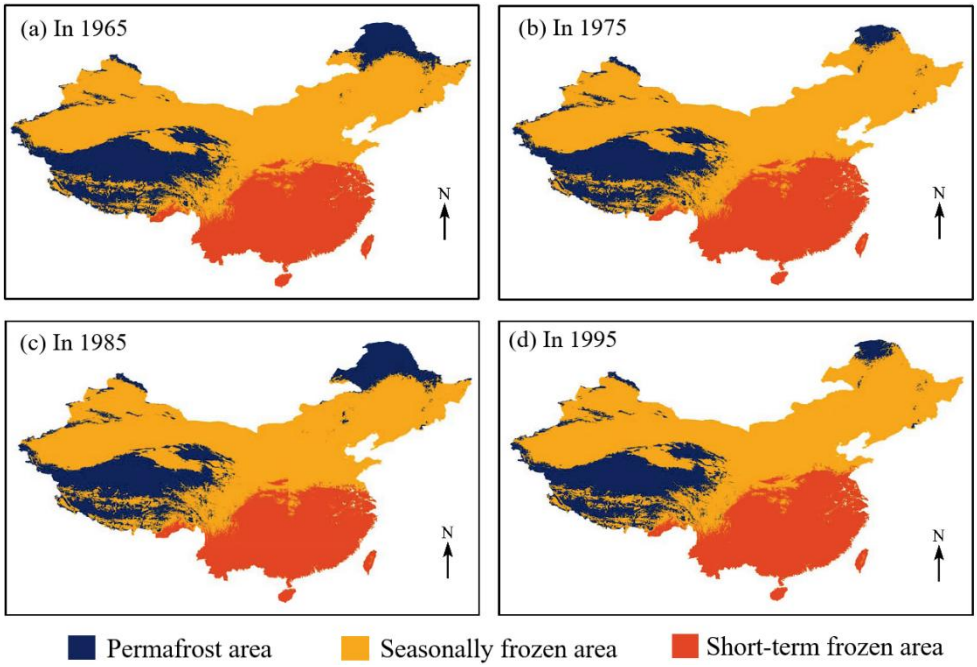

Figure 2.23: The Distribution of Frozen Soil in China in the Mid-to-late 20th Century (Wang et al., 2014)

The frost resistance of concrete is usually studied through freeze-thaw cycle tests. Luo et al. (2017) traced the evolution of the interior microstructure based on cross-sectional, 2D slice and 3D concrete images created during the freeze-thaw (F-T) cycle periods. The concrete's interfacial transition zone (ITZ) may be damaged during the F-T process. First, the ITZ is the weakest part of the concrete. In addition, the F-T effect not only causes the weak areas of concrete to crack, namely cement concrete and ITZ, but also weakens the composites after certain stages of F-T cycles. Compared to the 0 F-T cycle reference concrete, when the F-T cycle reaches 1500, the defect rate increases by about 9 times, and the porosity, pore volume, and pore surface area increase by 67. 38%, 66.67% and 322.12%. Hence, age F-T changes significantly affect the internal defects of aggregates and micropores in concrete. According to the analysis of pore distribution, most of these changes in size from 0.01 mm to 0.1 micropores occur when F-T is activated, and the number of micropores decreases as the F–T cycle increases. At temperatures below zero, the pore water trapped within the pores

transforms into crystallization—the crystal's expansion towards the pore wall increases pressure. When the stress is greater than the pore walls' resistance, damage can occur. The pores subsequently break and transform into transverse microcracks as the number of F-T cycles increases. Microcracks eventually cause the concrete mortar to flow and become more brittle (Luo et al., 2017). The growth of microcracks in concrete can be attributed to various factors. The majority of these are chemical reactions, such as the alkali-silica reaction, sulphate attack, carbonation, and combustion, while others are physical processes, like ice-freezing and cargo damage. The generated particles impair the cement matrix's cohesiveness and the interfacial bonding forces between the aggregates and their respective cement matrices.

One of the leading causes of concrete durability degradation in cold climates is temperature fluctuations, both positive and negative, and this freeze-thaw cycle typically does not occur on its own (Jiang et al., 2015). Moreover, the combined effects of salt corrosion and freeze-thaw cycles frequently affect buildings in saline soil areas, concrete structures near the coast, and concrete road and bridge structures using snow-melting salt. This can lead to various durability issues, including peeling concrete covers and corrosion on exposed steel bars (Kim & Yoon, 2010).

Liu et al. (2012) analyzed the effect of MnS content on the frost resistance of concrete. Before 60 days, the drying shrinkage of three specimens (consisting of 0%, 20% MnS, and 12% combined expansion agent) increases with age; however, after 60 days, it becomes stable. In the first four months of comparison, the concrete with 20% MnS shrinkage value is higher than the other two types of concrete. This indicates that the MnS negatively impacts the volume stability of concrete. The phenomenon could have something

to do with the alveolate pore structure or the fineness of the MnS. Adding a united expansive agent (UEA) expanding agent can limit the negative effect and considerably reduce drying shrinkage. The experimental results also showed that both ordinary C40 concrete and concrete with 20% MnS incorporated decreased in strength by more than 5% after undergoing freeze-thaw cycles (shown in Figure 2.24). It is noteworthy that after 50 freeze-thaw cycles, the strength loss of ordinary C40 concrete was 15.29%, which was significantly higher than that of concrete with 20% MnS (6.17%). This indicates that the introduction of MnS enhances the freeze-thaw resistance of concrete, which may be related to the optimization of the internal microstructure of concrete by MnS as well as the formation of special minerals (e.g., $Na(AlSi_2O_6)(H_2O)$), which are properties that contribute to the durability of concrete (Liu et al., 2012).

Chen et al. (2008) conducted experiments to analyze the durability performance indicators of MnS cement concrete, such as frost resistance, wear resistance and alkali-aggregate reaction. When the dosage of MnS admixture is less than or equal to 15%, the frost resistance grade of concrete remains unchanged, and the wear resistance of concrete decreases slightly but within the allowable range; when the dosage of MnS admixture is greater than 15%, the frost resistance and wear resistance of concrete decrease significantly, and some indicators have exceeded the permitted range of the specification. The internal analysis of the hydration process of manganese slag cement concrete found that when the dosage of MnS admixture is not greater than 15%, the MnS admixture does not affect the alkali-aggregate reaction of concrete (Chen et al., 2008).

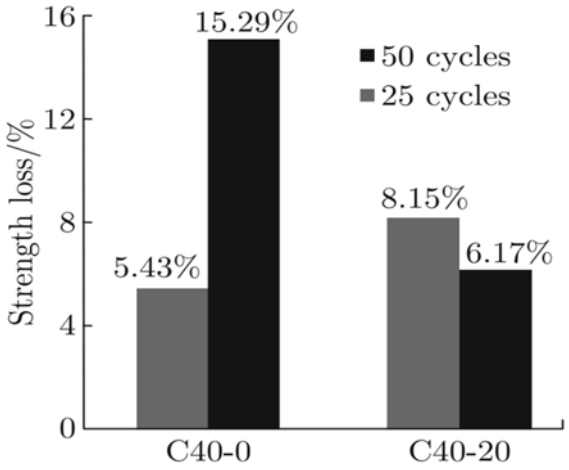

Figure 2.24: Strength Loss of Concrete after Freeze-thaw Cycles (Liu et al., 2012)

Chen et al. (2008) conducted experiments to analyze the durability performance indicators of MnS cement concrete, such as frost resistance, wear resistance and alkali-aggregate reaction. When the dosage of MnS admixture is less than or equal to 15%, the frost resistance grade of concrete remains unchanged, and the wear resistance of concrete decreases slightly but within the allowable range; when the dosage of MnS admixture is greater than 15%, the frost resistance and wear resistance of concrete decrease significantly, and some indicators have exceeded the permitted range of the specification. The internal analysis of the hydration process of MnS cement concrete found that when the dosage of MnS admixture is not greater than 15%, the MnS admixture does not affect the alkali-aggregate reaction of concrete (Chen et al., 2008).

Upon the systematic review of retrieved references, it becomes evident that the existing literature dedicated to the examination of the influence of MnS SSA on the frost resistance of manganese slag concrete is remarkably scarce. Furthermore, in the context of freeze-thaw cycling conditions, research exploring the relationships between MnS SSA and both the mass loss rate and compressive strength loss rate of concrete remains notably limited.

Consequently, these aspects warrant further investigation and analysis through experimental studies. It is one of the research gaps in this thesis.

Literature indicates that an appropriate amount of manganese slag can improve the frost resistance of concrete by optimizing the pore structure. Table 2.9 shows that a replacement level around 20% often yields significant improvement. However, excessive dosage (e.g., >15% or >25%) may lead to deterioration due to reduced strength or increased harmful pores. This supports the decision to control the replacement level at a moderate range (20%) in this study to ensure durability performance.

Table 2.9: Literature Summary on the Effect of Manganese Slag Content on Frost Resistance of Concrete

References	Content	Methods	Main Findings
Liu et al. (2012)	20%	Strength loss measurement after 50 freeze-thaw cycles	Concrete with 20% MnS showed 6.17% strength loss vs. 15.29% in plain concrete, indicating improved frost resistance
Fu et al. (2011)	54–58% (Alkali-activated)	Alkali-activated slag concrete (ASC) testing	Low-Ca/Si CSH gel improves freeze-thaw durability by limiting water ingress and stress buildup.
Chen et al. (2008)	⩽15% vs. >15%	Durability tests	MnS ⩽15% maintained frost resistance within limits; >15% caused significant deterioration.

2.10.2 Effect of Manganese Slag on the Resistance of Concrete to Chloride Ion Penetration

According to statistics, China's saline soil area exceeds 200,000 square kilometers, with more than 1,000 salt lakes primarily concentrated in the northwest. These saline soils

and salt lakes contain many chlorides, sulphates, carbonates and other salts that are harmful to concrete structures. Due to the long-term erosion of lake water, chlorides, sulphates and other erosion factors, the concrete in these areas is easily corroded and deteriorated, as shown in Figure 2.25. This poses a significant challenge to the durability of concrete.

Provis et al. (2015) discuss durability testing for alkaline activated materials (AAMs), including chloride ingress and binding, carbonation, sulphate attack, acid attack, and alkali-aggregate interactions. Efflorescence, also known as saltpeter, occurs naturally on the surface of geopolymer concretes due to high alkalinity and alkali mobility (Singh & Middendorf, 2020).

Figure 2.25: Morphology of Concrete Subjected to Long-term Chloride and Sulphate Attack

It is necessary to evaluate the protective properties of alkali-activated SiMnS mortars on steel reinforcements, with special attention to corrosion processes. Manganese in metallurgical slags may affect the corrosion of steel embedded in alkali-activated slag cement due to its redox-sensitive nature (Criado et al., 2018). Criado et al. (2018) examined steel corrosion in an alkali-activated mortar system with 90% blast furnace slag and 10% SiMnS. The goal was to investigate the impact of altering redox potential on the stability of

steel passivation when exposed to alkaline and alkaline chloride-rich solutions. Analysis showed that the high concentration of MnO in the slag had no important effect on the steel's corrosion process under the test conditions. Nevertheless, several diffusional processes were impacted by differences in pore structure detected between specimens (Criado et al., 2018).

Otieno et al. (2014) investigated the durability of concrete containing various industrial by-products, including MnS, in chloride-rich environments. At 20% MnS replacement, chloride ion penetration resistance increased by 25%, attributed to the pozzolanic activity of MnS, which filled capillary pores with secondary hydration products. Beyond 30% replacement, the resistance gains became marginal, as the dilution of clinker reduced the concrete's capacity to form a dense matrix (Otieno et al., 2014).

Liu et al. (2016) examined the chloride diffusion behavior in MnS-blended concrete. The study showed that incorporating 25% MnS reduced the chloride diffusion coefficient by 30% after 28 days of curing. This improvement was linked to the enhanced packing density and reduced pore connectivity. However, replacement levels above 35% resulted in diminished resistance, as the reduced content of primary hydration products limited the matrix's ability to block ion ingress (Liu et al., 2016).

Yang et al. (2024) explored the influence of MnS on chloride ion penetration resistance in high-performance concrete. The study showed that concrete with 20% MnS replacement exhibited a reduction in chloride ion diffusion coefficient by 35% compared to ordinary Portland cement (OPC) concrete. This improvement was attributed to the densified microstructure of the concrete matrix, resulting from the pozzolanic reaction of MnS, which generated additional C-S-H. However, at replacement levels above 35%, the resistance to

chloride ion penetration decreased slightly due to reduced binder efficiency and potential leaching of calcium hydroxide (Yang et al., 2024).

Zhou et al. (2021) analyzed the effect of MnS on chloride ion diffusion in blended concrete systems. Concrete with 25% MnS replacement exhibited a 28% reduction in chloride ion permeability after 56 days of curing. The study attributed this to the micro-filler effect of MnS, which reduced porosity and refined the pore structure. At replacement levels of 40%, however, the permeability reduction diminished to 15%, as excessive MnS content compromised the continuity of the hydrated cementitious matrix (Zhou et al., 2021).

He et al. (2024) studied concrete's chloride ion penetration resistance using MnS in coastal environments. The research demonstrated that replacing 30% of cement with MnS reduced the chloride migration coefficient by 40% after 90 days. The enhanced resistance was linked to the synergistic interaction between MnS and OPC, which improved the pore structure and delayed chloride ingress. However, at replacement levels exceeding 40%, the resistance plateaued, indicating that excessive MnS content could not sustain further improvements (He et al., 2024).

As summarized in Table 2.10, the incorporation of MnS can significantly enhance concrete's resistance to chloride ion penetration. The primary mechanisms are attributed to its micro-filling effect and pozzolanic activity, which refine the pore structure and densify the matrix, thereby hindering chloride ingress. The literature indicates an optimal MnS replacement level for this purpose typically within the range of 20% to 30%, with performance gains often plateauing or diminishing beyond approximately 30-35% due to the dilution of the cementitious binder. While this evidence confirms the efficacy of MnS, research focusing on the specific influence of MnS specific surface area on chloride transport

properties remains scarce. Therefore, investigating the relationship between concrete electrical flux (or diffusion coefficient) and MnS SSA constitutes a key research gap addressed in this study.

Table 2.10: Literature Summary on the Effect of Manganese Slag Content on Chloride Resistance of Concrete

References	Content	Methods	Main Findings
Otieno et al. (2014)	20–30%	Chloride exposure tests	20% MnS increased chloride resistance by 25% via pore-filling; gains diminished beyond 30%.
Liu et al. (2016)	⩽35%	Chloride ion penetration testing	20% MnS reduced diffusion coefficient by 35% vs OPC; due to pozzolanic reaction generating additional C-S-H.
Ismail et al. (2013)	20%	Permeability and strength tests	20% MnS reduced water permeability by 30%, enhancing durability against chloride ingress.

2.10.3 Effect of Manganese Slag on the Resistance of Concrete to Sulphate Corrosion

Sulphate attack can generally be divided into internal or external to the cement matrix, and the potential damage mode can be chemical or physical. The harm of sulphate attack mainly lies in the reaction of external sulphate ions with calcium hydroxide in concrete to form a larger trisulfide calcium sulfoaluminate hydrate. The trisulfide calcium sulfoaluminate hydrate will produce larger gypsum with the increase in sulphate ion concentration, and the continuous increase in volume will cause structural cracking (Zeng et al., 2015).

Yang et al. (2014) found that in making sulphur concrete (SC) with EMR, EMR can be dispersed in the molten sulfur and form a complete particle stacking structure through the hydrophobic modification of sulfur. This particle-stacking structure can effectively prevent corrosion inside and outside the concrete. The degree of corrosion in high concentrations of acid and alkali was lower than that of traditional Portland cement concrete. During the corrosion process, changes in quality and strength may be caused by the following chemical reactions: Equation 2.3 and 2.4 (Yang et al., 2014):

$$3S(s) + 6NaOH(aq) \rightarrow 2Na_2S(aq) + Na_2SO_3(aq) + 3H_2O(l) \quad \text{Equation 2.3}$$

$$S(s) + 6HNO_3(aq) \rightarrow H_2SO_4(aq) + 6NO_2(g) + 2H_2O(l) \quad \text{Equation 2.4}$$

Nevertheless, these reactions can be slowed down at ambient temperature. Because modified sulfur is hydrophobic, it is very difficult for acid solutions to permeate the surface of concrete, allowing the material to retain its high compressive strength. These results showed that SC still showed a high level of resistance to a harsh environment even with the EMR applied (Yang et al., 2014).

Xu et al. (2019) studied the sulphate corrosion resistance of concrete incorporating MnS at 10%, 20%, and 30% replacement levels. The results showed that concrete with 20% MnS exhibited a 22% reduction in mass loss and a 30% lower compressive strength loss after 180 days of exposure to a 5% sodium sulphate solution compared to ordinary Portland cement (OPC) concrete. This improvement was attributed to the ability of MnS to refine the pore structure and hinder sulphate ion ingress, which contributed to the formation of a denser matrix and subsequently limited expansive sulphate reactions (Xu et al., 2019).

Nasir et al. (2020) evaluated the sulphate resistance of MnS-blended concrete in highly aggressive environments. The study found that replacing 25% of cement with MnS reduced the expansion of concrete prisms by 35% after 12 months in a magnesium sulphate solution. The reduction in expansion was attributed to the pozzolanic reaction of MnS, which consumed calcium hydroxide and thereby suppressed the formation of expansive ettringite and gypsum. However, the resistance slightly decreased at 40% MnS replacement due to insufficient binder content and a lack of sufficient primary hydration products (Nasir et al., 2020).

Nath et al. (2022) investigated the durability of MnS-based concrete in sulphate-rich environments. The study revealed that concrete with 20% MnS exhibited 28% less strength loss and reduced cracking after 180 days of exposure to sulphate solutions compared to OPC concrete. This enhanced resistance was attributed to the reduced permeability of MnS concrete and the formation of stable hydration products. However, at higher MnS replacement levels (above 35%), the resistance to sulphate attack diminished due to a decline in the availability of reactive calcium silicates (Nath et al., 2022).

Yang et al. (2014) assessed the performance of MnS-blended cementitious materials under sulphate attack. The research found that at a 15% MnS replacement level, the expansion of mortar bars was reduced by 25% after 300 days in a 5% sodium sulphate solution. The improved performance was associated with the micro-filler effect of MnS and its contribution to reducing pore connectivity. Nevertheless, at replacement levels beyond 30%, the sulphate resistance gains were marginal, as excessive MnS diluted the overall matrix strength (Yang et al., 2014).

He et al. (2024) examined the effect of MnS on sulphate resistance in marine concrete applications. The study demonstrated that concrete with 30% MnS replacement showed a 33% improvement in resistance to sulphate-induced expansion and cracking after 180 days. This enhanced performance was linked to the densification of the microstructure and the reduction in calcium hydroxide content, which limited the formation of expansive phases like ettringite. However, at 40% replacement, sulphate resistance decreased slightly due to a reduction in early-age strength and binder efficiency (He et al., 2024).

Table 2.11 synthesizes the beneficial role of MnS in mitigating sulphate attack on concrete. The improvement is primarily due to pore structure refinement and the consumption of calcium hydroxide ($Ca(OH)_2$), which limits the formation of expansive ettringite and gypsum. A consensus from the literature suggests an effective MnS replacement level for sulphate resistance is generally between 15% and 30%, with performance declining at higher contents (>30-35%) as the cementitious matrix becomes overly diluted. However, parallel to the findings on chloride resistance, the specific impact of MnS SSA on the degradation mechanisms under sulphate exposure—such as its correlation with mass loss rate, strength retention, and corrosion resistance coefficient—is critically underexplored. This identified gap forms a central objective of the present experimental investigation.

Based on this established consensus and to ensure a balanced approach that prioritizes both durability enhancement and the integrity of the cementitious matrix, the MnS replacement level for the durability investigation in this study was selected as 10%. This conservative yet effective dosage is strategically chosen: it falls within the lower bound of the reported effective range to ensure a measurable improvement in durability, while

simultaneously minimizing the risk of any potential negative impact on the binder phase that could occur at higher replacement levels. This selection allows the subsequent experimental focus to remain squarely on the variable of SSA.

Table 2.11: Literature Summary on the Effect of Manganese Slag Content on Sulfate Resistance of Concrete

References	Content	Methods	Main Findings
Nath et al. (2022)	20% vs. >35%	Sulphate solution immersion for 180 days	20% MnS exhibited 28% less strength loss and reduced cracking vs OPC; Resistance diminished above 35% due to decline in reactive calcium silicates..
Xu et al. (2019)	⩽30%	Exposure to 5% Na_2SO_4 solution for 180 days	20% MnS reduced mass loss by 22% and compressive strength loss by 30% vs OPC, attributed to pore refinement and denser matrix formation.
Yang et al. (2014)	⩽30%	Expansion in 5% Na_2SO_4 solution for 300 days	15% MnS reduced expansion by 25% via micro-filling and pore refinement; gains plateaued beyond 30% due to matrix dilution.

However, similar to the findings in the previous sections, the literature analyzing the specific impact of MnS SSA on sulphate corrosion resistance is extremely limited. Within a sulphate environment, the relationships between concrete mass loss rate, compressive strength, corrosion resistance coefficient, and MnS SSA remain largely unexplored. Therefore, investigating these aspects constitutes a key research gap identified in Chapter 1, which this study aims to address through experimental analysis.

2.11 Microstructure of Manganese Slag

Liu et al. (2012) studied the chemical composition and microstructure of MnS from different sources. The study found significant variations in the glassy phase content, ranging from 30% to 60%. Liu highlighted that MnS with higher glassy content exhibited enhanced reactivity due to its greater capacity to participate in hydration reactions. Energy-dispersive spectrometry analysis also confirmed the presence of trace elements like magnesium and iron, which contributed to chemical stability (Liu et al., 2012).

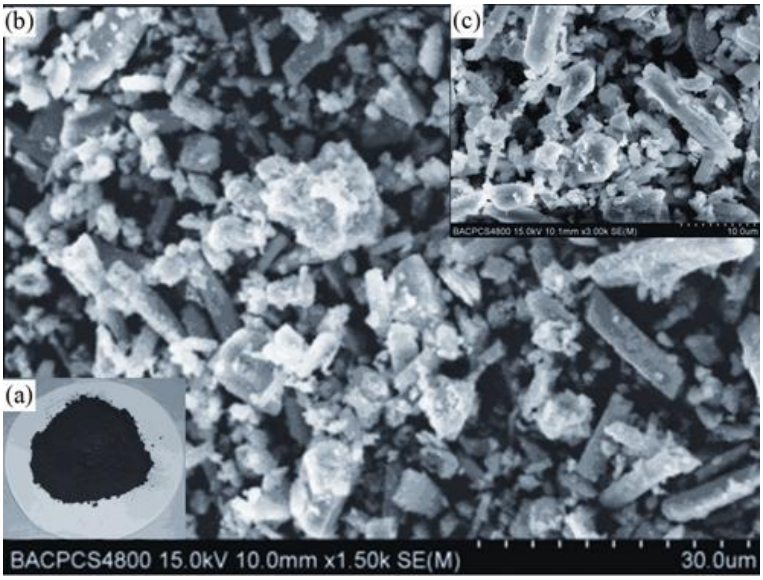

Figure 2.26: SEM Images of the Original MnS: (a) Overall Visual Representation, (b) Magnified at ×1500, (c) Magnified at ×3000 (Zhou et al., 2013)

Figure 2.26 presents the SEM images of the original MnS in the experiment of Zhou et al. (2013). In Figure 2.26(a), the material appears as a black powder. Generally, MnS is characterized as a non-magnetic and insoluble fine powder that resembles a sludge paste when it absorbs moisture, transforming into a hard block upon settling. The color of the residual powder varies depending on the raw materials and processes used in the MnS industry. Figure 2.26 (b) and (c) reveal that the particles primarily consist of regularly cylindrical shapes and irregular, loosely, and randomly interspersed forms. Between these

particles, there are small amounts of irregular flocculent residues. The particle sizes are inconsistent, ranging from a few microns to several hundred microns, and no significant bonds connect the particles (Zhou et al., 2013).

Nath and Kumar (2019) analyzed the microstructure of MnS using SEM and X-ray diffraction (XRD). The study revealed a heterogeneous structure composed of glassy and crystalline phases, primarily amorphous silica, calcium silicates, and manganese oxides. The amorphous phase exhibited high pozzolanic reactivity, constituting 45-50% of the material. Nath noted that the delicate crystalline phases improved the material's compatibility with cementitious systems, enhancing matrix densification and durability (Nath & Kumar, 2019).

Wang et al. (2021) investigated the mineralogical structure of MnS using XRD and Fourier-transform infrared spectroscopy (FTIR). The study identified dominant phases such as quartz, anorthite, and pyroxene. It is noted that the presence of reactive aluminosilicates in MnS contributed to its ability to form secondary hydration products, which improved the mechanical and durability properties of concrete (Wang et al., 2021).

Ma et al. (2021) focused on the thermal and morphological characteristics of MnS. Differential thermal analysis (DTA) indicated the presence of thermally stable phases, including manganese silicates and aluminosilicates. Scanning electron microscopy images revealed smooth and dense surfaces for thermally treated MnS, enhancing its suitability as a supplementary cementitious material. They emphasized that controlled thermal processing could optimize the microstructure to improve its reactivity (Ma et al., 2021).

Navarro et al. (2022) investigated how the particle size of MnS influences its microstructure. Using particle size analysis and SEM, Navarro observed that finer MnS particles (below 45 μm) exhibited a more homogeneous distribution of reactive phases than

coarser fractions. This uniformity facilitated better dispersion in concrete mixtures, leading to improved matrix densification and reduced porosity (Navarro et al., 2022).

Su et al. (2022) analyzed the microstructural evolution of MnS in concrete during hydration. The study found that MnS particles acted as nucleation sites for CSH growth, promoting a denser matrix structure. Scanning electron microscopy images showed that MnS reduced the pore connectivity of concrete by filling voids with secondary hydration products. Su concluded that this microstructural refinement was crucial for enhancing the durability of MnS-based concrete (Su et al., 2022).

Cheng et al. (2023) conducted a detailed examination of MnS using SEM and energy-dispersive X-ray spectroscopy. The results showed that MnS particles possessed a rough surface morphology and contained elemental oxides of manganese, silicon, calcium, and aluminum. The study emphasized that the abundance of manganese oxides contributed to chemical stability, while the rough surface improved the bond strength in concrete matrices by enhancing the interfacial transition zone (ITZ) (Cheng et al., 2023).

Wu et al. (2024) investigated the influence of the microstructure of MnS on its cementitious behavior. The study identified angular and irregularly shaped particles with crystalline phases, such as gehlenite and wollastonite. These phases improved early-age strength development by contributing to hydration reactions. It is noted that while the crystalline phases offered stability, the amorphous components provided long-term pozzolanic activity (Wu et al., 2024).

Dong et al. (2024) explored the hydration behavior of MnS in blended cement systems. The study found that the microstructure of MnS influenced its reactivity. High-resolution transmission electron microscopy (TEM) revealed that the slag contained

nanocrystalline manganese oxides embedded within an amorphous silicate matrix. Dong suggested that this unique structure accelerated the pozzolanic reaction, forming secondary CSH gels that refined the concrete matrix's pore structure (Dong et al., 2024).

The reviewed above studies collectively highlight the relationship between MnS particle size and density, though their analyses remain relatively general. Research has demonstrated that MnS exhibits significant microstructural variability, with both glassy and crystalline phases influencing its reactivity. While finer MnS particles (< 45 μm) facilitate better dispersion and matrix densification, the porous and irregular textures of coarser particles contribute to hydration and water retention. However, the connection between MnS SSA and its role in concrete microstructure remains insufficiently detailed. Future studies should aim to establish a theoretical foundation for understanding how MnS influences concrete performance. Specifically, it should explore the effects of MnS particle size, characterized by SSA, on hydration reactions, microstructural evolution, and porosity reduction. This is consistent with one of the research objectives of this thesis.

2.12 Statistical Methods for Multi-Criteria Decision-Making: AHP and Entropy Method

The comprehensive performance evaluation of construction materials like SiMnS concrete involves multiple, often conflicting criteria (e.g., mechanical strength, durability, workability). Selecting an optimal mix design requires balancing these criteria, which constitutes a classic Multi-Criteria Decision-Making (MCDM) problem. MCDM methods provide a systematic framework to determine the optimal solution by assigning weights to these criteria (Lai et al., 1994). This section reviews two prominent MCDM methods—the AHP and the Entropy Method—focusing on their principles, comparative advantages and limitations, and their documented applications in concrete technology. This review

establishes the rationale for employing a combined AHP-Entropy approach in this study to evaluate the effect of slag SSA on concrete performance.

2.12.1 Analytic Hierarchy Process (AHP)

Developed by Saaty, AHP is a structured technique for organizing and analyzing complex decisions (Wind & Saaty, 1980). It decomposes a problem into a hierarchy of goal, criteria, and alternatives. The core involves pairwise comparisons between elements at each level using a standardized scale (1-9), translating subjective expert judgments into quantitative weights. A consistency ratio (CR) check ensures the logical coherence of judgments (Hanim & Rahmadoni, 2020).

2.12.2 Entropy Method

The Entropy Method, rooted in information theory, determines objective weights based on the intrinsic information content of evaluation data (Rechberger, 2002). The principle is that an indicator with greater dispersion (higher variance) across different alternatives provides more information for discrimination and should thus be assigned a higher weight. It is purely data-driven.

2.12.3 Comparative Analysis of MCDM Methods and Rationale for Hybrid Approach

AHP and the Entropy Method represent subjective and objective weighting paradigms, respectively. Their core characteristics, along with other common MCDM techniques, are systematically compared in Table 2.12. As shown, AHP excels in incorporating expert knowledge and structuring complex decisions but is susceptible to subjective bias. Conversely, the Entropy Method eliminates subjectivity by relying solely on data variation but cannot incorporate qualitative judgments or expert experience.

Table 2.12: Comparison of Multi-Criteria Decision-Making Methods for Engineering Materials

References	Method	Advantages	Limitations
Li et al., 2020; Elkhayat et al., 2020	Analytic Hierarchy Process (AHP)	Provides a clear hierarchical structure of objectives, criteria, and indicators- Incorporates expert knowledge and practical experience- Facilitates interpretability and communication of results	Relies on subjective judgment- Pairwise comparisons can be cumbersome with many indicators- Consistency of expert scoring must be verified
Qin et al., 2014; Chan et al., 2024	Entropy Weight Method	Provides objective weighting based on variability of quantitative data- Reflects the informativeness of each indicator- Reduces human bias	Does not incorporate expert judgment- Sensitive to data quality and outliers- Less effective with sparse or incomplete data
Li et al., 2025; Ren et al., 2023	AHP-Entropy Integration	Combines subjective expert judgment (AHP) with objective data weighting (entropy)- Improves robustness and interpretability- Particularly suitable for multi-indicator evaluation problems	Computationally more complex than single-method approaches- Requires both reliable data and expert input- Interpretation may require careful explanation
Liu & Yu, 2007; Zhu et al., 2021	Gray Relational Analysis (GRA)	Suitable for systems with incomplete or uncertain data- Provides correlation-based ranking of evaluation objects	Weights cannot be directly derived- Results sensitive to sample selection- Less intuitive for non-experts

Table 2.12 continued

Pathak et al., 2020; Mahmudova, 2020	TOPSIS	Provides a clear ranking of alternatives based on distance from ideal and anti-ideal solutions- Widely applied in engineering decision-making	Requires standardized data- Weighting still relies on other methods- Computationally intensive with large datasets
Maćkiewicz & Ratajczak, 1993; Uddin et al., 2021	Principal Component Analysis (PCA)	Reduces data dimensionality- Improves computational efficiency- Highlights key sources of variance	Transformed components may lack direct interpretability- Some information loss is inevitable
Golany & Roll, 1989; Rostamzadeh et al., 2021	Data Envelopment Analysis (DEA)	Evaluates relative efficiency with multiple inputs and outputs- Allows selection of different models depending on application	Sensitive to data quality- Does not account for random errors- Results may be non-robust under noise

This complementary nature makes their integration particularly powerful. The hybrid AHP-Entropy method synthesizes subjective priorities from AHP with objective information from the Entropy Method, mitigating the limitations of each standalone approach (Al-Aomar, 2010). This hybrid strategy is especially suited for problems like concrete mix optimization, where both expert experience (e.g., the relative importance of strength versus durability in a specific environment) and objective experimental data are crucial and must be reconciled.

2.12.4 Applications in Concrete and Construction Materials

The practical utility of Multi-Criteria Decision-Making (MCDM) methods, such as AHP, the Entropy Method, and their hybrid, in addressing materials science problems is well-established. Table 2.13 summarizes key application cases of these methods in engineering materials research. These examples demonstrate that:

The AHP-Entropy hybrid has been directly applied to evaluate the influence of manganese slag SSA on concrete performance (Li et al., 2025), providing a direct precedent for the current study. It has also been used for damage assessment in railway slab systems (Ren et al., 2023). The Entropy Method alone is effective for objectively weighting performance indicators from experimental data, such as in green building material selection (Qin et al., 2014) and concrete durability analysis under sulfate attack (Mao et al., 2024). AHP alone is valuable for structuring expert-driven decisions, such as in selecting high-performance glazing systems (Elkhayat et al., 2020) or eco-friendly materials (Xiao et al., 2022).

These cases confirm that these methods are not merely theoretical but are actively used to solve multi-criteria evaluation problems analogous to the one in this thesis, involving trade-offs between workability, strength, and various durability metrics.

Table 2.13: Application Cases of Multi-Criteria Decision-Making Methods in Engineering Materials Research

References	Method	Research Object	Indicators Evaluated	Key Findings
He et al. (2019)	AHP-Entropy	Concrete with manganese slag (MnS)	Workability, compressive strength, flexural strength, freeze-thaw resistance, chloride ion permeability, sulfate corrosion resistance	Evaluated influence of MnS specific surface area (SSA) on concrete properties; AHP-Entropy provided a robust ranking of mix designs
Nath & Kumar (2017)	AHP-Entropy	Railway track slab system III	Cracking interface volume, debonding interface volume, other damage indicators	Combined expert judgment and objective measurements to assess damage levels and quality status; demonstrated method's suitability for multi-dimensional evaluation
Navarro et al. (2017)	Entropy Weight Method	Green building materials	Thermal insulation, energy efficiency, environmental impact, durability	Objectively determined weights of multiple performance indicators; provided quantitative evaluation of material sustainability
Nath & Kumar (2016)	Entropy Weight Method	Concrete durability under sulfate attack	Mass loss, compressive strength loss, sulfate resistance coefficient	Quantified contribution of each indicator to overall durability; enabled comparison of different concrete formulations
Allahverdi & Ahmadnezhad (2014)	AHP	Eco-friendly construction materials	Environmental impact, cost, mechanical performance, service life	Structured expert assessment of multiple criteria; facilitated material selection and prioritization

Table 2.13 continued

Frías et al. (2009); Frias et al. (2006); Kumar et al. (2013)	Entropy Weight Method	Concrete mixture performance	Slump, compressive strength, flexural strength, chloride permeability	Determined objective weights of performance indicators; used for comprehensive evaluation of concrete mix designs
Xie et al., 2012	AHP-Entropy	Construction project materials	Cost, environmental impact, mechanical properties	Hybrid weighting integrates subjective and objective evaluation for material selection.
Duan et al., 2016	AHP-Entropy	Infrastructure concrete materials	Strength, durability, workability, cost	Verified that combining AHP and entropy improves robustness of multi-criteria evaluation in civil engineering materials
Zhu et al., 2021	Gray Relational Analysis	Concrete mixture sustainability	CO_2 emissions, mechanical performance, durability, economic cost	Provided ranking of mixtures based on correlation to ideal solution; highlights alternatives with balanced performance
Ren et al., 2022	TOPSIS	High-performance concrete	Compressive strength, workability, durability	Assessed multiple concrete mixes and ranked by proximity to ideal performance, requiring weighting from other methods.

2.12.5 Justification and Suitability for the Present Study

Based on the foregoing analysis, the hybrid AHP-Entropy method is judiciously selected for this research. The justifications for this choice, synthesized from the literature and aligned with the research needs, are summarized in Table 2.14 and Table 2.15.

Table 2.14: Justification for Selecting the AHP Entropy Method

References	Reason	Explanation
Xie et al., 2012; Duan et al., 2016; Wu et al., 2022	Integration of Subjective and Objective Weights	AHP captures expert knowledge and practical judgment, while the entropy method assigns weights objectively based on experimental data. The combination improves comprehensiveness and scientific rigor.
Li et al., 2025; Ren et al., 2023	Suitable for Multi-Indicator Evaluation	Many indicators, such as mechanical properties and durability, need to be balanced simultaneously. A single method may not fully capture the overall performance.
Al-Aomar, 2010; Feng, 2023	Improved Stability and Reliability	By combining AHP and entropy, the method reduces bias inherent in single-method approaches and enhances robustness of results.
Singh, 2016; Chao et al., 2017	Enhanced Interpretability and Practicality	Weight derivation is transparent, making the evaluation process traceable and results easier to explain for decision-making.

The fundamental rationale for adopting the hybrid AHP-Entropy method in this study is multifaceted, as synthesized from the literature and summarized in Table 2.14. Primarily, its core strength lies in the integration of subjective and objective weights, which enhances the comprehensiveness and scientific rigor of the evaluation by balancing expert judgment with data-driven analysis. Furthermore, the method is inherently suitable for multi-indicator

evaluation, a common challenge in concrete technology where properties like mechanical strength and durability must be assessed simultaneously.

By combining AHP and the Entropy method, it also improves the stability and reliability of the weighting outcomes, mitigates individual method biases, and offers enhanced interpretability through a transparent weighting process. Finally, its proven applications in engineering materials research provide a solid precedent and validate its practical utility for problems analogous to the present investigation.

The specific suitability of the AHP-Entropy method for evaluating concrete performance, as detailed in Table 2.15, aligns precisely with the needs of this research. It is uniquely capable of handling the multiple, hierarchical performance indicators—from fresh properties (workability) to hardened properties (mechanical strength) and long-term behavior (durability)—that are central to assessing SiMnS concrete. The method effectively integrates expert judgment with experimental data, a necessity for concrete mix optimization where practical experience must inform the interpretation of laboratory results. It also addresses weight uncertainty by tempering subjective preferences with objective data dispersion. Crucially, there is direct evidence from existing studies on similar materials (e.g., evaluating slag effects or concrete durability), demonstrating its successful application in contexts that closely mirror the objectives of this work.

Table 2.15: Suitability of AHP Entropy Method for Concrete Performance Evaluation

References	Aspect of Suitability	Explanation
Li et al., 2025; Ren et al., 2023	Ability to Evaluate Multiple Performance Indicators	Concrete performance assessment typically involves workability, compressive strength, flexural strength, and durability metrics such as freeze-thaw, sulfate, and chloride ion resistance. AHP Entropy can synthesize these multiple indicators into a comprehensive evaluation.
Chan et al., 2024; Xie et al., 2012	Integration of Expert Judgment and Experimental Data	Concrete mix optimization requires combining experimental results with engineering experience. The hybrid method accommodates both sources of information.
Duan et al., 2016; Al-Aomar, 2010	Handling Weight Uncertainty	Importance of individual indicators may not be fully determined from data alone. The entropy method complements AHP to reduce subjective bias.
Singh, 2016; Chao et al., 2017	Support for Hierarchical Analysis	Concrete performance indicators can be organized hierarchically (e.g., workability → mechanical properties → durability). AHP allows clear structuring of these layers.
Li et al., 2025; Ren et al., 2023; Mao et al., 2024	Evidence from Existing Studies	Previous research has successfully applied this method to evaluate the effect of manganese slag specific surface area on concrete, damage assessment of railway slabs, and green building materials.

2.13 Knowledge Gap and Research Content of the Research

The increase in literature on application of MnS in concrete highlights the potential use of MnS as a supplementary cementitious material for concrete. However, significant gaps remain in understanding the effect of its SSA on various concrete properties. Current research largely focuses on the role of MnS dosage in influencing concrete performance, leaving the impact of SSA underexplored. This is a critical oversight since SSA significantly influences the reactivity, hydration process, and physical characteristics of MnS when used in concrete.

Firstly, the relationship between the SSA of MnS and the workability of cement mortar has not been thoroughly examined. Changes in SSA can affect mortar fluidity and consistency, directly influencing its applicability in construction. Similarly, the impact of SSA on the workability of fresh concrete such as slump, requires further study to establish its effect on ease of placement and construction efficiency.

Secondly, the influence of MnS SSA on the mechanical properties of concrete, such as compressive and flexural strength, is poorly understood. While finer particles typically enhance strength due to increased reactivity and filling capacity, the optimal SSA for achieving required mechanical performance remains unclear.

Lastly, and most crucially, the durability of MnS concrete under aggressive environmental conditions has not been adequately investigated concerning SSA variations. Key durability metrics, such as resistance to chloride ion penetration, frost damage, and sulphate attack, are essential for ensuring long-term structural integrity. The effect of SSA on these properties is yet to be fully elucidated, creating uncertainty about MnS concrete suitability in harsh environments.

This study aims at bridging the existing knowledge gaps by systematically analyzing the influence of the SSA of SiMnS on the workability of cement mortar and concrete, the mechanical properties of concrete, and its durability against chloride ion penetration, frost damage, and sulphate corrosion. The systematic evaluation consists of both individual and comprehensive assessments: the former is conducted through laboratory experiments, while the latter is performed using the AHP-entropy method. By addressing the research gaps identified herein, this study offers a thorough understanding of the role of SSA in enhancing the performance of SiMnS as a sustainable alternative to traditional cement.

2.14 Summary of Literature Review

This chapter provided an in-depth review of the current state of research regarding MnS as a supplementary cementitious material for concrete production. The chapter began by analyzing the SSA of MnS and its impact on its activity, highlighting how increased SSA enhances its pozzolanic and hydraulic properties, thereby improving its performance in the cement matrix.

The rationale for partially replacing cement with MnS, emphasizing its chemical compatibility with cement and its potential to reduce carbon emissions and promote sustainable construction is also presented herein. The benefits of MnS in improving concrete properties were examined, focusing on workability, mechanical strength, and durability. The literature review also highlighted the importance of SSA in influencing fresh-state properties such as fluidity and slump, as well as hardened-state properties like compressive and flexural strengths.

The durability aspects of MnS concrete were also explored, particularly its resistance to chloride ion penetration, frost damage, and sulphate corrosion. The role of SSA in enhancing these properties was underscored, as finer particles contribute to a denser and more durable cement matrix.

The literature review identified a research gap in the comprehensive, multi-criteria evaluation of how manganese slag SSA influences concrete performance. To address this gap, a robust methodological framework is required. The review of MCDM methods in Section 2.12 established that a hybrid AHP and Entropy method is particularly well-suited for this task. This conclusion is supported by comparative analysis (Table 2.12), which shows that the hybrid approach effectively balances subjective expert judgment (captured by AHP) with objective data-driven analysis (provided by the Entropy method), thereby mitigating the individual limitations of each standalone technique. Furthermore, documented applications in concrete and construction materials research (Table 2.13), including studies evaluating slag effects, confirm the practical utility and validity of this combined method for problems analogous to the present investigation. Therefore, this study will employ the AHP-Entropy integrated method to holistically evaluate the effects of MnS SSA on concrete's workability, mechanical properties, and durability.

While the potential of MnS as a sustainable cement replacement was evident, the review revealed critical research gaps. Most studies have focused on the effect of manganese slag dosage, with limited attention given to the influence of SSA on workability, mechanical performance, and durability. These gaps, as previously identified in Chapter One, were reiterated to emphasize the necessity of further investigation. ”

CHAPTER 3

METHODOLOGY

3.1 Introduction

This chapter discusses the process of preparing SiMnS concrete and conducts an experimental analysis of its mechanical properties and durability. The study includes five parts: preparation of SiMnS, preparation of SiMnS concrete, mechanical properties test of SiMnS concrete, durability test of SiMnS concrete, and microscopic analysis of SiMnS concrete.

Specifically, the first part studies the physical characteristics and chemical composition of manganese slag and determines the preparation method of SiMnS with different SSA. The second part selects cement, sand, coarse aggregate, and chemical admixtures and designs the preparation process of SiMnS concrete with different SSA. The third part includes the design of the compressive strength test and flexural strength test of SiMnS concrete. It analyses the influence of SiMnS SSA on the mechanical properties of SiMnS concrete. The fourth part describes the experimental procedure of SiMnS concrete's resistance to chloride ion penetration, freeze-thaw resistance, and sulphate corrosion resistance. It analyses the influence of SiMnS SSA on the durability of SiMnS concrete.

In the final stage of this research, firstly, the AHP is utilized to construct a hierarchical structural model and establish a judgment matrix, to obtain the subjective weights of multiple performance indicators of concrete. Subsequently, the entropy value method is adopted to set up an evaluation index system, carry out data standardization processing and indicator entropy value calculation, thereby determining the objective

weights of multiple performance indicators of concrete. By integrating the AHP-entropy method, the subjective and objective combined weights of multiple performance indicators of concrete are calculated. Based on the combined weights, a comprehensive evaluation is conducted on the influence of SiMnS SSA on the workability, mechanical properties and durability of concrete. The flow chart of the research process is shown in Figure 3.1.

3.2 Material Preparation

3.2.1 Silicomanganese Slag

The SiMnS is supplied by a metal smelting plant in Xingyang City, Henan Province. Silicomanganese slag is the filter press residue produced in the electrolytic manganese metal production process. Since the SiMnS has been piled outdoors for a long period, it is mixed with impurities such as soil and cemented into blocks, and its appearance is grey-black in color as shown in Figure 3.2.

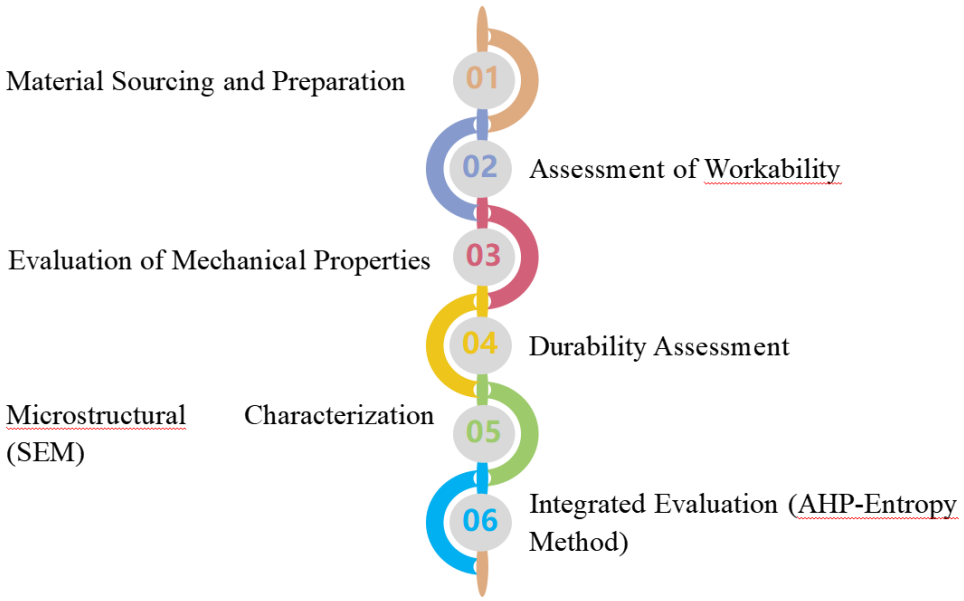

Figure 3.1: Flowchart of Research Process

Figure 3.2: The SiMnS Pilling Outdoor

The moisture content of SiMnS had been determined by the drying method. The sample had been dried at a constant temperature of 105±5 ℃ until reaching constant weight, taken out, and placed in a drying oven to cool to room temperature. The mass of wet and dry SiMnS were recorded, and the natural moisture content of SiMnS was calculated according to Equation 3.1. At least three parallel tests were carried out for each group of samples.

$$w = \frac{m - m_{\mathrm{d}}}{m_{\mathrm{d}}} \qquad \text{Equation 3.1}$$

where w = natural moisture content (%); m = wet SiMnS mass (g); m_{d} = dry SiMnS mass (g). The test results are shown in Table 3.1.

The average natural moisture content of the SiMnS sample calculated from Table 3.1 is 21.1%, an industrial solid waste with a high moisture content. Suppose it is directly piled in the open air without treatment, the water in the SiMnS will carry soluble harmful

substances into the surrounding soil ecological environment, causing harm to the environment.

Table 3.1: Test Results of Natural Moisture Content of SiMnS

Property	M1	M2	M3
Box weight (g)	40	40	40
Box with humidified soil (g)	143.6	139.8	141.2
Box with dry soil (g)	121.2	118.4	120.7
Moisture content (%)	21.6	21.4	20.3
Average moisture content (%)	21.1		

The density of SiMnS is determined by the pycnometer method in accordance with the test method for determining cement density (BS EN 12350-6: 2019). The density (ρ) of the SiMnS was calculated according to Equation 3.2.

$$\rho = \frac{m_{\mathrm{d0}}}{m_{\mathrm{d0}} + m_2 - m_1} \times \rho_w \qquad \text{Equation 3.2}$$

where ρ = the density of electrolytic SiMnS (g/cm^3); ρ_{w} = the density of distilled water (g/cm^3); m_{d0} = the mass of dried SiMnS sample (g); m_1 = mass of pycnometer + water + SiMnS (g); m_2 = mass of pycnometer + water (g). The density of SiMnS is calculated to be 2.911 g/cm^3 using Equation 3.2.

The chemical composition of the SiMnS used in this study was provided by the manufacturer and determined through X-ray fluorescence (XRF) spectroscopy, as detailed in the supplier's certified test report (see Table 3.2). The analysis was conducted by the supplier's quality control laboratory, ensuring the accuracy and reliability of the data. The

SiMnS in this study possesses a chemical composition typical of water-quenched slags, with high contents of SiO_2, Al_2O_3, and CaO. Slags with similar compositions have been consistently reported to exhibit a highly amorphous/vitreous structure, which is crucial for their pozzolanic reactivity. This is clearly demonstrated by the XRD patterns reported by He et al. (2019), Nath & Kumar (2017), and Nath & Kumar (2016), which all show a characteristic broad halo in the 2θ range of 20–40°, indicative of a glassy phase, alongside minor peaks for crystalline phases like quartz and various silicates.

Table 3.2: Main Chemical Composition of SiMnS

Compound	**MnO**	**SiO_2**	**Al_2O_3**	**CaO**	**Fe_2O_3**	**MgO**	**Na_2O**	**K_2O**	**SO_3**
Content (wt. %)	10.86	36.17	17.39	26.64	0.81	4.19	0.3	0.82	1.73

The specific surface area of the SiMnS had been determined by the Brunauer–Emmett–Teller (BET) method. The experimental equipment employed was a SSA and porosity analyzer (ASIQM0010-4), as illustrated in Figure 3.3. The SiMnS was dried and dehydrated (120 °C), and then 3 kg of the dried SiMnS was weighed and put into a cement test mill for ball milling. Samples were taken every 30 minutes during the ball-milling process, and four samples were taken (Figure 3.4). After cooling the SiMnS to room temperature, a dry sample weighing 0.5 grams was accurately weighed. The sample was then transferred into the sample tube of the BET adsorption apparatus, and a mercury porosimeter was utilized to compact the sample, thereby ensuring its uniform density. Subsequently, the sample tube was placed into a vacuum system and degassed at room temperature for a duration of five hours. Following degassing, the sample tube was connected to the BET adsorption apparatus, and nitrogen gas was employed as the adsorbate to measure the adsorption capacity of the sample. Ultimately, four sets samples of SSA values were

obtained through the BET method. The SSAs of SiMnS from four batches were measured as 60 m²/kg, 120 m²/kg, 235 m²/kg, and 400 m²/kg. Based on metal smelting plants' production experience, this range reflects a balance between technical feasibility, environmental benefits, and cost-effectiveness—aligning with the goal of repurposing SiMnS as a sustainable cement alternative.

Figure 3.3: The Specific Surface Area and Porosity Analyzer (ASIQM0010-4)

Figure 3.4: Silicomanganese Slag after Grinding

3.2.2 Water and Admixtures

The water used in the mortar and concrete mix was potable water. The admixture used was a polycarboxylic acid water reducer produced by Henan Wanshan New Materials Technology Co.; Ltd. Table 3.3 shows the principal properties of the admixture.

Table 3.3: Performance Indexes of Water-reducing Agent

Project	Solid content (%)	PH value	Density (kg/m^3)	Water reduction rate (%)
Value	24.923	8.25	1.12	27

3.2.3 Cement and Aggregate

Henan Yongan Cement Co., Ltd. provided the materials used in this test, including 42.5-grade ordinary Portland cement and aggregates. The main chemical components of cement are shown in Table 3., and the performance indicators are shown in Table 3.5. The fine aggregate is manufactured grade II medium sand and the particle size modulus is 2.69. The performance indicators of sand are shown in Table 3.. The coarse aggregate used has a particle size of 5–20mm, an apparent density of 2645 kg/m^3, a bulk density of 1410 kg/m^3, and a silt content of 0.3%.

Table 3.4: Main Chemical Composition of Cement

Compound	SiO_2	Al_2O_3	CaO	Fe_2O_3	MgO	Na_2O	K_2O	SO_3	Cl^-
Percentage (%)	22.37	6.87	52.41	2.87	7.97	0.47	0.12	2.07	0.029

Table 3.5: Properties of Cement

Property	Density (g/cm^3)	SSA (m^2/kg)	Compressive strength (MPa)		Flexural strength (MPa)		Setting time (min)		Stability	Water consumption for standard consistency (%)
			3d	28d	3d	28d	Initial	Final		
Value	3.04	348	30.1	54.9	6.7	9.1	157	218	Boil the qualified	26.3

Table 3.6: Performance Indexes of Sand

Property	Apparent density (kg/m^3)	Loose bulk density (kg/m^3)	Compact packing density (kg/m^3)	Mud content (%)	Water absorption (%)
Value	2675	1493	1754	2.4	1.56

3.3 Preparation and Testing of Cement Mortar

3.3.1 Mix Ratio

The mix ratio for the trial cement mortar was set at a water-cement ratio of 0.5 and a cement-to-sand ratio of 1:2.5. Each batch comprised 1500 g of standard sand and 250 g of water. This formulation was designed to achieve a target compressive strength of approximately 40MPa at 28 days (Qiang et al., 2011; Adaway & Wang, 2015).

The SiMnS was the key variable. To investigate the effect of specific surface area (SSA), the raw slag was processed using a planetary ball mill (model XQM-2L). The SSA of the ground SiMnS was determined using the Brunauer–Emmett–Teller (BET) nitrogen adsorption method (see Section 3.2.1 for detailed procedure). This yielded four distinct SSA levels: 60, 120, 235, and 400 m²/kg (these are the measured values). The grinding duration and intensity were carefully adjusted to obtain powders within these target ranges.

In the mortar mixtures, SiMnS replaced Portland cement at four replacement levels: 10%, 20%, 30%, and 40% by weight. This created a full-factorial experimental design combining the four SSA levels with the four replacement ratios.

3.3.2 Test Specimen Preparation and Fluidity Test of Cement Mortar

The benchmark group cement mortar was numbered CM0, representing the cement mortar test specimen with 0%wt SiMnS content. The control group had 16 groups, among which there were four groups of cement mortar with SiMnS particle size of 60 m^2/kg, numbered CM60-10, CM60-20, CM60-30 and CM60-40. CM60-10 represents the cement mortar test specimen with a SiMnS SSA of 60 m^2/kg and a SiMnS content of 10%wt. Similarly, CM120-40 represents the cement mortar test specimen with a SiMnS SSA of 120

m^2/kg and a SiMnS content of 40%wt; following which other test specimens were marked accordingly.

In accordance with the ASTM C1437-20 standard, cement (SiMnS) and standard sand had been weighed in a specified ratio (cement: standard sand: water = 1: 2.5: 0.5), and subsequently mixed in a mixer. Water was gradually added during the mixing process, and after stirring for 180±5 seconds, the cement mortar was obtained. The cement mortar was then rapidly filled into the mold in two layers, followed by compaction to ensure that the mortar fully occupies the mold. Once compaction is completed, the mold was removed, and the flow table test was conducted to determine the mortar flowability. The jolting table completes 25 jumps at a frequency of one jump per second. Finally, the diameters of the mortar base in two mutually perpendicular directions were measured, and their average value was calculated, which represented the flowability of the cement mortar with the specified water content. The entire process had been completed within 5 minutes.

3.3.3 Compressive Strength Test of Cement Mortar

The compressive strength test of cement mortar is conducted in accordance with the test method of cement mortar strength (ISO method) (GB/T 17671-2021). The specimens were formed using a standard cubic mould (70.7 mm × 70.7 mm × 70.7 mm), and the prepared cement mortar specimens were cured under standard conditions. The curing temperature was 20 ± 2 ℃, the relative humidity was above 95%, and the curing time was 3 days, 7 days, and 28 days.

After the prescribed curing period, the specimens were taken out and tested for compressive strength. The test was performed using a standard pressure testing machine with

a loading rate of 0.5 MPa/s. The compressive strength of the cement mortar specimens had been calculated according to Equation 3.3:

$$f_{\mathrm{m}} = \frac{P_m}{A_m} \qquad \text{Equation 3.3}$$

where f_{m} = the compressive strength of cement mortar (unit: MPa); P_{m} = the maximum load when the cement mortar specimen is destroyed (unit: N); A_{m} = the compressive area of the cement mortar specimen (unit: mm²).

3.4 Preparation and Testing for Workability and Mechanical Properties of Concrete

3.4.1 Mix Ratio

To achieve a target compressive strength of approximately 40MPa at 28 days, the water-cement ratio for the trial concrete mix was designed at 0.38 (Abrams, 1918; Popovics, 1990; Park, 2022). The sand ratio is 35%, and the coarse aggregate particle size is 5–20 mm with an apparent density of 2645 kg/m^3 and bulk density of 1410 kg/m^3. The water reducer dosage is 0.4% (2.9 kg/m^3). The SSA of SiMnS is 60 m^2/kg, 120 m^2/kg, 235 m^2/kg, and 400 m^2/kg, respectively. Silicomanganese replaces 5%wt, 10%wt, 15%wt, and 20%wt of cement.

Based on the results of the mortar tests (presented in Chapter 4, Section 4.2), it was found that cement mortars with high SiMnS replacement levels (30% and 40% by weight) exhibited significantly reduced workability and compromised compressive strength, which would be unfavorable for practical applications. For instance, at all specific surface areas (SSA), mortars with 40% replacement showed a fluidity reduction of up to 14.0% (from 193 mm to 166 mm at SSA=60 m²/kg) and 28-day compressive strength significantly lower than

the control. Therefore, to optimize the performance for concrete, the replacement ratio was limited to a maximum of 20%.

Consequently, the concrete mixtures were designed with four SiMnS replacement levels: 5%, 10%, 15%, and 20% by weight of cement. To achieve adequate workability (target slump of 170±25 mm, aligning with the control group C0's slump of 170 mm) and target strength grade (C40) for structural concrete, the water-to-binder ratio was adjusted to 0.38. This adjustment, along with the use of a water reducer (polycarboxylate-based superplasticizer) at a dosage of 0.4% by weight of the binder (equivalent to 2.9 kg/m³), ensured that the fresh and hardened properties of the concrete were within an acceptable range for further evaluation.

3.4.2 Test Specimen Preparation

The compressive strength and flexural strength specimens were prepared using steel moulds with dimensions of 150×150×150 mm and 150×150×750 mm, respectively. Prior to casting, the inner surfaces of the moulds were evenly coated with a thin layer of mould release oil using a brush. The compressive and flexural strength tests were conducted according to the guidelines of BS EN 12390-3:2019 and BS EN 12390-5:2019 standards.

According to the mix proportion, weighed the masses of cement, electrolytic manganese slag, sand, gravel, water, and water reducer. Gravel, cement, electrolytic manganese slag, and sand were put into the concrete mixer in sequence, stirred evenly, and then water and water reducer were added. After sufficient mixing, the concrete was poured out for slump test. Fill the concrete into the mould on the vibration table and vibrate until the concrete slurry overflows and covers the exposed surface. To avoid confusion in specimen identification, label the concrete with paper indicating the electrolytic manganese

slag dosage and specific surface area. Immediately after the specimen is formed, cover its surface with plastic film. Upon demolding, the specimen should be promptly placed in a standard curing chamber with a temperature of 20°C ± 2°C and a relative humidity of over 95% for curing, as illustrated in Figure 3.5.

Figure 3.5 Concrete Curing in the Curing Room

The benchmark concrete, containing no SiMnS, is designated as F0. The experimental groups comprised 16 different mixes, incorporating SiMnS at four specific surface areas (60, 120, 235, and 400 m²/kg) and four cement replacement ratios (10%, 20%, 30%, and 40% by mass). The mix coding follows the convention F[SSA]-[Replacement Ratio]. For example: F60-10 denotes the mix with SiMnS SSA of 60 m²/kg and 10% cement replacement. F120-20 denotes the mix with SiMnS SSA of 120 m²/kg and 20% cement replacement.

Other specimens are numbered accordingly. It is important to note that the code (e.g., F60-10) refers to a specific mix design. Separate batches of specimens were cast and cured for each distinct test series (e.g., compressive strength, chloride penetration, freeze-thaw).

3.4.3 Workability Test of Concrete

The slump test, conducted in compliance with GB/T 50080-2002, was employed to evaluate the workability of fresh concrete. The test procedure is illustrated in Figure 3.6.

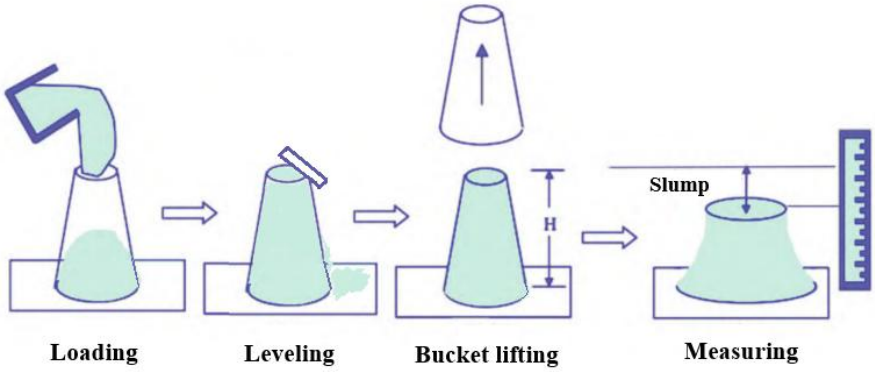

Figure 3.6: Slump Test Diagram

3.4.4 Compressive Strength Test of Concrete

After curing periods of 3, 7, 14, and 28 days, the specimens were removed from curing conditions and tested for compressive strength. The compressive strength test was conducted in accordance with GB/T 50081-2019 using a YAW-4306 microcomputer-controlled fully automatic pressure testing machine. The compressive strength of the specimen is calculated according to Equation 3.4:

$$f_c = \frac{P}{A} \qquad \text{Equation 3.4}$$

where f_c = the compressive strength of concrete; P = the maximum load when the specimen is crushed; and A = the compressive area of the specimen.

3.4.5 Flexural Strength Test of Concrete

The flexural strength test followed the same experimental design matrix as the compressive strength test, encompassing all combinations of the four SiMnS SSA and the four replacement ratios. The complete set of test specimens and their numbering scheme is summarized in Table 3.7.

Table 3.7: Experimental Design Matrix for Concrete Strength Test Specimens

Specimen ID	SiMnS SSA (m^2/kg)	Cement Replacement (%)	Primary Test
F0	0 (Control)	0	Compressive & Flexural
F60-5	60	5	Compressive & Flexural
F60-10	60	10	Compressive & Flexural
F60-15	60	15	Compressive & Flexural
F60-20	60	20	Compressive & Flexural
F120-5	120	5	Compressive & Flexural
F120-10	120	10	Compressive & Flexural
F120-15	120	15	Compressive & Flexural
F120-20	120	20	Compressive & Flexural
F235-5	235	5	Compressive & Flexural
F235-10	235	10	Compressive & Flexural
F235-15	235	15	Compressive & Flexural
F235-20	235	20	Compressive & Flexural
F400-5	400	5	Compressive & Flexural

Table 3.7 continued

F400-10	400	10	Compressive & Flexural
F400-15	400	15	Compressive & Flexural
F400-20	400	20	Compressive & Flexural

After the designated curing periods (3, 7, 14, and 28 days), the prismatic specimens (150×150×750 mm) were tested for flexural strength. The flexural strength test is performed using the three-point loading method according to BS EN 12390-5:2019. The flexural strength was calculated according to the following Equation 3.5:

$$f_f = \frac{P \times L}{b \times d^2} \qquad \text{Equation 3.5}$$

where f_f = the bending strength (unit: MPa); P = the maximum load when the specimen is damaged (unit: N); L = the support distance (unit: mm); b is the specimen width (unit: mm); d is the specimen height (unit: mm).

3.5 Durability Properties Test of Concrete

This part of the thesis describes the durability properties test of SiMnS concrete, including three tests, namely, resistance to chloride ion penetration performance test, freeze-thaw resistance performance test, and sulphate corrosion resistance performance.

3.5.1 Chloride Ion Penetration Resistance Test

There are many methods to evaluate the resistance of concrete to chloride ion corrosion, which can be roughly divided into two categories. One is the standard method: testing the chloride ion content at different depths of the specimen (immersion method) or

the change of solution concentration in the diffusion tank (diffusion tank method) and then using mathematical models to calculate the chloride ion propagation speed. The other is the accelerated method, which mainly includes the electric flux, rapid chloride penetration test (RCPT), accelerated chloride migration test (ACMT), etc. The advantage of this method is that the experimental cycle is extremely short. This thesis employs the RCPT in accordance with ASTM C1202 *Standard Test Method for Electrical Indication of Concrete's Ability to Resist Chloride Ion Penetration*.

(1) Mix design and test specimen numbering

The SSA of SiMnS are 60 m^2/kg, 120 m^2/kg, 235 m^2/kg, and 400 m^2/kg respectively. Silicomanganese slag was added to concrete to replace 10%wt of cement in equal mass percentage. Cylindrical specimens with diameter $\Phi = 100 \pm 1$ mm and height $h = 50 \pm 2$ mm are used for SiMnS concrete to conduct electric flux tests.

The benchmark group SiMnS concrete is numbered C0, representing the concrete test specimen with 0 SiMnS content; The remaining four groups of SiMnS concrete are numbered F60-10, F120-10, F235-10, and F400-10, respectively. Among them, C60-10 represents a SiMnS concrete test specimen with a SiMnS SSA of 60 m^2/kg and a SiMnS content of 10%, and other test specimens are numbered accordingly.

(2) Test process

The chloride ion penetration resistance test is performed using the RCPT method as specified in ASTM C1202.

The specimens were prepared using standard cylindrical molds with dimensions of 100 mm diameter and 50 mm thickness. After casting, the concrete specimens were cured

under standard conditions at 23 ± 2 ℃ and relative humidity above 95% for curing periods of 28 and 56 days.

The specimens were cured for 28 days and 56 days. Cement was replaced by SiMnS at a percentage of 10%wt, and the SSA of the four types of SiMnS were 60 m^2/kg, 120 m^2/kg, 235 m^2/kg, and 400 m^2/kg. The electric flux test was conducted using the following steps to test the current value.

Prior to testing, the specimens were prepared as follows. Upon reaching the specified curing age, they were air-dried. The cylindrical surfaces were then sealed with an impermeable coating epoxy resin to confine ionic migration to the cross-sectional area. Any imperfections or holes in the coating were filled to ensure complete sealing.

The sealed specimens were subsequently vacuum-saturated to achieve a fully water-saturated condition. Each specimen was placed in a vacuum desiccator, and a vacuum pressure of 10–50 mbar (1–5 kPa) was maintained for 3 hours. Following this, the desiccator was flooded with deionized water to immerse the specimens. After 1 hour under vacuum, atmospheric pressure was restored, and the specimens were soaked for an additional 18 ± 2 hours.

After saturation, the surface moisture was removed, and the specimen was mounted between two test cells. The assembly was tightly clamped using screws, with vulcanized rubber gaskets placed at the interfaces to prevent leakage. All tests were conducted in a controlled environment maintained at 20–25°C with a relative humidity of not less than 95%.

For the test itself, the cell on one side of the specimen was filled with a 3.0% NaCl solution, and the embedded copper mesh was connected to the negative terminal (cathode)

of a DC power supply. The opposing cell was filled with a 0.3 mol/L NaOH solution, with its copper mesh connected to the positive terminal (anode). Upon filling both cells, a constant DC voltage of 60 ± 0.1 V was applied. The initial current was recorded immediately after power-on.

After the test, the equipment was cleaned promptly. The test solutions were drained, and the cells were rinsed thoroughly with tap water and detergent, followed by a distilled water rinse, and finally dried with a stream of cool air.

(3) Electric flux calculation

The total electric flux of each specimen is calculated using the simplified Equation 3.6:

$$Q = 900(I_0 + 2I_{30} + 2I_{60} + \cdots + 2I_t + \cdots + 2I_{300} + 2I_{330} + I_{360}) \qquad \text{Equation 3.6}$$

where Q = the total electric flux through the cylindrical specimen (C); I_0 = the initial current of the cylindrical specimen (A); I_t = the current corresponding to t (min) of the cylindrical specimen (A).

Following the test procedure of ASTM C1202, the measured charge passed (Q) was obtained. For the purpose of comparison with results reported in the Chinese context or in accordance with local practice, this value was further converted into the equivalent electric flux of a standard cylindrical specimen with a diameter of 95 mm, as stipulated in the Chinese standard GB/T 50082-2009, using Equation 3.7.

$$Q = Q_x \times \left(\frac{95}{x}\right)^2 \qquad \text{Equation 3.7}$$

where Q = the electric flux through a cylindrical specimen with a cross-sectional diameter of 95 mm (C); Q_x = the electric flux through a cylindrical specimen with a cross-sectional diameter of x mm (C); x = the actual diameter of the cylindrical specimen (mm).

3.5.2 Sulphate Corrosion Resistance Test

The degradation of concrete caused by sulphate attack is complex. It is characterized by various microstructural changes and multiple physical manifestations, including volume expansion, cracking, spalling, softening, and in some cases, mushiness. This study analyses the concrete mass loss rate and compressive strength loss rate under sulphate corrosion conditions.

The SSA of SiMnS were 60 m²/kg, 120 m²/kg, 235 m²/kg, and 400 m²/kg respectively. Cement was replaced by SiMnS at a percentage of 10%wt in the concrete. Silicomanganese slag concrete was prepared using a 100 mm × 100 mm × 100 mm cubic standard-size specimen mould. After the concrete was mixed, it was placed in the mould and vibrated to make it dense. The specimens were cured under standard conditions, with a curing temperature of 20 ± 2 ℃, immersed in a 5% sodium sulfate solution at a relative humidity of more than 95%, and the immersion times were 30 days, 60 days, 90 days, 120 days, 150 days, and 180 days.

The benchmark group of SiMnS concrete is numbered C0, which represents a concrete test specimen with a SiMnS content of 0. The remaining four groups of SiMnS concrete are numbered F60-10, F120-10, F235-10, and F400-10, respectively. Among them, C60-10 represents a SiMnS concrete test specimen with a SiMnS SSA of 60 m²/kg and a SiMnS content of 10%wt, and other test specimens are numbered accordingly.

The sulphate corrosion resistance test is performed according to ASTM C1012-15 and ASTM C157/C157M-17, as shown in Figure 3.7.

Figure 3.7: Immersion of Concrete Test Blocks

The test ages were: 30 days, 60 days, 90 days, 120 days 150 days and 180 days. In addition, the Na_2SO_4 corrosion solution was replaced regularly within the specified age to ensure that the concentration of the corrosion solution remained constant. The mass loss and compressive strength were measured after reaching the specified age. The mass loss rate was calculated according to Equation 3.8, and the sulfate resistance coefficient of SiMnS concrete was calculated according to Equation 3.9

$$W_L = \frac{m_0 - m_t}{m_0} \times 100\% \qquad \text{Equation 3.8}$$

in which W_L = the mass loss rate of the specimen after immersion for t days; m_0 = the initial mass of the specimen before immersion; and m_t = the mass of the specimen after immersion for t days.

$$K_f = \frac{f_{cn}}{f_{c0}} \times 100\% \qquad \text{Equation 3.9}$$

in which K_f = the sulfate resistance coefficient after immersion for n days; f_{cn} = the compressive strength of the control group concrete specimens of the same age (MPa), accurate to 0.1 MPa; f_{c0} = the compressive strength of the SiMnS concrete specimens after n days of sulphate corrosion resistance (MPa), accurate to 0.1 MPa.

The mass loss rates of concrete specimens incorporating SiMnS (with SSA of 60, 120, 235, and 400 m^2/kg) were calculated after exposure to a Na_2SO_4 solution for periods of 30, 60, 90, 120, 150, and 180 days. These results were then visualized using a bar graph, with SiMnS SSA, curing age, and mass loss rate as the key parameters. Based on this graphical representation, the influence of different SiMnS SSA values on the sulfate resistance (quantified by mass loss) of concrete was analyzed.

The compressive strength of concrete made with SiMnS having SSA values of 60 m^2/kg, 120 m^2/kg, 235 m^2/kg, and 400 m^2/kg was calculated at curing ages of 30, 60, 90, 120, 150, and 180 days. A bar graph was drawn with the SSA of SiMnS, curing days and compressive strength as parameters to analyze the effect of different SiMnS SSA on the compressive strength of concrete in the corrosive environment of Na_2SO_4 solution.

The effect of SiMnS SSA on the sulphate corrosion resistance of SiMnS concrete was comprehensively analyzed.

3.5.3 Concrete Freeze-Thaw Resistance Test

The freeze-thaw resistance of concrete refers to the ability to resist damage caused by the combined action of water and freeze-thaw cycles. From a macroscopic perspective, freeze-thaw damage refers to the internal cracks and surface erosion caused by the freeze-thaw water cycle in concrete. Many scholars have explained freeze-thaw damage from a

microscopic perspective, but the most representative and recognized ones are the frost heave theory and the osmotic pressure theory.

The SSA of SiMnS were 60 m^2/kg, 120 m^2/kg, 235 m^2/kg and 400 m^2/kg respectively. Concrete was mixed with SiMnS to substitute 10%wt of cement by equivalent mass percentage. Silicomanganese slag concrete was prepared using a 100×100×100 mm cubic standard specimen mould. After the concrete was mixed, it was placed in the mould and vibrated to make it dense. The specimens were cured under standard conditions, with a curing temperature of 20 ± 2 °C and a relative humidity of more than 95%.

The benchmark group of SiMnS concrete was numbered F0, and the SiMnS content of the F0 benchmark group was 0. The remaining four groups of SiMnS concrete were numbered F60-10, F120-10, F235-10, and F400-10, and the SiMnS content was added to the concrete in an equal mass percentage to replace 10%wt of cement. The SSA of manganese slag in groups F60-10, F120-10, F235-10, and F400-10 were 60 m^2/kg, 120 m^2/kg, 235 m^2/kg, and 400 m^2/kg, respectively.

The test was carried out using a concrete freeze–thaw test chamber. According to BS EN 12390-9:2019, cubic specimens with dimensions of 100 mm × 100 mm × 100 mm were prepared. Four days prior to the target age of 28 days, the specimens were immersed in saturated limewater at 20 ± 2 °C. After immersion, they were placed in a rapid freeze–thaw chamber and subjected to cyclic freezing and thawing between –17 °C and 5 °C.

The mass of the specimens with freeze-thaw cycles of 0~300 times (measured every 25 times) was measured, and the mass loss rate was calculated to explore the influence of SiMnS SSA on the freeze-thaw resistance of concrete. The mass loss rate of concrete under freeze-thaw cycle conditions is calculated using Equation 3.10.

$$M_d = \frac{m_0 - m_t}{m_0} \times 100\% \quad \text{Equation 3.9}$$

where M_d = mass loss rate of the specimen after t freeze-thaw cycles; m_0 = the initial mass of the specimen before immersion; m_t = the mass of the specimen after t freeze-thaw cycles.

The test measured the compressive strength of concrete after 0, 50, 100, 150, 200, 250, and 300 freeze-thaw cycles. When the compressive strength loss is greater than 25%, the freeze-thaw cycle number was used to evaluate the concrete's frost resistance grade. The compressive strength of SiMnS concrete under freeze-thaw cycle conditions was calculated according to Equation 3.4.

The degradation of SiMnS concrete under freeze-thaw cycling was assessed by monitoring the evolution of mass loss rate and compressive strength. Specimens with four SiMnS SSA values (60, 120, 235, and 400 m²/kg) were tested. Mass loss rates were calculated at 25-cycle intervals, while compressive strength was measured after 0, 50, 100, 150, 200, 250, and 300 cycles. The effects of SSA and cycle number on both mass loss and compressive strength were graphically represented using line charts and analyzed to determine the influence of slag fineness on frost resistance.

3.6 Microscopic Analysis

The internal hydration microstructure of SiMnS concrete determines its macroscopic properties. Studying the types and microstructure of hydration products of SiMnS concrete can provide a more adequate theoretical basis for studying the influence of manganese slag on concrete performance. Scanning electron microscopy was used to analyze the microscopic morphology of hydration products of SiMnS cement concrete, and the

relationship between the microstructure and macroscopic properties of SiMnS concrete was studied.

3.7 The AHP-entropy Method

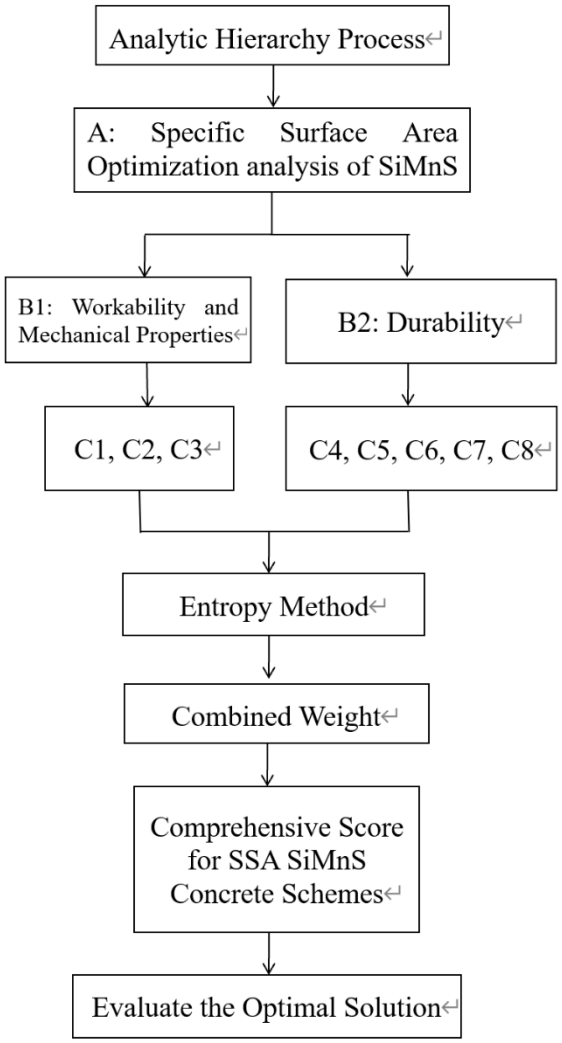

Figure 3.8: Flowchart of the integrated AHP-entropy weight method applied for the mix proportion selection of SiMnS concrete

The specific procedure of the AHP-entropy weight method is illustrated in the flowchart shown in Figure 3.8. The experimental data were statistically evaluated using a combination of the AHP and the entropy weight method, referred to as the AHP - entropy method, assigning subjective and objective weights to various indicators. By integrating

these two types of weights, this approach yielded more reasonable and objective indicator weights. This method mitigates the influence of subjective factors inherent in the AHP and addresses potential biases in objective weighting caused by significant variability in the original data. In this study, the AHP-entropy method was employed to determine the weights of indicators affecting the comprehensive performance of SiMnS concrete. Subsequently, a weighted scoring method is applied to comprehensively compare and select SSA-modified mix proportions for SiMnS concrete.

3.7.1 Analytic Hierarchy Process

Analytic hierarchy process (Saaty, 1980) is a prevalent methodology within multi-criteria decision-making frameworks. It relies on an eigenvalue-based technique to perform pairwise comparisons, offering a structured approach to evaluating both quantitative and qualitative criteria. This method employs a numerical scale that spans from 1/9 (indicating the "least importance") to 1 (signifying "equal importance") and up to 9 (representing "absolute importance") to reflect the relative significance of decision elements across the comparison matrix.

Analytic hierarchy process enables the incorporation of group consensus by employing instruments like structured questionnaires to collect expert assessments for pairwise comparisons. Individual judgments are aggregated into a collective decision using the geometric mean. The hierarchical structure of AHP provides notable benefits in decision-making, as demonstrated in various applications (Saaty, 1980).

The varying SSA values have a certain impact on the overall performance of manganese slag concrete. Applying the AHP statistical method can comprehensively analyze these experimental data to provide an integrated evaluation.

(1) Development of the Hierarchical Analysis Model

A hierarchical analysis model was constructed based on the relational factors influencing the comprehensive performance of SiMnS concrete. The resulting structure was illustrated in Figure 3.9. This model consists of four levels: the goal level (Level 0), the criteria levels (Levels 1 and 2), and the alternatives level (Level 3).

The hierarchical structure, particularly the grouping of Slump (C1), Compressive Strength (C2), and Flexural Strength (C3) under the primary criterion "Workability and Mechanical Properties (B1)", is directly aligned with the first research objective of this study (as stated in Chapter 1): "*To investigate the effect of silicomanganese slag's SSA on concrete workability (slump) and the mechanical properties of mortar and concrete (compressive and flexural strengths)*."

This grouping reflects the integrated analysis intended for these three key fresh and hardened state properties, which are collectively influenced by the SSA of SiMnS and are evaluated together to address Objective 1. Treating them under a unified criterion (B1) allows for a coherent pairwise comparison regarding their relative importance within the context of this specific research aim. Durability properties (B2) are treated as a separate criterion, corresponding to the study's broader scope of comprehensive performance evaluation.

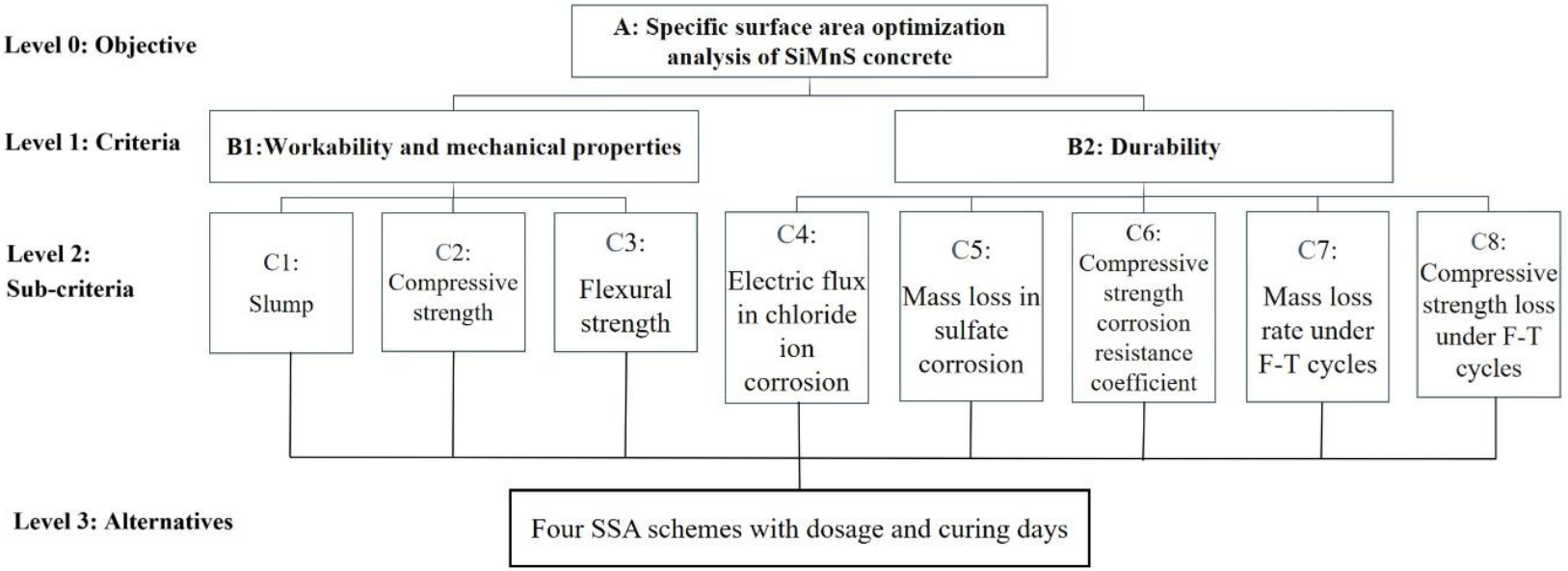

Figure 3.9: A Hierarchical Analysis Structure Model for Comprehensive Performance Analysis of SiMnS Concrete

(2) Construction of Judgment Matrices

The judgment matrix between the goal level (Level 0) and the first criteria level (Level 1) is denoted as *A*. The matrices between Level 1 and the second criteria level (Level 2) are denoted as *B1* and *B2*, respectively. Similarly, the matrices between Level 2 and the alternative level (Level 3) are represented as *C1*, *C2*, *C3*, *C4*, *C5*, *C6*, *C7* and *C8*. In summary, the hierarchical judgment matrices are as follows: *A* [*B1*, *B2*], *B1* [*C1*, *C2*, *C3*], B2 [*C4*, *C5*, *C6*, *C7*, *C8*], with the numerical relationships between factors within each matrix defined as shown in Figure 3.10.

$$A1 = [B1, B2] = \begin{bmatrix} 1 & 1/A12 \\ A12 & 1 \end{bmatrix}$$

$$B1 = [C1, C2, C3] = \begin{bmatrix} 1 & 1/B12 & 1/B13 \\ B12 & 1 & 1/B23 \\ B13 & B23 & 1 \end{bmatrix}$$

$$B2 = [C4, C5, C6, C7, C8] = \begin{bmatrix} 1 & 1/C12 & 1/C13 & 1/C14 & 1/C15 \\ C12 & 1 & 1/C23 & 1/C24 & 1/C25 \\ C13 & C23 & 1 & 1/C34 & 1/C35 \\ C14 & C24 & C34 & 1 & 1/C45 \\ C15 & C25 & C35 & C45 & 1 \end{bmatrix}$$

Figure 3.10: Matrix Relationship Diagram

To construct the pairwise comparison matrices for the AHP and to ensure a comprehensive, balanced perspective from both industry and academia, a panel of sixteen experts was invited. The panel was composed of professionals from local construction firms, design institutes, supervision companies, and university faculty to ensure a comprehensive and balanced perspective from both industry and academia. The primary purpose of engaging this number and diversity of experts was to mitigate individual bias and enhance the scientific validity, reliability, and consistency of the subjective weight allocation process.

A total of 13 electronic scoring sheets were collected, with 12 deemed valid for subsequent analysis.

Based on these valid expert judgments, the pairwise comparison matrices (*A*, *B1*, and *B2* in Fig. 3.3) were constructed. The elements within these matrices, denoted as a_{ij}, b_{ij}, and c_{ij}, quantitatively represent the relative importance of criterion i over criterion j. These values were assigned using the standardized Saaty scale (Table 3.8) (Saaty & Alexander, 1981). For instance, in the *B2* matrix, the element *C12* represents the relative importance of Sub-criterion C5 (Electric flux in chloride corrosion) compared to Sub-criterion C4 (Mass loss in sulfate corrosion). If an expert judged that "C4 is slightly more important than C5," this judgment would correspond to a score of 3 on the Saaty scale, with the definition "Moderate importance." Conversely, the reciprocal value (1/3) would be assigned to the symmetric element *C21* in the matrix.

Given that pairwise comparisons are provided independently by multiple experts, group judgment is necessary to construct the final comparison matrix. Based on the ratio scale properties of the AHP, the geometric mean method is used to aggregate the pairwise judgments of the experts, as only the geometric mean strictly maintains the principle of reciprocity. Specifically, if the aggregated a_{ij} is x, then a_{ji} must equal 1/x, ensuring that the combined matrix remains a reciprocal matrix; arithmetic averaging would violate this axiom, causing subsequent weight calculations to lose their theoretical foundation. Saaty & Vargas (1987) illustrated the significance of group judgment through pairwise comparisons of energy alternatives by five experts. In their case, four experts judged $a_{12}=3$, and one expert judged $a_{12}=9$; using the arithmetic mean, $(4\times3 + 9)/5 = 21/5 = 4.2$, and its reciprocal $0.24 \neq 1/4.2$, thus destroying reciprocity. However, the geometric mean yields $\sqrt[5]{(3^4\times9)} = 3.74$,

and its reciprocal is approximately $0.27 \approx 1/3.74$, maintaining the reciprocity of the group matrix. Therefore, the geometric mean method maintains the structural consistency of the judgment matrix during the group judgment integration process, making the subsequent weight calculations based on the principal eigenvector more robust and reliable.

To further ensure the logical consistency of the expert-derived matrices and to mitigate the potential bias inherent in subjective judgment, the Consistency Ratio (CR) was employed as a critical validity check. The CR quantifies the degree of logical coherence in the pairwise comparisons. According to the AHP theory, a judgment matrix is considered acceptably consistent if its CR is less than 0.1 ($CR < 0.1$). This threshold indicates that any inconsistencies are within an acceptable, random margin and do not significantly distort the resulting priority weights. In this study, the CR was calculated for each aggregated matrix (A, B1, B2). Any matrix with a $CR \geqslant 0.1$ was identified as having unacceptable inconsistency and was iteratively reviewed and refined by the expert panel until the $CR < 0.1$ criterion was met for all matrices. This rigorous process guarantees that the final subjective weights are both scientifically reliable and logically sound. The detailed mathematical formulation and criteria for the Consistency Ratio (CR) are elaborated in the following section (Consistency Testing of Judgment Matrices).

Specifically, starting from the criteria level of the hierarchical structure model and proceeding downward, all factors at the same level associated with a factor in the previous level are pairwise compared in terms of importance using the Saaty scale method (Saaty & Alexander, 1981), as shown in Table 3.. This process continues until the final level is reached. For instance, when comparing the importance of compressive strength and flexural strength in manganese slag concrete, the scale value can be set to 3, as the material primarily resists

compressive and shear forces after the curing period, with relatively less tensile stress. Ultimately, all scale values are used to construct the judgment matrices for each hierarchical level.

Table 3.8: Saaty Scale Method

Intensity of Importance	Definition	Explanation
1	Equal importance	Factor i and factor j have the same importance to the factors in the previous level
3	Moderate importance	Factor i is slightly more important than factor j
5	Strong importance	Factor i is strongly important compared to factor j
7	Very strong importance	Factor i is very strongly important compared to factor j
9	Absolute importance	Factor i is absolutely important compared to factor j
2, 4, 6, 8	Intermediate values	An intermediate state between the above adjacent scales
$1/a_{ij}$	Opposite importance	If criterion i has one of the above non-zero numbers assigned to it when compared with criterion j, then j has the reciprocal value when compared with i.

(3) Consistency Testing of Judgment Matrices

When comparing the importance of performance factors in manganese slag concrete, it is essential to conduct consistency testing on all judgment matrices to ensure logical

coherence and reliability. This process enhances the scientific rigor and credibility of the decision-making results. In the AHP, commonly used consistency testing metrics include the Consistency Index (CI) and the Consistency Ratio (CR). The calculation methods for these two metrics are provided in Equations 3.11 and 3.12.

$$CI = \frac{\lambda_{max} - n}{n - 1} \quad \text{Equation 3.11}$$

$$CR = \frac{CI}{RI} \quad \text{Equation 3.12}$$

among them, $\lambda_{\max}$ = the largest eigenvalue of the judgment matrix, n is the order of the matrix, and RI = the average random consistency index for the matrix, with values provided in Table 3. (Saaty, 1980).

The Consistency Ratio (CR) serves a critical function in the AHP by quantifying the logical consistency of the pairwise comparison judgments provided by the experts. The Consistency Index (CI) measures the deviation from perfect consistency; a CI of 0 indicates a perfectly consistent matrix, and as CI approaches 0, the matrix exhibits a high degree of consistency. According to AHP theory (Saaty, 1980), the primary function of CR is to act as a standardized validity check. A judgment matrix is considered acceptably consistent if its CR is less than 0.1 (CR < 0.1). This threshold indicates that any remaining inconsistencies in the experts' comparisons are within an acceptable, random range and do not significantly distort the resulting priority weights. If the calculated CR for a matrix is $\geqslant$ 0.1, it signifies unacceptable inconsistency. In such cases, the pairwise comparison data for that matrix must be re-evaluated by the expert panel to identify and resolve contradictory judgments (e.g., if Factor A is preferred over B, and B over C, but C is preferred over A). This iterative process

of checking and refining continues until all matrices achieve CR < 0.1, thereby ensuring the reliability and logical soundness of the derived subjective weights.

Table 3.9: Values of Average Random Consistency Index RI (Saaty, 1980)

Matrix order n	1	2	3	4	5	6	7	8	9
RI	0	0	0.58	0.90	1.12	1.24	1.32	1.41	1.45

(4) Calculation of Subjective Weight Coefficients for Indicators.

The subjective weight coefficients of factors in the judgment matrix can be derived using Equation 3.13. By multiplying the weight coefficients associated with the same factor across different hierarchical levels, the subjective weight coefficients for various performance evaluation indicators can be obtained.

$$W_i = \frac{1}{n} \sum_{j=1}^{n} \frac{a_{ij}}{\sum_{k=1}^{n} a_{kj}}$$ Equation 3.13

among them, W_i = the weight coefficient of the *i*-th factor in the judgment matrix. The elements a = the values in the *i*-th row and *j*-th column, as well as the *k*-th row and *j*-th column of the judgment matrix (i.e., the scale values). Here, i, j, k = 1, 2, …, n, where n denotes the number of indicators.

3.7.2 Entropy Method

The entropy method is an analytical approach based on objective conditions and has been widely applied across various fields, including socioeconomics, science, technology, and engineering practices. By utilizing the entropy method, the influence of subjective

factors on the evaluation results can be minimized, ensuring that the outcomes align more closely with objective realities.

(1) Establishment of the evaluation index system

Based on the provided data, an evaluation index system is established based on the dimensions of the evaluation objectives.

(2) Data Standardization

The raw data is standardized using the extremum method. Specifically, Equation 3.14 is applied for positive indicators, Equation 3.15 is used for negative indicators, while Equation 3.16 is utilized for handling moderate indicators. This process results in a standardized matrix, eliminating differences in measurement units among indicators (Peng et al., 2024).

$$y_{ij} = \frac{x_{ij} - \min(x_{ij})}{\max(x_{ij}) - \min(x_{ij})} \quad \text{Equation 3.14}$$

$$y_{ij} = \frac{\max(x_{ij}) - x_{ij}}{\max(x_{ij}) - \min(x_{ij})} \quad \text{Equation 3.15}$$

$$y_{ij} = \frac{\left| x_{ij} - \frac{\max(x_{ij}) + \min(x_{ij})}{2} \right|}{\max(x_{ij}) - \min(x_{ij})} \quad \text{Equation 3.16}$$

among them, x_{ij} = the value of the j-th indicator for the *i*-th sample (*i*= 1, 2, ⋯, m; *j*= 1, 2, ⋯n), and y_{ij} = the standardized data. To prevent the occurrence of extremely low or negative values in the standardized data.

The attributes of each secondary indicator are presented in Table 3.10 in the analysis of performance evaluation indicators for SiMnS concrete.

Table 3.10: The Attributes of Each Secondary Indicator

Objective level	Primary indicator	Secondary indicator	Attributes
Comprehensive performance of SiMnS concrete under SSA (A)	Working and mechanical properties (B1)	Slump (C1) S_c	Moderate
		Compressive strength (C2) f_c	Positive
		Flexible strength (C3) f_f	Positive
	Durability (B2)	Electric flux in chloride ion corrosion (C4) Q	Negative
		Mass loss in sulfate corrosion (C5) W_L	Negative
		Sulfate resistance coefficient (C6) K_f	Positive
		Mass loss rate under F-T cycles (C7) M_d	Negative
		Compressive strength loss under F-T cycles (C8) f_t	Negative

(3) Calculation of Indicator Entropy

The information entropy of performance evaluation indicators for manganese slag concrete reflects the degree of dispersion of the indicators. A smaller information entropy indicates a higher degree of dispersion, implying a greater weight for the indicator and a more significant influence on the comprehensive selection results of SSA proportions. The information entropy of the evaluation indicators can be calculated using Equations 3.17 to 3.18.

$$p_{ij} = \frac{y_{ij}}{\sum_{i=1}^{m} y_{ij}} \quad \text{Equation 3.17}$$

$$e_j = -\ln n \sum_{i=1}^{m} p_{ij} \ln p_{ij}$$ Equation 3.18

in which p_{ij} = proportion or contribution of the *i*-th SiMnS concrete SSA modification scheme under the *j*-th indicator; and e_j = denotes the entropy value of the *j*-th indicator.

(4) Calculation of Objective Weight Coefficients for Indicators

The objective weight coefficients of the performance indicators can be determined using Equations 3.19 and 3.20.

$$g_j = 1 - e_j$$ Equation 3.19

$$S_j = \frac{g_j}{\sum_{j=1}^{n} g_j}$$ Equation 3.20

among them, g_j = the differentiation coefficient of the *j*-th indicator, and S_j = the objective weight coefficient of the *j*-th indicator.

3.7.3 Calculation of Combined Weight

Using the AHP-entropy method, the combined weight of subjective and objective indicators for the overall performance evaluation of SiMnS concrete is calculated as shown in Equation 3.21 (Liang, 2023).

$$Z_j = 0.5 \times W_j + 0.5 \times S_j$$ Equation 3.21

where = Z_j is the comprehensive weight; and W_j and S_j = subjective and objective weights of the *j*-th indicator, respectively.

3.7.4 Calculation of the Comprehensive Score for SSA SiMnS Concrete Schemes

Based on the structural characteristics of the established comprehensive performance evaluation index system for SiMnS concrete, a weighted average method is applied to assess 30 SSA SiMnS concrete schemes. The weighted average approach employs a linear equation to evaluate the comprehensive performance of SiMnS concrete, as shown in Equation 3.22 (Hou, 2024).

$$f(c) = \sum_{i=1}^{8} (Z_j y_i) \qquad \text{Equation 3.22}$$

among them, f(c) = the comprehensive score of each SSA SiMnS concrete scheme, y_i = the standardized experimental data, and Z_j = the respective comprehensive weight.

By substituting the standardized experimental data and comprehensive weights into Equation 3.22, the comprehensive scores for the 30 SSA SiMnS concrete schemes were calculated. The schemes were then ranked based on their comprehensive scores, leading to the identification of the optimal SSA SiMnS concrete solution under the AHP-entropy method.

CHAPTER 4

RESULTS AND DISCUSSION

4.1 Overview

This chapter presents and discusses the results of various experiments in Chapter 3. There are five parts in this chapter, namely: the effect of SiMnS SSA on cement mortar properties; the effect of SiMnS SSA on concrete slump; the effect of SiMnS SSA on concrete mechanical properties; microscopic analysis of SiMnS concrete by using SEM; the effect of SiMnS SSA on concrete durability; and identifying of the optimal SSA SiMnS concrete solution using the AHP-entropy method.

4.2 Effect of SiMnS SSA on Cement Mortar Properties

This section will discuss the effect of the SSA of SiMnS on the fluidity and compressive strength of cement mortar in terms of its variation.

4.2.1 Effect of SiMnS SSA on Cement Mortar Fluidity

The effect of SSA of SiMnS on the fluidity of cement mortar is illustrated in Figure 4.1, with corresponding data provided in Table 4.1. The marking on the specimens follows the convention of CM*x*-*y*, where *x* is SSA and *y* is the percentage of cement replacement by SiMnS. For instance, CM60-10 represents the cement mortar specimens with a SiMnS SSA of 60 m^2/kg and replacement of cement by SiMnS of 10%wt. For the control specimen without any cement replacement by SiMnS, it is specifically marked as CM0.

The SiMnS was processed to four distinct SSA levels—60, 120, 235, and 400 m^2/kg—selected to systematically evaluate the effect of fineness across a practical spectrum.

This range spans from a coarse, as-received state (60 m²/kg) to a finely ground condition (400 m²/kg) approaching the recognized economic upper limit for industrial-scale valorization (470–492 m²/kg), beyond which further grinding incurs disproportionate energy and cost (Fan et al., 2024; Liu et al., 2017). Cement replacement levels of 10%, 20%, 30%, and 40% by weight were chosen based on a comprehensive literature review, which indicates that studies on SiMnS and similar supplementary cementitious materials commonly focus on the 5–30% range (e.g., Frias et al., 2006; Rai et al., 2002; Wang et al., 2013; Xu et al., 2019). Our 10–40% range aligns with established research practices and spans from low to high incorporation to identify performance thresholds and the optimal dosage. The results from this mortar study, such as the significant workability loss at higher replacements, subsequently informed the narrower, more practical range (5–20%) adopted for the concrete phase of the research.

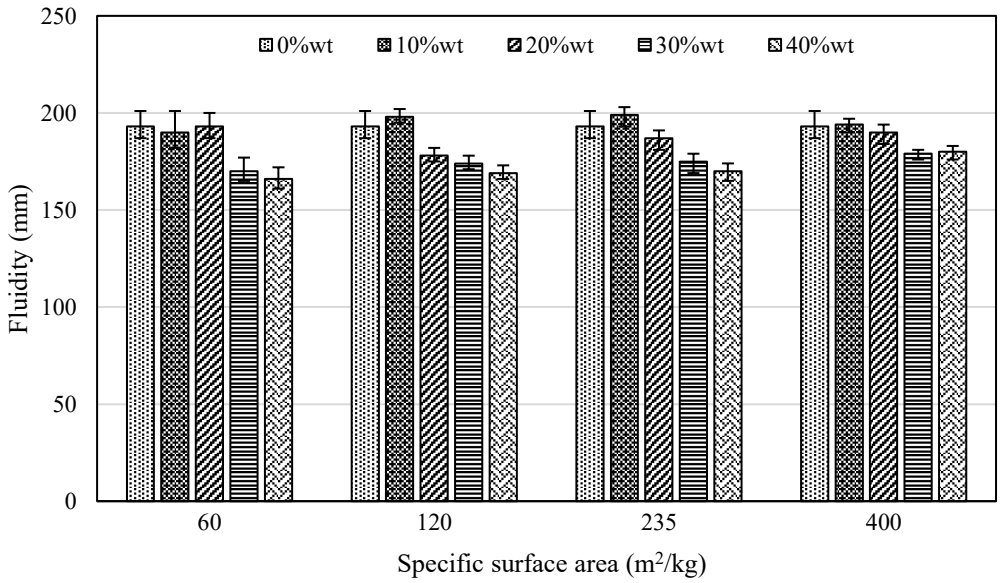

Figure 4.1: Effect of SSA of SiMnS on the Fluidity of Cement Mortar

As depicted in Figure 4.1, the fluidity of cement mortar increases with the increase in SiMnS SSA in general. The fluidity of the cement mortar exhibits a decreasing trend as

the percentage of SiMnS increases when SSA = 60 m²/kg. The control sample (CM0) and CM60-10 maintain relatively high fluidity, whereas CM60-20, CM60-30, and CM60-40 show a continuous reduction. This indicates that at a low SSA, increasing SiMnS content adversely affects the fluidity of the mortar. A similar decreasing trend is observed with increasing SiMnS replacement when SSA = 120 m²/kg. The control sample and CM120-10 maintain relatively higher fluidity, whereas CM120-20, CM120-30, and CM120-40 exhibit a significant decrease. The reduction in fluidity is more pronounced compared to SSA = 60 m²/kg, suggesting that finer SiMnS particles lead to a greater adverse impact on fluidity. The control sample remains the most fluid, with CM235-10 still exhibiting high fluidity. However, as the SiMnS content increases, the fluidity declines substantially, especially in CM235-30 and CM235-40. This trend suggests that at higher SSA values, the incorporation of SiMnS leads to a more noticeable deterioration in workability. The control sample and CM400-10 exhibit relatively high fluidity. However, in contrast to the other groups, the fluidity reduction is less severe across CM400-20, CM400-30, and CM400-40. This indicates that at very high SSA values, the negative impact of SiMnS on fluidity is somewhat mitigated.

Comparing different SSA groups, the control specimen (CM0) exhibited consistently high fluidity. A clear inverse relationship was observed between the SiMnS replacement percentage and fluidity within each SSA group. For instance: At the lowest SSA (60 m^2 /kg), increasing the replacement percentage from 10% to 40% resulted in a progressive decline in fluidity: 190 mm (10%) → 178 mm (20%) → 170 mm (30%) → 166 mm (40%). This represents a total decrease of 12.6% within this SSA group. Compared to the control specimen (CM0), the fluidity at 40% replacement was 14.0% lower, with the most significant drop occurring between 30% and 40% replacement.

This declining trend was consistent across all SSA levels. At 235 m^2 /kg, for example, fluidity measured 199 mm (10%) → 190 mm (20%) → 175 mm (30%) → 170 mm (40%), showing a total reduction of 14.6% across the replacement levels. Compared to the control, the fluidity at 40% replacement was 11.9% lower. Therefore, the statement "as the SiMnS content increases, the fluidity declines substantially" is quantitatively supported. The most substantial decline (14.0% lower than the control) occurred at the highest replacement percentage (40%) with the lowest SSA (60 m^2/kg). Critically, the marked reduction in workability at 30% and 40% replacement levels informed the subsequent experimental design for concrete, where the replacement ratio was adjusted to a lower range of 5%, 10%, 15%, and 20% to mitigate adverse effects on fresh properties.

Conversely, for a given replacement percentage, increasing SSA generally improved fluidity. The most pronounced positive effect was observed at a 10% replacement level: fluidity increased from 190 mm (60 m^2/kg) to 199 mm (235 m^2/kg), representing a 4.7% improvement. This supports the observation that with higher SSA, a lower replacement percentage can yield a positive effect on fluidity.

An equilibrium point was identified: at 400 m^2/kg SSA and 20% replacement, the fluidity (193 mm) matched that of the control specimen. This suggests that with sufficiently high SSA, the cement replacement percentage can be optimized to achieve equivalent or superior performance, indicating that high-SSA SiMnS can be effective at lower, optimized incorporation levels.

Table 4.1: Variation of Cement Mortar Fluidity with SSA of SiMnS

Specimen	SSA (m^2/kg)	Particle size (µm)	Cement replacement by SiMnS (%wt)	SiMnS (g)	Cement (g)	Cement mortar fluidity (mm)
CM0	/	/	0	0	500	193
CM60-10	60	41	10	50	450	190
CM60-20	60	41	20	100	400	178
CM60-30	60	41	30	150	350	170
CM60-40	60	41	40	200	300	166
CM120-10	120	19	10	50	450	198
CM120-20	120	19	20	100	400	187
CM120-30	120	19	30	150	350	174
CM120-40	120	19	40	200	300	169
CM235-10	235	9	10	50	450	199
CM235-20	235	9	20	100	400	190
CM235-30	235	9	30	150	350	175
CM235-40	235	9	40	200	300	170
CM400-10	400	4	10	50	450	194
CM400-20	400	4	20	100	400	193
CM400-30	400	4	30	150	350	179
CM400-40	400	4	40	200	300	180

The observed behavior of silico-manganese slag (SiMnS) particles in cement paste can be attributed to their physicochemical properties, particularly particle size and specific

surface area (SSA), which influence their interaction mechanisms with the cement matrix (Nath et al., 2022). This directly explains the fluidity trends presented in Figure 4.1. At low to moderate replacement levels (⩽20%), high SSA SiMnS particles, owing to their finer size, enhance particle packing density and provide a ball-bearing effect, which improves lubrication within the slurry. This accounts for the enhanced or maintained fluidity observed for high SSA groups (e.g., 235 and 400 m^2/kg) at these replacement levels.

However, beyond an optimal threshold, excessive incorporation of high SSA SiMnS (e.g., at 30% and 40% replacement) can lead to particle agglomeration. This is primarily due to the dramatically increased water demand and surface energy of the ultra-fine particles, which, when insufficiently spaced and wetted, promotes flocculation through strong interparticle van der Waals forces. This agglomeration increases effective particle size and slurry viscosity, leading to the marked reduction in fluidity observed at high replacement levels for even the high SSA mixtures (Chen & Kwan, 2012; Ma et al., 2022).

Conversely, low SSA SiMnS particles, characterized by larger particle sizes, exhibit reduced cementitious activity. Their limited ability to fill voids diminishes packing density from the outset, leading to increased water demand and higher viscosity, thereby reducing fluidity even at moderate replacement levels. This phenomenon aligns with findings by Bentz et al. (2012) on the negative impact of larger particles on rheology. More critically, at high replacement levels, these coarse particles are prone to physical agglomeration due to poor packing and reduced interparticle spacing, which further exacerbates the fluidity loss, as seen in the sharpest decline for the 60 m^2/kg group.

Therefore, the non-linear relationship between fluidity, SSA, and replacement percentage (as summarized in Figure 4.1) arises from two distinct agglomeration mechanisms: 1) a surface-energy-driven mechanism dominating in high SSA, high dosage

scenarios, and 2) a packing-efficiency-driven mechanism dominating in low SSA, high dosage scenarios. Optimal fluidity is achieved at an intermediate replacement level where the positive packing effect of fine particles is maximized before the negative agglomeration effects of either mechanism become dominant.

4.2.2 Effect of SiMnS SSA on the Compressive Strength of Cement Mortar

The compressive strength development of the cement mortar specimens is shown in Figure 4..

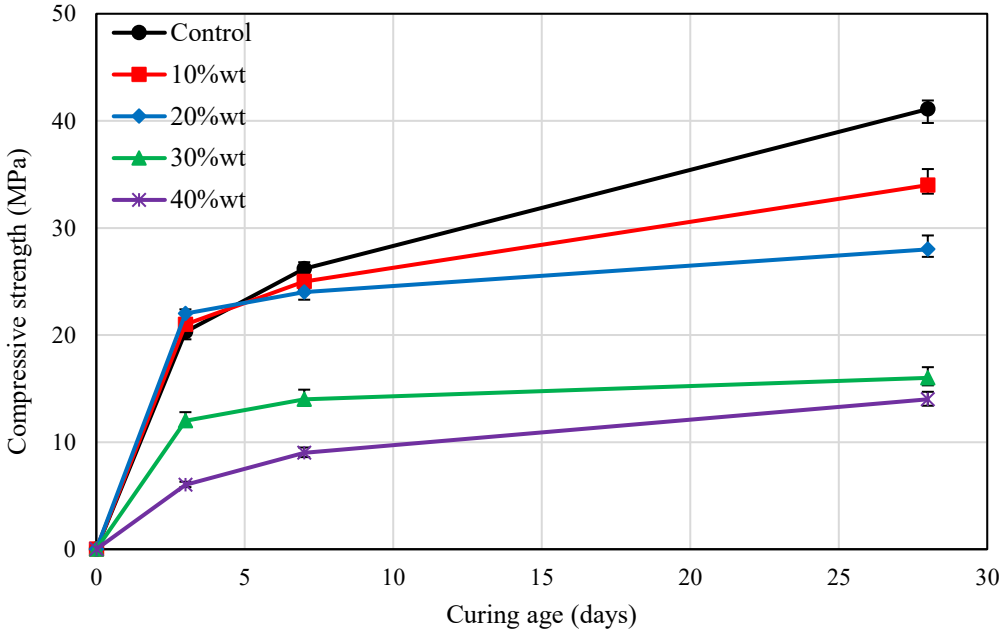

(a) SSA = 60 m^2/kg

Figure 4.2: Effect of SSA of SiMnS on Compressive Strength of Cement Mortar

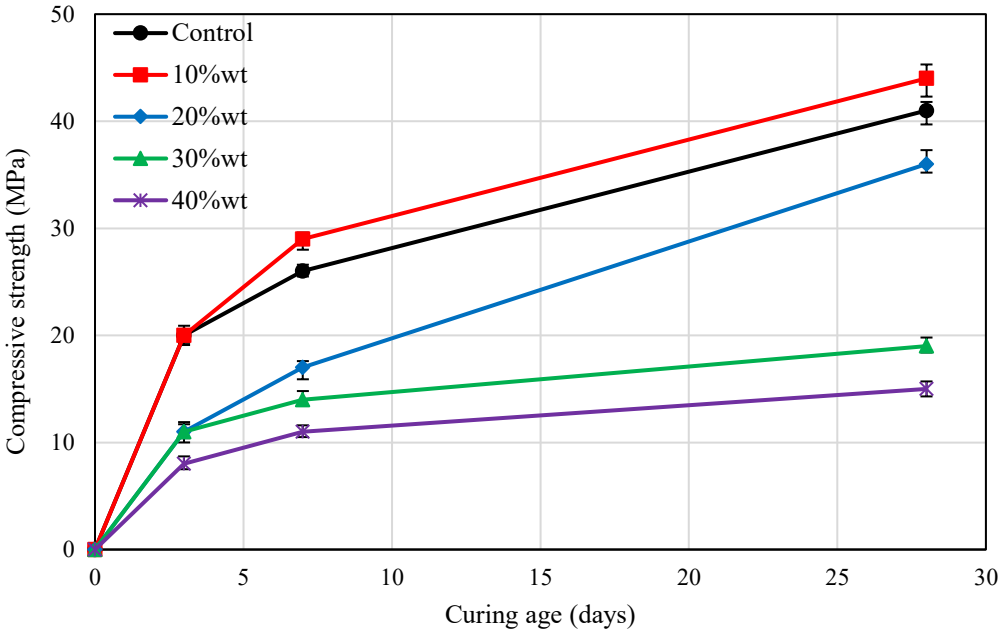

(b) SSA = 120 m^2/kg

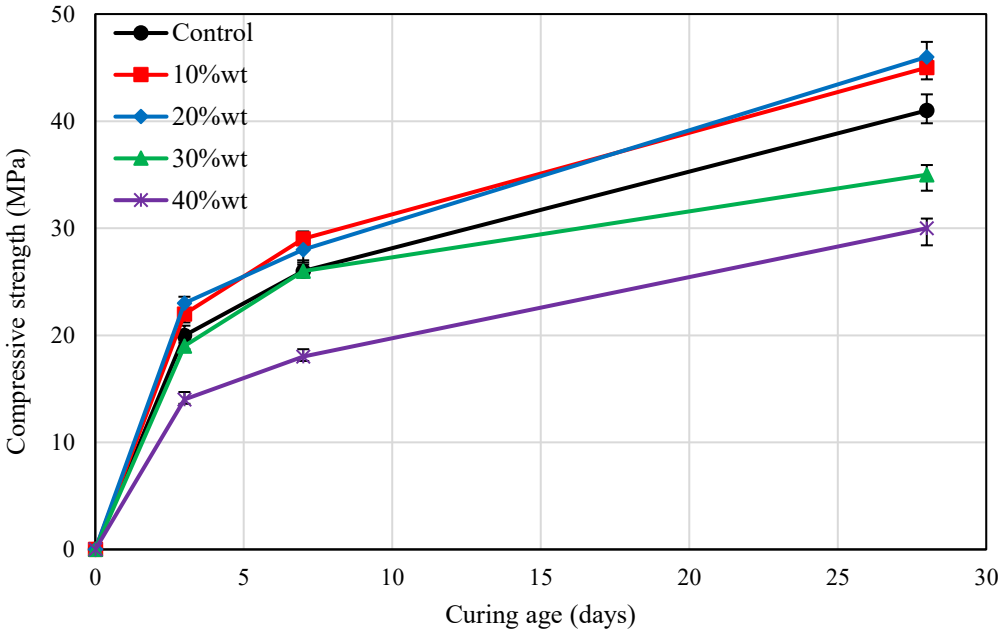

(c) SSA = 235 m^2/kg

Figure 4.2 continued

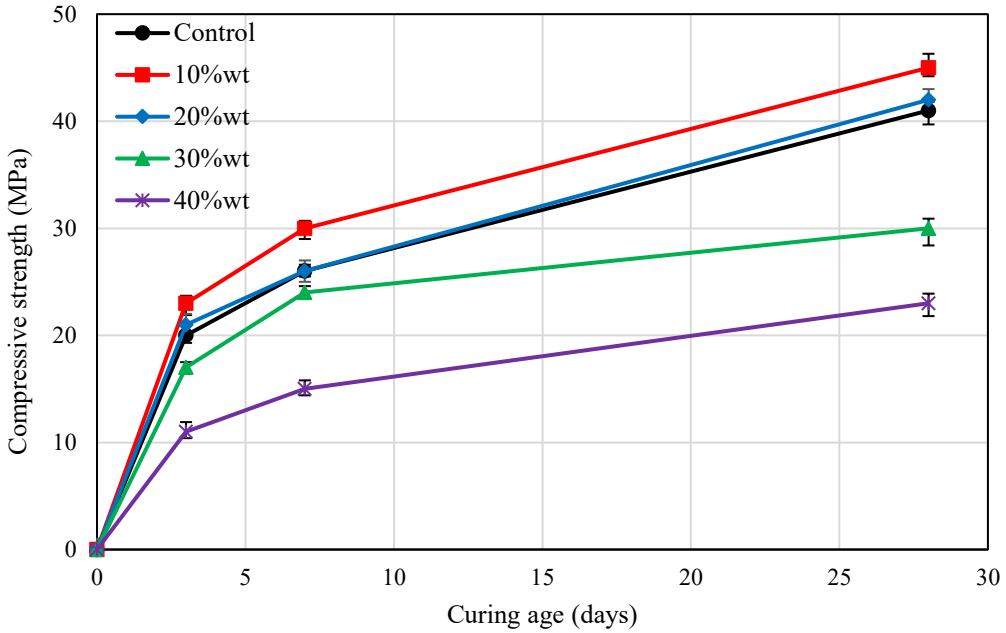

(d) SSA = 400 m^2/kg

Figure 4.2 continued

At SSA = 60 m^2/kg, the compressive strength of cement mortar exhibits distinct trends at different curing ages (3, 7, and 28 days) as the SiMnS replacement level increases. At 3 days, the specimens with 10%wt and 20%wt SiMnS replacement achieve higher compressive strength than the control (0%wt), indicating that a small amount of SiMnS may enhance early-age strength, possibly due to filler effects or accelerated hydration. However, by 7 days, the strength of these specimens begins to slow down as compared to the control specimen, suggesting a reduction in cementitious activity. At 28 days, the control sample maintains the highest strength, while specimens with increasing SiMnS replacement levels exhibit progressively lower compressive strength, with 30%wt and 40%wt showing significant reductions. This trend highlights that while moderate SiMnS replacement may temporarily enhance early-age strength, excessive substitution weakens later curing age mechanical performance due to the reduced availability of reactive cementitious material.

Overall, the compressive strength of cement mortar decreases with increasing SiMnS content, particularly at later curing ages.

At SSA = 120 m^2/kg, the compressive strength of cement mortar exhibits distinct trends over different curing ages (3, 7, and 28 days) as the SiMnS replacement level increases. At 3 days, the specimen with 10%wt SiMnS replacement shows a compressive strength nearly identical to that of the control (0%wt), indicating that a moderate amount of SiMnS does not significantly hinder early-age strength development. The 20%wt specimen achieves a slightly lower strength, while the 30%wt and 40%wt specimens exhibit a more pronounced reduction in early-age strength. At 7 days, the 10%wt specimen surpasses the control, suggesting that an optimal replacement level can enhance strength development, potentially due to improved particle packing and hydration kinetics. However, by 28 days, the control and 10%wt specimens remain comparable in strength, while the 20%wt, 30%wt, and 40%wt specimens show progressively lower strength levels, indicating that excessive SiMnS replacement limits later curing age strength gains. In general, compressive strength first remains stable at low replacement levels but declines as the SiMnS content increases, with higher replacement levels (> 30%wt) significantly reducing mechanical performance at all curing ages.

At SSA = 235 m^2/kg, the compressive strength of cement mortar varies with SiMnS replacement levels over 3, 7, and 28 days. At 3 days, the 10%wt and 20%wt specimens exhibit slightly higher strength than the control (0%wt), while the 30%wt specimen is comparable to the control, indicating that moderate SiMnS replacement does not hinder early-age strength development. At 7 days, the 10%wt and 20%wt specimens continue to outperform the control, with the 10%wt specimen achieving approximately 11.5% higher

strength and the 20%wt specimen around 7.7% higher, while the 30%wt specimen remains similar to the control. By 28 days, the 10%wt and 20%wt specimens still surpass the control in compressive strength, while the 30%wt specimen shows a steady increase but stays slightly below the control, and the 40%wt specimen remains the weakest. In general, at 3 and 7 days, the compressive strength increases with 10%wt and 20%wt SiMnS replacement, and at 28 days, these two levels still outperform the control, while 30%wt and 40%wt replacements result in lower compressive strength at all curing ages.

At SSA = 400 m^2/kg, the compressive strength of cement mortar varies with SiMnS replacement levels over 3, 7, and 28 days. At 3 days, the 10%wt and 20%wt specimens show slightly higher strength than the control (0%wt), while the 30%wt specimen is slightly lower, and the 40%wt specimen remains the weakest. At 7 days, the 10%wt specimen continues to outperform the control by approximately 15.4%, while the 20%wt specimen is comparable to it. The 30%wt and 40%wt specimens remain lower. By 28 days, the 10%wt specimen achieves the highest strength, surpassing the control, while the 20%wt specimen remains nearly the same as the control. The 30%wt and 40%wt specimens continue to show lower strength. In general, 10%wt replacement enhances strength at all ages, 20%wt maintains strength similar to the control at 7 and 28 days, while 30%wt and 40%wt lead to reductions across all curing ages.

Figure 4.2 demonstrates the effect of SSA on the compressive strength of cement mortar with different levels of SiMnS replacement over 3, 7, and 28 days. As SSA increases from 60 m^2/kg to 400 m^2/kg, the overall compressive strength of cement mortar improves, particularly at moderate SiMnS replacement levels. At low SSA (60 m^2/kg), the control specimen (0%wt) consistently achieves the highest strength, and all SiMnS replacement

levels result in lower compressive strength, indicating limited pozzolanic activity. However, as SSA increases to 120 m²/kg and 235 m²/kg, the 10%wt and 20%wt specimens begin to surpass the control at later ages, showing that finer SiMnS particles contribute more effectively to hydration and strength development in cement mortar.

At high SSA (400 m²/kg), the 10%wt specimen consistently achieves the highest compressive strength across all ages, while the 20%wt specimen remains comparable to the control at 7 and 28 days, demonstrating an optimal balance between SiMnS reactivity and cement dilution. The 30%wt and 40%wt specimens show strength reductions at all ages, indicating that excessive SiMnS replacement is detrimental to the compressive strength of cement mortar, despite the increased SSA. This suggests that while higher SSA improves SiMnS reactivity, it cannot fully compensate for the reduction in cementitious material at high replacement levels.

In general, increasing SSA enhances the effectiveness of SiMnS in cement mortar, particularly at 10%wt and 20%wt replacement levels. However, beyond 30%wt, the compressive strength of cement mortar declines regardless of SSA, suggesting a threshold for effective SiMnS utilization. The most significant improvement is observed at SSA = 400 m²/kg, where 10%wt replacement consistently outperforms the control, indicating that finely ground SiMnS can be beneficial when used at optimal levels. When the substitution ratio was greater than 20%wt and increased to 30%wt and 40%wt, the total amount of SiMnS particles was too much for either SSA value and began to interfere significantly with the hydration of the cement, causing the compressive strength growth to be inhibited and resulting in the compressive strength of the cement mortar being significantly lower than that of the control specimen. Therefore, the percentage of cement replacement by SiMnS

should not exceed 20%wt. For the subsequent concrete tests, cement replacement by SiMnS concentrates on 5%wt, 10%wt, 15%wt, and 20%wt based on the results of cement mortar.

The observed phenomena regarding the influence of SiMnS on cement paste properties can be attributed to the reactivity and particle dispersion characteristics of SiMnS, particularly its SSA. Higher SSA in SiMnS particles indicates a greater number of surface-active sites, enhancing their reactivity. For instance, increasing SSA from 60 m^2/kg to 400 m^2/kg results in finer particles, which increases the contact area with water and calcium hydroxide in the cement paste. This promotes accelerated hydration reactions at early ages (e.g., 3 days), facilitating the formation of CSH and contributing to early strength development. This is consistent with findings by Celik (2009), who reported that finer cement particles with higher SSA lead to increased early-age strength due to enhanced hydration rates. However, at higher replacement levels (e.g., 30%wt and 40%wt), excessive SiMnS can encapsulate cement particles, hindering their hydration and resulting in reduced late-age strength. This phenomenon aligns with observations by Bentz et al. (1999), who noted that excessive fine particles could impede cement hydration by forming a dense layer around cement grains, limiting water ingress.

High SSA SiMnS particles tend to disperse more uniformly within the cement matrix. At an SSA of 400 m^2/kg and a 10%wt replacement level, SiMnS particles are well-dispersed, effectively filling voids and enhancing the microstructure without obstructing cement hydration. This uniform dispersion contributes to improved mechanical properties at all ages. Such behavior is supported by research indicating that well-dispersed fine particles enhance the packing density and reduce the porosity of cementitious materials, leading to improved strength (Damineli et al., 2017). Conversely, low SSA SiMnS particles (e.g., SSA = 60 m^2/kg)

are prone to agglomeration, especially at higher replacement levels. These agglomerates can create weak zones within the cement paste, adversely affecting its overall performance and leading to reduced strength. This observation is in line with findings by Ma et al. (2022), who reported that poor dispersion of supplementary cementitious materials could negatively impact the mechanical properties of cement-based composites.

4.3 Effect of the SSA of SiMnS on the Workability of Concrete

The workability of concrete mixtures, prepared with the mix proportions detailed in Section 3.4.1. Figure 4.3 and Table 4.2 show the variation in slump flow with the SSA of SiMnS at different replacement levels (5%, 10%, 15%, and 20%).

Specifically, C0 represents the control concrete specimen without any cement replacement by SiMnS. The labeling of other concrete specimens follows the convention C*x*-*y*, where *x* denotes the SSA of SiMnS, and *y* represents the percentage of cement replaced by SiMnS. For example, C60-10 indicates a concrete specimen incorporating SiMnS with an SSA of 60 m²/kg and a cement replacement level of 10%wt. The Effect of SSA of SiMnS on the concrete slump is illustrated in Figure 4.3, while Table 4.2 presents the variation in the slump of concrete as a function of the SSA of SiMnS.

Figure 4.3 shows that with the increase in SiMnS SSA, the slump of concrete increases with an increase in SiMnS SSA up to 235 m^2/kg. When the SSA of SiMnS increases to 400 m^2/kg, the slump values decrease. As SSA increases from 60 m²/kg to 400 m²/kg, the slump behavior varies with different SiMnS replacement levels, showing an initial increase at 5%wt and 10%wt, followed by a sharp decrease at higher replacement levels. Notably, the 5%wt specimen consistently achieves a higher slump than the control at all SSA levels, reaching its peak at SSA = 235 m²/kg.

Table 4.2: Variation of the Slump of Concrete with SSA of SiMnS

Specimen	SSA (m^2/kg)	Particle size (µm)	Cement replacement by SiMnS (%wt)	SiMnS (g)	Cement (g)	Slump of concrete (mm)
C0	/	/	0	0	500	170
C60-5	60	41	10	50	450	173
C60-10	60	41	20	100	400	150
C60-15	60	41	30	150	350	69
C60-20	60	41	40	200	300	19
C120-5	120	19	10	50	450	182
C120-10	120	19	20	100	400	165
C120-15	120	19	30	150	350	81
C120-20	120	19	40	200	300	23
C235-5	235	9	10	50	450	195
C235-10	235	9	20	100	400	165
C235-15	235	9	30	150	350	115
C235-20	235	9	40	200	300	35
C400-5	400	4	10	50	450	189
C400-10	400	4	20	100	400	175
C400-15	400	4	30	150	350	109
C400-20	400	4	40	200	300	27

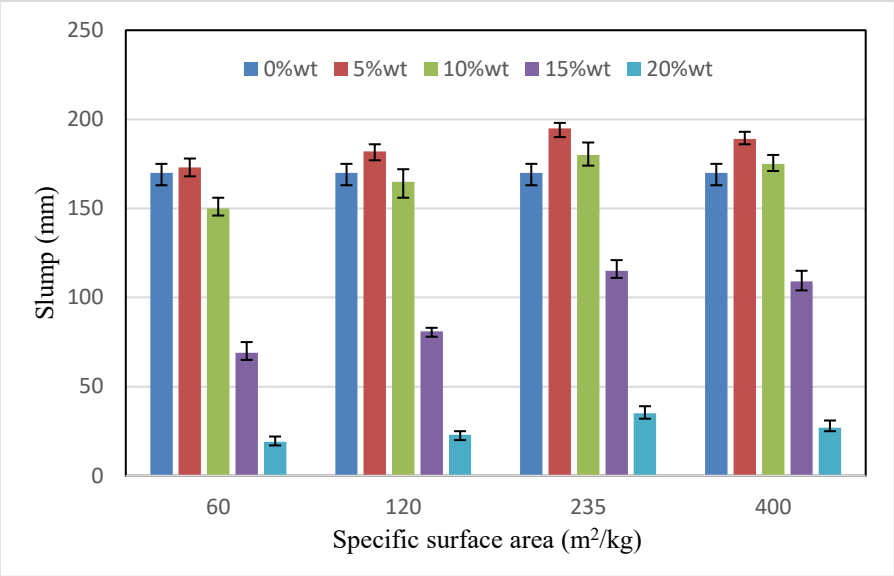

Figure 4.3: Effect of SSA of SiMnS on the Slump of Concrete

At SSA = 60 m²/kg, the slump at 5%wt increases by 1.76% to 173 mm, indicating that a small amount of SiMnS has no detrimental effect on workability. However, at 10%wt, the slump decreases by 13.6% to 150 mm, and a drastic decrease is observed at 15%wt (59.4% reduction to 69 mm). The lowest slump is recorded at 20%wt (88.8% reduction to 19 mm), highlighting the significant impact of excessive SiMnS replacement at low SSA.

At SSA = 120 m²/kg, the 5%wt specimen increases the slump by 7.1% to 182 mm, showing a moderate improvement. At 10%wt, the slump decreases by 8.2% to 165 mm, while at 15%wt, a drastic decrease of 55.5% is recorded at 81 mm. The lowest slump occurs at 20%wt, with an 86.5% reduction to 23 mm, following the trend seen at SSA = 60 m²/kg.

At SSA = 235 m²/kg, the 5%wt specimen reaches the highest slump increase of 14.7% to 195 mm, marking the peak improvement across all cases. At 10%wt, the slump remains relatively high at 165 mm (2.9% reduction from control). However, at 15%wt, the slump

decreases by 32.3% to 115 mm, and at 20%wt, the lowest slump is recorded at 35 mm (79.4% decrease).

At SSA = 400 m²/kg, the 5%wt specimen still records a higher slump than the control, increasing by 11.2% to 189 mm. At 10%wt, the slump is 175 mm (2.9% higher than control), maintaining better workability. However, at 15%wt, the slump drastically decreases by 35.9% to 109 mm, and at 20%wt, the lowest slump is recorded at 27 mm (84.1% reduction), confirming that excessive SiMnS replacement leads to severe workability loss despite increased fineness.

Across all SSA levels, the 5%wt SiMnS specimen consistently exhibits a higher slump than the control, demonstrating that a small amount of SiMnS enhances workability. The peak slump occurs at SSA = 235 m²/kg, where the 5%wt replacement increases slump by 14.7%, indicating that SiMnS at this fineness level optimally balances dispersion and particle packing. However, as SiMnS content increases beyond 10%wt, the slump gradually decreases, and at 15%wt and 20%wt, a sudden and significant reduction is observed, with the lowest slump occurring at 20%wt replacement across all SSA values. Regardless of SSA variation, the 10%wt specimen maintains a slump closest to the control, with a deviation of less than 15 mm in all cases, suggesting that moderate SiMnS replacement has a relatively minor impact on workability. The slump reduction is most severe at SSA = 60 m²/kg (88.8%) and least severe at SSA = 235 m²/kg (79.4%), indicating that higher SSA mitigates workability loss but cannot fully compensate for excessive SiMnS replacement. The trend suggests that while SiMnS can enhance workability at low replacement levels (≤10%wt), particularly at higher SSA, excessive substitution negatively impacts fluidity, making it unsuitable for maintaining high workability in concrete mixes.

The influence of SiMnS SSA on the slump of concrete exhibits a fluctuating trend, initially increasing and subsequently decreasing. When the SSA reaches 235 m²/kg, the slump attains its maximum value of 195 mm, representing a 14.7% increase compared to concrete without SiMnS. However, as the SSA continues to increase or the dosage of SiMnS rises, the slump of concrete gradually declines. The underlying mechanism of this phenomenon can be attributed to the combined effects of the filling effect, the acceleration of the hydration reaction, and variations in water demand.

The first reason of the above phenomenon is the filling effect of the SiMnS particles. An appropriate SSA (235 m²/kg) contributes to improved workability. Finer SiMnS particles can effectively fill the voids between cement particles, enhancing the compactness of concrete and promoting a more uniform distribution of the cement paste. This results in a reduced demand for cement paste, thereby increasing the fluidity of concrete. The filling effect also helps to minimize interparticle friction, leading to an increase in slump. The reduction in workability is attributed to an excessive SSA exceeding 235 m²/kg. When the particle size decreases further (i.e., SSA increases), the specific surface area increases drastically, leading to higher water adsorption. This reduces the amount of free water available in the mixture and increases internal friction within the concrete, thereby decreasing its workability. If the water-to-cement ratio remains unchanged, SiMnS with excessively high SSA will elevate the water demand, ultimately reducing the slump of the concrete.

The second reason for the phenomenon is that the higher SSA accelerates the hydration reaction. An appropriate SSA facilitates the hydration process and increases the slump of the cement mortar. A larger SSA provides more reactive interfaces, accelerating

the cement hydration process and generating more early-stage hydration products, thereby enhancing the initial workability of concrete. This is one of the key reasons why the slump reaches its highest value at SSA of 235 m²/kg. However, an excessively high SSA exceeding 235 m²/kg reduces the availability of free water and decreases workability. Due to the strong water absorption capacity of finer SiMnS particles, they adsorb more free water within the concrete, reducing the amount of available water and subsequently lowering the slump. Additionally, higher SSA of SiMnS accelerates the hydration reaction, causing more water to participate in hydration, further depleting free water content and leading to a decline in concrete fluidity.

In general, the slump of concrete with 235 m²/kg is consistently the highest (14.7% higher than the control group C0), regardless of the replacement ratio. The slumps of concrete with 400 m²/kg, 120 m²/kg, and 60 m²/kg decrease progressively. When the replacement ratio is 5%, the slumps of all four SSA types are higher than that of the control group C0. However, at a 10% replacement ratio, the slumps of concrete with 235 m²/kg and 400 m²/kg remain higher, while those with 120 m²/kg and 60 m²/kg are lower than the control group C0. When the replacement ratio is between 15% and 20%, the slumps of SiMnS concrete are significantly lower than that of the control group C0, with the reduction ratios ranging from 32.4% to 88.9%. As a result, the cement replacement ratio of SiMnS should not be too high (>10%wt). The reasons of this phenomenon are related to the cementitious material content of the SiMnS and the amount of water used for hydration. High SiMnS dosage reduces the proportion of cement in the mix, thereby limiting the availability of cementitious materials necessary for maintaining workability. The reactive components in SiMnS interact with water to produce additional hydration products. This reaction further consumes free water, which is essential for maintaining fluidity in the concrete mixture. The

combined effects of reduced cement content and the excessive consumption of free water due to hydration reactions lead to a drastic decrease in workability, ultimately resulting in a significant reduction in slump. Thus, an excessive SiMnS content (>10%wt) negatively affects slump by reducing the cementitious material content, increasing water demand, and accelerating hydration product formation, all of which contribute to a severe loss of fluidity.

Based on the fluidity results, both 5% and 10% replacement ratios provided adequate workability. The 10% ratio was ultimately selected for subsequent durability tests based on a comprehensive evaluation. Firstly, it maintained sufficient slump (e.g., 175 mm, +2.9% vs. control) for practical casting and compaction. Secondly, and more importantly, it represents a more substantial and practically meaningful level of SiMnS utilization, which aligns with the core objective of maximizing the valorization of this industrial by-product. Finally, it establishes a clear safety margin, given the drastic deterioration in workability observed at 15% and 20% replacement. Therefore, the 10% replacement ratio was chosen as it strikes an optimal balance between achieving significant cement substitution and preserving the essential fresh properties of concrete.

In summary, the SSA of SiMnS affects the slump of concrete through both the filling effect and the promotion of hydration, exhibiting an initial increase followed by a subsequent decrease. The optimal scheme of SSA (235 m^2/kg) and replacement level (10%wt) maintain fluidity and slump compared with the control specimen by effectively filling voids between cement particles and accelerating hydration reactions. Higher SSA (> 235 m^2/kg) leads to increased water absorption, raising the overall water demand of the concrete mix and consequently reducing slump. A significant reduction in slump is observed due to excessive SiMnS content (> 15%wt), which depletes free water and adversely affects cement hydration.

4.4 Effect of SSA of SiMnS on Mechanical Properties of Concrete

The mechanical properties of concrete are closely related to the mechanical properties of cement mortar, so it is also a critical factor in evaluating the quality of concrete and is an essential requirement to ensure engineering application. Section 3.2 shows that when cement replacement by SiMnS is 20%wt, the SiMnS SSA is 235 m^2/kg, and the curing age is 28 days, the compressive strength of cement mortar reaches the maximum 46 MPa. In addition, existing studies have shown that when the SiMnS content is less than 20%, the initial strength of concrete will be affected to a certain extent. However, when the SiMnS content is more than 40%wt, the strength of concrete will show a noticeable trend of decline. Therefore, the strength of concrete can be controlled to some extent by controlling the particle size and the dosage of SiMnS. On this basis, the effects of the SSA of SiMnS, dosage, and water-binder ratio on the mechanical properties of coagulation were discussed.

4.4.1 Effect of SSA of SiMnS on Compressive Strength of Concrete

While ensuring concrete's workability, its compressive strength must also meet the code's requirements. The development of compressive strength over curing time (3, 7, 14, and 28 days) for concrete with different SSA SiMnS is presented in Figure 4.4 to 4.7. These figures illustrate the key trends of strength evolution with age for each SSA group at varying replacement ratios.

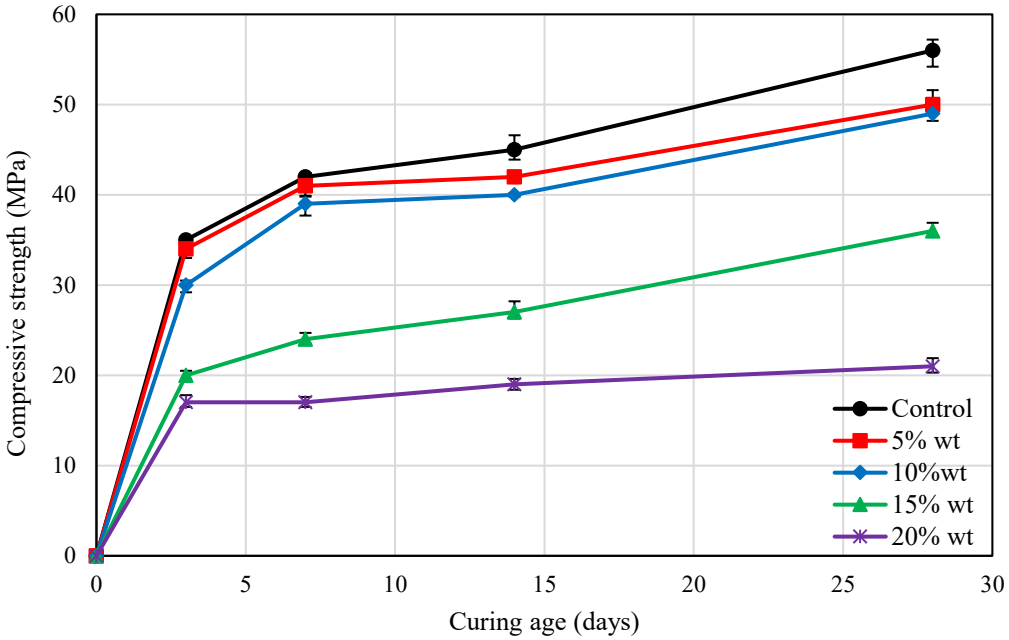

Figure 4.4: Compressive Strength of SiMnS Concrete with SSA of 60 m^2/kg

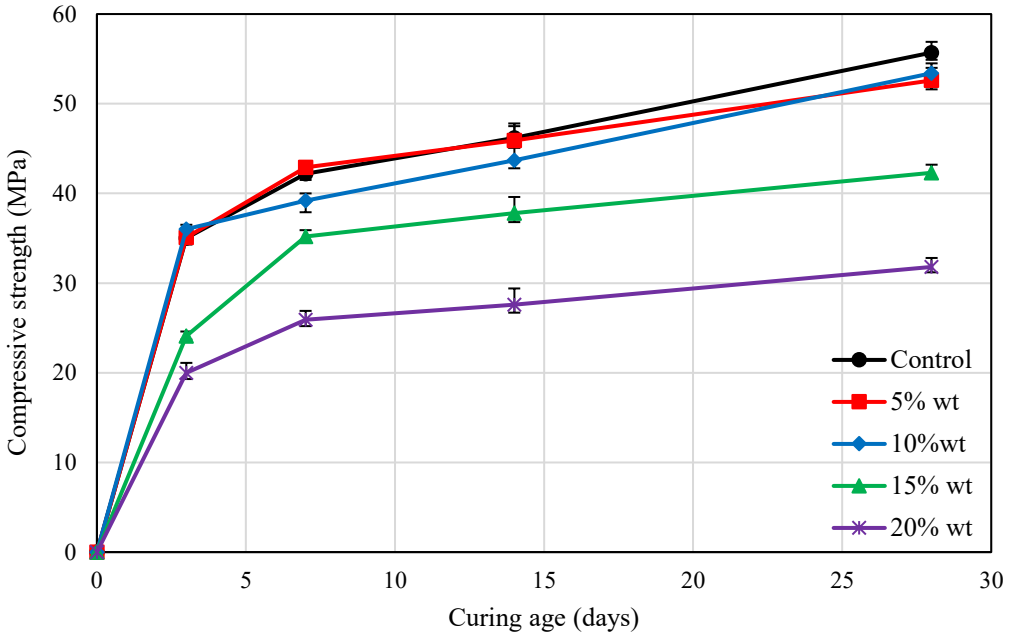

Figure 4.5: Compressive Strength of SiMnS Concrete with SSA of 120 m^2/kg

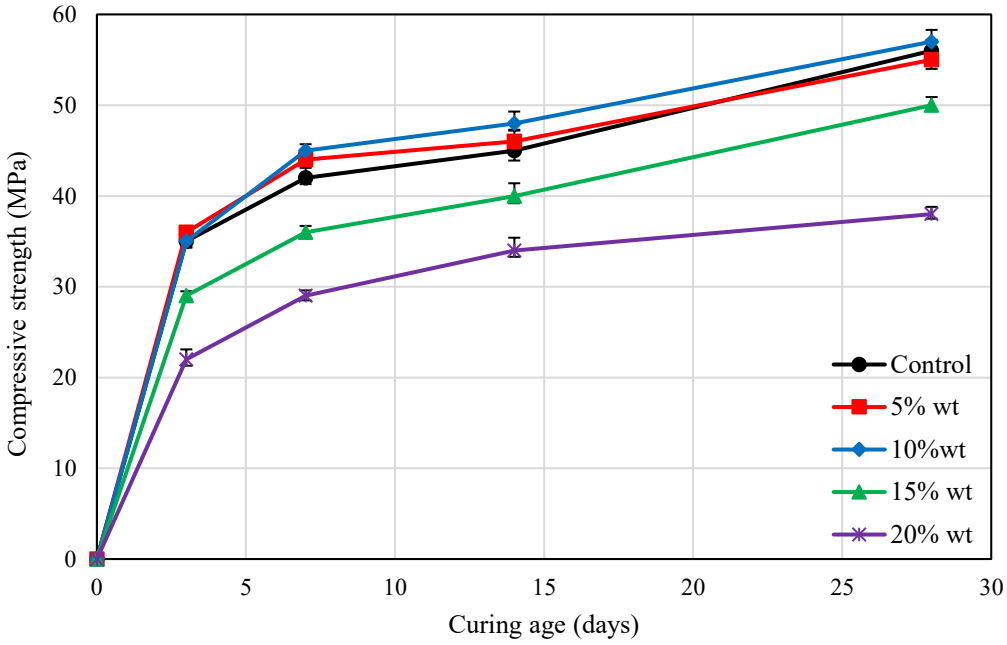

Figure 4.6: Compressive Strength of SiMnS Concrete with SSA of 235 m^2/kg

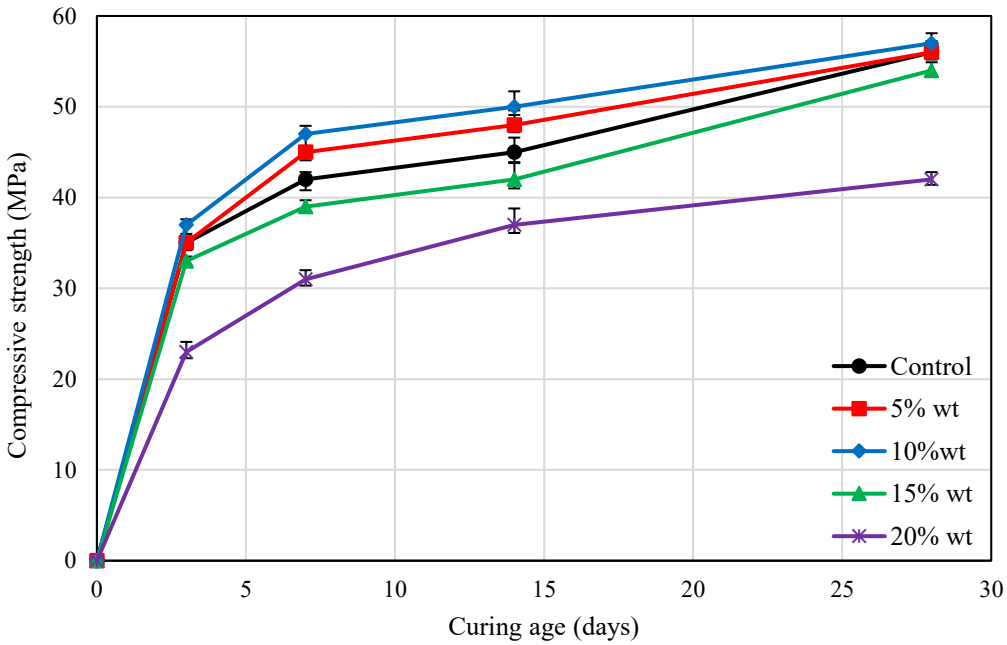

Figure 4.7: Compressive Strength of SiMnS Concrete with SSA of 400 m^2/kg

While ensuring concrete's workability, its compressive strength must also meet the code's requirements. The development of compressive strength over curing time (3, 7, 14, and 28 days) for concrete with different SSA SiMnS is presented in Figure 4.4 to 4.8. These figures illustrate the key trends of strength evolution with age for each SSA group at varying replacement ratios.

At SSA = 60 m^2 /kg (Figure 4.4), the results indicate that low SSA values lead to significant strength reductions when SiMnS is used as a cement replacement, regardless of age. Higher SiMnS content (⩾15%wt) results in severe compressive strength losses (up to 62.50% at 28 days), while lower replacement levels (5–10%wt) mitigate the impact but still cause reductions of 10.71–12.50% at 28 days. The control specimen consistently achieves the highest compressive strength across all ages, suggesting that at this low SSA, SiMnS does not contribute to strength enhancement and may act primarily as an inert diluent. Therefore, SiMnS should not be used at high replacement levels when SSA is low (60 m^2/kg), as it leads to significant performance degradation.

At SSA = 120 m^2 /kg (Figure 4.5), the findings indicate a transitional behavior. Low SiMnS replacement levels (⩽5%wt) can maintain early and long-term strength close to the control, while higher replacements (⩾15%wt) significantly weaken compressive strength over time. The optimal replacement level appears to be 5%wt SiMnS, which shows comparable or slightly improved early-age strength but results in a minor decrease (by 5.36%) at 28 days. The strength decline curves for 15% and 20% replacements are pronounced, indicating that excessive replacement (⩾15%wt) should be avoided due to its substantial negative impact on strength development.

At SSA = 235 m²/kg (Figure 4.6), a clear positive effect of fineness emerges. A 10% SiMnS replacement consistently enhances compressive strength across all curing ages, showing an increase of up to 3.57% at 28 days. The 5% replacement also performs well, maintaining strength comparable to the control. Conversely, higher replacement levels (⩾ 15%wt) lead to substantial and progressive reductions in strength with age, with the 20%wt replacement exhibiting the largest decrease of 32.14% at 28 days. These findings suggest that 10%wt SiMnS is the optimal replacement level for this SSA in maintaining or improving compressive strength, while excessive replacement (⩾15%) should be avoided to prevent significant strength degradation.

At SSA = 400 m²/kg (Figure 4.7), the benefits of high SSA are most apparent. The 10% SiMnS replacement consistently yields the highest strength, confirming it as the optimal replacement level. A 5%wt replacement also maintains strength levels comparable to or slightly higher than the control group. The strength development curves for these two ratios are above or parallel to the control curve. In contrast, higher replacements (⩾15%wt) negatively impact strength development, with their curves diverging negatively from the control over time. The highest recorded improvement (11.90%) occurs at 7 days with 10%wt SiMnS, while the most severe decline (25.0%) occurs at 28 days with 20%wt SiMnS.

In summary, the analysis of strength development curves reveals that when the SSA of SiMnS is low (60 m²/kg), it generally impairs strength development at all replacement ratios. At medium SSA (120 m²/kg), a low replacement (5%) can be tolerated. However, when the SSA ranges from 235 to 400 m²/kg, a cement replacement by SiMnS of 10%wt represents the optimal solution to achieve the best compressive strength development over

time. Under this condition, the compressive strength of SiMnS concrete can be appropriately maintained or enhanced.

This phenomenon can be attributed to the reactivity and physical effects of SiMnS. At lower SSA values, the reactivity of SiMnS is insufficient, and its larger particle size provides a less effective filler effect, impeding its beneficial participation in the hydration reaction and consequently leading to strength reduction. However, at medium and higher SSA values, the finer particles improve packing density and provide more surface area for pozzolanic reactions. An appropriate proportion (e.g., 10%) of such SiMnS can actively engage in the hydration process, thereby improving the microstructure and strength of concrete. Nevertheless, an excessive replacement ratio ($\geqslant$ 15%wt) may dilute the cementitious phase excessively, adversely affecting the continuity and integrity of the hydration product matrix, ultimately resulting in a decrease in compressive strength. Therefore, selecting suitable SSA values and replacement ratios is crucial for achieving a balance between sustainability and concrete performance.

The maximum compressive strength was observed with C235-10 and C400-10, showing a 1.79% increase compared to the control specimen C0 at 28 days. Conversely, the minimum strength was recorded with C60-20, resulting in a 62.50% decrease at 28 days. The results indicate that higher SSA values (235–400 m^2/kg) help mitigate strength loss and even provide enhancement at optimal replacement ratios (10%wt), while lower SSA values (60 m^2/kg) lead to significant strength reductions at all replacement ratios. Consistent with the results of Section 4.3, an excessive cement replacement ratio of SiMnS (>10%wt) not only results in a significant loss of fluidity but also consistently leads to substantial strength

degradation across all SSA values and curing ages, emphasizing the need for a balanced replacement strategy.

4.4.2 Effect of SSA of SiMnS on the Flexural Strength of Concrete

Figures 4.8 to 4.11 present the flexural strength development of concrete incorporating SiMnS. The results indicate a significant divergence in performance based on material parameters: certain combinations of SSA and replacement ratio enhance strength relative to the control, while others lead to a marked reduction.

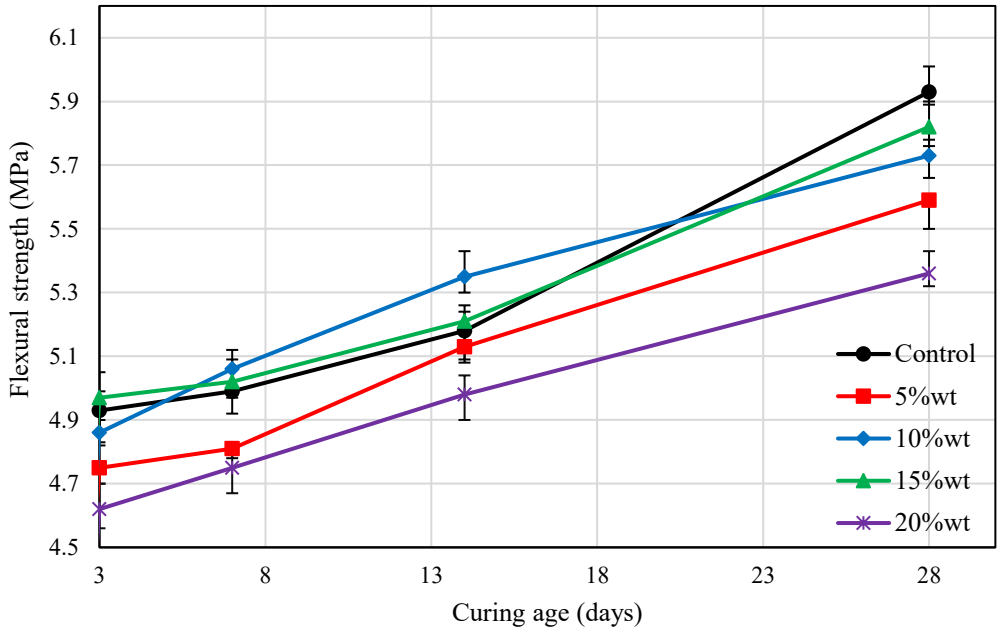

Figure 4.8: Flextural Strength of SiMnS Concrete with SSA of 60 m^2/kg

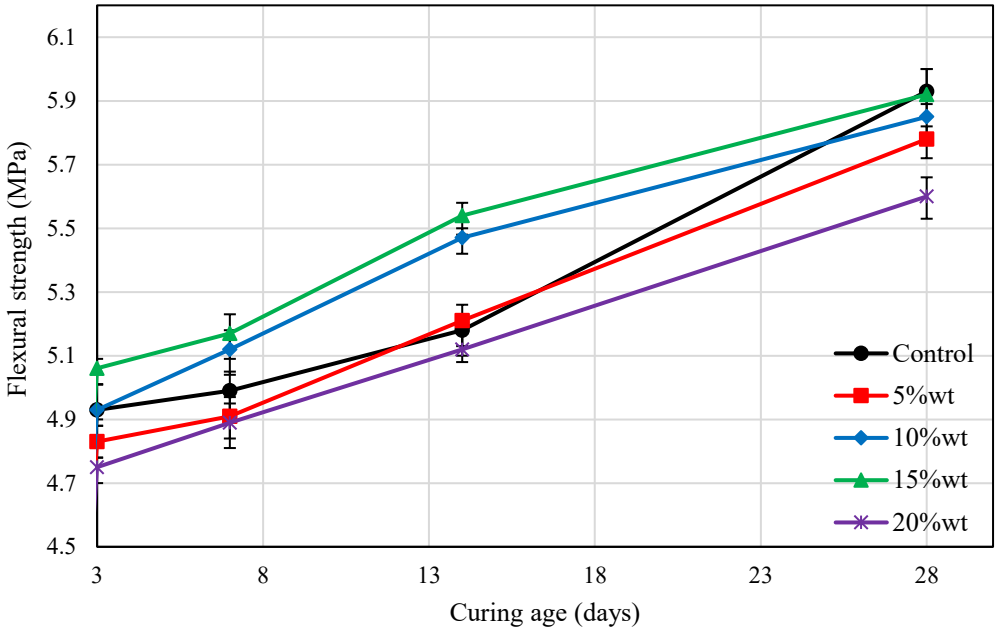

Figure 4.9: Flextural Strength of SiMnS Concrete with SSA of 120 m^2/kg

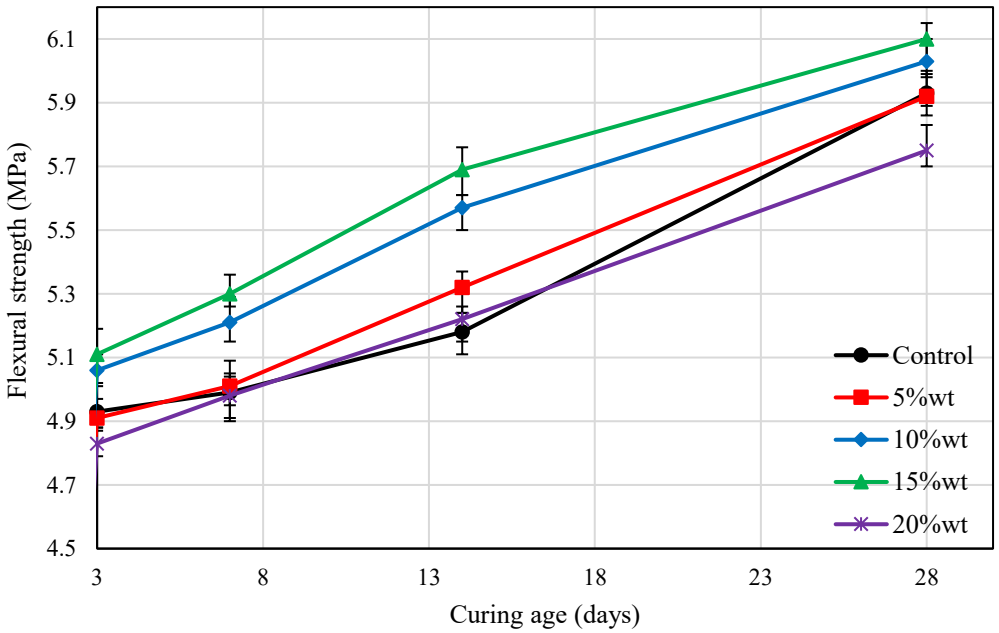

Figure 4.10: Flextural Strength of SiMnS Concrete with SSA of 235 m^2/kg

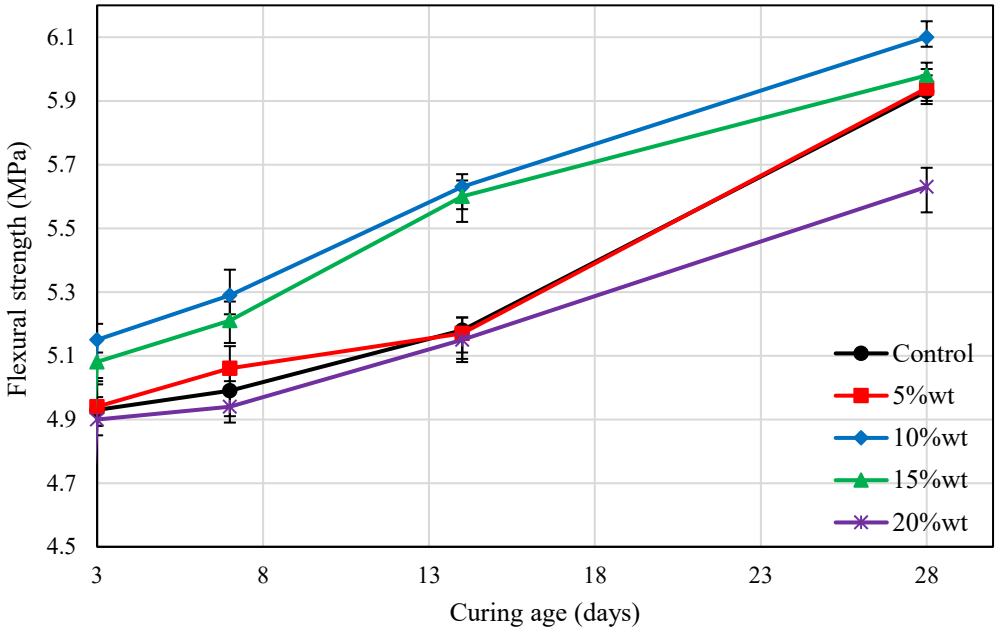

Figure 4.11: Flexural Strength of SiMnS Concrete with SSA of 400 m^2/kg

At SSA = 60 m^2/kg (Figure 4.8), the results indicate that low SSA values generally lead to inferior flexural strength development. While mixtures with 10% and 15% replacement (C60-10 and C60-15) show a slight early-age (7 and 14 days) strength improvement compared to the control (up to +3.28% for C60-10 at 14 days), their strength at 28 days falls below the control. The performance degrades significantly with higher replacement, with C60-20 exhibiting the lowest flexural strength at all ages, being 9.61% lower than the control at 28 days. This suggests that at low SSA, SiMnS may provide limited early physical filler benefits but is insufficient for sustained pozzolanic contribution, leading to long-term strength reduction, especially at high replacement levels.

At SSA = 120 m^2/kg (Figure 4.9), a more complex trend is observed. Moderate replacement levels (10% and 15%) show a clear benefit at early and mid-ages. Specifically, C120-15 and C120-10 achieve peak strength improvements of approximately 6.95% and

5.60%, respectively, over the control at 14 days. However, by 28 days, only C120-15 maintains strength comparable to the control, while others, particularly C120-20 (5.56% lower), show a decline. This indicates that at this moderate SSA, an optimal replacement level (around 10-15%) can enhance early to mid-term strength, but the benefit may diminish or vanish at later ages if the replacement is too high.

At SSA = 235 m^2/kg (Figure 4.10), the benefits of higher SSA become evident. Most mixtures, except the highest replacement (20%), exhibit flexural strengths equal to or exceeding the control across all ages. The optimal performance is observed with C235-15, which shows the highest strength at both 14 days (+9.85%) and 28 days (+2.87%). C235-10 also performs well, showing a 1.86% improvement at 28 days. Conversely, C235-20 shows a negative effect, being 2.87% lower than the control at 28 days. This demonstrates that at this SSA, a replacement level of 10-15% can effectively enhance flexural strength throughout the curing period.

At SSA = 400 m^2/kg (Figure 4.11), the positive effect of high SSA is most pronounced. All mixtures with replacement $\leqslant$15% maintain or improve strength relative to the control. The optimal combination is C400-10, which shows consistent strength gain, reaching a maximum of +8.48% at 14 days and +2.87% at 28 days. C400-15 and C400-5 maintain strength levels close to the control at 28 days. Only C400-20 shows a consistent negative trend, finishing 5.06% lower than the control at 28 days. This confirms that high SSA (400 m^2/kg) combined with a moderate replacement ratio (10%) provides the most reliable enhancement in flexural strength development.

In summary, the analysis of strength development curves reveals that the optimal combinations for enhancing flexural strength are C235-15 and C400-10, both achieving a

maximum strength approximately 2.87% higher than the control (C0) at 28 days. Conversely, the least favorable combination is C60-20, which results in a strength 9.61% lower than the control at 28 days. Higher SSA values (235–400 m²/kg) combined with moderate cement replacement ratios (10–15%wt) are most beneficial for improving flexural strength. In contrast, lower SSA values (e.g., 60 m²/kg) and excessively high replacement ratios (e.g., 20%wt) consistently lead to significant performance degradation, especially at later ages.

This behavior can be attributed to the dual role of SiMnS. Finer particles (higher SSA) improve packing density and provide greater surface area for pozzolanic reactions, leading to better microstructural development and enhanced long-term strength at optimal replacement levels. However, excessive replacement dilutes the cementitious phase regardless of SSA, and low SSA particles lack sufficient reactivity, leading to weaker interfaces and reduced strength over time.

Through comprehensive analysis of the influences of SiMnS concrete's compressive strength (Section 4.4.1) and flexural strength, the optimal combination scheme of SSA and cement replacement ratio can be identified. Specifically, combinations with SSA values of 235 m²/kg or 400 m²/kg and cement replacement ratios by SiMnS of 10%wt or 15%wt exhibit the best overall performance. In terms of slump (Section 4.3), the combination with an SSA value of 235 m²/kg and a cement replacement ratio of 5%wt provides the best fluidity. For compressive strength at 28 days, C235-15 and C400-10 achieve the maximum value, which is 1.79% higher than the control group C0. Regarding flexural strength at 28 days, the same combinations (C235-15 and C400-10) exhibit a strength 2.87% higher than the control group C0. Therefore, combinations with SSA values of 235 m²/kg or 400 m²/kg and cement replacement ratios by SiMnS of 10%wt or 15%wt not only ensure adequate workability but

also provide higher compressive and flexural strength, ensuring the optimal overall performance of the concrete. Conversely, the combination with an SSA value of 60 m²/kg and a cement replacement ratio of 20%wt performs the worst across all performance indicators and should be avoided.

4.4.3 Mechanism Analysis: How SSA Influences the Mechanical Properties of SiMnS Concrete

The distinct trends in compressive and flexural strength observed in Sections 4.4.1 and 4.4.2—specifically, the enhancement of strength with moderate SSA (235–400 m²/kg) and replacement ratio (10–15%wt), and its degradation with low SSA (60 m²/kg) or high replacement ($\geqslant$ 20%wt)—can be systematically explained by the interplay of three fundamental mechanisms: the filling and microstructure densification effect, the hydration and pozzolanic reaction, and the modification of the interfacial transition zone (ITZ).

i. Filling Effect and Microstructure Densification

The particle size distribution of SiMnS, dictated by its SSA, is a primary factor controlling the packing density of the cementitious matrix. Finer particles (higher SSA, e.g., 235–400 m²/kg) act as efficient micro-fillers, occupying the voids between cement grains (Li et al., 2024). This physical densification reduces overall porosity and creates a more continuous solid skeleton, which is crucial for enhancing mechanical strength. This mechanism directly explains the superior performance of mixtures like C235-10 and C400-10 compared to C60-10 at a constant 10% replacement. The denser matrix in high-SSA mixtures facilitates more efficient load transfer and minimizes stress concentration points, leading to higher compressive and flexural strength. Conversely, coarser particles (low SSA, e.g., 60 m²/kg) provide an inefficient filling effect, resulting in a more porous and

heterogeneous matrix that is prone to crack initiation under load, as reflected in the consistently poor performance of the C60 series across all replacement levels.

ii. Hydration Reaction and Pozzolanic Activity

Beyond physical filling, SiMnS participates chemically in the hydration process. Its pozzolanic activity, strongly dependent on SSA, allows it to react with portlandite $Ca(OH)_2$ to form additional calcium silicate hydrate (CSH) and calcium aluminate hydrate (CAH) gels. Higher SSA provides a greater reactive surface area, accelerating this secondary reaction. The additional gel not only contributes directly to strength but also further refines the pore structure. This chemical contribution synergizes with the physical filling effect. It accounts for the continued strength gain observed in optimal mixtures (e.g., C235-15, C400-10) beyond 7 and 28 days, whereas mixtures with low SSA (C60 series) showed stagnated early strength due to slow release of active components, and mixtures with excessive replacement (e.g., C235-20, C400-20) exhibited reduced later-age strength due to cement dilution and potential over-consumption of calcium hydroxide , weakening the cementitious matrix.

iii. Interfacial Transition Zone (ITZ) Modification

The ITZ between aggregate and paste is a critical weak link in concrete. The incorporation of fine, reactive SiMnS particles can significantly improve the ITZ microstructure (Korouzhdeh et al., 2022). These particles can fill the porous space around aggregates and act as nucleation sites for hydration products, leading to a denser and stronger ITZ. This modification is particularly effective with higher SSA materials at optimal dosages. This mechanism is key to understanding the improved flexural strength trends, as flexural performance is highly sensitive to bond strength at the ITZ. The severe strength loss in

mixtures like C60-20 can be partly attributed to a weak, porous ITZ resulting from the combined effects of coarse (ineffective filling), less reactive particles and the increased water demand or poor particle distribution at high replacement levels.

The optimal performance results from a synergy of these mechanisms, which will be further linked to microstructural evidence. The optimal mechanical performance observed for combinations like C235-15 and C400-10 arises from a positive synergy of these three mechanisms: efficient physical packing, substantial pozzolanic reaction, and ITZ densification. However, excessive replacement (⩾20%wt), even with high SSA, disrupts this balance. It leads to an over-dilution of Portland cement, increased water demand for workability (Mehdipour & Khayat, 2017), and potential particle agglomeration, ultimately weakening the overall matrix and the ITZ, as seen in the performance decline of C235-20 and C400-20.

The proposed mechanisms above, derived from the macroscopic strength data, will find direct visual and quantitative support in the microstructural analysis presented later in this thesis. Scanning Electron Microscopy (SEM) observations in Section 4.6 will reveal the contrasting matrix density, porosity, and ITZ morphology between high-performance (e.g., C400-10) and low-performance (e.g., C60-20) mixtures, providing conclusive evidence for the filling effect and ITZ modification discussed here.

In summary, the mechanical properties of SiMnS concrete are governed by a complex interaction between physical filling, chemical reaction, and interfacial enhancement. Moderate SSA (235–400 m^2/kg) and replacement ratio (10–15%wt) optimize these interactions, leading to enhanced strength. Deviating from this optimum, either through low SSA (ineffective filling and low activity) or high replacement (cement dilution and ITZ

weakening), negatively impacts one or more of these mechanisms, resulting in inferior performance. This mechanistic framework cohesively explains all experimental observations and provides a scientific basis for optimizing SiMnS utilization in concrete.

4.5 Effect of SiMnS SSA on Concrete Durability

n this thesis, concrete durability is analyzed in terms of freeze-thaw resistance, chloride ion penetration resistance, and sulfate corrosion resistance. Based on workability and mechanical performance tests, the optimal mixture is achieved with 10 %wt SiMnS replacement of cement, as shown by slump, compressive strength, and flexural strength results. Therefore, a 10 %wt SiMnS replacement level is selected for subsequent durability tests to investigate the effect of SSA on SiMnS concrete performance. Unless otherwise stated, error bars in all figures represent the mean ± standard deviation based on three independent replicates (n = 3).

4.5.1 Effect of SiMnS SSA on Freeze-Thaw Resistance of Concrete

The SSA of SiMnS greatly influences the compactness of concrete and even plays a decisive role. Therefore, it is necessary to explore the influence of SiMnS SSA on the freeze-thaw resistance of concrete. This study analyses the concrete mass loss rate and compressive strength loss rate under freeze-thaw cycle conditions.

(1) Concrete mass loss rate under freeze-thaw cycle conditions

The concrete specimens were divided into five groups: F0, F60-10, F120-10, F235-10, and F400-10. The SiMnS content of the control specimen F0 is 0, and the SiMnS content of the other four groups replaces 10%wt cement at an equal mass percentage. The SiMnS SSA of F60-10, F120-10, F235-10, and F400-10 are 60 m^2/kg, 120 m^2/kg, 235 m^2/kg, 400

m^2/kg, respectively. Under the concrete freeze-thaw cycle test conditions in Chapter 3, the mass of the specimens with freeze-thaw cycles of 0 to 300 times was measured, and the mass loss rate was calculated every 25 measurements. Based on this, the effect of SiMnS SSA on the mass loss rate of concrete under freeze-thaw cycle conditions was analyzed. The test results are shown in Figure 4.12.

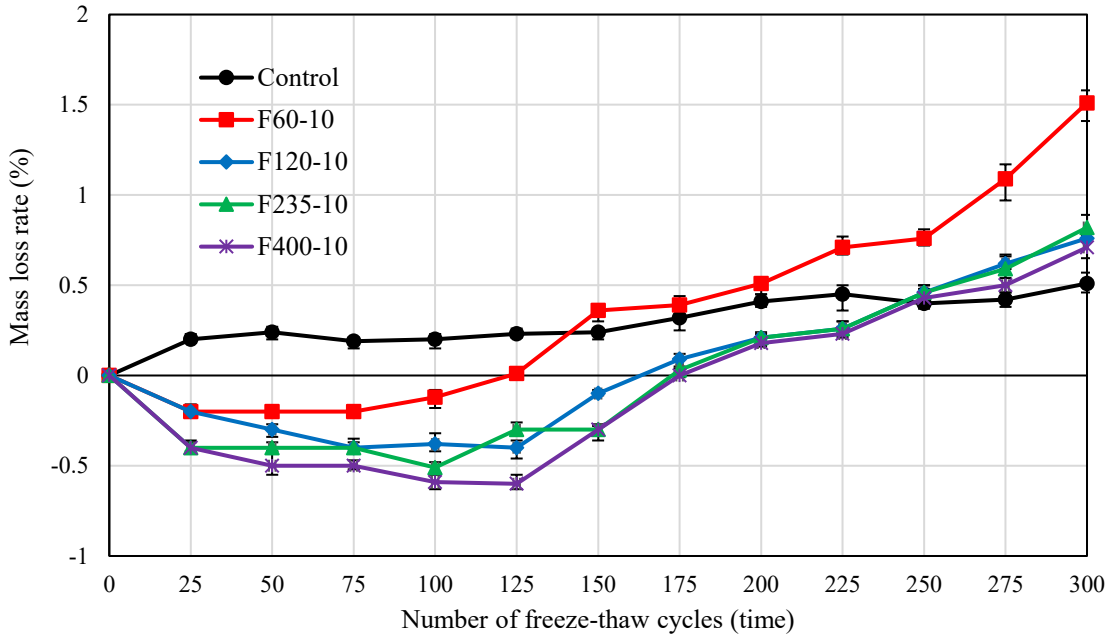

Figure 4.12: Effect of SSA of SiMnS on the Mass Loss Rate of Concrete under Freeze-thaw Cycles

In general, with the increase in the number of freeze-thaw cycles, the mass loss rate of concrete in groups F60-10, F120-10, F235-10, and F400-10 with the addition of SiMnS showed a trend of initial decrease followed by later increase, that is, the mass first increased and then decreased; where before 125 freeze-thaw cycles, the mass of SiMnS concrete increased, and after 175 freeze-thaw cycles, the mass of SiMnS concrete began to decrease. With the increase in freeze-thaw cycles, the F0 benchmark group without adding SiMnS was always above 0.00 and always maintained an upward trend; that is, the mass continually decreased. In the early stage of the freeze-thaw cycle, the smaller the SiMnS particle size,

the more significant the increase in the mass of the SiMnS concrete; in the later stage of the freeze-thaw cycle, the larger the SiMnS SSA, the greater the mass loss of the SiMnS concrete.

From the details, the mass loss rate of the F0 benchmark group was between 0.19% and 0.24% when the freeze-thaw cycles were between 25 and 150, and the mass loss did not fluctuate much. Between 150 and 300 freeze-thaw cycles, the mass loss rate increased from 0.24% to 0.51%, and the mass loss growth rate accelerated. When the number of freeze-thaw cycles was less than 100, the mass of the F60-10, F120-10, F235-10, and F400-10 groups increased, and the mass increase rate of each group reached 0.12%, 0.38%, 0.51%, and 0.59%, respectively. The mass of the F60 group concrete began to decrease after 125 freeze-thaw cycles, and the mass loss rate reached the maximum value of 1.51% after 300 freeze-thaw cycles; the mass of the F120-10, F235-10, and F400-10 groups concrete began to decrease after 175 freeze-thaw cycles, and the mass loss rates after 300 freeze-thaw cycles were 0.76%, 0.82%, and 0.71%, respectively. From this trend, if the freeze-thaw time is long enough and the freeze-thaw cycles are frequent enough, the quality loss of concrete will continue to increase. As for the influence of SiMnS SSA, from the overall trend, before 250 freeze-thaw cycles, the increase of SiMnS SSA is conducive to reducing the quality loss of SiMnS concrete; after 250 freeze-thaw cycles, the addition of SiMnS is not conducive to the quality maintenance of concrete. At this stage, the smaller the SiMnS SSA, the greater the quality loss of concrete.

(2) Concrete compressive strength loss rate under freeze-thaw cycle conditions

To determine the compressive strength loss rate, a separate but identical set of specimens for each mix proportion (F0, F60-10, F120-10, F235-10, F400-10) was prepared. These specimens were dedicated solely for destructive compressive strength testing at

predefined freeze-thaw intervals (0, 50, 100, 150, 200, 250, and 300 cycles). This means that after being subjected to a specific number of cycles (e.g., 50 cycles), a set of specimens was removed from the freeze-thaw chamber and tested for compressive strength. Different sets of specimens were used for testing at different cycle numbers; the same specimens were not subjected to strength testing and then returned for further freeze-thaw cycling. This approach ensures that the measured strength at each interval reflects the damage accumulated up to that point without the confounding effect of pre-existing damage from the compression test itself.

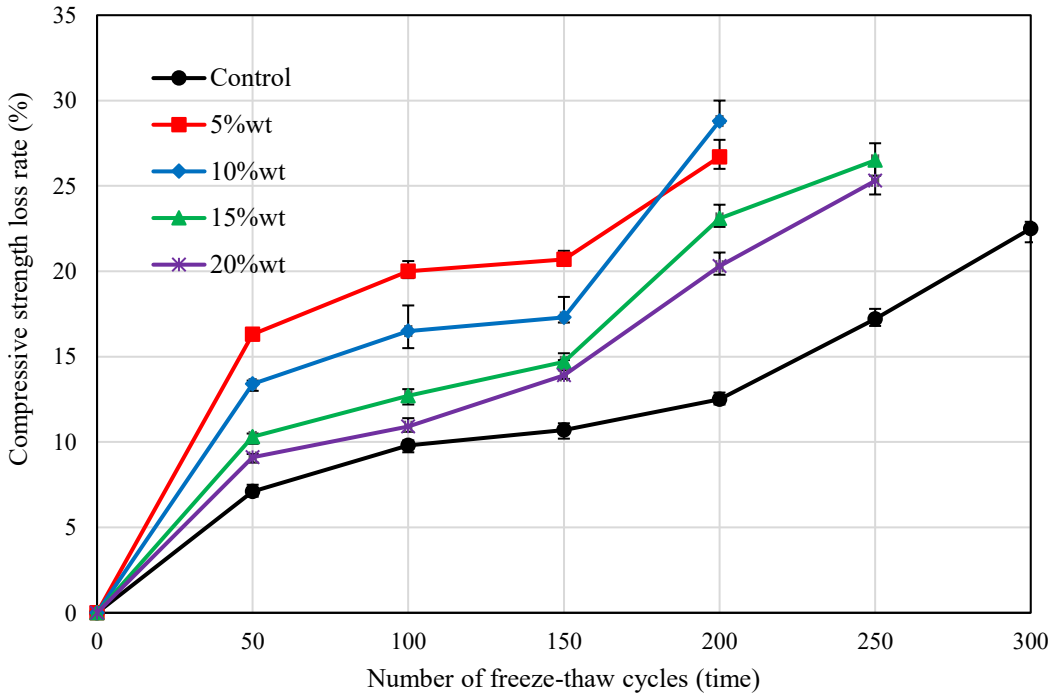

Figure 4.13: Effect of SSA of SiMnS on the Compressive Strength Loss Rate of Concrete under Freeze-thaw Cycles

While testing the compressive strength loss rate of concrete, the strength loss of five groups of test blocks, F0, F60-10, F120-10, F235-10, and F400-10, and the compressive strength after 0, 50, 100, 150, 200, 250, and 300 freeze-thaw cycles were tested, respectively. The test results are shown in Figure 4.13.

Overall, with the increase in the number of freeze-thaw cycles, the test curves of the five groups of test blocks all showed an upward trend; that is, the loss rate of compressive strength continued to increase. After 300 freeze-thaw cycles, the loss rate of compressive strength of the F0 benchmark group reached 22.5% but did not reach 25%, so its frost resistance grade was above 300 cycles. In contrast, all SiMnS-modified concrete mixtures reached the 25% strength loss threshold earlier: the F60-10 and F120-10 groups exceeded it after 200 cycles (with measured losses of 26.7% and 28.8%, respectively, corresponding to a frost resistance grade of 200 cycles), and the F235-10 and F400-10 groups exceeded it after 250 cycles (with losses of 26.5% and 25.3%, respectively, corresponding to a grade of 250 cycles).

The observation that the control concrete (F0) exhibited superior frost resistance compared to all SiMnS mixtures can be attributed to several interconnected mechanisms arising from the cement replacement:

Firstly, the incorporation of SiMnS, despite its potential filling effect, alters the pore structure. Finer SiMnS particles can increase the volume of very fine pores or the overall specific surface area of the pore system, potentially leading to higher water absorption and saturation during freeze-thaw testing. Since damage is driven by the expansion of freezing pore water, a higher saturation degree typically results in greater internal stress and more severe damage.

Secondly, replacing 10% of cement with SiMnS (a less reactive material) dilutes the primary cementitious phase. This can result in a slightly higher porosity and a potentially weaker interfacial transition zone (ITZ) before significant pozzolanic reaction occurs, creating a matrix inherently more susceptible to crack initiation under freeze-thaw stresses.

Finally, under the specific conditions of cyclic freezing and thawing, the beneficial effects of SiMnS (filling, pozzolanic reaction) that enhance standard mechanical strength may be counteracted. Stress concentration around harder, unreacted SiMnS particles, or differences in thermal expansion coefficient between the particles and the cement paste, can become pronounced, creating preferential sites for microcrack initiation.

From Figure 4.12 and Figure 4.13 collectively, it can be seen that due to the slow development of concrete mass loss rate, the frost resistance of SiMnS concrete should be primarily evaluated by the loss rate of compressive strength. The strength loss process can be analyzed in two stages. In the first stage (before approximately 150 freeze-thaw cycles), the strength loss is primarily due to the formation of microcracks from freeze-thaw pressure. In the second stage (after more than 150 cycles), accumulated damage leads to crack interconnection and accelerated strength loss, marking the destruction stage.

The figures show that as the SSA of SiMnS increases (particle size decreases), the early compressive strength loss rate decreases, owing to the enhanced filling effect and pozzolanic activity which create a denser matrix resistant to initial microcracking. However, with the increase in freeze-thaw cycles, the relative advantage conferred by higher SSA diminishes. This is why the difference between the F235-10 and F400-10 groups at the final testing interval is small (1.2%). The long-term frost resistance is dominated by the factors mentioned above (water absorption, matrix dilution).

In summary, under water freeze-thaw action, the frost resistance performance, ranked from best to worst based on the number of cycles to reach 25% strength loss, is: F0 (Control) > F400-10 $\approx$ F235-10 > F120-10 > F60-10. This indicates that ordinary Portland cement concrete exhibits superior frost resistance under these testing conditions. Among SiMnS-

modified concretes, those with higher SSA (400 m²/kg and 235 m²/kg) perform better than those with lower SSA (120 m²/kg and 60 m²/kg), as the densification effect partially mitigates the inherent vulnerability introduced by the cement replacement. The overall lower frost resistance of SiMnS concretes compared to the control highlights the need for further optimization, possibly with air-entraining agents or lower replacement ratios, to improve durability under cyclic freezing conditions.

4.5.2 Effect of SiMnS SSA on Concrete Resistance to Chloride Ion Penetration

The main factor of structural damage of concrete is steel corrosion, and chloride ion penetration is the most important cause of steel corrosion. Chloride is a highly corrosive medium that will affect the performance of concrete. Chloride ions from the external environment can enter concrete through diffusion and convection, react with cement hydration products to lower the pH value, and cause corrosion. At the same time, when chloride ions in the external environment enter the concrete interior, they corrode the passivation film on the surface of the steel bar, destroy its protective function, and cause the steel bar to rust and corrode. The volume of the rusted steel bar will expand, and when severe cracks occur, it will endanger the entire structure.

Referring to the provisions of standard for long-term performance and durability test methods for plain concrete (GB/T50082, 2009), the test uses the electric flux method to complete the chloride ion corrosion resistance test of SiMnS concrete. According to the test, the SiMnS dosage is 10%, the SSA of the four types of SiMnS are 60 m^2/kg, 120 m^2/kg, 235 m^2/kg, 400 m^2/kg, and the electric flux data of the specimens cured to 28 days and 56 days are shown in Table 4.3.

The SiMnS concrete and the reference concrete were tested for chloride ion penetration resistance, and the test results are shown in Figure 4..

Table 4.3: Electric Flux of SiMnS Concrete under Chloride Ion Penetration

Specimen	SSA (m^2/kg)	Cement replacement by SiMnS (%wt)	28-day Electric flux（C）	Basic increment（%）	56-day Electric flux（C）	Basic increment（%）
C0	/	0	2150	/	1520	/
C60-10	60	10	2030	5.58	1122	16.18
C120-10	120	10	1840	14.42	786	48.29
C235-10	235	10	1723	19.86	680	55.26
C400-10	400	10	1702	20.84	653	57.04

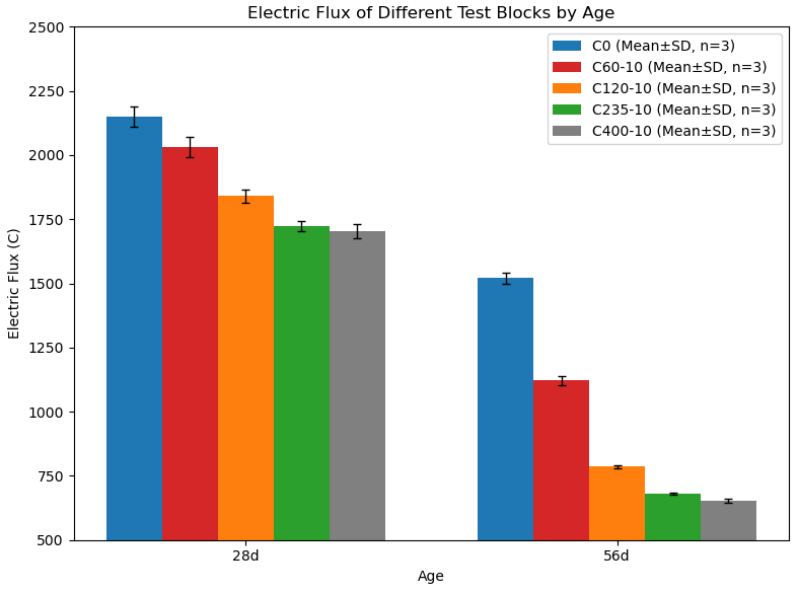

Figure 4.14: Electric Flux at 28-day and 56-day Curing Ages of SiMnS Concrete

As can be seen from the Figure 4.14, SiMnS admixture has a significant improvement in the chloride ion penetration resistance of concrete. Overall, as the SSA of SiMnS

continues to increase (from 60 m^2/kg to 400 m^2/kg), the electric flux of concrete decreases, and the ability to resist chloride ion erosion continues to improve.

There are three primary reasons for the occurrence of this outcome. Firstly, the larger the SSA of SiMnS, the smaller its particle size, which can be better mixed with cement and other components to fill the voids in concrete, thereby improving the density of concrete (Mehdipour et al., 2017). Secondly, the volcanic ash effect of SiMnS can continuously react with $Ca(OH)_2$ in the hydration product to form a hydrated calcium silicate gel. The secondary hydration forms a low-alkalinity CSH gel with a particular adsorption effect on chloride ions (Thomas et al., 2012). Finally, the dense filling effect and volcanic ash effect of SiMnS admixture, the filling effect of the tiny particles of the admixture and the secondary hydration reaction can effectively reduce the porosity of the hardened paste in concrete and change the pore structure of concrete, making the concrete structure dense (Khan et al., 2011). After the density is improved, the porosity of the concrete is reduced, which prevents the formation of permeation channels and makes it more difficult for chloride ions to penetrate. Therefore, the SiMnS concrete will have an enhanced ability to resist chloride ion corrosion with increasing SSA.

In terms of details, when the concrete age is 28 days, the SSA of SiMnS increases from 60 m^2/kg to 120 m^2/kg, and the concrete electric flux decreases the most, which is 8.84%. When the SSA of SiMnS increases from 235 m^2/kg to 400 m^2/kg, the concrete electric flux decreases the least, which is 0.98%. Currently, the SSA of SiMnS has little effect on the electric flux. Similarly, when the concrete age is 56 days, the SiMnS SSA increases from 60 m^2/kg to 120 m^2/kg, and the concrete electric flux decreases the most, which is 32.11%. When the SiMnS SSA increases from 235 m^2/kg to 400 m^2/kg, the concrete

electric flux decreases the least, which is 1.78%. The SiMnS SSA has little effect on the electric flux.

The occurrence of these details can be attributed to three primary reasons. Firstly, when the curing time increases from 28 days to 56 days, the decrease in the size of the SiMnS SSA is more conducive to the longer reaction time of the active components of the SiMnS with the cement hydration products, and more secondary hydration products are generated. These products can further fill the tiny pores in the concrete, improve its density, prevent the formation of permeation channels, and enhance its ability to resist chloride ion corrosion (Snellings, 2016). Secondly, when the SiMnS SSA is too big (greater than 120 m^2/kg), the particle size has little effect on the electric flux. This is because the too-small particle size causes the surface of the SiMnS particles to hydrate quickly, forming a more rigid shell, which prevents water from penetrating the particles, resulting in an incomplete internal hydration reaction (Yang et al., 2014). In this case, the pores inside the concrete are not conducive to being effectively filled but instead form tiny channels, which may increase the risk of chloride ion penetration in long-term use. Finally, SiMnS particles with too small a particle size may increase the mixture's viscosity, affect the workability of the concrete, and make it challenging to ensure the uniformity and density of the concrete during construction. In this way, there may be insufficiently filled pores in local areas, which may become a weak link for chloride ion penetration (Zhou et al., 2011).

Overall, the experimental data conclusively demonstrate that increasing the SSA of SiMnS significantly enhances the concrete's resistance to chloride ion penetration. As the SSA increased from 60 to 400 m^2/kg, the electric flux at both 28 and 56 days decreased monotonically. A key performance threshold was observed at an SSA of 120 m^2/kg, where

the permeability rating improved from "Moderate" to "Low" at 28 days and reached "Very Low" at 56 days according to GB/T 50082-2009. However, a law of diminishing returns was evident; the most substantial improvement occurred when SSA increased from 60 to 120 m^2/kg, while further increases to 235 and 400 m^2/kg yielded progressively smaller gains. This suggests that while higher SSA is beneficial, an optimal range likely exists around 120-235 m^2/kg for the tested replacement ratio (10%), beyond which additional refinement may not be cost-effective. Furthermore, the superior long-term performance (greater percentage reduction at 56 days) of mixtures with higher SSA underscores the sustained pozzolanic activity contributing to ongoing pore structure refinement.

4.5.3 Effect of SiMnS SSA on Concrete Resistance to Sulphate Attack

Many environmental factors can affect concrete's durability, including sulphate attack, which is also the most complicated and harmful factor. Sulphate attack is related to environmental water erosion. When sulphate ions in the external environment enter the concrete and react with hydration products, they destroy the internal structure of the concrete, causing expansion, cracks, and peeling, reducing the strength and viscosity of the concrete, or even completely losing it.

Sulphate attack on concrete is essentially the ingress of ions from the ambient water into the concrete, which react chemically with $Ca(OH)_2$ in the concrete to form insoluble substances. These insoluble substances absorb a large amount of water and expand in volume, which harms the entire structure of the concrete. Sulphate attack on concrete is divided into two types: external and internal. Internal attack is the addition of sulphate-containing admixtures and aggregates during concrete production. These materials allow sulphate inside the concrete to cause corrosion without diffusion. However, the internal corrosion rate will

gradually decrease due to the limited number of internal ions. External corrosion depends on the diffusion of ions and only causes corrosion after penetrating the concrete, which in turn leads to a decrease in the quality of the concrete. Sulphate corrosion is an important indicator for measuring concrete structures' durability. Like the freeze-thaw resistance of concrete, it can also cause substantial economic losses.

The sulphate corrosion resistance test was conducted under the specification. Three specimens in each group were immersed in tap water after the initial standard curing for 28 days as the control group. The other group was immersed in a 5% Na_2SO_4 solution. The test ages were 30 days, 60 days, 90 days, 120 days, 150 days, and 180 days. In addition, the Na_2SO_4 corrosion solution was replaced regularly within the specified age to ensure that the concentration of the corrosion solution remained constant. After reaching the specified age, the mass loss rate and compressive strength were measured, and the mass loss rate and sulfate resistance coefficient were calculated according to Equation 4.1 and Equation 4.2, respectively.

$$W_{\mathrm{L}} = \frac{m_0 - m_{\mathrm{t}}}{m_0} \times 100\% \qquad \text{Equation 4.1}$$

where W_{L} = the mass loss rate of the specimen after immersion for t days; m_0 = the initial mass of the specimen before immersion; m_{t} = the mass of the specimen after immersion for t days.

$$K_f = \frac{f_{cn}}{f_{c0}} \times 100\% \qquad \text{Equation 4.2}$$

in which K_f = the sulfate resistance coefficient after immersion for n days; f_{c0} = the compressive strength of the concrete specimens in the control group of the same age (MPa), accurate to 0.1MPa; f_{cn} = the compressive strength of the specimens after n days of sulphate corrosion resistance (MPa), accurate to 0.1MPa.

The impending discussion analyses the concrete mass loss rate and compressive strength loss rate under sulphate corrosion conditions.

(1) Concrete mass loss rate under sulphate corrosion conditions

The compactness of concrete will affect the diffusion of SO_4^{2-} ions and the fineness of manganese slag determines the compactness of concrete to a large extent. The experiment selected concrete without SiMnS as the reference specimen C0, and four types of manganese slag with SSA of 60 m^2/kg, 120 m^2/kg, 235 m^2/kg, and 400 m^2/kg were added to concrete (C60-10, C120-10, C235-10, and C400-10) at a level of 10%wt to replace cement, to study the effect of SiMnS SSA on the sulphate corrosion resistance of SiMnS concrete. The mass loss chart is shown in Figure 4.15 and Table 4.4.

In general, in the corrosive environment of Na_2SO_4 solution, before the concrete specimens were immersed for 90 days, as the SSA of SiMnS increased, the particle size of SiMnS decreased, and the concrete mass gradually increased. The decrease in particle size accelerated the increase in concrete mass. Among them, at 60 days, the mass loss rate of 400 m^2/kg of SiMnS concrete is -0.55%, reaching the maximum absolute value. After the concrete specimens were immersed for 120 days, the concrete of the control specimen (without SiMnS) cracked and showed positive mass loss, while the concrete containing SiMnS continued to increase in mass, and the smaller the SiMnS slag particle size, the greater the mass increase. When the concrete specimens were immersed for 150 days, the

mass loss rate of 120 m^2/kg of SiMnS concrete was the smallest at 0.01%. When the concrete specimens were immersed for 180 days, all concrete specimens showed cracking and positive mass loss. The larger the SiMnS SSA, the smaller the SiMnS particle size, the lower the mass loss rate; at the same time, the mass loss of SiMnS concrete is 0.39% less than that of the control specimen (without SiMnS).

Table 4.4: Sulphate Corrosion Mass Loss Rate of SiMnS Concrete

Specimen	SSA (m^2/kg)	Cement replacement by SiMnS (%wt)	Mass loss rate (%)					
			30d	60d	90d	120d	150d	180d
C0	/	0	-0.04	-0.01	-0.05	0.11	0.12	0.39
C60-10	60	10	-0.12	-0.06	-0.08	-0.09	0.11	0.31
C120-10	120	10	-0.19	-0.20	-0.16	-0.12	0.01	0.33
C235-10	235	10	-0.34	-0.49	-0.40	-0.41	-0.22	0.13
C400-10	400	10	-0.41	-0.55	-0.50	-0.47	-0.25	0.08

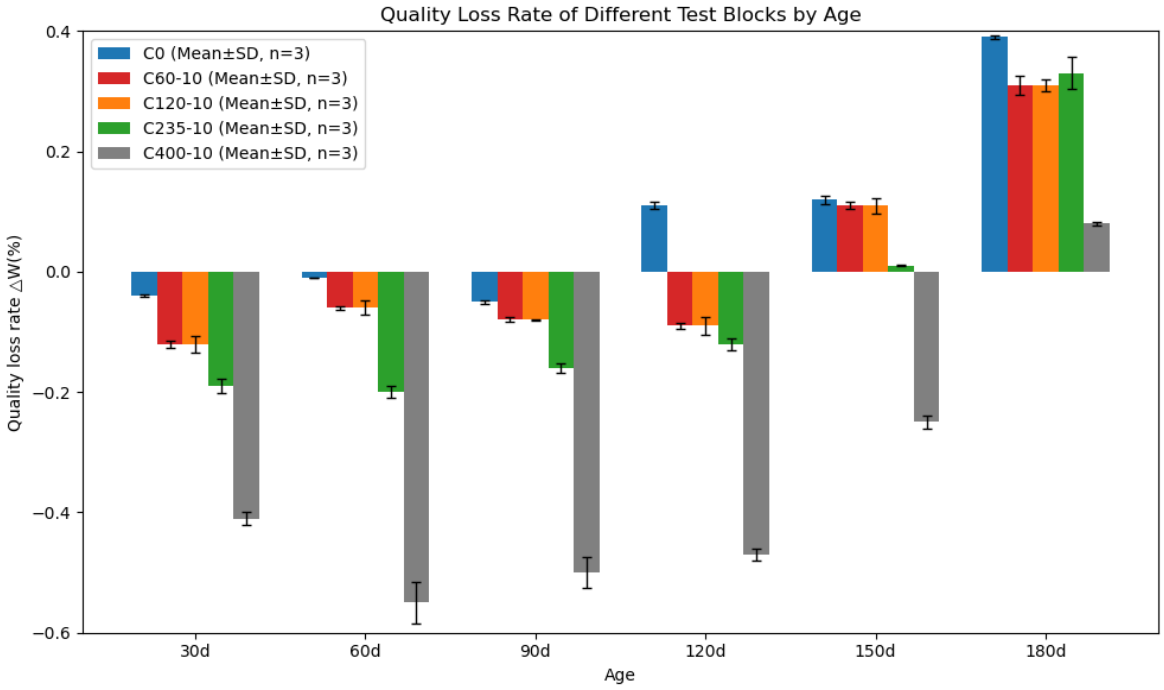

Figure 4.15: Effect of SiMnS SSA on Concrete Sulphate Corrosion Mass Loss Rate

From the details, the quality of the control specimen (without SiMnS) concrete did not change much before 90 days of immersion, and the mass loss rate is less than -0.05%. The mass loss rate increased after immersion for more than 90 days, reaching about 0.11% at 120 days and 150 days. The mass loss rate at 180 days reached 0.41%, an increase of nearly 4 times. The mass loss rate of SiMnS concrete shows a trend of initial decrease and later increase with the immersion age, which was the same as that of the control specimen. The mass of the C60-10 and C120-10 SiMnS concretes increased before immersion for 120 days, and the mass loss rates ΔW at 120 days are -0.09% and -0.12%, respectively; the mass loss rate accelerated after 120 days, and the mass loss after immersion for 180 days reaches 0.31% and 0.33% respectively. The mass of the C235-10 and C400-10 groups increased rapidly before 60 days of immersion, and the mass loss of the two groups reached a peak of -0.49% and -0.55%, respectively, after 60 days of immersion. Mass loss gradually increased after 60 days, reaching 0.13% and 0.08% at 180 days.

The results show that in the corrosion environment of Na_2SO_4 solution, the size of the SiMnS SSA affects the sulphate resistance of concrete. SO_4^{2-} in the corrosive solution penetrates the SiMnS concrete. The smaller the SiMnS particle size, the larger the SSA, the higher the hydration activity, and the faster the reaction with SO_4^{2-}, which is conducive to the generation of insoluble salt products that expand in volume and compact the voids inside the concrete, resulting in an increase in the mass of the concrete before 120 days of immersion. As the corrosion reaction continues, the volume of insoluble salt products expands and increases. After 150 days of immersion, the expansion stress exceeds the bearing limit of the concrete and causes microcracks in the concrete. The generation of microcracks connects the interior and surface of the concrete, prompting SO_4^{2-} to continue to penetrate the concrete through the microcracks and generate new insoluble salt products inside. The filling and compacting process continues, resulting in expansion cracking and mass loss of the concrete. In this process, the smaller the SiMnS particle size, the more conducive it is to reducing mass loss.

(2) Sulfate resistance coefficient of concrete under sulphate corrosion conditions

Five groups of concrete specimens were subjected to sulphate corrosion resistance tests. Table 4.5 shows the test results of the sulfate resistance coefficient of concrete at 30 days, 60 days, 90 days, 120 days, 150 days, and 180 days, and Figure 4.16 shows the trend of the coefficient.

In general, in the Na_2SO_4 solution corrosion environment, within the same age, as the SiMnS SSA increases, the sulfate resistance coefficient K_f of concrete continues to increase, and the sulfate resistance coefficient increases with the increase of SiMnS SSA. When the concrete specimens were immersed for 90 days, the sulfate resistance coefficient

K_f value of 400 m^2/kg SiMnS concrete was the maximum value of 109.9% among the five groups of specimens. Compared with the control specimen C0, before 90 days, the addition of SiMnS is beneficial to improving the sulfate resistance coefficient of concrete. The larger the SiMnS SSA, the more significant the increase in sulfate resistance coefficient; after 120 days, adding SiMnS improves the concrete's sulfate resistance coefficient. The larger the SiMnS SSA, the closer the sulfate resistance coefficient K_f is to 1. However, with the continuous increase of age, the gain effect of SiMnS continues to decrease. After 180 days, 60 m^2/kg and 120 m^2/kg SiMnS concrete were more severely corroded by sulphate, and their sulfate resistance coefficient is lower than that of the control specimen.

Table 4.5: Sulfate Resistance Coefficient of SiMnS Concrete

Specimen	**SSA (m^2/kg)**	**Cement replacement by SiMnS (%wt)**	**Sulfate Resistance Coefficient K_f (%)**					
			30d	**60d**	**90d**	**120d**	**150d**	**180d**
C0	/	0	101.1	99.2	98.8	95.3	92.1	92.0
C60-10	60	10	102.3	102.7	102.2	93.5	91.0	88.5
C120-10	120	10	104.1	104.8	105.9	97.1	93.9	90.9
C235-10	235	10	107.3	106.9	108.8	100.0	96.5	93.0
C400-10	400	10	108.5	109.2	109.9	102.6	98.9	94.9

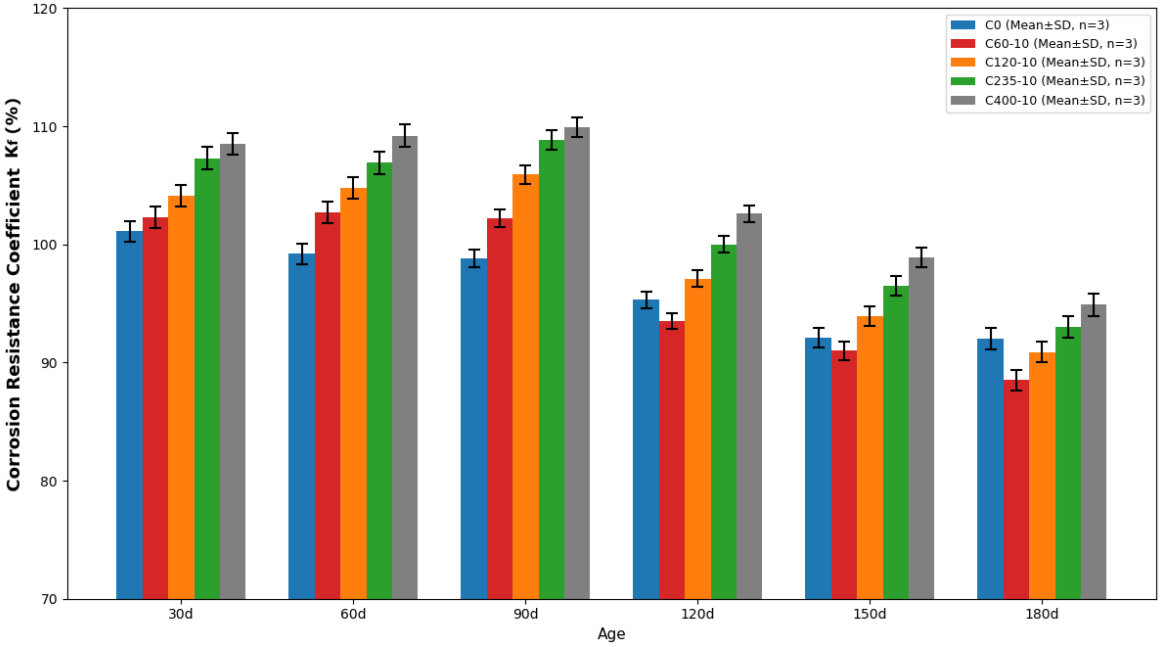

Figure 4.16: Effect of SiMnSg SSA on Concrete Sulfate Resistance Coefficient

From the detailed data, the sulfate resistance coefficient (K_f) of the control specimen (C0) exhibited a slight increase to 101.1% after 30 days of immersion, attributable to ongoing cement hydration. Subsequently, the K_f value decreased monotonically, reaching 92.0% at 180 days, which indicates progressive damage due to sulfate attack.

In contrast, the K_f values of the four SiMnS-modified concrete groups followed a distinct "increase-first-then-decrease" trend. The peak values at 90 days were 102.2%, 105.9%, 108.8%, and 109.9% for SSAs of 60, 120, 235, and 400 m²/kg, respectively. This initial enhancement confirms that finer SiMnS (higher SSA) promotes the formation of expansive, pore-filling insoluble salts (e.g., ettringite, gypsum), thereby densifying the microstructure and temporarily improving both strength and corrosion resistance.

A crucial observation is the rapid decline in K_f after 90 days. By 180 days, the K_f values for the mixtures with lower SSA (60 and 120 m²/kg) had decreased to 88.5% and 90.9%, respectively—values even lower than that of the control group (92.0%). Conversely,

mixtures with higher SSA (235 and 400 m²/kg) maintained superior performance, with K_f values of 93.0% and 94.9%.

This phenomenon, particularly the inferior long-term performance of the lower SSA mixtures compared to the control, can be explained by the dual role of the expansive reaction products. Initially, these products are beneficial, filling pores and increasing density (the early beneficial effect). However, as corrosion progresses, continued formation and water absorption of these products lead to sustained internal expansion. In mixtures with lower SSA SiMnS, the coarser, less reactive particles result in a slower, more dispersed, and less uniform formation of expansive products over time. This prolonged and uneven expansion can induce more severe micro-cracking in the later stages compared to the control, ultimately leading to greater strength loss and a lower final K_f value.

In contrast, higher SSA SiMnS possesses greater pozzolanic activity and filler efficiency. This facilitates a faster and more complete reaction in the early stages, creating a denser matrix that more effectively resists sulfate ion penetration and distributes expansion stresses uniformly. Consequently, these mixtures maintain better long-term resistance.

In summary, while SiMnS incorporation can initially enhance sulfate resistance, its long-term efficacy is critically dependent on SSA. The results suggest the existence of an SSA threshold (between 120 and 235 m²/kg under these conditions) for achieving long-term benefit. Below this threshold, the delayed and damaging expansive forces may eventually outweigh the initial densification benefit, leading to performance that is inferior to plain concrete after prolonged exposure.

4.5.4 Mechanism Analysis of SSA Affecting Durability Performance

The enhancement of durability performance in SiMnS concrete with increasing SSA can be attributed to three interlinked mechanisms that operate synergistically yet exhibit a threshold-dependent efficacy.

i. Physical filling and pore structure refinement serve as the foundational mechanism. Finer SiMnS particles with higher SSA act as efficient micro-fillers within the capillary pore network and between cement grains (Mohammed et al., 2014). This direct physical occupation reduces total porosity and, more critically, decreases pore connectivity. The resultant denser microstructure directly explains the observed systematic reduction in electric flux with increasing SSA, as it presents a more tortuous and hindered pathway for chloride ion ingress. This initial densification is also primarily responsible for the early-stage increase in the sulfate corrosion resistance coefficient (K_f). However, it is noted that an excessively high SSA may increase water demand and influence early-age shrinkage (Holt & Leivo, 2004).

ii. Enhanced pozzolanic reactivity and ITZ optimization constitute the subsequent, performance-sustaining mechanisms. The increased surface area of high-SSA SiMnS significantly accelerates its pozzolanic reaction with portlandite $Ca(OH)_2$, generating additional CSH gel (Tang et al., 2021; Nath et al., 2022). This secondary hydration product further infills pores and strengthens the cementitious matrix. Concurrently, the fine particles densify the ITZ through micro-filling and localized pozzolanic activity, transforming this typically weak and porous region into a more robust barrier (Scrivener et al., 2004; Sharma & Khan, 2021). The combined effect of matrix strengthening and ITZ refinement underpins the peak K_f values observed at 90 days and contributes to sustained resistance against the

progressive ingress and damaging action of sulfate ions (Zhang et al., 2019). It is important to note that the long-term durability is not governed solely by the filler effect; the continuation of hydration reactions and ITZ improvement are also critical to mitigating degradation under aggressive environments (Fei et al., 2023).

iii. The existence of an effective SSA threshold governs the long-term net durability benefit. The efficacy of the mechanisms is contingent upon achieving a sufficient degree of microstructural densification. For SiMnS with lower SSA (e.g., $\leqslant$120 m^2/kg), the physical and chemical effects are insufficient to create a microstructure capable of withstanding the prolonged expansive stresses from sulfate attack, where excessive ettringite (AFt) generation may lead to detrimental expansion and microcracking (Zhang et al., 2024). Consequently, the damaging expansion eventually outweighs the initial benefits, leading to K_f values falling below the control after extended exposure (180 days). Conversely, for SiMnS with SSA at or above a critical threshold (between 120 and 235 m^2/kg under these conditions), the mechanisms of filling, reaction, and ITZ optimization act in potent synergy. This synergy creates a sufficiently dense and coherent matrix that not only resists ion penetration but also better distributes internal expansive stresses, thereby delivering superior and sustained long-term durability performance, as evidenced by the highest Kf values maintained by the C235-10 and C400-10 mixtures.

In summary, while increased SSA universally promotes the filling effect, its long-term durability benefit is realized only when a threshold SSA is exceeded, enabling the synergistic contribution of enhanced pozzolanic reactivity and ITZ optimization to establish a microstructure resistant to both penetration and progressive deterioration. The microstructural features associated with these mechanisms, including pore structure

refinement, ITZ morphology, and the distribution of hydration and corrosion products, will be further examined and corroborated through SEM analysis in the following section.

4.6 Microscopic Analysis of SiMnS Concrete

The internal hydration microstructure of SiMnS concrete determines its macroscopic properties. Studying the types and hydration microstructure of SiMnS concrete hydration products can provide a more adequate theoretical basis for studying the influence of SiMnS on concrete performance. The microscopic morphology of the hydration products of SiMnS cement concrete was analyzed by scanning electron microscopy (SEM) to study the relationship between the microstructure and macroscopic properties of SiMnS concrete.

Scanning electron microscopy was performed on four SiMnS concrete specimens with SiMnS SSA of 60, 120, 235, and 400 m^2/kg. The specimens were fabricated using 10 %wt SiMnS replacement and cured for 14 days, as shown in Figure 4.17.

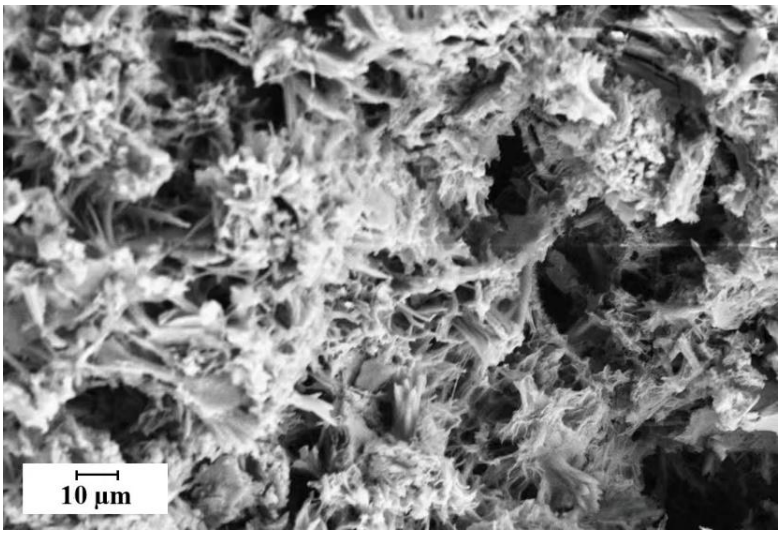

(a) SSA=60 m^2/kg

Figure 4.17: Scanning Electron Microscopy of SiMnS Concrete

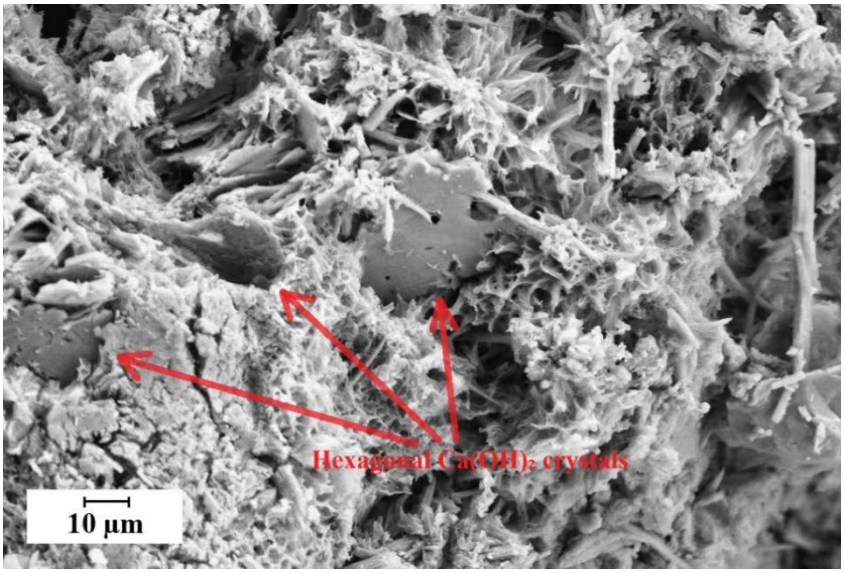

(b) SSA=120 m^2/kg: Red arrows indicate representative hexagonal $Ca(OH)_2$ crystals.

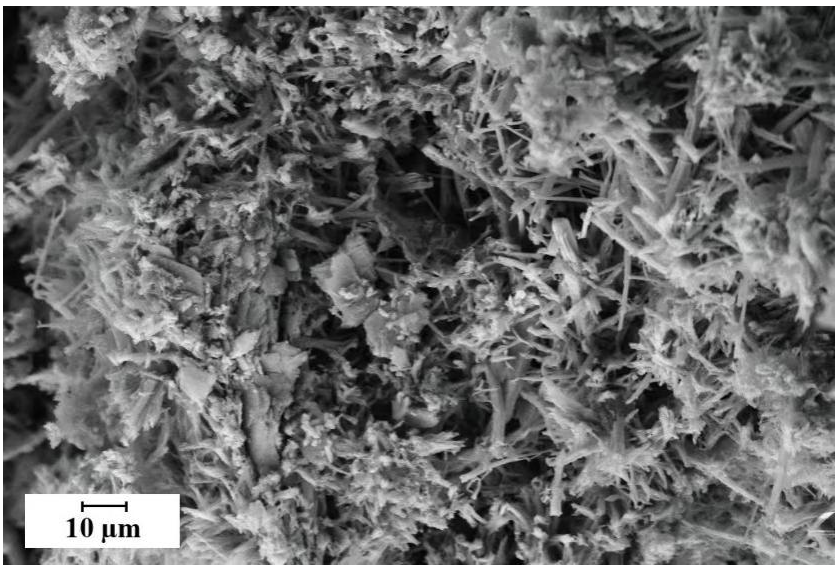

(c) SSA=235 m^2/kg

Figure 4.17 continued

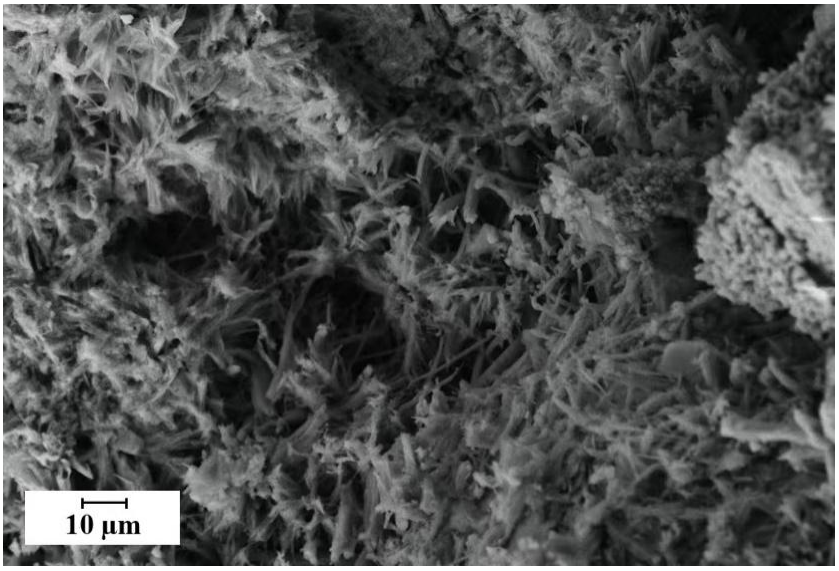

(d) SSA=400 m^2/kg

Figure 4.17 continued

As shown in Figure 4.17, with increasing SSA, the microstructure of SiMnS concrete undergoes significant transformations, characterized by a reduction in SiMnS particle size and pore structure, primarily driven by the hydration process and the evolution of CSH gel and $Ca(OH)_2$ crystals.

At low SSA levels (60 m^2/kg) as shown in Figure 4.17(a), the SiMnS particles remain large, and the pore structure is highly porous, leading to visible cracks. The hydration reaction is insufficient, resulting in a sparse distribution of CSH gel, which is unable to fill voids effectively. A significant amount of unhydrated SiMnS remains, indicating limited participation in hydration.

As SSA increases to 120 m^2/kg as shown in Figure 4.17(b), hydration reactions intensify, and more CSH gel is formed, improving void filling and particle connectivity. However, the persistence of distinct hexagonal thin-plate $Ca(OH)_2$ crystals (see arrow in Figure 4.17(b)) indicates an incomplete reaction where pozzolanic reactions have not fully

consumed excess $Ca(OH)_2$. While hydration is more advanced than at SSA = 60 m^2/kg, some residual porosity remains, suggesting further potential for microstructural refinement.

At higher SSA levels (235 m^2/kg) as shown in Figure 4.17(c), the hydration process becomes more efficient, producing an increased amount of CSH gel, which forms an interconnected, compact network. The previously observed large, unhydrated SiMnS blocks are significantly reduced, indicating improved hydration. The interaction between CSH gel and secondary hydration products, such as ettringite, further enhances microstructural integrity. At this stage, the $Ca(OH)_2$ crystals become less pronounced, suggesting that the pozzolanic reaction between SiMnS and cement has effectively consumed free $Ca(OH)_2$, contributing to improved durability.

At an ultra-high SSA of 400 m^2/kg as shown in Figure 4.17(d), the CSH gel forms a highly interconnected, near-continuous network characterized by fine, needle-like, and fibrous structures that establish a robust spatial framework, representing a significantly densified microstructure compared to lower SSA samples. The absence of substantial $Ca(OH)_2$ crystals indicates that pozzolanic reactions have effectively consumed free $Ca(OH)_2$. However, as noted in the SEM image, residual pores remain within this densified matrix. These pores may result from several mechanisms: during the mixing process, trapped air bubbles may become incorporated into the cementitious matrix, and if not eliminated before setting, these bubbles can create residual voids within the hardened concrete. Additionally, excess water in the mixture, particularly in areas with elevated local water-to-binder ratios, may evaporate during hydration and drying, forming small pores. This phenomenon is more pronounced in high-SSA SiMnS concrete, where the increased fineness accelerates water demand and hydration kinetics. Furthermore, the constrained growth of

hydration products, notably CSH gel and ettringite, can induce internal stresses within the hardened matrix. In ultra-high SSA SiMnS concrete, excessive densification may result in localized crystalline pressure, potentially giving rise to microcracks or void formation in specific regions.

In summary, increasing SSA enhances CSH gel formation, which evolves from a sparse and uneven distribution at low SSA to a well-structured and highly interconnected network at higher SSA, significantly reducing porosity and enhancing concrete strength. However, at SSA = 120 m^2/kg, the presence of hexagonal $Ca(OH)_2$ crystals suggests an incomplete reaction, whereas, at 235–400 m^2/kg, the pozzolanic activity effectively incorporates $Ca(OH)_2$ into hydration products. While SSA values between 120–235 m^2/kg provide an optimal balance between hydration efficiency and structural integrity, excessive densification at 400 m^2/kg necessitates careful mix design adjustments to mitigate potential microcracking risks.

4.7 Evaluation of SSA Impact on Concrete Performance Using the AHP-entropy Method

Based on the workability performance test data of SiMnS concrete, the optimal SSA (235 m^2/kg) and substitution ratio (10%wt) have been identified. This combination effectively fills the voids between cement particles, accelerates the hydration reaction, enhances fluidity, and improves slump performance. According to the mechanical performance test data, a moderate SSA (235–400 m^2/kg) and a substitution ratio of 10–15% contribute to optimizing the filling effect, hydration reaction, and densification of the ITZ, thereby enhancing both compressive and flexural strength. Furthermore, based on the durability test data, the optimal SSA range is determined to be 235–400 m^2/kg, as it

effectively balances the filling effect, hydration reaction, and ITZ optimization, thereby improving the overall durability of the concrete.

The experimental data will be statistically analyzed (AHP-entropy method) to identify the most optimal specific surface area (SSA) scheme for SiMnS concrete.

4.7.1 Subjective Weight Calculation Using the AHP Method

A hierarchical analytical structure model was established based on the relationships among factors influencing the comprehensive performance of SiMnS concrete, as illustrated in Figure 3.9. In accordance with the AHP procedure detailed in Chapter 3, a panel of experts was involved to ensure robust weight allocation. The validity of the expert judgments was established through a structured two-stage process. First, during the qualification screening stage, sixteen (16) experts from academia (universities, research institutes) and industry (design institutes, construction companies) were invited. All were specialists in concrete materials, solid waste utilization, or civil engineering, possessing senior professional titles (Professors, Associate Professors, and Senior Engineers) and a minimum of ten years of documented experience. Second, in the data validation stage, thirteen (13) completed questionnaires were received. Twelve (12) of these were deemed valid after checks for logical completeness and internal consistency in the pairwise comparisons. The subsequent mathematical consistency check ($CR < 0.1$) of the aggregated group judgment matrices (Tables 4.18 and 4.19) further confirms the logical coherence and reliability of the expert inputs used in the AHP model. Following this, judgment matrices were constructed, and the subjective weights were calculated using the AHP method. Data processing was performed with SPSS software.

(1) Construction of the First-Level Judgment Matrix

Based on the relationships among factors influencing the comprehensive performance of SiMnS concrete, the hierarchical analytical structure model was developed, as shown in Figure 3.9. For each expert's scoring results, a first-level judgment matrix was constructed, as presented in Table 4.6 and Table 4.7.

Table 4.6: First-level Judgment Matrix (Experts 1-6)

	Expert 1		**Expert 2**		**Expert 3**		**Expert 4**		**Expert 5**		**Expert 6**	
A	B1	B2	B1	B2	B1	B2	B1	B2	B1	B2	B1	B2
B1	1	4	1	3	1	3	1	2	1	3	1	3
B2	1/4	1	1/3	1	1/3	1	1/2	1	1/3	1	1/3	1

Table 4.7: First-level Judgment Matrix (Experts 7-12)

	Expert 7		**Expert 8**		**Expert 9**		**Expert 10**		**Expert 11**		**Expert 12**	
A	B1	B2	B1	B2	B1	B2	B1	B2	B1	B2	B1	B2
B1	1	5	1	4	1	5	1	3	1	3	1	2
B2	1/5	1	1/4	1	1/5	1	1/3	1	1/3	1	1/2	1

The geometric mean method calculates the first-level matrix data to obtain the first-level (Layer A) group decision-making judgment matrix, as shown in Table 4.8.

Table 4.8: First-level (layer A) Group Decision-making Judgment Matrix

A	**B1**	**B2**	**Wi**
B1	1	3.203100948	0.7621
B2	0.312197466	1	0.2379

For a second-order judgment matrix, since it contains only one independent judgment value, there is no transitivity inconsistency, and its largest eigenvalue is always equal to the matrix order. Therefore, the consistency index CI is always zero, and a second-order matrix does not require a consistency check. This conclusion has been verified by the classic theory of the Analytic Hierarchy Process and is widely adopted (Saaty, 1980; Saaty & Vargas, 1987). Based on this conclusion, the consistency check of the second-order judgment matrix is assumed to be satisfied by default. Moreover, the table indicates that the weighting of influencing factors for SiMnS concrete is ranked as follows: workability and mechanical properties (B1) hold greater significance than durability (B2).

Table 4.9: Second-level B1 Judgment Matrix (Experts 1–4)

	Expert 1			**Expert 2**			**Expert 3**			**Expert 4**		
B1	C1	C2	C3	C1	C2	C3	C1	C2	C3	C1	C2	C3
C1	1	1	2	1	1/2	2	1	1/3	2	1	1/4	3
C2	1	1	3	2	1	4	3	1	3	4	1	3
C3	1/2	1/3	1	1/2	1/4	1	1/2	1/3	1	1/3	1/3	1

Table 4.10: Second-level B1 Judgment Matrix (Experts 5–8)

	Expert 5			**Expert 6**			**Expert 7**			**Expert 8**		
B1	C1	C2	C3	C1	C2	C3	C1	C2	C3	C1	C2	C3
C1	1	1	2	1	1/2	2	1	1/3	3	1	1	2
C2	1	1	2	2	1	2	3	1	4	1	1	1
C3	1/2	1/2	1	1/2	1/2	1	1/3	1/4	1	1/2	1	1

Table 4.11: Second-level B1 Judgment Matrix (Experts 9–12)

	Expert 9			**Expert 10**			**Expert 11**			**Expert 12**		
B1	C1	C2	C3	C1	C2	C3	C1	C2	C3	C1	C2	C3
C1	1	1/4	2	1	1/3	1	1	1/2	2	1	1/2	3
C2	4	1	4	3	1	2	2	1	3	2	1	1
C3	1/2	1/4	1	1	1/2	1	1/2	1/3	1	1/3	1	1

(2) Construction of the Second-Level Judgment Matrices

Second-level judgment matrices were constructed based on each expert's scoring results. The second-level B1 judgment matrices are presented in Tables 4.9–4.11. The second-level B2 judgment matrices are presented in Tables 4.12 to 4.17.

Table 4.12: Second-level B2 Judgment Matrix (Experts 1–2)

	Expert 1					**Expert 2**				
B2	C4	C5	C6	C7	C8	C4	C5	C6	C7	C8
C4	1	1/4	1/4	1/3	1/3	1	1/3	1/3	1/2	1/3
C5	4	1	1/3	1	1/2	3	1	1/3	1	1/2
C6	4	3	1	2	1/2	3	3	1	2	1/2
C7	3	1	1/2	1	1/3	2	1	1/2	1	1/3
C8	3	2	2	3	1	3	2	2	3	1

Table 4.13: Second-level B2 Judgment Matrix (Experts 2–4)

	Expert 3					**Expert 4**				
B2	C4	C5	C6	C7	C8	C4	C5	C6	C7	C8
C4	1	1/3	1/3	1/3	1/3	1	1/4	1/4	1/3	1/4

Table 4.13 continued

C5	3	1	1/3	1	1/2	4	1	1/3	1	1/2
C6	3	3	1	3	1/2	4	3	1	3	1/2
C7	3	1	1/3	1	1/3	3	1	1/3	1	1/3
C8	3	2	2	3	1	4	2	2	3	1

Table 4.14: Second-level B2 Judgment Matrix (Experts 5–6)

	Expert 5					**Expert 6**				
B2	C4	C5	C6	C7	C8	C4	C5	C6	C7	C8
C4	1	1/4	1/4	1/3	1/3	1	1/4	1/4	1/3	1/4
C5	4	1	1/3	1	1/2	4	1	1/3	1	1/3
C6	4	3	1	2	1/2	4	3	1	2	1/2
C7	3	1	1/2	1	1/3	3	1	1/2	1	1/2
C8	3	2	2	3	1	4	3	2	2	1

Table 4.15: Second-level B2 Judgment Matrix (Experts 7–8)

	Expert 7					**Expert 8**				
B2	C4	C5	C6	C7	C8	C4	C5	C6	C7	C8
C4	1	1/3	1/3	1/3	1/3	1	1/4	1/4	1/2	1/3
C5	3	1	1/3	1	1/2	4	1	1/3	1	1/2
C6	3	3	1	3	1/2	4	3	1	2	1/2
C7	3	1	1/3	1	1/3	2	1	1/2	1	1/3
C8	3	2	2	3	1	3	2	2	3	1

Table 4.16: Second-level B2 Judgment Matrix (Experts 9–10)

	Expert 9					**Expert 10**				
B2	C4	C5	C6	C7	C8	C4	C5	C6	C7	C8
C4	1	1/4	1/4	1/3	1/3	1	1/4	1/4	1/2	1/3
C5	4	1	1/3	1	1/2	4	1	1/3	1	1/2
C6	4	3	1	2	1/2	4	3	1	2	1/2
C7	3	1	1/2	1	1/3	2	1	1/2	1	1/3
C8	3	2	2	3	1	3	2	2	3	1

Table 4.17: Second-level B2 Judgment Matrix (Experts 11–12)

	Expert 11					**Expert 12**				
B2	C4	C5	C6	C7	C8	C4	C5	C6	C7	C8
C4	1	1/3	1/3	1/3	1/3	1	1/4	1/4	1/3	1/3
C5	3	1	1/3	1	1/2	4	1	1/3	1	1/2
C6	3	3	1	3	1/2	4	3	1	2	1/2
C7	3	1	1/3	1	1/3	3	1	1/2	1	1/3
C8	3	2	2	3	1	3	2	2	3	1

Based on the group judgment aggregation method described in Chapter 3, this study integrates the pairwise comparison judgments independently provided by multiple experts using the geometric mean method. This process yields a Level 2 (B-layer) collective decision-making judgment matrix regarding the workability and mechanical properties of SiMnS concrete. This matrix serves as the foundation for subsequent weight calculations and consistency checks, with the results presented in Tables 4.18 and 4.19.

Table 4.18: Second-level (layer B1) Group Decision-making Judgment Matrix

B1	C1	C2	C3	W_i
C1	1	0.478666487	2.089137273	0.3019
C2	2.089137273	1	2.425564987	0.5250
C3	0.478666487	0.389135858	1	0.1731

The consistency check of the matrix (Layer B1) was conducted, with the results presented in Table 4.20. The consistency ratio (CR) is 0.030, less than the threshold of 0.1. These findings indicate that the group decision-making judgment matrix B1 is feasible and valid. Furthermore, as shown in Table 4.18, the weight ranking of influencing factors on the workability and mechanical performance of SiMnS concrete is as follows: compressive strength (C2) > slump (C1) > flexural strength (C3).

Furthermore, as shown in Table 4.18, the subjective weight ranking derived from the expert panel for factors influencing the workability and mechanical performance is: compressive strength (C2) > slump (C1) > flexural strength (C3). This ranking reflects the collective judgment of the experts, who evaluated the relative importance of these criteria within the specific context of optimizing the SSA of SiMnS concrete (Objective A). While compressive and flexural strength are mechanically correlated, the experts assigned higher importance to compressive strength as it is the fundamental and most widely used indicator for evaluating the structural adequacy of concrete, serving as the primary basis for design in major international codes such as the American Concrete Institute's building code (ACI 318) and the European standard for concrete structure design (Eurocode 2) (ACI Committee 318, 2019; BS EN 1992-1-1, 2004). Slump (C1), representing workability, was ranked second due to its direct impact on the constructability and uniformity of SiMnS concrete mixes,

which is a critical practical constraint in achieving optimal SSA. The lower relative weight of flexural strength (C3) does not diminish its importance but indicates that, for the primary optimization goal (SSA selection), experts deemed compressive strength and workability as more decisive factors in the initial screening and comparison of mix designs.

Table 4.19: Second-level (layer B2) Group Decision-making Judgment Matrix

B2	C4	C5	C6	C7	C8	W_i
C4	1	0.275161	0.275161	0.368894	0.317728	0.0690
C5	3.634241	1	0.333333	1	0.483388	0.1580
C6	3.634241	3	1	2.368107	0.5	0.2826
C7	2.710806	1	0.422278	1	0.344789	0.1388
C8	3.147345	2.068732	2	2.900327	1	0.3516

Table 4.20: Results of Consistency Check (B1)

λ_{max}	CI	RI	CR	Consistency test results
3.031	0.016	0.520	0.030	Verified

The consistency check of the matrix (Layer B2) was conducted, with the results presented in Table 4.21. The consistency ratio (CR) is 0.050, less than the threshold of 0.1. These findings indicate that the group decision-making judgment matrix B2 is feasible and valid. Furthermore, as shown in Table 4.19, the weight ranking of influencing factors on the workability and mechanical performance of SiMnS concrete is as follows: compressive strength loss under F-T cycles (C8) > sulfate resistance coefficient (C6) > mass loss in sulfate

corrosion (C5) > Mass loss rate under F-T cycles (C7) > Electric flux in chloride ion corrosion (C4).

Table 4.21: Results of Consistency Check (B2)

λ_{max}	CI	RI	CR	Consistency test results
5.225	0.056	1.120	0.050	Verified

(3) The comprehensive weights of various factors influencing the overall performance of SiMnS concrete were calculated using the AHP.

Table 4.22: Comprehensive Weights of Influencing Factors under the AHP

A	B	B1	B2	Comprehensive weight	Ranking
		0.7621	0.2379		
C					
	C1	0.3019		0.2301	2
	C2	0.5250		0.4001	1
	C3	0.1731		0.1319	3
	C4		0.0690	0.0164	8
	C5		0.1580	0.0376	6
	C6		0.2826	0.0672	5
	C7		0.1388	0.0330	7
	C8		0.3516	0.0836	4

The results demonstrate that the group decision-making judgment matrices for A, B1, and B2 successfully passed the consistency test. To compute the comprehensive weights of

the eight factors under the sub-criterion level C concerning the objective level A, it was necessary to weight the criterion level B results based on the sub-criterion level C. The detailed outcomes of the comprehensive weight calculations are shown in Table 4.22.

4.7.2 Objective Weight Calculation Using the Entropy Method

Following the calculation procedure of the entropy method detailed in Chapter 3, an objective assessment was performed to evaluate the indicators influencing the overall performance of SiMnS concrete under varying SSA. Based on experimental data for SiMnS concrete with four SSA values (60 m^2/kg, 120 m^2/kg, 235 m^2/kg, 400 m^2/kg), the percentage of cement replacement by SiMnS of 10%wt, a curing period of 28 days, and six-time parameters (50, 100, 150, 200, 250, 300), the weights of eight evaluation indicators were calculated using the entropy method.

(1) Establishment of the evaluation indicators system

An evaluation index system for the comprehensive performance of SiMnS concrete was constructed, drawing on the types of experiments conducted in this study. The system considers two dimensions: workability and mechanical performance, as well as durability performance. The specific details of the evaluation indicators system are presented in Table 4.23.

(2) Calculation of the entropy value and weight of each indicator

Referring to the calculation method of entropy value and weight in Chapter 3, the entropy value and weight of the eight evaluation indicators of the comprehensive performance of manganese slag concrete are obtained. The results are shown in Table 4.24.

Table 4.23: The Evaluation Indicators System

Objective level	Primary indicator	Secondary indicator	Code
Comprehensive performance of SiMnS concrete under SSA (A)	Working and mechanical properties (B1)	Slump (C1)	S_c
		Compressive strength (C2)	f_c
		Flexible strength (C3)	f_f
	Durability (B2)	Electric flux in chloride ion corrosion (C4)	Q
		Mass loss in sulfate corrosion (C5)	W_L
		Sulfate resistance coefficient (C6)	K_f
		Mass loss rate under F-T cycles (C7)	M_d
		Compressive strength loss under F-T cycles (C8)	f_t

4.7.3 Calculation of Combined Weight

From the calculation process outlined above, it is evident that the analytic hierarchy process (AHP) method provides a subjective evaluation of the eight indicators influencing the comprehensive performance of SiMnS concrete, while the entropy method offers an objective evaluation based on experimental data for these same indicators.

The next step involves integrating the AHP-entropy method by utilizing both subjective and objective weight values to calculate the combined weights of the eight indicators affecting the comprehensive performance of SiMnS concrete. The combined weight values are determined using a linear combination weighting method. Since both the AHP and entropy methods hold equal importance in the combined weighting process, the

formula for calculating the composite weight of the performance indicators of SiMnS concrete is presented in Equation (3.23).

The calculated combined weights of the eight evaluation indicators are shown in Table 4.25.

Table 4.24: The Entropy Value and Weight of the Eight Evaluation Indicators

Secondary indicator	Entropy value e_j	Differentiation coefficient g_j	Objective weight coefficient S_j
C1	0.9055	0.0945	0.1942
C2	0.9422	0.0578	0.1187
C3	0.9266	0.0734	0.1508
C4	0.8879	0.1121	0.2303
C5	0.9658	0.0342	0.0702
C6	0.9585	0.0415	0.0852
C7	0.9697	0.0303	0.0623
C8	0.957	0.043	0.0883

Table 4.25: The Combined Weight of the Eight Evaluation Indicators

Indicator	Weights based on the AHP	Weights derived from the entropy method	Combined weights
C1	0.2301	0.1942	0.2122
C2	0.4001	0.1187	0.2594
C3	0.1319	0.1508	0.1414
C4	0.0164	0.2303	0.1234

Table 4.25 continued

C5	0.0376	0.0702	0.0539
C6	0.0672	0.0852	0.0762
C7	0.033	0.0623	0.0477
C8	0.0836	0.0883	0.0860

The eight evaluation indicators within the system were hierarchically ranked according to the relative magnitudes of their aggregated weight values. The corresponding results are presented in Table 4.26.

Table 4.26: Combined Weight Ranking of the Eight Evaluation Indicators

Objective level	Primary indicator	Secondary indicator	Combined weights	Rank
Comprehensive performance of SiMnS concrete under SSA (A)	Working and mechanical properties (B1)	Slump (C1)	0.2122	2
		Compressive strength (C2)	0.2594	1
		Flexible strength (C3)	0.1414	3
	Durability (B2)	Electric flux in chloride ion corrosion (C4)	0.1234	4
		Mass loss in sulfate corrosion (C5)	0.0539	7
		Sulfate resistance coefficient (C6)	0.0762	6
		Mass loss rate under F-T cycles (C7)	0.0477	8
		Compressive strength loss under F-T cycles (C8)	0.086	5

4.7.4 Comprehensive Analysis of the Effect of SiMnS SSA on the Performance of Concrete Based on the AHP-entropy Method

Based on four SiMnS SSA values (60 m^2/kg, 120 m^2/kg, 235 m^2/kg, 400 m^2/kg), a percentage of cement replacement by manganese slag of 10%wt, a curing period of 28 days, and six-time parameters (50, 100, 150, 200, 250, 300), 30 SSA-based SiMnS concrete configurations were generated. The experimental data for these 30 configurations were comprehensively evaluated using weights calculated through the AHP-entropy method. The resulting scores were ranked to determine the performance of each configuration as shown in Figure 4.18.

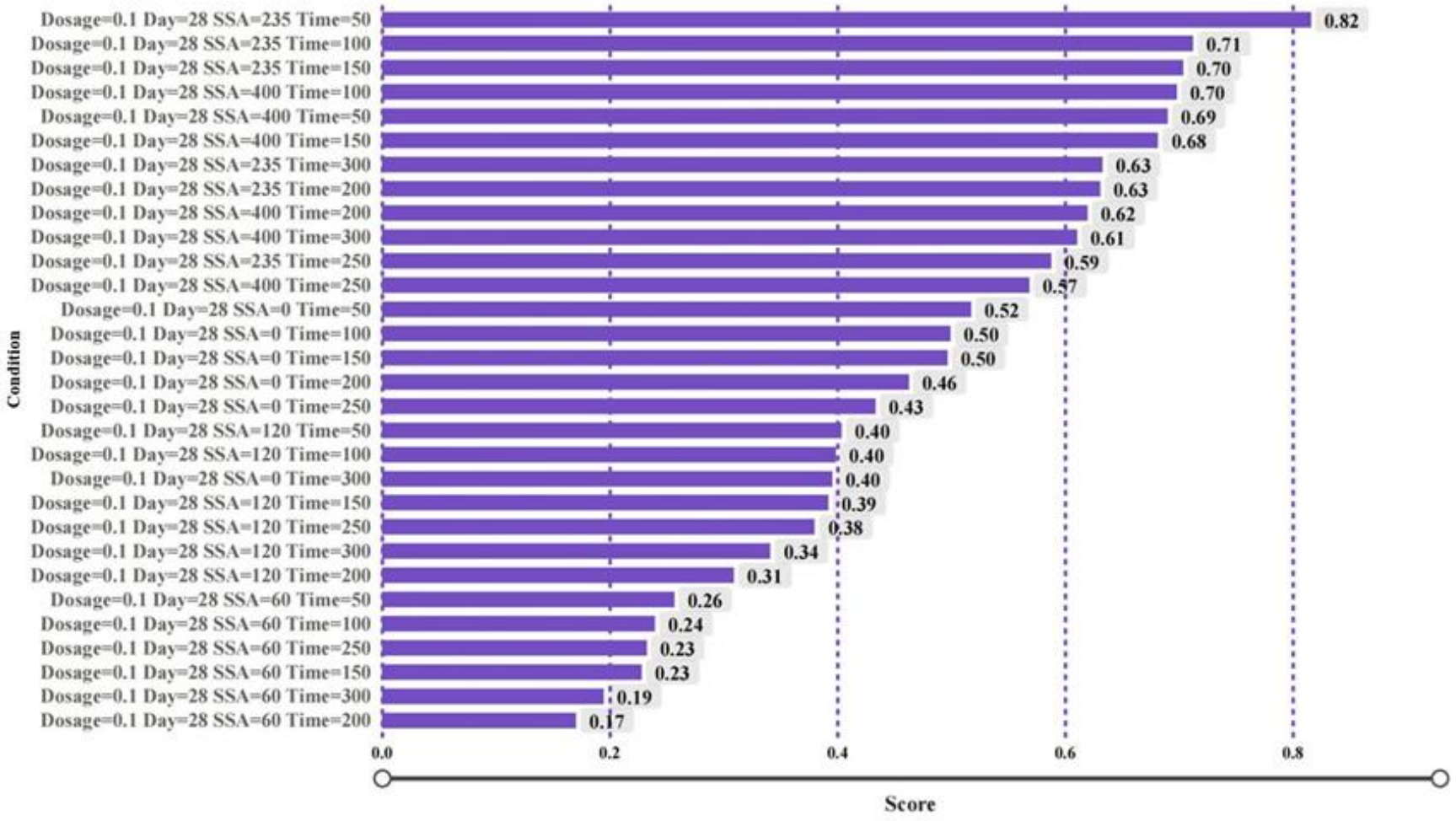

Figure 4.18: Comprehensive evaluation scores of 30 schemes

The bar chart illustrates the scores under various experimental conditions defined by different dosage combinations, curing days, SSA, and curing time. The horizontal axis represents the scores, while the vertical axis lists the conditions.

The highest score of 0.82 is achieved under the condition "Dosage = 0.1, Day = 28, SSA = 235 m²/kg, Time = 50," followed by scores of 0.71, 0.70, and 0.69 under similar conditions with varying curing times and SSA values. Scores generally decrease as SSA and curing time reduce. The lowest score of 0.17 is observed for the condition "Dosage=0.1, Day=28, SSA=60 m²/kg, Time=200."

In summary, the AHP-entropy method, as a statistical approach combining subjective and objective evaluation criteria, was employed to evaluate the experimental data of 30 SSA schemes comprehensively. The comprehensive evaluation results indicate that the optimal scheme corresponds to SiMnS SSA = 235 m²/kg, cement replacement by SiMnS = 10%wt, curing period = 28 days, and time parameter = 50. This finding aligns with the experimental results for SiMnS concrete as described in section 4.4, thereby validating the influence of SiMnS SSA on the performance of SiMnS concrete.

4.8 Chapter Summary

This chapter presents a comprehensive evaluation of the effect of SiMnS SSA on properties of concrete, including workability, mechanical properties, durability, and microstructural characteristics. The research findings provide critical insights into optimizing the use of SiMnS as a cement replacement in concrete, thereby enhancing performance while ensuring sustainable construction practices.

4.8.1 Influence of SiMnS SSA on Workability

The workability, assessed by slump, is governed by the combined effect of SiMnS SSA and its replacement percentage. Experimental data indicate that for replacement levels between 10%wt and 15%wt, slump increases with SSA up to a range of approximately 235 to 400 m^2/kg, primarily due to the micro-filling effect and improved particle dispersion. Within this optimal SSA range, the slump can be improved by 15% to 20% compared to the plain concrete control. However, when SSA exceeds approximately 400 m^2/kg, the increased water demand outweighs the beneficial effects, leading to a reduction in workability. Similarly, replacement percentages exceeding 15%wt consistently result in lower slump, even within the optimal SSA range. Therefore, achieving high workability requires balancing both parameters, with the most favorable conditions found within the SSA range of 235–400 m^2/kg and a replacement percentage not exceeding 15%wt.

4.8.2 Influence of SiMnS SSA on Mechanical Properties

The mechanical properties (compressive and flexural strengths) of SiMnS concrete are determined by the combined effects of its SSA and replacement percentage. The strengths increase with SSA and reach their peak within an optimal SSA range of 235–400 m^2/kg coupled with an optimal replacement percentage of 10–15%wt. Specifically, the mix with 10%wt replacement and an SSA of 235 m^2/kg achieved the highest compressive strength, exhibiting an increase of approximately 18–22% compared to the plain concrete control. Flexural strength showed a similar improvement of about 15–20% within this optimal parameter range. These enhancements are attributed to improved particle packing, densification of the interfacial transition zone (ITZ), and the pozzolanic activity of SiMnS, which promotes additional CSH formation. However, when the replacement percentage

exceeds 15%wt, strength reductions of up to 10–15% compared to the peak value can occur, even at high SSA, due to incomplete hydration and weakened matrix cohesion.

4.8.3 Influence of SiMnS SSA on Durability

The durability of SiMnS concrete, encompassing freeze-thaw resistance, chloride ion penetration resistance, and sulfate resistance, is contingent upon both the SSA and the replacement percentage. Significant improvements are achieved within the optimal parameter range of SSA (235–400 m^2/kg) and a replacement percentage of 10%wt. Specifically:

Freeze-thaw resistance: Significant improvement in freeze-thaw resistance was achieved when the SSA of SiMnS was 235 m^2/kg or higher, combined with a replacement percentage of 10%wt. Under these conditions, mass loss and compressive strength loss after 100 cycles were reduced by up to ~40% and ~35%, respectively, compared to the control mix. This enhancement is attributed to the densified microstructure which effectively limits water ingress and ice formation pressure.

Chloride ion penetration resistance: The resistance to chloride ion penetration increased monotonically with higher SSA. Experimental data indicated that a key performance threshold was reached at an SSA of approximately 120 m^2/kg, where the permeability rating improved to “Low”. Within the SSA range of 120 to 400 m^2/kg, the charge passed (ASTM C1202) was substantially reduced, with the optimal observed reduction of 50–60% achieved within the SSA range of 235–400 m^2/kg under a 10% replacement ratio.

Sulfate resistance: At moderate SSA (235–400 m^2/kg) with 10%wt replacement, expansion after 90 days of exposure was reduced by approximately 30%. It is noted that while higher SSA generally promotes a denser microstructure, excessive SSA (>400 m^2/kg) may increase the long-term risk of expansion due to ettringite formation under prolonged sulfate attack.

4.8.4 Microstructural Insights from SEM Analysis

Scanning electron microscopy analysis corroborates the observed mechanical and durability performance trends. The SEM images reveal that increasing SSA results in a denser microstructure with fewer visible pores and enhanced ITZ integrity. The absence of large Ca $(OH)_2$ crystals in high-SSA samples suggests that SiMnS effectively promotes secondary hydration, refining the cement paste matrix. At SSA levels of 235 m^2/kg and 400 m^2/kg, SiMnS particles exhibit effective dispersion, contributing to improved strength and durability. Conversely, at lower SSA levels (60–120 m^2/kg), incomplete hydration and weaker ITZ bonding are evident, leading to inferior mechanical properties.

4.8.5 Analysis via the AHP-Entropy Method

The integrated AHP-Entropy weighting analysis yielded definitive priorities for the concrete performance criteria. The compressive strength (C2) emerged as the most critical factor, followed by slump (workability, C1), and then flexural strength (C3). The durability criteria—resistance to chloride ion penetration (C4), freeze-thaw cycles (C8), and sulfate attack (C6, C5, C7)—were assigned comparatively lower but still significant weights in the decision model. This ranking underscores that for optimizing SiMnS concrete, structural integrity and practical workability are paramount considerations, informed by both expert judgment (AHP) and objective data variability (Entropy method). Based on these

comprehensive weights, the analysis identified the mix with an SSA of 235 m²/kg and a 10%wt cement replacement as the optimal solution. Furthermore, mixes with SSA up to 400 m²/kg also performed excellently, indicating a practically viable and high-performance SSA range of 235–400 m²/kg.

4.8.6 Optimal SSA Selection and Practical Implications

The multi-criteria decision analysis culminates in a clear, actionable guideline for mix design. The optimal parameters are an SSA of 235 m²/kg with a 10%wt cement replacement. This specific mix proportion delivers a balanced enhancement across all key properties: it improves compressive strength by approximately 20%, increases slump (workability) by about 18%, and enhances durability resistance by 35-60% across various tests, compared to control or baseline mixes. A key practical finding is that superior performance is not confined to a single SSA value but exists within a window of 235 to 400 m²/kg. Within this range, the benefits of high SSA—such as improved particle packing and pozzolanic activity—are fully realized without introducing detrimental effects like excessive water demand. Therefore, the primary practical implication is that successful SiMnS concrete optimization must move beyond a focus on any single property. Engineers are advised to target the SSA range of 235–400 m²/kg at a 10%wt replacement level to reliably achieve a synergistic improvement in strength, workability, and durability, providing a robust scientific basis for its use in sustainable construction.

CHAPTER 5

CONCLUSION

5.1 Review of Work Done

This research comprehensively investigated the potential of SiMnS as a supplementary cementitious material, focusing on the effect of its SSA on the properties of concrete. Through an extensive experimental program encompassing workability, mechanical strength, and durability tests, coupled with a novel AHP-Entropy integrated decision-making model, the study aimed to identify the optimal SSA and replacement ratio for practical application.

5.2 Conclusion of Study

The findings of this thesis effectively address the four research objectives:

Effect of SSA on workability: Increasing the SSA of SiMnS generally enhances the fluidity of cement mortar and the slump of concrete, but only up to an optimal SSA of approximately 235 m^2/kg, which provides the optimal workability for concrete. Compared with the control case C0 (slump = 170 mm), increasing SSA up to 235 m^2/kg enhances the slump to 195 mm, an increase of about 14.7%. This improvement is due to enhanced particle dispersion and micro - filling effects. However, SSA values exceeding 235 m^2/kg lead to increased water demand, reducing workability. For example, although the slump of C235-15 is 182 mm, still higher than C0, it is lower than that of C235-5 and C235-10, indicating that there is an optimal range around 235 m^2/kg for achieving the best workability.

Effect of SSA on mechanical properties: The SSA of SiMnS significantly affects the mechanical properties of concrete, showing a general trend of strength improvement with

increasing SSA. For compressive strength, higher SSA leads to higher strength. The 28 - day compressive strength of C235-10 and C400-10 reaches 57 MPa, which is an increase of approximately 1.8% compared to the control specimen C0 (56 MPa). This indicates that within a certain range, the addition of SiMnS with appropriate SSA can enhance the compressive strength of concrete. Similarly, flexural strength improves with SSA. Finer particles enhance pozzolanic activity and matrix densification. At an early age (3 days), higher SSA (235 - 400 m^2/kg) results in better flexural strength, especially at 10 - 15% replacement. At 28 days, the highest flexural strength (6.1 MPa) is achieved with SSA = 235 m^2/kg at 15%wt replacement, which is also higher than that of C0 (5.93 MPa). However, excessive replacement (20%wt) leads to strength reduction due to the insufficient cementitious binder. Overall, the optimal mix is SSA = 235 m^2/kg with 10%wt SiMnS, which balances workability, compressive strength, and flexural strength while maintaining good mechanical performance compared to C0.

Effect of SSA on durability: The durability of SiMnS concrete is significantly influenced by SSA, affecting its freeze-thaw resistance, chloride ion penetration resistance, and sulphate attack resistance. Under freeze-thaw cycles, compared with C0 (mass loss rate = 1.5%, compressive strength loss = 17.2%), SiMnS concrete initially experiences mass gain due to pore water freezing and expansion, followed by mass loss as cycles progress. Higher SSA (235 - 400 m^2/kg) enhances resistance in the early stages but leads to higher long - term deterioration compared to plain concrete. For example, F60-10 shows a mass loss rate of -0.2% and a compressive strength loss of 26.5%, while F235-10 has a mass loss rate of 0.46% and a compressive strength loss of 25.3%. In terms of chloride ion resistance, as SSA increases, the electric flux decreases, improving impermeability. The most significant reduction occurs when SSA increases from 60 to 120 m^2/kg. The electric flux of C400-10 is

653 C, much lower than that of C0 (1520 C), indicating a great improvement in chloride ion penetration resistance. For sulfate resistance, before 120 days of immersion, higher SSA reduces mass loss by facilitating secondary hydration and pore refinement. However, after 150 days, expansion stress from sulfate reactions induces cracking, with smaller SSA leading to higher mass loss. The sulfate resistance coefficient of C400-10 is 94.9%, higher than that of C0 (92.0%). In general, an optimal SSA range of 120 - 235 m^2 /kg balances durability and mechanical performance in aggressive environments compared to C0.

Comprehensive performance evaluation using the AHP-entropy method: The AHP-entropy method provided a statistical evaluation of SSA's impact on workability, mechanical properties, and durability. Based on the final combined weights derived from Table 4.26, the relative significance of the evaluation indicators was ranked as follows: Compressive strength (C2) > Slump (C1) > Flexible strength (C3) > Electric flux in chloride ion corrosion (C4) > Compressive strength loss under F-T cycles (C8) > Sulfate resistance coefficient (C6) > Mass loss in sulfate corrosion (C5) > Mass loss rate under F-T cycles (C7). The analysis confirmed that SSA = 235 m^2/kg with a 10% replacement percentage is the optimal combination, achieving the best balance among all performance criteria when compared with C0. This systematic approach validated the effectiveness of SiMnS as a supplementary cementitious material and reinforced its potential application in sustainable construction practices.

These findings demonstrate that SiMnS, when ground to an appropriate SSA (235 m^2/kg) and used in the optimal percentage of cement replacement (10%wt), can be more effectively employed as a supplementary cementitious material, contributing to both performance enhancement and environmental sustainability.

5.3 Recommendation for Future Work

Based on the findings presented in this study, several avenues for future research are recommended to address the limitations and further enhance the performance and applicability of SiMnS as a cement replacement material.

A key challenge for future work lies in balancing SSA optimization with workability. While this study highlights the benefits of higher SSA (235 m^2/kg) in improving the mechanical properties of concrete, challenges such as increased water demand and reduced workability were observed at excessively high SSA values (>235 m^2/kg). Future research should focus on developing strategies to optimize SSA while mitigating workability issues. This could include exploring water-reducing admixtures, modifying the slag grinding process, or combining SiMnS with other supplementary cementitious materials to maintain a balance between strength enhancement and usability.

Further research should also prioritise the assessment of environmental compatibility through leaching studies, crucial for quantifying the release of potential contaminants under varying SSA conditions and ensuring that performance optimisation does not compromise long-term ecological safety. Concurrently, efforts to enhance long-term durability—particularly under extended freeze-thaw cycles—are warranted. This could involve exploring chemical admixtures, supplementary cementitious materials, or tailored processing techniques, supported by microstructural analysis to elucidate degradation mechanisms.

To bridge the gap between laboratory research and industrial adoption, studies must address practical challenges related to slag source variability, quality control, and workability management in production-scale mixes. Research into regional and process-

induced variations in SiMnS composition is essential for developing robust, standardised application guidelines. Furthermore, a comprehensive sustainability appraisal, including life-cycle assessment and carbon footprint analysis, is needed to rigorously quantify the environmental benefits of SiMnS concrete. Finally, large-scale pilot projects and long-term field trials are indispensable for validating structural performance and durability under real-world conditions, thereby providing the necessary evidence base for widespread implementation.

REFERENCES

Abrams, D. A. (1918). *Design of concrete mixtures* (Bulletin No. 1). Structural Materials Research Laboratory, Lewis Institute.

Adaway, M., & Wang, Y. (2015). Recycling waste glass as fine aggregate in cementitious materials. *Procedia Engineering, 125*, 750–756.

Al-Aomar, R. (2010). A combined ahp-entropy method for deriving subjective and objective criteria weights. *The International Journal of Industrial Engineering: Theory, Applications and Practice*, *17*(1), 12–24.

Allahverdi, A., & Ahmadnezhad, S. (2014). Mechanical activation of silicomanganese slag and its influence on the properties of Portland slag cement. *Powder Technology*, *251*, 41–51.

Ameri, F., Shoaei, P., Musaeei, H. R., Zareei, S. A., & Cheah, C. B. (2020). Partial replacement of copper slag with treated crumb rubber aggregates in alkali-activated slag mortar. *Construction and Building Materials*, *256*, 119468.

Ameri, F., Shoaei, P., Zareei, S. A., & Behforouz, B. (2019). Geopolymers vs. alkali-activated materials (AAMs): A comparative study on durability, microstructure, and resistance to elevated temperatures of lightweight mortars. *Construction and Building Materials*, *222*, 49–63.

Amran, Y. M., Alyousef, R., Alabduljabbar, H., & El-Zeadani, M. (2020). Clean production and properties of geopolymer concrete; A review. *Journal of Cleaner Production*, *251*, 119679.

ASTM International. (2015). *Standard test method for length change of hydraulic-cement mortars exposed to a sulfate solution* (ASTM C1012-15). ASTM International.

ASTM International. (2017). *Standard test method for electrical indication of concrete's ability to resist chloride ion penetration* (ASTM C1202-17). ASTM International.

ASTM International. (2017). *Standard test method for length change of hardened hydraulic-cement mortar and concrete* (ASTM C157/C157M-17). ASTM International.

ASTM International. (2020). *Standard test method for flow of hydraulic cement mortar* (ASTM C1437-20). ASTM International.

Awoyera, P., & Adesina, A. (2019). A critical review on application of alkali activated slag as a sustainable composite binder. *Case Studies in Construction Materials*, *11,* e00268.

Benhelal, E., Zahedi, G., Shamsaei, E., & Bahadori, A. (2013). Global strategies and potentials to curb CO2 emissions in cement industry. *Journal of Cleaner Production*, *51*, 142–161.

Bentz, D. P., Ferraris, C. F., Galler, M. A., Hansen, A. S., & Guynn, J. M. (2012). Influence of particle size distributions on yield stress and viscosity of cement–fly ash pastes. *Cement and Concrete Research, 42*(2), 404–409.

Bentz, D. P., Garboczi, E. J., Haecker, C. J., & Jensen, O. M. (1999). Effects of cement particle size distribution on performance properties of Portland cement-based materials. *Cement and Concrete Research, 29*(10), 1663–1671.

British Standards Institution. (2019). *Testing fresh concrete – Part 2: Slump test* (BS EN 12350-2:2019). British Standards Institution.

British Standards Institution. (2019). *Testing fresh concrete – Part 6: Density* (BS EN 12350-6:2019). British Standards Institution.

British Standards Institution. (2019). *Testing hardened concrete – Part 3: Compressive strength of test specimens* (BS EN 12390-3:2019). British Standards Institution.

British Standards Institution. (2019). *Testing hardened concrete – Part 5: Flexural strength of test specimens* (BS EN 12390-5:2019). British Standards Institution.

British Standards Institution. (2019). *Testing hardened concrete – Part 8: Depth of penetration of water under pressure* (BS EN 12390-8:2019). British Standards Institution.

British Standards Institution. (2019). *Testing hardened concrete – Part 9: Freeze–thaw resistance with de-icing salts – Scaling* (BS EN 12390-9:2019). British Standards Institution.

Cai, H., & Liu, X. (1998). Freeze-thaw durability of concrete: ice formation process in pores. *Cement and Concrete Research*, *28*(9), 1281–1287.

Celik, I. B. (2009). The effects of particle size distribution and surface area upon cement strength development. *Powder Technology, 188*(3), 272–276.

Chan, J., Papaioannou, I., & Straub, D. (2024). Bayesian improved cross entropy method with categorical mixture models for network reliability assessment. *Reliability Engineering & System Safety*, *252*, 110432.

Chang, P. K., Peng, Y. N., & Hwang, C. L. (2001). A design consideration for durability of high-performance concrete. *Cement and Concrete Composites, 23*(4-5), 375–380.

Chao, L., Zhenneng, L., Yulie, G., & Zhitong, M. (2017). The comprehensive evaluation of optimization air-condition system based on analytic hierarchy methodology. *Energy Procedia*, *105*, 2095–2100.

Chen, J. J., & Kwan, A. K. H. (2012). Superfine cement for improving packing density, rheology and strength of cement paste. *Cement and Concrete Composites, 34*(1), 1–10.

Chen, P., Liu, R., & An, Q. (2008). Experimental study on durability of cement concrete with manganese slag mineral admixture. *Concrete,* (10), 77–79.

Chen, P., Wang, Z., & Liu, R. J. (2010). Experimental study on concrete of manganese slag in different dosage. *Concrete*, *2*, 71–73.

Cheng, Z., Cheng, X., Cheng, Z., Suo, C., Zhang, H., Liu, L., & Liu, Y. (2023). Mechanical, structural and microstructural properties of CFB desulfurization slag and silico-manganese slag based-geopolymer pastes. *Silicon*, *15*(4), 1835–1846.

Chousidis, N., Ioannou, I., & Batis, G. (2018). Utilization of electrolytic manganese dioxide (EMD) waste in concrete exposed to salt crystallization. *Construction and Building Materials*, *158*, 708–718.

Chousidis, N., Rakanta, E., Ioannou, I., & Batis, G. (2015). Anticorrosive effect of electrochemical manganese dioxide by-products in reinforced concrete. *Journal of Materials Science and Chemical Engineering*, *3*(5), 9–20.

Cota, T. G., Cheloni, L. M. D. M. S., Guedes, J. J. M., & Reis, É. L. (2023). Silico-manganese slag and its utilization into alkali-activated materials: A critical review. *Construction and Building Materials*, *399*, 132589.

Coussy, O. (2005). Poromechanics of freezing materials. *Journal of the Mechanics and Physics of Solids*, *53*(8), 1689–1718.

Coussy, O., & Fen-Chong, T. (2005). Crystallization, pore relaxation and micro-cryosuction in cohesive porous materials. *Comptes Rendus. Mécanique*, *333*(6), 507–512.

Criado, M., Bernal, S. A., Garcia-Trinanes, P., & Provis, J. L. (2018). Influence of slag composition on the stability of steel in alkali-activated cementitious materials. *Journal of Materials Science*, *53*(7), 5016–5035.

Crossin, E. (2015). The greenhouse gas implications of using ground granulated blast furnace slag as a cement substitute. *Journal of Cleaner Production*, *95*, 101–108.

Dai, J., Wang, Q., Xie, C., Xue, Y., Duan, Y., & Cui, X. (2019). The effect of fineness on the hydration activity index of ground granulated blast furnace slag. *Materials*, *12*(18), 2984.

Damineli, B. L., Pileggi, R. G., & John, V. M. (2017). Influence of packing and dispersion of particles on the cement content of concretes. *Revista IBRACON de Estruturas e Materiais, 10*(05), 998–1024.

Delgado-Plana, P., García-Díaz, A., Bueno-Rodríguez, S., & Eliche Quesada, D. (2023). Influence of NaOH molarity and Portland cement addition on performance of alkali activated cements based in silicomanganese slags. Construction and Building *Materials, 407*, 133544.

Deng, Y., Liu, Y., Li, T., Ren, S., Zhou, J., & Wang, X. (2024). Development and application of SiMn slag-based early high-strength shotcrete using an inorganic–organic activation system. *Concrete World*, (04), 18–24.

Dong, X., Han, F., Hua, W., Liu, T., Zheng, J., An, C., & Li, M. (2024). Preparation and properties of microcrystalline foam ceramics from silicon manganese smelting slag. *Ceramics International*, *50*(1), 2073–2082.

Du, B., Zhou, C., Dan, Z., Luan, Z., & Duan, N. (2014). Preparation and characteristics of steam-autoclaved bricks produced from electrolytic manganese solid waste. *Construction and Building Materials*, *50*, 291–299.

Duan, N., Dan, Z., Wang, F., Pan, C., Zhou, C., & Jiang, L. (2011). Electrolytic manganese metal industry experience based China's new model for cleaner production promotion. *Journal of Cleaner Production*, *19*(17-18), 2082–2087.

Duan, Y., Mu, H., Li, N., Li, L., & Xue, Z. (2016). Research on comprehensive evaluation of low carbon economy development level based on AHP-entropy method: A case study of Dalian. *Energy Procedia*, *104*, 468–474.

Durastanti, C., & Moretti, L. (2020). Environmental impacts of cement production: a statistical analysis. *Applied Sciences*, *10*(22), 8212.

Elhaik, E. (2022). Principal component analyses (PCA)-based findings in population genetic studies are highly biased and must be reevaluated. *Scientific Reports*, *12*(1), 14683.

Elkhayat, Y. O., Ibrahim, M. G., Tokimatsu, K., & Ali, A. A. M. (2020). Multi-criteria selection of high-performance glazing systems: A case study of an office building in New Cairo, Egypt. *Journal of Building Engineering*, *32*, 101466.

Escalante-Garcia, J. I., Espinoza-Perez, L. J., Gorokhovsky, A., & Gomez-Zamorano, L. Y. (2009). Coarse blast furnace slag as a cementitious material, comparative study as a partial replacement of Portland cement and as an alkali activated cement. *Construction and Building Materials*, *23*(7), 2511–2517.

Fahim, A., Tan, Q., Naz, B., Ain, Q. u., & Bazai, S. U. (2021). Sustainable higher education reform quality assessment using SWOT analysis with integration of AHP and entropy models: A case study of Morocco. *Sustainability*, *13*(8), 4312.

Fan, J., Liu, R., Chen, P., Zhang, J., Tang, X., & Li, L. (2024). Activation of superfine-powder admixture of water-cooled manganese，slag-furnace and slag-limestone. *Journal of Guilin University of Technology, 44*(1), 149–154.

Fei, X. P., Guo, L. P., Bian, R. S., Lyu, B. C., & Wu, J. D. (2023). Research progress on sulfate durability of high ductility cementitious composites. *Construction and Building Materials, 385*, 131509.

Fen-Chong, T., Fabbri, A., & Azouni, A. (2006). Transient freezing–thawing phenomena in water-filled cohesive porous materials. *Cold Regions Science and Technology*, *46*(1), 12–26.

Feng, Q. (2023). Supply chain financial credit evaluation mechanism under the background of big data. *Optik*, *272*, 170266.

Feng, Q, & Zhou, S. (2009). Application of manganese slag-cement concrete in harbor and channel engineering. *Journal of Concrete, 13*(3), 101–103.

Feng, Y. L., & Xu, X. S. (2006). Syndepositional structural slope-break zone controls on lithologic reservoirs—A case from Paleogene Bohai Bay Basin. *Petroleum Exploration and Development*, *33*(1), 22–32.

Frías, M., de Rojas, M. I. S., & Rodríguez, C. (2009). The influence of SiMn slag on chemical resistance of blended cement pastes. *Construction and Building Materials*, *23*(3), 1472–1475.

Frias, M., de Rojas, M. I. S., Santamaría, J., & Rodríguez, C. (2006). Recycling of silicomanganese slag as pozzolanic material in Portland cements: Basic and engineering properties. *Cement and Concrete Research*, *36*(3), 487–491.

Fu, Y., Cai, L., & Wu, Y. (2011). Freeze-thaw cycle test and damage mechanics models of alkali-activated slag concrete. *Construction and Building Materials*, *25*(7), 3144–3148.

Gagg, C. R. (2014). Cement and concrete as an engineering material: An historic appraisal and case study analysis. *Engineering Failure Analysis*, *40*, 114–140.

Gao, Z., Han, J., Song, X., & Wang, Z. (2009). Effect of manganese slag admixture on concrete properties under excitation. *China Concrete and Cement Products,* (6), 16–19.

Ghasemi, Y., Emborg, M., & Cwirzen, A. (2018). Estimation of specific surface area of particles based on size distribution curve. *Magazine of Concrete Research*, *70*(10), 533–540.

Golany, B., & Roll, Y. (1989). An application procedure for DEA. *Omega*, *17*(3), 237–250.

Greco, S., Figueira, J., & Ehrgott, M. (Eds.). (2016). *Multiple criteria decision analysis* (Vol. 37). Springer.

Groot, D. R., Kazadi, D., Pollmann, H., De Villiers, J., Redtmann, T., & Steenkamp, J. (2013). The recovery of manganese and generation of a valuable residue from ferromanganese slags by a hydrometallurgical route. In *Proceedings of the Thirteenth International Ferroalloys Congress*, (pp. 9-13). Almaty, Kazakhstan: INFACON XIII.

Hagelstein, K. (2009). Globally sustainable manganese metal production and use. *Journal of Environmental Management*, *90*(11), 36–46.

Han, D., Yoon, J. Y., & Kim, J. H. (2019). Control of viscosity of cementitious materials using waste limestone powder. *International Journal of Concrete Structures and Materials, 13*, 1–12.

Han, F., Wu, L. E., Han, F., & Wu, L. (2019). Resource utilization of electrolytic manganese residues. *Industrial Solid Waste Recycling in Western China*, 127–164.

Han, G., Feng, G., Tang, C., Pan, C., Zhou, W., & Zhu, J. (2023). Evaluation of the ventilation mode in an ISO class 6 electronic cleanroom by the AHP-entropy weight method. *Energy*, *284*, 128586.

Hanifa, M., Agarwal, R., Sharma, U., Thapliyal, P., & Singh, L. P. (2023). A review on CO2 capture and sequestration in the construction industry: Emerging approaches and commercialised technologies. *Journal of CO2 Utilization*, *67*, 102292.

Hanim, H., & Rahmadoni, J. (2020). Determination of lecturer reception using Analytical Hierarchy Process (AHP). *Journal of Applied Engineering and Technological Science*, *1*(2), 136–141.

He, D., Shu, J., Wang, R., Chen, M., Wang, R., Gao, Y., Liu, R., Liu, Z., Xu, Z., Tan, D., Gu, H., & Wang, N. (2021). A critical review on approaches for electrolytic manganese residue treatment and disposal technology: Reduction, pretreatment, and reuse. *Journal of Hazardous Materials*, *418*, 126235.

He, J., Sun, C., Hu, W., Ni, Z., Yin, X., & Wang, X. (2024). Study on the effect of silica–manganese slag mixing on the deterioration resistance of concrete under the action of salt freezing. *Buildings*, *14*(9), 2684.

He, P. Y., Zhang, Y. J., Chen, H., & Liu, L. C. (2019). Development of an eco-efficient CaMoO4/electroconductive geopolymer composite for recycling silicomanganese slag and degradation of dye wastewater. *Journal of Cleaner Production*, *208*, 1476–1487.

He, S., Jiang, D., Hong, M., & Liu, Z. (2021). Hazard-free treatment and resource utilisation of electrolytic manganese residue: A review. *Journal of Cleaner Production*, *306,* 127224.

Heidari, M., Torabi-Kaveh, M., & Mohseni, H. (2017). Assessment of the effects of freeze–thaw and salt crystallization ageing tests on Anahita Temple Stone, Kangavar, West of Iran. *Geotechnical and Geological Engineering*, *35*, 121–136.

Her, J. W., & Lim, N. G. (2010). Physical and chemical properties of nano-slag mixed mortar. *Journal of the Korea Institute of Building Construction*, *10*(6), 145–154.

Holt, E., & Leivo, M. (2004). Cracking risks associated with early age shrinkage. *Cement and Concrete Composites, 26*(5), 521–530.

Hong, S. K. (2011). Status of China Mn-ore in resources exploitation and the sustainable development. *China's Manganese Industry*, *29*(3), 13–16.

Hou, P. K., Qian, J. S., Wang, Z., & Deng, C. (2012). Production of quasi-sulfoaluminate cementitious materials with electrolytic manganese residue. *Cement and Concrete Composites*, *34*(2), 248–254.

Hou, Y. (2024). Credit risk assessment of commercial banks based on AHP and entropy method. *Economic Outlook The Bohai Sea*(01), 159–162.

Ismail, I., Bernal, S. A., Provis, J. L., San Nicolas, R., Brice, D. G., Kilcullen, A. R., Hamdan, S., & Van Deventer, J. S. (2013). Influence of fly ash on the water and chloride permeability of alkali-activated slag mortars and concretes. *Construction and Building Materials*, *48*, 1187–1201.

Jayakantha, D. R., Gunawardhana, N., Bandara, H. M. N., Comini, E., Gunawardana, N. M., & Karunarathne, S. M. M. L. (2021). Low cost automated instrumentation for the measurement of the specific surface area of powders by the Brunauer–Emmett–Teller (BET) method. *Instrumentation Science & Technology*, *50*(1), 47–56.

Jiang, L., Niu, D., Yuan, L., & Fei, Q. (2015). Durability of concrete under sulfate attack exposed to freeze–thaw cycles. *Cold Regions Science and Technology*, *112*, 112–117.

Khan, K., & Amin, M. N. (2017). Influence of fineness of volcanic ash and its blends with quarry dust and slag on compressive strength of mortar under different curing temperatures. *Construction and Building Materials*, *154*, 514–528.

Khan, M. I., & Siddique, R. (2011). Utilization of silica fume in concrete: Review of durability properties. *Resources, Conservation and Recycling, 57*, 30–35.

Kim, Y. J., & Yoon, D. K. (2010). Identifying critical sources of bridge deterioration in cold regions through the constructed bridges in North Dakota. *Journal of Bridge Engineering*, *15*(5), 542–552.

Korouzhdeh, T., Eskandari-Naddaf, H., & Kazemi, R. (2022). The ITZ microstructure, thickness, porosity and its relation with compressive and flexural strength of cement mortar; influence of cement fineness and water/cement ratio. *Frontiers of Structural and Civil Engineering, 16*(2), 191–201.

Kumar, S., García-Triñanes, P., Teixeira-Pinto, A., & Bao, M. (2013). Development of alkali activated cement from mechanically activated silico-manganese (SiMn) slag. *Cement and Concrete Composites*, *40*, 7–13.

Kumar, S., Kumar, R., Bandopadhyay, A., Alex, T. C., Kumar, B. R., Das, S. K., & Mehrotra, S. P. (2008). Mechanical activation of granulated blast furnace slag and its effect on the properties and structure of portland slag cement. *Cement and Concrete Composites*, *30*(8), 679–685.

Kwan, A. K. H., & Chen, J. J. (2013). Adding fly ash microsphere to improve packing density, flowability and strength of cement paste. *Powder Technology*, *234*, 19–25.

Lai, Y. J., Liu, T. Y., & Hwang, C. L. (1994). Topsis for MODM. *European Journal of Operational Research*, *76*(3), 486–500.

Lan, J., Sun, Y., Tian, H., Zhan, W., Du, Y., Ye, H., Du, D., Zhang, T. C., & Hou, H. (2021). Electrolytic manganese residue-based cement for manganese ore pit backfilling: Performance and mechanism. *Journal of Hazardous Materials, 411*, 124941.

Lan, J. Q. (2006). A test to corn production with fertilizer of Mn-dregs. *China's Manganese Industry*, *2*, 43–44.

Lan, J. Q., & Wang, H. A. (2006). Waste dregs of EMM for usage of crops. *China's Manganese Industry*, *24*(4), 23–25.

Lavanya, P., & VenkatRao, N. (2023). Study on the engineering properties of concrete made of poypropylene fiber and combination of silico manganese slag. *Materials Today: Proceedings, 36*(8), 223–126.

Lee, Y. E., & Kolbeinsen, L. (2021). Behavior of slag in ferromanganese and silicomanganese smelting process. *Metallurgical and Materials Transactions B*, *52*(5), 3142–3150.

Li, F., Qin, J., & Ma, X. (2022). Research on the evaluation of enterprise competitiveness based on AHP-entropy TOPSIS method—take Xinjiang listed companies as an Example. *Frontiers in Management Science*, *1*(2), 8–15.

Li, J., Xu, W., Cui, P., Qiao, B., Feng, X., Xue, H., Wang, X., & Xiao, L. (2020). Optimization configuration of regional integrated energy system based on standard module. *Energy and Buildings*, *229*, 110485.

Li, M., Lu, Y., Liu, Y., Chu, J., Zhang, T., & Wang, W. (2024). Influence of the Steel Slag Particle Size on the Mechanical Properties and Microstructure of Concrete. *Sustainability, 16*(5), 2083.

Li, T. P., Xie, H. L., He, X. M., & Zhou, X. Z. (2007). Experimental study of calcined electrolysis manganese residue and fly ash complex admixture. *Bulletin of the Chinese Ceramic Society*, *26*(3), 567–592.

Li, X., Wang, W., Zhu, Z., & Zheng, K. (2021). Investigation on durability behaviour and optimization of concrete with triple-admixtures subjected to freeze-thaw cycles in salt solution. *Advances in Materials Science and Engineering*, *2021*(1), 5572011.

Li, Z. Y., Cui, Y. P., Jia, J. Q., & Xin, C. P.(2022). Long-term stability of tunnels in cold regions under freeze-thaw cycles. *Science Technology and Engineering*, *22*(5), 2032–2039.

Liang, D. Q., Qin, F., Li, X. G., & Jiang, J. B. (2011). Performance of concrete made with manganese slag. *Advanced Materials Research*, *335*, 333–338.

Liang, X. (2023). Research on the quality evaluation of archival patents based on AHP-entropy method. *Master's degree thesis of Liaoning University*, 31–35.

Liu, G., & Yu, J. (2007). Gray correlation analysis and prediction models of living refuse generation in Shanghai city. *Waste Management*, *27*(3), 345–351.

Liu, R. J., Ding, Q. J., Chen, P., & Yang, G. Y. (2012). Durability of concrete made with manganese slag as supplementary cementitious materials. *Journal of Shanghai Jiaotong University (Science)*, *17*(3), 345–349.

Liu, S., & Li, L. (2014). Influence of fineness on the cementitious properties of steel slag. *Journal of Thermal Analysis and Calorimetry*, *117*, 629–634.

Liu, S., Wang, L., & Chou, K. (2016). A novel process for simultaneous extraction of iron, vanadium, manganese, chromium, and titanium from vanadium slag by molten salt electrolysis. *Industrial & Engineering Chemistry Research*, *55*(50), 12962–12969.

Liu, L., Wang, Y., Wan, J., Zhan, M., & Zheng, Z. (2017). Activation of water-quenched manganese slag and its experimental application in concrete. *Building Materials Development Guide, 15*(24), 75–77.

Lomboy, G. R., Wang, K., & Quanji, Z. (2012). Properties of cementitious materials in their dry state and their influences on viscosity of the cementitious pastes. *Powder Technology*, *229*, 104–111.

Luo, Q., Liu, D. X., Qiao, P., Feng, Q. G., & Sun, L. Z. (2018). Microstructural damage characterization of concrete under freeze-thaw action. *International Journal of Damage Mechanics*, *27*(10), 1551–1568.

Ma, J., Zhang, H., Wang, D., Wang, H., & Chen, G. (2022). Rheological properties of cement paste containing ground fly ash based on particle morphology analysis. *Crystals, 12*(4), 524.

Ma, S., Li, K., Zhang, J., Jiang, C., Bi, Z., Sun, M., & Wang, Z. (2021). Effect of MnO content on slag structure and properties under different basicity conditions: A molecular dynamics study. *Journal of Molecular Liquids*, *336*, 116304.

Ma, Y., Moosavi-Khoonsari, E., Kero, I. T., & Tranell, G. M. (2018). Element distribution in the silicomanganese production process. *Metallurgical and Materials Transactions B*, *49*(5), 2444–2457.

Maćkiewicz, A., & Ratajczak, W. (1993). Principal components analysis (PCA). *Computers & Geosciences*, *19*(3), 303–342.

Mahmudova, S. (2020). Application of the TOPSİS method to improve software efficiency and to optimize its management. *Soft Computing*, *24*(1), 697–708.

Mao, C., Joneurairatana, E., & Vongphantuset, J. (2024). Evaluation of regional green building weight calibration system based on AHP entropy weight method. *Revista Ibérica de Sistemas e Tecnologias de Informação,* (E67), 433–450.

Mehdipour, I., & Khayat, K. H. (2017). Effect of particle-size distribution and specific surface area of different binder systems on packing density and flow characteristics of cement paste. *Cement and Concrete Composites, 78*(2), 120–131.

Mehta, P. K., & Monteiro, P. (2006). Concrete: microstructure, properties, and materials. *Preticehall International*, *13*(4), 499–499.

Michalski, D. J., & Bearman, C. (2017). Factors affecting the decision making of pilots who fly in Outback Australia. In *Decision Making in Aviation* (pp. 409–414). Routledge.

Miller, S. A., Horvath, A., Monteiro, P. J., & Ostertag, C. P. (2015). Greenhouse gas emissions from concrete can be reduced by using mix proportions, geometric aspects, and age as design factors. *Environmental Research Letters*, *10*(11), 114017.

Miller, S. A., John, V. M., Pacca, S. A., & Horvath, A. (2018). Carbon dioxide reduction potential in the global cement industry by 2050. *Cement and Concrete Research*, *114*, 115–124.

Ministry of Housing and Urban-Rural Development of the People's Republic of China. (2009). *Standard for test methods of long-term performance and durability of ordinary concrete* (GB/T 50082-2009). China Architecture & Building Press.

Mohamed, O. A., Rens, K. L., & Stalnaker, J. J. (2000). Factors affecting resistance of concrete to freezing and thawing damage. *Journal of Materials in Civil Engineering, 12*(1), 26–32.

Narayan, R. S., & Goodchild, C. H. (2006). Concise Eurocode 2. *The Concrete Centre, UK*.

Nasir, M., Johari, M. A. M., Maslehuddin, M., & Yusuf, M. O. (2020). Magnesium sulfate resistance of alkali/slag activated silico-manganese fume-based composites. *Construction and Building Materials*, *265*, 120851.

Nath, S. K., & Kumar, S. (2019). Influence of granulated silico-manganese slag on compressive strength and microstructure of ambient cured alkali-activated fly ash binder. *Waste and Biomass Valorization*, *10*, 2045–2055.

Nath, S. K., & Kumar, S. (2016). Evaluation of the suitability of ground granulated silico-manganese slag in Portland slag cement. *Construction and Building Materials*, *125*, 127–134.

Nath, S. K., & Kumar, S. (2017). Reaction kinetics, microstructure and strength behavior of alkali activated silico-manganese (SiMn) slag–Fly ash blends. *Construction and Building Materials*, *147*, 371–379.

Nath, S. K., Randhawa, N. S., & Kumar, S. (2022). A review on characteristics of silico-manganese slag and its utilization into construction materials. *Resources, Conservation and Recycling*, *176*, 105946.

Navarro, R., Alcocel, E. G., Sánchez, I., Garcés, P., & Zornoza, E. (2018). Mechanical properties of alkali activated ground SiMn slag mortars with different types of aggregates. *Construction and Building Materials*, *186*, 79–89.

Navarro, R., Zornoza, E., Garcés, P., Sánchez, I., & Alcocel, E. G. (2017). Optimization of the alkali activation conditions of ground granulated SiMn slag. *Construction and Building Materials*, *150,* 781–791.

Navarro, R., Zornoza, E., Sánchez, I., & Alcocel, E. G. (2022). Influence of the type and concentration of the activator on the microstructure of alkali activated SiMn slag pastes. *Construction and Building Materials*, *342*, 128067.

Ng, C. K., Ting, J. K. S., Jack, N. L., Lim, L. L. P., & Nee, S. (2024). The properties of normal concrete with ground manganese slag as binder replacement. *Journal of Advanced Research in Applied Mechanics*, *116*(1), 62–74.

Olsen, S. E., Tangstad, M., & Lindstad, T. (2007). *Production of manganese ferroalloys*. Tapir academic press.

Onn, C. C., Mo, K. H., Radwan, M. K., Liew, W. H., Ng, C. G., & Yusoff, S. (2019). Strength, carbon footprint and cost considerations of mortar blends with high volume ground granulated blast furnace slag. *Sustainability*, *11*(24), 7194.

Otieno, M., Beushausen, H., & Alexander, M. (2014). Effect of chemical composition of slag on chloride penetration resistance of concrete. *Cement and Concrete Composites*, *46*, 56–64.

Panchal, S., & Shrivastava, A. K. (2022). Landslide hazard assessment using analytic hierarchy process (AHP): A case study of National Highway 5 in India. *Ain Shams Engineering Journal*, *13*(3), 101626.

Papadakis, V. G., Antiohos, S., & Tsimas, S. (2002). Supplementary cementing materials in concrete: Part II: A fundamental estimation of the efficiency factor. *Cement and Concrete Research*, *32*(10), 1533–1538.

Papadakis, V. G., & Tsimas, S. (2002). Supplementary cementing materials in concrete: Part I: efficiency and design. *Cement and Concrete Research*, *32*(10), 1525–1532.

Paris, J. M., Roessler, J. G., Ferraro, C. C., DeFord, H. D., & Townsend, T. G. (2016). A review of waste products utilized as supplements to Portland cement in concrete. *Journal of Cleaner Production*, *121*, 1–18.

Park, J., Song, H., & Choi, H. (2022). Estimation of water-to-cement ratio in cementitious materials using electrochemical impedance spectroscopy and artificial neural networks. *Construction and Building Materials, 329*, 128843.

Pathak, D. K., Verma, A., & Kumar, V. (2020). Performance variables of GSCM for sustainability in Indian automobile organizations using TOPSIS method. *Business Strategy & Development*, *3*(4), 590–602.

Peng, Y., Duan, J., & Sun, B. (2024). Measurement and evaluation of high-quality development of logistics industry based on new development concepts. *Journal of Hengshui University*, *26*(4), 51–57.

Popovics, S. (1990). Analysis of concrete strength versus water-cement ratio relationship. *ACI Materials Journal, 87*(5), 517–529.

Pourchez, J., Grosseau, P., & Ruot, B. (2009). Current understanding of cellulose ethers impact on the hydration of C3A and C3A-sulphate systems. *Cement and Concrete Research*, *39*(8), 664–669.

Provis, J. L., Palomo, A., & Shi, C. (2015). Advances in understanding alkali-activated materials. *Cement and Concrete Research*, *78*, 110–125.

Qian, J., Hou, P., Wang, Z., & Qu, Y. (2012). Crystallization characteristic of glass-ceramic made from electrolytic manganese residue. *Journal of Wuhan University of Technology-Mater. Sci. Ed.*, *27*(1), 45–49.

Qiang, W., Yan, P., Kong, X., & Yang, J. (2011). Compressive strength development and microstructure of cement-asphalt mortar. *Journal of Wuhan University of Technology-Materials Science Edition, 26*(5), 998–1003.

Qiao, D., Qian, J., Wang, Q., Dang, Y., Zhang, H., & Zeng, D. (2010). Utilization of sulfate-rich solid wastes in rural road construction in the Three Gorges Reservoir. *Resources, Conservation and Recycling*, *54*(12), 1368–1376.

Qin, L. J., Sun, Z. Y., Liu, L., & He, Y. (2014). Research on Assessment of Coordinated Evaluation in Electricity Ecosystem Based on Entropy Weight and AHP. *Applied Mechanics and Materials*, *644*, 3773–3779.

Rai, A., Prabakar, J., Raju, C. B., & Morchalle, R. K. (2002). Metallurgical slag as a component in blended cement. *Construction and Building Materials*, *16*(8), 489–494.

Ramachandran, V. S., Paroli, R. M., Beaudoin, J. J., & Delgado, A. H. (2002). Supplementary cementing materials and other additions. In *Handbook of thermal analysis of construction materials* (pp. 293–353). William Andrew.

Raveendran, N., & Vasugi, K. (2024). Synergistic effect of nano silica and metakaolin on mechanical and microstructural properties of concrete: An approach of response surface methodology. *Case Studies in Construction Materials, 20*, e03196.

Rechberger, H., & Graedel, T. E. (2002). The contemporary European copper cycle: statistical entropy analysis*, Ecological Economics, 42*(1-2), 59–72.

Ren, J. J., Zhang, Q., Zhang, Y. C., Wei, K., Zhang, K. Y., Ye, W. L., & Zhang, Y. (2023). Evaluation of slab track quality indices based on entropy weight-fuzzy analytic hierarchy process. *Engineering Failure Analysis*, *149*, 107244.

Rostamzadeh, R., Akbarian, O., Banaitis, A., & Soltani, Z. (2021). Application of DEA in benchmarking: a systematic literature review from 2003–2020. *Technological and Economic Development of Economy*, *27*(1), 175–222.

Saaty, T. L. (1980). The analytic hierarchy process (AHP). *The Journal of the Operational Research Society*, *41*(11), 1073–1076.

Saaty, T. L., & Alexander, J. M. (1981). *Thinking with models: Mathematical models in the physical, biological, and social sciences*. RWS Publications.

Saha, A. K., Khan, M. N. N., & Sarker, P. K. (2018). Value added utilization of by-product electric furnace ferronickel slag as construction materials: A review. *Resources, Conservation and Recycling, 134*, 10–24.

Scrivener, K. L., Crumbie, A. K., & Laugesen, P. (2004). The interfacial transition zone (ITZ) between cement paste and aggregate in concrete. *Interface Science, 12*, 411–421.

Shahidan, S., Aminuddin, E., Noor, K. M., Hannan, N. I. R. R., & Bahari, N. A. S. (2017). Potential of hollow glass microsphere as cement replacement for lightweight foam

concrete on thermal insulation performance. In *MATEC Web of Conferences*, *103*, 01014. EDP Sciences.

Shahrajabian, F., & Behfarnia, K. (2018). The effects of nano particles on freeze and thaw resistance of alkali-activated slag concrete. *Construction and Building Materials*, *176*, 172–178.

Sharma, R., & Khan, R. A. (2021). Sulfate resistance of self compacting concrete incorporating copper slag as fine aggregates with mineral admixtures. *Construction and Building Materials, 287*, 122985.

Sharmila, P., & Dhinakaran, G. (2015). Strength and durability of ultra fine slag based high strength concrete. *Structural Engineering and Mechanics: An International Journal*, *55*(3), 675–686.

Sharmila, P., & Dhinakaran, G. (2016). Compressive strength, porosity and sorptivity of ultra fine slag based high strength concrete. *Construction and Building Materials*, *120*, 48–53.

Shen, Y., & Liao, K. (2022). An application of analytic hierarchy process and entropy weight method in food cold chain risk evaluation model. *Frontiers in Psychology*, *13*, 825696.

Shen, Y., Wang, Y., Wei, X., Jia, H., & Yan, R. (2020). Investigation on meso-debonding process of the sandstone–concrete interface induced by freeze–thaw cycles using NMR technology. *Construction and Building Materials*, *252*, 118962.

Shi, C., Wang, D., Wu, L., & Wu, Z. (2015). The hydration and microstructure of ultra high-strength concrete with cement–silica fume–slag binder. *Cement and Concrete Composites*, *61*, 44–52.

Shoaei, P., Ameri, F., Reza Musaeei, H. R., Ghasemi, T., & Cheah, C. B. (2020). Glass powder as a partial precursor in Portland cement and alkali-activated slag mortar: A comprehensive comparative study. *Construction and Building Materials*, *251*, 118991.

Shoaei, P., Musaeei, H. R., Mirlohi, F., Ameri, F., & Bahrami, N. (2019). Waste ceramic powder-based geopolymer mortars: Effect of curing temperature and alkaline solution-to-binder ratio. *Construction and Building Materials*, *227*, 116686.

Sikalidis, C., & Zaspalis, V. (2007). Utilization of Mn–Fe solid wastes from electrolytic MnO_2 production in the manufacture of ceramic building products. *Construction and Building Materials, 21*(5), 1061–1068.

Singh, B. (2016). Analytical hierarchical process (AHP) and fuzzy AHP applications-A review paper. *International Journal of Pharmacy and Technology*, *8*(4), 4925–4946.

Singh, N. B., & Middendorf, B. (2020). Geopolymers as an alternative to Portland cement: An overview. *Construction and Building Materials*, *237*, 117455.

Snellings, R. (2016). Assessing, understanding and unlocking supplementary cementitious materials. *RILEM Technical Letters, 1*, 50–55.

Snellings, R., Suraneni, P., & Skibsted, J. (2023). Future and emerging supplementary cementitious materials. *Cement and Concrete Research*, *171*, 107199.

Song, H., & Li, X. (2021). An overview on the rheology, mechanical properties, durability, 3D printing, and microstructural performance of nanomaterials in cementitious composites. *Materials, 14*(11), 2950.

Song, W., Zhang, M., & Wu, H. (2024). Gray correlation analysis between mechanical performance and pore characteristics of permeable concrete. *Journal of Building Engineering*, *86*, 108793.

Sparta, M., & Risinggård, V. K. (2021). A finite-element method model for a ferromanganese and silicomanganese pilot furnace. *Journal of The Southern African Institute of Mining and Metallurgy*, *124*(3), 85–92.

Standardization Administration of China. (2005). *Test method for fluidity of cement mortar* (GB/T 2419-2005). China Standards Press.

Standardization Administration of China. (2021). *Test method of cement mortar strength (ISO method)* (GB/T 17671-2021). China Standards Press.

Su, H., Zhou, W., Lyu, X., Liu, X., Gao, W., Li, C., & Li, S. (2023). Remediation treatment and resource utilization trends of electrolytic manganese residue. *Minerals Engineering*, *202*, 108264.

Su, Z., Liu, Z., Wang, H., Xu, S., Wang, D., & Han, F. (2022). Reaction kinetics, microstructure and phase evolution of alkali-activated Si-Mn slag during early age. *Construction and Building Materials*, *333*, 127437.

Sun, H., Wang, J., Ren, J., Zhang, W., Tang, W., Wu, X., & Gu, A. (2021). Current situation of global manganese resources and suggestions for sustainable development in China. *Conservation and Utilization of Mineral Resources, 40*(6), 169–174.

Tamayo, P., García del Angel, G., Setién, J., Soto, A., & Thomas, C. (2023). Feasibility of silicomanganese slag as cementitious material and as aggregate for concrete. *Construction and Building Materials, 364*, 129938.

Tang, S., Wang, Y., Geng, Z., Xu, X., Yu, W., & Chen, J. (2021). Structure, fractality, mechanics and durability of calcium silicate hydrates. *Fractal and Fractional, 5*(2), 47.

Tangstad, M. (2013). Manganese ferroalloys technology. In *Handbook of ferroalloys* (pp. 221–266). *Butterworth-Heinemann*.

Tangstad, M., Bublik, S., Haghdani, S., Einarsrud, K. E., & Tang, K. (2021). Slag properties in the primary production process of Mn-Ferroalloys. *Metallurgical and Materials Transactions B*, 1–20.

Teh, S. H., Wiedmann, T., Castel, A., & de Burgh, J. (2017). Hybrid life cycle assessment of greenhouse gas emissions from cement, concrete and geopolymer concrete in Australia. *Journal of Cleaner Production*, *152*, 312–320.

Thomas, M. D. A., Hooton, R. D., Scott, A., & Zibara, H. (2012). The effect of supplementary cementitious materials on chloride binding in hardened cement paste. *Cement and Concrete Research, 42*(1), 1–7.

Ting, J. J., Low, W. W., Wong, K. S., Ting, T. Z. H., & Hamzah, A. R. (2023). Feasibility of recycling silicomanganese slag as a cementitious material. *AIP Conference Proceedings*, *2847*(1), 156–158.

Ting, M. Z. Y., Wong, K. S., Rahman, M. E., & Joo, M. S. (2020). Mechanical and durability performance of marine sand and seawater concrete incorporating silicomanganese slag as coarse aggregate. *Construction and Building Materials, 254*, 119195.

Uddin, M. P., Mamun, M. A., Afjal, M. I., & Hossain, M. A. (2021). Information-theoretic feature selection with segmentation-based folded principal component analysis (PCA) for hyperspectral image classification. *International Journal of Remote Sensing*, *42*(1), 286–321.

Vélez, W., Matta, F., & Ziehl, P. (2016). Electrochemical characterization of early corrosion in prestressed concrete exposed to salt water. *Materials and Structures*, *49*, 507–520.

Wan, G., Sun, D. J., Peng, B., & Mao, X. (2024). Risk Assessment of Urban Transportation Complex Hub from Resilience Perspective: An empirical study on Xi'an north railway station. *Natural Hazards Review*, *25*(4), 04024042.

Wang, B., Mu, L., Guo, S., & Bi, Y. (2019). Lead leaching mechanism and kinetics in electrolytic manganese anode slime. *Hydrometallurgy*, *183*, 98–105.

Wang, C., Jin, S., & Shi, H. (2014). Area change of the frozen ground in China in the next 50 years. *Journal of Glaciology and Geocryology*, *36*(1), 1–8.

Wang, D., Wang, Q., & Xue, J. (2020). Reuse of hazardous electrolytic manganese residue: Detailed leaching characterization and novel application as a cementitious material. *Resources, Conservation and Recycling*, *154*, 104645.

Wang, F., Long, G., Bai, M., Wang, J., Zhou, J. L., & Zhou, X. (2022). Application of electrolytic manganese residues in cement products through pozzolanic activity motivation and calcination. *Journal of Cleaner Production*, *338*, 130629.

Wang, J., Hu, X., Jiang, F., & Chen, H. (2024). The role and mechanism of rice husk ash particle characteristics in cement hydration process. *Materials*, *17*(22), 5594.

Wang, J., & Niu, D. (2016). Influence of freeze–thaw cycles and sulfate corrosion resistance on shotcrete with and without steel fiber. *Construction and Building Materials*, *122*, 628–636.

Wang, J., Peng, B., Chai, L., Zhang, Q., & Liu, Q. (2013). Preparation of electrolytic manganese residue–ground granulated blastfurnace slag cement. *Powder Technology*, *241*, 12–18.

Wang, Y., Zhang, N., Ren, Y., Xu, Y., & Liu, X. (2021). Effect of electrolytic manganese residue in fly ash-based cementitious material: Hydration behavior and microstructure. *Materials*, *14*(22), 7047.

Wanke, P. F., Jabbour, C. J. C., Antunes, J. J. M., de Sousa Jabbour, A. B. L., Roubaud, D., Sobreiro, V. A., & Gonzalez, E. D. S. (2021). An original information entropy-based

quantitative evaluation model for low-carbon operations in an emerging market. *International Journal of Production Economics*, *234*, 108061.

Wei, M. A., & Wang, D. Y. (2012). Studies on frozen soil mechanics in China in past 50 years and their prospect. *Chinese Journal of Geotechnical Engineering*, *34*(4), 625–640.

Wind, Y., & Saaty, T. L. (1980). Marketing applications of the analytic hierarchy process. *Management Science*, *26*(7), 641–658.

Wu, Z., Feng, Z., Pu, S., Zeng, C., Zhao, Y., Chen, C., Song, H., & Feng, X. (2024). Mechanical properties and environmental characteristics of the synergistic preparation of cementitious materials using electrolytic manganese residue, steel slag, and blast furnace slag. *Construction and Building Materials*, *411*, 134480.

Wu, J., Chen, X., & Lu, J. (2022). Assessment of long and short-term flood risk using the multi-criteria analysis model with the AHP-Entropy method in Poyang Lake basin. *International Journal of Disaster Risk Reduction*, *75*, 102968.

Wu, J., Zhao, G., Wang, N., Xu, Y., & Wang, M. (2024). Research on optimization of mining methods for broken ore bodies based on interval-valued pythagorean fuzzy sets and TOPSIS-GRA. *Scientific Reports*, *14*(1), 23397.

Xiao, K., Tamborski, J., Wang, X., Feng, X., Wang, S., Wang, Q., Lin, D., & Li, H. (2022). A coupling methodology of the analytic hierarchy process and entropy weight theory for assessing coastal water quality. *Environmental Science and Pollution Research*, 1–18.

Xie, C., Dong, D., Hua, S., Xu, X., & Chen, Y. (2012). Safety evaluation of smart grid based on AHP-entropy method. *Systems Engineering Procedia*, *4*, 203–209.

Xing, Z. B., Han, F. L., Li, M. H., Yang, B. G., Zheng, B., & Liu, T. T. (2024). Mechanical grinding characteristics of water-quenched siliconmanganese slag. *Comprehensive Utilization of Mineral Resources*, *45*(1), 174–180.

Xu, W., Yu, J., & Wang, H. (2024). The influence of manganese slag on the properties of ultra-high-performance concrete. *Materials*, *17*(2), 91–97.

Xu, Y., Liu, X., Zhang, Y., Tang, B., & Mukiza, E. (2019). Investigation on sulfate activation of electrolytic manganese residue on early activity of blast furnace slag in cement-based cementitious material. *Construction and Building Materials*, *229*, 116831.

Yan, W. (2008). Development of manganese ore resources and manganese slag industry in China. *Abstr Chin Acad J*, *26*, 7–11.

Yang, J., Wang, H., Peng, L., & Zhao, F. (2024). The Properties of high-performance concrete with manganese slag under salt actio. *Materials*, *17*(7), 1483.

Yang, C., Lv, X., Tian, X., Wang, Y., & Komarneni, S. (2014). An investigation on the use of electrolytic manganese residue as filler in sulfur concrete. *Construction and Building Materials*, *73*, 305–310.

Ye, F., Cheng, H., Xiang, Y., Liu, S., & Shi, W. (2023). Preparation of ceramic aggregate from electrolytic manganese slag and its application in concrete. *Inorganic Chemicals Industry*, *56*(6), 127–132.

Lee, Y. E., & Kolbeinsen, L. (2021). Behavior of slag in ferromanganese and silicomanganese smelting process. *Metallurgical and Materials Transactions B, 52*(5), 3142–3150.

Zamanabadi, S. N., Zareei, S. A., Shoaei, P., & Ameri, F. (2019). Ambient-cured alkali-activated slag paste incorporating micro-silica as repair material: Effects of alkali

activator solution on physical and mechanical properties. *Construction and Building Materials*, *22*9, 116911.

Zareei, S. A., Ameri, F., Bahrami, N., Shoaei, P., Musaeei, H. R., & Nurian, F. (2019). Green high strength concrete containing recycled waste ceramic aggregates and waste carpet fibers: Mechanical, durability, and microstructural properties. *Journal of Building Engineering*, *26*, 100914.

Zhang, C., Li, J., Yu, M., Lu, Y., & Liu, S. (2024). Mechanism and Performance Control Methods of Sulfate Attack on Concrete: A Review. *Materials, 17*(19), 4836.

Zhang, D., Xiao, D., Yu, Q., Chen, S., Chen, S., & Miao, M. (2017). Preparation of mesoporous silica from electrolytic manganese slags by using amino-ended hyperbranched polyamide as template. *ACS Sustainable Chemistry & Engineering*, *5*(11), 10258–10265.

Zhang, F., Hu, Z., Wei, F., Wen, X., Li, X., Dai, L., & Liu, L. (2021). Study on concrete deterioration in different NaCl-Na_2SO_4 solutions and the mechanism of Cl^- diffusion. *Materials (Basel)*, *14*(17), 5054.

Zhang, H., Ji, T., & Liu, H. (2019). Performance evolution of the interfacial transition zone (ITZ) in recycled aggregate concrete under external sulfate attacks and dry-wet cycling. *Construction and Building Materials, 229*, 116938.

Zhang, L., Li, X., & Guo, Y. (2024). Research on the Influencing Factors of Spatial Vitality of Night Parks Based on AHP–Entropy Weights. *Sustainability*, *16*(12), 5165.

Zhang, L., Xu, X., & Guo, Y. (2022). Comprehensive evaluation of the implementation effect of commercial street quality improvement based on AHP-Entropy weight method—taking Hefei Shuanggang old street as an example. *Land*, *11*(11), 2091.

Zhou, C., Wang, J., & Wang, N. (2013). Treating electrolytic manganese residue with alkaline additives for stabilizing manganese and removing ammonia. *Korean Journal of Chemical Engineering*, *30*(11), 2037–2042.

Zhou, D. J., Wu, F., & Shi, Q. (2012). Basic characteristics of manganese slag and research progress of application study of manganese slag in concrete. *Concrete,*(2), 63–65.

Zhou, X., Ma, Y., Liu, X., Tang, J., Zhou, C., Guo, L., & Yang, J. (2021). Synergistic leaching mechanism of chloride ions for extracting manganese completely from manganese carbonate ores. *Journal of Environmental Chemical Engineering*, *9*(1), 104918.

Zhou, Y., Hou, D., Jiang, J., Liu, L., She, W., & Yu, J. (2018). Experimental and molecular dynamics studies on the transport and adsorption of chloride ions in the nano-pores of calcium silicate phase: the influence of calcium to silicate ratios. *Microporous and Mesoporous Materials, 255*, 23–35.

Zhu, L., Zhao, C., & Dai, J. (2021). Prediction of compressive strength of recycled aggregate concrete based on gray correlation analysis. *Construction and Building Materials*, *273*, 121750.

APPENDICES

Appendix A: Journal Publications

1. **Li, F.**, Ng, C. K., & Zhao, Q. (2025). Using AHP-entropy method to evaluate the effect of specific surface area of manganese slag on concrete properties: A case study on sustainable cementitious materials. *SSRG International Journal of Civil Engineering, 12*(6), 177–189.
2. **Li, F.**, & Ng, C. K. (2025). Optimization of mechanical and durability properties of manganese slag hybrid fiber concrete using an L9 orthogonal design and grey relational analysis. *International Journal of Design & Nature and Ecodynamics, 20*(7), 1471–1481.
3. **Li, F.**, & Shi, B. (2025). Sensor placement optimization of civil engineering structures using GA-SA algorithm. *Archives of Civil Engineering, 71*(3), 97–110.